Title

Brain Imaging with Positron Emission Tomography: Quantification and Biomedical Applications in Alzheimer's Disease and Brain Tumors

Author

Wardak, Mirwais

Publication Date

2013

UNIVERSITY OF CALIFORNIA

Los Angeles

Brain Imaging with Positron Emission Tomography: Quantification and Biomedical Applications in Alzheimer's Disease and Brain Tumors

A dissertation submitted in partial satisfaction
of the requirements for the degree
Doctor of Philosophy in Biomedical Physics

by

Mirwais Wardak

2013

ABSTRACT OF THE DISSERTATION

Brain Imaging with Positron Emission Tomography: Quantification and Biomedical Applications in Alzheimer's Disease and Brain Tumors

by

Mirwais Wardak

Doctor of Philosophy in Biomedical Physics

University of California, Los Angeles, 2013

Professor Sung-Cheng Huang, Chair

Positron emission tomography (PET) is a unique and powerful imaging technique that is used to visualize and quantify various biological processes in living subjects in health and disease. PET imaging can also provide biological information for the assessment of therapies. In this dissertation, we will cover three projects that utilize the quantitative capability of PET for studying two neurological disorders: Alzheimer's disease and brain tumors.

One of the goals in PET imaging is to produce an image volume that accurately describes the true distribution of the injected radioactivity. The correction factor that has the most significant impact on the quantitative aspects of a PET image is attenuation correction. Without it, the reconstructed images will give a distorted view of the true activity distribution. Head movement during a PET scan (especially a dynamic scan) can also lead to a loss in the information content contained in a PET image. This is especially true when scanning patients with dementia or movement disorders. The transmission scan, which is typically acquired at the start of a PET study, corrects for photon attenuation in each of the serial emission scans that are acquired afterwards.

In the first project of this dissertation, we developed a retrospective image-based movement correction (MC) method and evaluated its implementation on dynamic ^{18}F-FDDNP PET images of cognitively intact control subjects and patients with Alzheimer's disease (AD), each with varying degrees of head movement. ^{18}F-FDDNP is a PET probe that binds to beta-amyloid plaques and neurofibrillary tangles, the neuropathological hallmarks of AD. The MC method corrected for transmission-emission misalignments as well as for emission-emission misalignments that might have been present in the dynamic PET scan. The image quality, tracer kinetics, and diagnostic accuracy of the ^{18}F-FDDNP PET images were significantly improved after applying the MC method.

In the second project of this dissertation, we investigated whether changes in ^{18}F-FLT kinetic parameters, taken early after the start of therapy, could predict overall survival and progression-free survival in patients with recurrent malignant glioma undergoing treatment with bevacizumab (an angiogenesis inhibitor) and irinotecan (a chemotherapeutic agent). ^{18}F-FLT is a radiotracer used in PET to measure cellular proliferation. We found that when a group of optimal kinetic parameter changes are incorporated into a linear discriminant function, one could accurately classify patients into their known survival groups. This method is advantageous because by reliably identifying short- and long-term survivors early during therapy, clinicians

can discontinue ineffective treatment strategies and switch to more advanced treatment regimens that could improve patient outcome.

Our third project expanded on what we did in our second project in that we acquired longitudinal ^{18}F-FDOPA PET scans in addition to ^{18}F-FLT PET scans. We also tried to predict overall survival as a continuous outcome variable using multiple linear regression (as opposed to a dichotomous categorical variable with discriminant analysis from before). In brain tumors, ^{18}F-FDOPA is used to image amino acid transport. We found that in patients with recurrent malignant glioma, kinetic information from ^{18}F-FLT alone was more predictive than using information from ^{18}F-FDOPA alone. Using both probes combined provided comparable results to using ^{18}F-FLT alone, suggesting that a single tracer may provide sufficient information for predicting OS with reasonable accuracy.

The studies reported in this dissertation have demonstrated in three examples that the utility of kinetic quantification can significantly improve the value of PET for imaging biological functions in brain tissues *in vivo*. The developed methodologies in these examples are also expected to be useful in other quantitative brain PET imaging studies – for other applications or using other tracers.

The dissertation of Mirwais Wardak is approved.

Jorge R. Barrio

Magnus Dahlbom

Timothy Deming

Christiaan Schiepers

Sung-Cheng Huang, Committee Chair

University of California, Los Angeles

2013

DEDICATION

I would like to dedicate this dissertation to my parents, Soorgul and Setara Wardak, for their love and continuous support throughout my life. I love you very much.

My dad and mom.

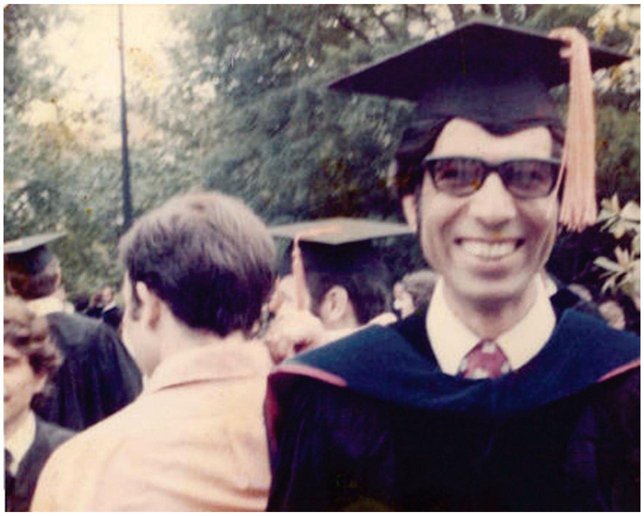

My dad at his doctoral commencement ceremony (Raleigh, North Carolina; May 1976)

TABLE OF CONTENTS

LIST OF FIGURES

LIST OF TABLES

SUPPLEMENTARY MATERIALS

Page

LIST OF SUPPLEMENTARY FIGURES

LIST OF SUPPLEMENTARY TABLES

LIST OF SUPPLEMENTARY MOVIES

ACKNOWLEDGEMENTS

This dissertation represents the culmination of my time here at UCLA. As I complete the final pages of this thesis, I cannot help but reflect on all of the support that has enabled me to reach where I am today.

First, I would like to express my sincerest appreciation to my dissertation advisor, Dr. Sung-Cheng (Henry) Huang, for all of his guidance and support throughout my Ph.D. study. Dr. Huang has been a phenomenal advisor and an exceptional role model. His breadth of knowledge, creativity, and infectious enthusiasm has always made it a pleasure to work with him. On a more personal level, I have really appreciated his generosity, great sense of humor, honesty, friendliness, and hosting of great parties! I could not have asked for a better advisor, mentor, or friend.

I would also like to thank my committee members, Dr. Jorge R. Barrio, Dr. Christiaan Schiepers, Dr. Magnus Dahlbom, and Dr. Timothy Deming for their valuable insights and helpful feedback over the years. Together with Dr. Huang, they make up my “Dream Team”. They are also some of the smartest people I have come across in my life.

Dr. Christiaan Schiepers, Dr. Tim Cloughesy, and Dr. Wei Chen provided excellent clinical support for the brain tumor projects in this work. They also gave valuable suggestions and skillful reflection concerning these projects. Dr. Gary W. Small provided terrific clinical support for the Alzheimer’s disease project in this work.

I am eternally grateful to Dr. Michael E. Phelps for giving me my first PET book. Dr. Phelps has been a great source of inspiration and I am deeply appreciative of all his help and advice. I want to further express my gratitude to Dr. Michael McNitt-Gray, Director of the Biomedical Physics Program, for providing an excellent academic environment and for his wonderful classroom instruction.

Graduate school has been one of the best times of my life. Part of the reason for this is that I had an incredible group of colleagues to work with in the lab. I would like to extend my deepest thanks to all the current and former members of the Huang Lab, including Dr. Koon-Pong Wong, Moses Wilks, Hu Ye, Dr. Chin-Lung (James) Yu, Dr. Hillary Protas, Dr. Wei Sha, and Dr. Greg Ferl. They have bestowed wonderful experiences and memories to last a lifetime. Special appreciation also goes out to many friends and classmates for their encouragement through all phases of the doctoral program. Moreover, I am indebted to all the teachers I had the pleasure to take classes with at UCLA.

I have benefited from many insightful discussions with Dr. Johannes Czernin, Dr. Nagichettiar Satyamurthy, Dr. Dan Silverman, Dr. Christine Wu, Dr. Kei Iwamoto, Dr. Carol Newton, Dr. Elliot Landaw, Dr. Bill McBride, Dr. Heinz Schelbert, Dr. Jie Liu, and Dr. Ernest Wright.

In addition, I want to express my gratitude to David Truong, Dat Vu, and Weber Shao for their computer and database support, the UCLA Cyclotron staff for help with preparation of the PET tracers used in this work, and the UCLA Nuclear Medicine staff for acquisition of the PET scans.

I would like to send heartfelt thanks to all the wonderful administrative staff at UCLA for making my life as a graduate student a much smoother one. In particular, I appreciate the help of Terry Moore, Reth Thach, David Tomita, Martha Riemer, Bernadette Omote, Amber Luke, and Michelle Yu.

Additionally, I am very lucky to have a wonderful family whose love, support, and humor have always been a constant source of happiness for me. My parents, Soorgul and Setara, have provided me with every opportunity to achieve my dreams. They have been my number one supporters in life and I am forever grateful for everything they have sacrificed on my behalf. There is no way I could adequately pay them back for all they have given me, but as a start, I dedicate this dissertation to them. I would also like to extend my deepest thanks to my three beautiful sisters (Malalai, Gulalai, and Kochai) for their patience, thoughtful encouragement, and sage advice during my doctoral journey. I love you all very much.

Last, but certainly not least, I would like to thank God for continually guiding and supporting me throughout my journey in life. I could not have completed this endeavor without His help.

The work presented in this dissertation was supported by the National Institutes of Health (grants P01-AG025831, P50-CA086306, and R01-EB001943) and the U.S. Department of Energy (contracts DE-FG02-02ER63420 and DE-FG02-06ER64249). Furthermore, I would like to thank the Biomathematics Department for their generous support during the early part of my graduate studies. A deep debt of gratitude is also owed to Carolyn Hoffman for her kind support.

Chapter 2 is a version of:

Wardak M, Wong KP, Shao W, Dahlbom M, Kepe V, Satyamurthy N, Small GW, Barrio JR, Huang SC. Movement correction method for human brain PET images: application to quantitative analysis of dynamic ^{18}F-FDDNP scans. *J Nucl Med.* Feb 2010;51(2):210-218.

Chapter 3 is a version of:

Wardak M, Schiepers C, Dahlbom M, Cloughesy T, Chen W, Satyamurthy N, Czernin J, Phelps ME, Huang SC. Discriminant analysis of ^{18}F-fluorothymidine kinetic parameters to predict survival in patients with recurrent high-grade glioma. *Clin Cancer Res.* Oct 15 2011;17(20):6553-6562.

Chapter 4 is based on a submitted manuscript:

Wardak M, Schiepers C, Cloughesy T, Dahlbom M, Phelps ME, and Huang SC. ^{18}F-FLT and ^{18}F-FDOPA PET kinetics in recurrent brain tumors.

Figure 1.2 is reprinted by permission of SNMMI from:

Phelps ME. PET: the merging of biology and imaging into molecular imaging. *J Nucl Med.* Apr 2000;41(4):661-681.

Figure 1.7B is reprinted with permission of Springer from:

Dahlbom M. PET Imaging: Basics and New Trends. In: Grupen C, Buvat I, eds. *Handbook of particle detection and imaging*. Berlin ; New York: Springer; 2012.

Figure 1.11 is adapted with permission of the National Academy of Sciences, U.S.A. from:

Phelps ME. Positron emission tomography provides molecular imaging of biological processes. *Proceedings of the National Academy of Sciences of the United States of America.* Aug 1 2000;97(16):9226-9233.

Figure 1.17 is reprinted with permission of Elsevier from:

Hutton BF, Braun M. Software for image registration: algorithms, accuracy, efficacy. *Seminars in nuclear medicine.* Jul 2003;33(3):180-192.

Figure 1.18 is reprinted with permission of the Radiological Society of North America from:

Schlemmer HP, Pichler BJ, Schmand M, et al. Simultaneous MR/PET imaging of the human brain: feasibility study. *Radiology.* Sep 2008;248(3):1028-1035.

Figure 1.19 is reprinted with permission of Springer from:

Ratib O, Schwaiger M, Beyer T. Atlas of PET/MR imaging in oncology. Berlin; New York: Springer; 2013.

Figures 1.20, 1.22, 1.23, and 1.25 are reprinted by permission of Pearson Education, Inc. from:

Marieb EN, Wilhelm PB, Mallatt J. *Human anatomy*. 6th ed. San Francisco, California: Pearson Benjamin Cummings; 2010.

VITA

August 2000 – Dec. 2004	B.S., Biomedical Engineering Summa Cum Laude; Tau Beta Pi University of Southern California Los Angeles, CA
May 2005	Fred S. Grodins Award for Academic Excellence in Biomedical Engineering University of Southern California Los Angeles, CA
2005 – 2006	Staff Scientist Dr. Jorge R. Barrio Lab / Dr. Henry Huang Lab Department of Molecular and Medical Pharmacology David Geffen School of Medicine at UCLA Los Angeles, CA
2006 – 2012	Graduate Student Researcher Department of Molecular and Medical Pharmacology David Geffen School of Medicine at UCLA Los Angeles, CA
2006 – 2008	Biomathematics Fellowship Department of Biomathematics David Geffen School of Medicine at UCLA Los Angeles, CA
2008 – 2009	National Institute of Biomedical Imaging and Bioengineering Training Grant Biomedical Physics Interdepartmental Program David Geffen School of Medicine at UCLA Los Angeles, CA
May 2008	Travel Award Education and Research Foundation for the Society of Nuclear Medicine
June 2008	First Place Prize in the Brain Imaging Council Young Investigator Award Symposium at the 55th Annual Meeting of the Society of Nuclear Medicine in New Orleans, LA

November 2008	Travel Award Department of Molecular and Medical Pharmacology David Geffen School of Medicine at UCLA University of California, Los Angeles Los Angeles, CA
May 2009	UCLA Quality of Graduate Education Travel Award Biomedical Physics Interdepartmental Program David Geffen School of Medicine at UCLA Los Angeles, CA
May 2009	Best oral presentation at the 10th Annual UCLA Biomedical Physics Research Colloquium
June 2009	First Place Prize in the Nuclear Oncology Council Young Investigator Award Symposium at the 56th Annual Meeting of the Society of Nuclear Medicine in Toronto, Canada
October 2009	Sylvia Sorkin Greenfield Award for Excellence in Molecular and Medical Imaging Biomedical Physics Interdepartmental Program David Geffen School of Medicine at UCLA Los Angeles, CA
May 2011	UCLA Quality of Graduate Education Travel Award Biomedical Physics Interdepartmental Program David Geffen School of Medicine at UCLA Los Angeles, CA
May 2011	Best poster presentation at the 12th Annual UCLA Biomedical Physics Research Colloquium
June 2011	Alavi-Mandell Prize for outstanding original article in the Journal of Nuclear Medicine
September 2011	M.S., Biomedical Physics Biomedical Physics Interdepartmental Program Depts. of Radiological Sciences, Radiation Oncology, and Molecular and Medical Pharmacology David Geffen School of Medicine at UCLA Los Angeles, CA
Fall 2011	Teaching Assistant under Dr. Tim Deming Department of Bioengineering University of California, Los Angeles Los Angeles, CA

2010 – 2011	Graduate Student Representative Service Award from Dr. Michael E. Phelps Department of Molecular and Medical Pharmacology David Geffen School of Medicine at UCLA Los Angeles, CA
2010 – 2012	Seminar Organizing Committee Member Institute for Molecular Medicine David Geffen School of Medicine at UCLA Los Angeles, CA
Fall 2012	Edward J. Hoffman Graduate Fellowship Biomedical Physics Interdepartmental Program David Geffen School of Medicine at UCLA Los Angeles, CA

PUBLICATIONS AND PRESENTATIONS

JOURNAL PUBLICATIONS

Wilks MQ, Protas H, **Wardak M**, Kepe V, Small GW, Barrio JR, Huang S-C. Automated VOI Analysis in FDDNP PET Using Structural Warping: Validation through Classification of Alzheimer's Disease Patients. *International Journal of Alzheimer's Disease*. 2012;2012:512069.

Wardak M, Schiepers C, Dahlbom M, Cloughesy T, Chen W, Satyamurthy N, Czernin J, Phelps ME, Huang S-C. Discriminant analysis of ^{18}F-fluorothymidine kinetic parameters to predict survival in patients with recurrent high-grade glioma. *Clinical Cancer Research*. 2011;17(20):6553-6562.

Wong K-P, **Wardak M**, Shao W, Dahlbom M, Kepe V, Liu J, Satyamurthy N, Small GW, Barrio JR, Huang S-C. Quantitative analysis of [^{18}F]FDDNP PET using subcortical white matter as reference region. *European Journal of Nuclear Medicine and Molecular Imaging*. 2010;37(3):575-588.

Wardak M, Wong K-P, Shao W, Dahlbom M, Kepe V, Satyamurthy N, Small GW, Barrio JR, Huang S-C. Movement correction method for human brain PET images: application to quantitative analysis of dynamic ^{18}F-FDDNP scans. *Journal of Nuclear Medicine*. 2010;51(2):210-218.

CONFERENCE PAPERS

Huang S-C, Ye H, **Wardak M**, Wong K-P, Dahlbom M, Shao W, Small GW, Barrio JR. A bootstrap method for identifying image regions affected by intra-scan body movement during a PET/CT scan. Paper presented at: Nuclear Science Symposium and Medical Imaging Conference (NSS/MIC), 2011 IEEE; 23-29 Oct. 2011; 2011. p. 2905-2908.

Wilks M, Protas H, **Wardak M**, Small GW, Barrio JR, Huang S-C. Automated VOI analysis in ^{18}F-FDDNP PET using structural warping: Validation through classification of Alzheimer's disease patients. Paper presented at: Nuclear Science Symposium and Medical Imaging Conference (NSS/MIC), 2010 IEEE; Oct. 30 2010-Nov. 6 2010; 2010. p. 2963-2965.

Wong K-P, **Wardak M**, Shao W, Zhou Z, Dahlbom M, Smid L, Truong D, Kepe V, Small GW, Barrio JR, Huang S-C. Movement correction of [^{18}F]FDDNP PET studies for brain amyloid imaging. Paper presented at: Nuclear Science Symposium and Medical Imaging Conference (NSS/MIC), 2007 IEEE; Oct. 26 2007-Nov. 3 2007; 2007. p. 3974-3977.

ABSTRACTS

Wardak M, Schiepers C, Wong K-P, Huang S-C. Simplified reference tissue models for kinetic analysis of dynamic ^{18}F-FLT PET imaging in patients undergoing brain tumor treatment. *Society of Nuclear Medicine Annual Meeting Abstracts*. 2013;54(Supplement 2):1415.

Wardak M, Schiepers C, Dahlbom M, Cloughesy T, Chen W, Czernin J, Huang S-C. FLT and FDOPA PET kinetics in recurrent brain tumors: A multitracer approach. *Society of Nuclear Medicine Annual Meeting Abstracts*. 2012;53(Supplement 1):1997.

Wardak M, Schiepers C, Dahlbom M, Cloughesy T, Chen W, Czernin J, Huang S-C. Predicting overall survival of patients with malignant glioma using relative changes in ^{18}F-3′-deoxy-3′-fluoro-L-thymidine PET kinetics. *Society of Nuclear Medicine Annual Meeting Abstracts*. 2012;53(Supplement 1):1254.

Ye H, Wong K-P, **Wardak M**, Dahlbom M, Barrio JR, Nelson L, Small GW, Huang S-C. Movement correction method for dynamic PET/CT images: Application to Down syndrome ^{18}F-FDDNP dynamic scans. *Society of Nuclear Medicine Annual Meeting Abstracts*. 2011;52(Supplement 1):213.

Wardak M, Huang S-C, Wong K-P, Czernin J, Phelps ME, Schiepers C. FDOPA kinetics using PET/CT to diagnose recurrent brain tumors. *Society of Nuclear Medicine Annual Meeting Abstracts*. 2010;51(Supplement 2):340.

Ye H, **Wardak M**, Wong K-P, Dahlbom M, Huang S-C. Movement correction improves the quality of dynamic PET-CT images. *Society of Nuclear Medicine Annual Meeting Abstracts*. 2010;51(Supplement 2):518.

Wardak M, Schiepers C, Dahlbom M, Chen W, Cloughesy T, Czernin J, Huang S-C. Prediction of survival time using ^{18}F-FLT kinetics and discriminant analysis in recurrent glioma therapy. *Society of Nuclear Medicine Annual Meeting Abstracts*. 2009;50(Supplement 2):187.

Wardak M, Huang S-C, Chen W, Dahlbom M, Cloughesy T, Czernin J, Schiepers C. FLT kinetics predict survival in brain tumor therapy. *Society of Nuclear Medicine Annual Meeting Abstracts*. 2009;50(Supplement 2):103.

Wardak M, Huang S-C, Dahlbom M, Chen W, Cloughesy T, Schiepers C. Monitoring brain tumor therapy with ^{18}F-FLT. *Society of Nuclear Medicine Annual Meeting Abstracts*. 2008;49(Supplement 1):5P.

Wardak M, Wong K-P, Shao W, Dahlbom M, Kepe V, Satyamurthy N, Small GW, Barrio JR, Huang S-C. Movement correction improves quantitative analysis of dynamic ^{18}F-FDDNP PET images. *Society of Nuclear Medicine Annual Meeting Abstracts*. 2008;49(Supplement 1):378P-b.

Wong K-P, **Wardak M**, Shao W, Dahlbom M, Kepe V, Satyamurthy N, Small GW, Barrio JR, Huang S-C. Quantitative analysis of [^{18}F]FDDNP PET using subcortical white matter as reference region. *Society of Nuclear Medicine Annual Meeting Abstracts*. 2008;49(Supplement 1):117P-c.

Ringman JM, **Wardak M**, Kepe V, Barrio JR, Huang S-C, Yu CL, Geschwind D, Schaffer B, Rodriguez Y, Small GW, Cummings JL. [^{18}F]FDDNP-PET imaging in persons at-risk for familial AD. *Alzheimer's & Dementia : The Journal of the Alzheimer's Association*. 2006;2(3):S66.

Chapter 1

Introduction

"Disease is an abnormal state of the body which primarily and independently produces a disturbance in the normal functions of the body." – Avicenna, The Canon of Medicine (circa 1025 CE)

"Every chemical element on Earth tells a story written in the heavens." – Unknown

Before we delve into the individual projects themselves, let us first start off with some background information to help motivate the topics that will be the focus of this dissertation.

1.1 SPECIAL ASPECTS OF MEDICAL IMAGING

Medical imaging plays an important role in our lives and opens up some of the most striking vistas in all of medicine (*1-6*). It empowers physicians and scientists with a *sixth* sense: the ability to non-invasively peer into the body without having to surgically open it up. Nearly every medical specialty depends on imaging as the primary diagnostic method and few can do without it. Through its images, medical imaging technology enables views of the internal structure and function of the human body in health and disease. Information obtained from imaging modalities can be used to diagnose abnormalities, guide therapeutic procedures, and monitor disease treatment (*1, 7*). The author has been fascinated with medical imaging ever since he was a kid and he hopes the reader will find a similar fascination with this dynamic field after reading this dissertation.

1.2 GENERAL PRINCIPLES OF NUCLEAR MEDICINE IMAGING

1.2.1 Fundamental Concepts

Nuclear medicine imaging techniques are performed by administering compounds that are labeled or "tagged" with radionuclides so that diagnostic information in a wide range of disease states can be obtained (*7-11*). The radioactive compounds (also called radiopharmaceuticals or radiotracers) are introduced into the body in very small amounts (typically nanograms) via inhalation into the lungs, direct injection into the bloodstream, subcutaneous administration, or oral administration. The radiopharmaceutical is designed to image or measure a particular structure or physiologic process in the body. Images are then obtained using a gamma camera, which is sensitive to detecting the gamma rays that are emitted from the administered radiotracers. The distribution or pattern of uptake of the radiotracer depends on the biochemical or physiologic state of the individual. For example, an abnormal tissue distribution or an increase or decrease in the rate at which the radiopharmaceutical accumulates in a particular tissue can be a strong indicator of disease.

1.2.2 The Power of Molecular Imaging

The strength of nuclear medicine lies in its ability to provide *functional* information (i.e., it gives us an indication on how the body is *functioning* at the physiologic and biochemical level) (*3, 9*). In nuclear medicine, biologic measurements are made at the nano-molar to pico-molar concentration range (*9*). This sensitivity advantage, together with the ever-growing selection of radiolabeled compounds, allows nuclear medicine studies to be targeted to the very specific biological processes underlying disease (*9, 12, 13*). In addition to functional information, nuclear medicine images can provide limited anatomical information, but these images are not as exquisite or have the same spatial resolution as those produced by structural imaging modalities such as computed tomography (CT) or magnetic resonance imaging (MRI). Nuclear medicine techniques are valuable for assessing tissue function and depicting disease-related molecular changes that can occur independently of or before structural changes (*12-14*). Examples of the diverse biologic processes that can be measured by nuclear medicine techniques include tissue perfusion, substrate metabolism, enzyme activity, the density of dopamine receptors in the brain, and gene expression (*9, 15*). Nuclear medicine thus plays a complementary, but quite distinct role from other commonly used medical imaging modalities such as CT and MRI.

Two key 3-dimensional (3D) imaging technologies in nuclear medicine are positron emission tomography (PET) and single photon emission tomography (SPECT) (*9*). In the case of PET, a positron-emitting radiotracer is administered. PET detectors detect a pair of "back-to-back" annihilation photons that are produced when a positron interacts with an electron in tissue. SPECT, however, employs gamma-emitting radionuclides that decay by emitting single gamma rays. In both PET and SPECT, data are collected from many angles around the patient and tomographic images are reconstructed using mathematical techniques. PET and SPECT have also been individually combined with anatomic CT to produce integrated PET/CT and SPECT/CT scanners that provide detailed anatomical and functional information about an organ of interest. In this dissertation, we will limit ourselves to the study of PET, which will be reviewed next.

1.3 POSITRON EMISSION TOMOGRAPHY

One of the most important imaging modalities we have today in radiology and nuclear medicine is PET. It is the principal focus of this dissertation. PET was developed by Michael E.

Phelps, Edward J. Hoffman, and colleagues (*16-23*) as an imaging technology to examine the biology of normal cellular function and its transformation to disease in the living subject (*1, 4*). PET was for many years used in a research setting to study the function of single organs, primarily the brain and the heart. With the introduction of whole-body PET imaging (*24, 25*) and the combination of PET and CT into one imaging system (*26*), PET has become an advanced diagnostic imaging tool that is routinely used in oncology, neurology, and cardiology. A photograph of Mike Phelps, Ed Hoffman, and Henry Huang during the early days of PET at UCLA is shown in Figure 1.1.

1.3.1 Overview of PET

PET is a nuclear imaging technique that uses the unique decay characteristics of radionuclides that decay by positron emission (*1, 27-29*) (Figure 1.2). These radionuclides are produced in a cyclotron and are then used to label various compounds of biological interest (*1, 7*). The labeled compound is introduced into the body, usually by intravenous injection, and is distributed in tissues in a manner that is dictated by its biochemical and pharmacokinetic properties. These labeled compounds are used to "trace" or "probe" biological processes and are therefore referred to as radiotracers or molecular imaging probes. At any given time, some of the positron-emitting isotopes, which are attached to the probe molecules, will decay and emit a positron from their nucleus. The ejected positron will travel a short distance from its site of emission and eventually lose most of its energy in collisions with electrons in tissue. It will then attract an electron and form a positronium, which will annihilate within 10^{-12} s (*4*). The annihilation process converts the mass of the electron and positron into electromagnetic energy, which is liberated in the form of two gamma rays (also called annihilation photons). In order to conserve energy and momentum, the annihilation photons each have an energy of 511 keV (one-half of the combined rest mass energy of an electron and positron) and they are emitted at approximately 180 degrees apart (net momentum is close to zero when annihilation occurs). The high-energy of the annihilation photons gives them a good probability of escaping the body and allows them to be detected by external detector systems.

A PET scanner consists of a large number of detectors that surround the subject to be imaged and are designed to convert the high-energy photons into an electrical signal that can be fed to subsequent electronics (*1, 27, 28*) (Figure 1.3). A true coincidence event is recorded when a pair of detectors simultaneously registers the detection of two annihilation photons that originate from the same radioactive decay. Knowing the location of the two detectors in the system, one can determine that the annihilation (and therefore the positron emission) must of occurred somewhere along the line connecting the two detectors. After the measured data are corrected for a number of factors (e.g., attenuation, scatter, and detector normalization), a reconstruction algorithm is used to convert the data collected at various angles around the subject into three-dimensional tomographic images (*1*). The output of the reconstruction process is a three-dimensional image volume, where the signal intensity in any particular image volume element is proportional to the amount of the radionuclide (and, hence, the amount of the labeled molecule to which it is attached) in that voxel. Thus, PET images allow the spatial distribution of radiolabeled tracers to be mapped quantitatively in a living human. The temporal resolution of PET is on the order of seconds to minutes and the sensitivity of PET is high (i.e., it is able to detect radioisotope concentrations in the nano-molar to pico-molar range) (*27*). By taking a time series of PET images, the tissue concentration of the radiolabeled molecules can be measured as a function of time, and with appropriate mathematical modeling, the rate of specific biological processes in which the probe is involved can be determined (*1*). A diagram illustrating the procedure of a PET study from an information-flow perspective is shown in Figure 1.4.

Moreover, PET imaging produces *emission* images (as opposed to *transmission* images) because the radiation detected by the imaging device originates from *within* the subject's body and is *emitted* outward. This differs from CT, where an X-ray source is located *outside* of the subject and the radiation is *transmitted* through the subject's body.

1.4 BASIC PHYSICS OF POSITRON EMISSION AND ANNIHILATION

1.4.1 Positron Emission

One common method by which a radionuclide with an excess of protons in its nucleus may decay is through positron emission (*1*). Essentially, a proton (p) in the nucleus is converted into a neutron (n) and a positron (β^+) in the radioactive decay process.

$$\mathrm{p} \rightarrow \mathrm{n} + \beta^+ + \nu \qquad \text{Eq. 1.1}$$

A positron has the same mass as an electron but the opposite electric charge. The positron is ejected from the nucleus, along with a neutrino (ν). Positron decay is denoted as:

$$^{\mathrm{A}}_{\mathrm{Z}}\mathrm{X} \rightarrow {}^{\mathrm{A}}_{\mathrm{Z-1}}\mathrm{Y} + \beta^+ + \nu \qquad \text{Eq. 1.2}$$

where X is the parent radionuclide with mass number A and atomic number Z, and Y is the daughter nuclide. The daughter Y has the same mass number as parent X but the atomic number has decreased by 1 after the decay process. The neutrino has no electric charge and has very little mass. The net energy released during positron emission is shared between the daughter nucleus, the positron, and the neutrino. Positrons are therefore emitted with a range of energies, from zero up to a maximum endpoint energy E_{max}. The mean kinetic energy of the emitted positrons is approximately 1/3 of E_{max} (*1*). Table 1.1 lists some of the properties of radionuclides that are commonly used in PET.

Proton-rich radionuclides can also decay by a process known as electron capture. Here, the nucleus captures an orbital electron and converts a proton into a neutron, thus decreasing the atomic number Z by one. Once again, a neutrino is released. Decay by electron capture and positron emission compete with one another, with positron emission usually being the dominant process in low Z nuclei, and electron capture being more likely in higher Z nuclei (*1*). Radionuclides that decay predominantly by positron emission and not by electron capture (i.e., they have a high positron branching fraction) are preferred for PET imaging.

1.4.2 Annihilation

After a positron is emitted, it will travel a certain distance in matter, losing its kinetic energy through inelastic interactions with atomic electrons. When the positron has lost most of its energy, it will come to rest. At this point, it will combine with an electron and form a hydrogen-like state known as positronium. The positronium is very unstable and the electron-positron pair will annihilate to produce two "back-to-back" photons, each with an energy of 511 keV. The law of conservation of energy is obeyed, in that the masses of the positron and electron are converted into a total energy of 1.022 MeV which is shared equally between the two photons (i.e., 1.022 MeV/2 = 511 keV). In addition, the law of conservation of momentum is obeyed such that the two photons travel away from the annihilation site at 180 degrees from each other. If the momentum is non-zero at the time of annihilation, then there will be a slight deviation from 180 degrees between the two photons. It must be noted that the unique simultaneous emission of two 511 keV photons 180 degrees apart and the use of coincidence detection are what satisfy the mathematical requirements of the image reconstruction algorithm (*1*). Nature has been kind to us in that only *two* annihilation photons are emitted back-to-back after an annihilation event. It is possible that three (or even four) annihilation photons can be produced (all with a net momentum of zero), but these events occur with a small percentage (0.5% or less) (*30*).

1.5 PHOTON INTERACTIONS

Not all of the annihilation photons emitted from the body reach the surrounding detector system. These photons can either interact with the body tissue or pass through it without interaction. The interactions of photons with the body occur mainly in the form of the photoelectric effect or Compton scattering (*1, 31*). In the photoelectric effect, all of the incident photon energy is transferred to an electron in the inner shell of the atom (e.g., the K or L shell), which is then ejected from the atom. The kinetic energy of the ejected electron is equal to the incident photon energy minus the binding energy of the orbital electron. Annihilation photons involved in a photoelectric interaction are therefore completely absorbed and do not reach the detectors. The dominant form of photon interaction at 511 keV in tissue is Compton scattering, which is caused by the collision of a photon with a loosely bound electron in the outer "valence" shell of an atom (*1, 31*). In this type of interaction, only a portion of the photon energy is transferred as kinetic energy to the electron. The remaining energy appears as a secondary scattered photon, which is emitted in a different direction from the primary photon. At 511 keV, it can be shown that the scattering cross section is peaked in the forward direction (i.e., small scattering angles are favored) and that one third of all events will scatter within 40°, which corresponds to an energy loss of 100 keV or less (*32*). Interaction by Compton scattering thus reduces the number of annihilation photons that would otherwise reach the detectors in the PET scanner. The loss in photon flux due to interactions in a body (or any other object) is called attenuation. In PET, the probability that two 511 keV gamma photons "survive" the attenuation in the body after undergoing an annihilation event is independent of where the annihilation occurred along the line joining the two detectors (*1, 31*). Therefore, it is possible to correct for the attenuation effect by performing a transmission scan using an external positron-emitting source. This will be discussed in more detail in the Attenuation Correction section.

1.6 GAMMA PHOTON DETECTORS IN PET

Detectors commonly used in PET are a combination of (1) a scintillation crystal, which converts the incident gamma radiation into a flash of visible light, and (2) a photon detector, which collects the visible light and converts it into an electrical pulse (Figure 1.5).

1.6.1 Detector Basics

Coincidence detection of the 511 keV annihilation photons requires a detection system that is sensitive to the relatively high photon energy and allows to accurately determine the energy of each photon that is detected at a fairly high count rate (*4*). In addition, these detectors need to have a fast response time (i.e., they need to be able to accurately determine a coincidence within 6-12 ns) (*4*). This property is sometimes referred to as the coincidence time resolution and is specific to different detector materials. The time resolution has a direct impact on the randoms rate (i.e., a better or smaller time resolution will reduce the randoms rate), which will in turn improve the image quality. We will talk more about random coincidences in the next section. The time resolution for any given detector material is a function of both the light decay time (i.e., how fast the scintillation light is generated in the detector) and the amount of light produced per absorbed photon. In general, the shorter the light decay time and the more light produced, the faster the detector (*4*). Some common scintillator materials used in current PET scanners are bismuth germanate (BGO), lutetium oxyorthosilicate (LSO), and gadolinium oxyorthosilicate (GSO). The properties of these scintillators are listed in Table 1.2.

1.6.2 Block Detector

The most common detector design in PET is the “block detector,” which consists of a block of scintillator material (typically 4 cm × 4 cm in area by 3 cm deep) that is segmented into an array of smaller detector elements (typically 8×8 or 12×12) (*1, 33*). Four photomultiplier tubes (PMTs) are attached to the back of the scintillator block. The PMTs detect the scintillation light emitted from the scintillator and identify the element in which the photon interaction occurred.

The whole-body ECAT EXACT HR+ PET scanner (Siemens/CTI, Inc.) consists of four rings of 72 BGO block detectors each (*34*). A single block detector is divided into an 8×8 matrix, giving a total of 32 rings with 576 detector elements each. The axial and transaxial field of view of the ECAT EXACT HR+ PET is 15.5 cm and 58.5 cm, respectively. The ECAT EXACT HR+ PET scanner was used in the studies performed in this dissertation.

In addition to the PMT, there are other types of photon detectors based on different semiconductor technologies. These include the avalanche photodiodes (APD) and the silicon photomultipliers (SiPM). In contrast to conventional photodiodes, both the APDs and SiPM provide an internal amplification of the signal and are very compact devices (*1, 32*).

Furthermore, both devices are, in contrast to conventional PMTs, insensitive to magnetic fields, which has allowed the construction of PET systems that can operate simultaneously within or near an MRI system (*32, 35-37*).

1.7 COINCIDENCE DETECTION

PET uses coincidence detection for determining the location of annihilation events within the body (*1, 4*). Because the point of annihilation is very close to the point of positron emission, this also gives a good indication of where the positron-emitting radionuclide is in the body. Two annihilation photons are considered to be in coincidence if they are detected within a specific time interval known as the coincidence timing window (typically 6 to 12 nanoseconds). If a detected gamma ray is not accompanied by a second gamma ray within this timing window, the event is discarded.

1.7.1 Types of Coincidence Events

In an ideal PET system, only true coincidences should be detected (i.e., when both annihilation photons originating from the same annihilation event escape the body and are detected by a pair of detectors) (Figure 1.6). However, due to the limitations of the detectors used in PET and the possible interaction of the 511-keV photons in the body before they reach the detector, unwanted coincidence events are also recorded.

The first type of unwanted event is the random (or accidental) event, which originates from two unrelated annihilation events (Figure 1.6). If not corrected for, the random coincidences generated form an undesirable contrast, reducing background in the images and also compromising quantitation (*4*). Fortunately, there are accurate methods to measure and correct for random events (*1*); however, these result in increased image noise levels. Therefore, the random coincidence rate needs to be kept at a minimum. In contrast to the true coincidence rate which increases linearly with administered activity, the randoms rate increases with the square of the activity (*4*). Therefore, an increase in injected activity does not always translate into an improvement in image quality due to the increase in random events.

The second undesirable event type is the scattered event, which occurs when one or both of the two annihilation photons interact in the subject prior to being detected (Figure 1.6). The scatter process changes the direction and energy of the photon such that the position information on the event is lost. Although the scattered photons have a lower energy compared to the primary photons, the limited energy resolution of the detectors used in PET systems makes it hard to differentiate these from the primary 511-keV photons. The presence of scatter in the reconstructed image reduces image contrast and compromises the quantitative accuracy of the image. Unlike the random events, scatter cannot be directly measured. Instead, the scatter needs to be estimated from the acquired emission and attenuation data and the accuracy of this correction has a direct impact on the image contrast, quantitation and quality (*1, 4*).

1.8 ATTENUATION CORRECTION

One of the goals in PET imaging is to produce an image volume that accurately describes the true distribution of the injected radioactivity. The correction that has the most significant impact on the image data is attenuation correction (*32*). It is the largest correction factor applied in PET (*28*). Without correction for photon attenuation, the reconstructed images will give a distorted view of the true activity distributions. Furthermore, the images will not be quantitative.

1.8.1 Attenuation

In PET, for a true coincidence event to be detected, both photons must exit the body. This is less likely for annihilations located deep within the body than for ones occurring near the body's surface. One convenient aspect of PET imaging is that the attenuation correction factor for a given line of response is the same for a positron annihilation occurring anywhere along that line (Figure 1.7A) (*1, 7, 28*). For example, the probability that both annihilation photons will escape a uniformly attenuating object and be available for detection is the product of the individual probabilities:

$$p_1 \times p_2 = e^{-\mu x} \times e^{-\mu(L-x)} = e^{-\mu L} \qquad \text{Eq. 1.3}$$

where μ is the linear attenuation coefficient for the 511 keV photons in the uniformly attenuating object, and x_1 and x_2 are the distances that the two photons must travel through the object to reach their respective detectors. The sum of x_1 and x_2 is the total path length L of the object along a given line of response. The attenuation correction for the line of response shown in Figure 1.7A is simply:

$$(p_1 \times p_2)^{-1} = e^{\mu L} \qquad \text{Eq. 1.4}$$

As can be seen from this equation, the attenuation correction factor is dependent on both the total thickness of the object along the line of response and the attenuation coefficient of the object along that same line; however, it is independent of the position of the annihilation event along a given line of response. This is unique to annihilation coincidence detection and makes attenuation correction straightforward.

The mass attenuation coefficient for 511 keV photons in tissue is ~0.095 cm^2/g. The half-value layer for tissue at 511 keV is ~7.2 cm. For a head-sized object (~20 cm in diameter), the attenuation could be more than 85% of the available photons (*38*). For body imaging situations, 45-cm tissue widths are not uncommon and more than 95% of the annihilation photons in that dimension could be attenuated (*38*).

1.8.2 Attenuation Correction in PET

The most accurate method to determine the attenuation correction is through direct measurements (*1*). This approach typically uses the ^{68}Ge/^{68}Ga external rod sources that are rotated around the field of view. Most sources contain the positron emitter ^{68}Ga (half-life = 68 min), which is produced when the parent ^{68}Ge (half-life = 271 days) decays by electron capture. The slow decay of ^{68}Ge provides a steady supply of positron-emitting ^{68}Ga, allowing these sources to be used continually over a period of many months before replacement is needed. During attenuation correction, two scans are acquired: (1) a “blank” scan that is acquired with nothing in the field of view and (2) a “transmission” scan where the subject is in the field of view. The attenuation correction factors for each line of response are simply given by taking the ratio between the blank sinograms and the transmission sinograms. For example, if a particular line of response has 1000 counts in the blank scan, but only 200 counts in the transmission scan, the correction factor for the emission data along that line of response will be 5. The ability to directly measure and correct for the attenuation for each line of response is one of the reasons why PET data has been known for its ability to produce quantitative measurements.

1.8.3 Attenuation Correction in PET/CT

For a combined PET/CT scanner, the CT transmission scan can be conveniently used to make attenuation correction of the PET emission data (*4, 39*). The CT scan can be acquired in less than a minute using the latest generation of multi-slice CT scanners, while the transmission scan in PET can take as long as 20 minutes or more depending on the activity level of the ^{68}Ge source. Similar to the PET-only scanner correction method, a blank CT scan and a CT transmission scan are performed. One additional step that needs to be done with the PET/CT correction method is that the attenuation correction factors derived from the ~70 keV CT X-rays must be scaled to the 511 keV photons of PET by applying a scaling factor. This is necessary because the attenuation correction factor depends on the attenuation coefficient, which in turn depends on the energy of the photon. The scaling factor is defined as the ratio of the mass attenuation coefficient of the 511 keV photons to that of the 70 keV X-rays in a given tissue (*40*). This factor is assumed to be the same for all tissues except bone, which has a slightly higher mass attenuation coefficient.

1.9 IMAGE RECONSTRUCTION

The goal of image reconstruction is to provide cross-sectional images of the distribution of positron-emitting radiopharmaceuticals in the body. This is done by using the coincidence events detected by the PET scanner along with the mathematical algorithms of computed tomography. Each detector pair in a PET scanner sees the sum (or projection) of the radioactivity along the line joining the two detectors, not the activity at any one point. The image reconstruction process seeks to recover the activity distribution from the measured projection data taken at many different angles around the body.

Projection data for a ring of PET detectors are conveniently represented as a sinogram (Figure 1.8). The sinogram is a 2D matrix of projection data, where each row in the sinogram forms a one-dimensional projection representing a view of the body from a particular angle. Each element in the sinogram represents the sum of activity along a line joining two detectors (i.e., the line of response).

There are essentially two approaches for reconstructing the sinogram data into cross-sectional images: (1) filtered backprojection and (2) iterative reconstruction methods.

1.9.1 Filtered Backprojection

Filtered backprojection is an analytic approach which applies a filter to the projection data in the Fourier domain and then backprojects the data into image space (*28*). The backprojection process involves distributing the counts from a sinogram element along the line in image space which it represents. In broad terms, the filtered backprojection reconstruction process can be summarized as follows:

1. Take projection for angle 1 (row 1 in the sinogram)
2. Calculate the Fourier transform of this projection
3. Multiply by the reconstruction filter
4. Calculate the inverse Fourier transform of the filtered projection
5. Backproject the data for angle 1
6. Repeat for all other angles in the sinogram

The result of backprojecting all the filtered projections is a faithful representation of the original object.

1.9.2 Iterative Reconstruction Methods

In iterative reconstruction methods, an initial estimate of an image is made, and the projections are computed from the image and compared with the measured projections (*40*). If there is a difference between the estimated and measured projections, corrections are made to improve the estimated image, and a new iteration is performed to assess the convergence between the estimated and measured projections. Iterations are continued until a reasonable agreement between the two sets of projections is achieved. The basic flowchart for iterative reconstruction methods is shown in Figure 1.9.

In comparison to the line-integral model used by filtered backprojection, iterative methods allow for a more accurate modeling of the data-acquisition system as well as the statistical noise in the emission and transmission images (*7*). An additional advantage is that iterative methods can incorporate *a priori* information about the object being scanned into the reconstruction process. For example, because we are imaging radiotracer concentration, we know all image values must be greater than or equal to zero. Thus, a non-negativity constraint can be included in the optimization process. Excellent reviews on the principles and mathematics of image reconstruction have been previously published (*41-45*).

1.10 POSITRON-EMITTING TRACERS AND THEIR PRODUCTION

1.10.1 Positron-Emitting Radionuclides

Among the readily prepared positron-emitting radionuclides are isotopes of carbon (^{11}C; $t_{1/2} = 20$ min), nitrogen (^{13}N; $t_{1/2} = 10$ min), and oxygen (^{15}O; $t_{1/2} = 2$ min). Since these elements are contained in essentially all the compounds that constitute or are consumed by the human body, PET is an obvious technique for the study of the fate of these compounds *in vivo*. There is no positron emitting isotope of hydrogen, and so, fluorine-18 (^{18}F; $t_{1/2} = 110$ min) is often used as a substitute for hydrogen (the van der Waals radius of fluorine is similar to that of hydrogen). Fluorine-18 can also be substituted for a hydroxyl (OH) group in a molecule. There are positron emitters of Cu, Zn, K, Br, Rb, I, P, Fe, Ga and others as well (*13, 46*). Some commonly used positron-emitting radionuclides for brain PET imaging are shown in Table 1.1.

Over 2000 molecular imaging probes have been developed and labeled with positron emitting isotopes (*1, 2, 7, 47*), and the list continues to grow. These probes range from simple labeled molecules such as $H_2{}^{15}O$ (water), $C^{15}O$ (carbon monoxide) and $^{15}O_2$ (oxygen gas) to many forms of sugars, amino acids, fatty acids, ligands for receptor systems, numerous substrate analogs, hormones, antibodies, drugs (medical and illicit), oligonucleotides, and all the way up to intact cells (e.g., immune cells and stem cells) (*2, 13, 38, 48*).

1.10.1.1 Fluorine-18

From a purely physical perspective, fluorine-18 is the archetypal PET radionuclide (*49*). The 110-minute half-life of ^{18}F is very convenient for radiopharmaceutical synthesis and imaging. The half-life further enables centralized production of radiotracers, minimizing the need for in-house cyclotron production. Fluorine-18 also has a high percentage of positron emission (97%) and relatively low positron energy (0.63 MeV), making this the ideal PET isotope. Other favorable features of ^{18}F are that the fluorine atom is small, that it can accept a hydrogen bond, and that the carbon-fluorine bond is very strong. Furthermore, 2-deoxy-2-[^{18}F]-fluoro-D-glucose (^{18}F-FDG), an analog of glucose, is tagged with ^{18}F and is the most widely used PET tracer in the world today. Many pathological conditions can cause regionally specific alterations in glucose metabolism which can be detected using ^{18}F-FDG PET (*1*). The first ^{18}F-FDG PET scans were performed at UCLA in 1977 by Phelps *et al*. (*50, 51*). In 1989, Jorge R. Barrio and colleagues developed the first automated chemistry module for synthesizing ^{18}F-FDG (*52*).

1.10.2 Production of Positron-Emitting Radionuclides

Positron emitters are generally produced in a cyclotron. Here, stable nuclei are bombarded with protons or deuterons (hydrogen with an added neutron) to produce the proton-rich state necessary for positron emission (*1, 28*). Some positron emitters that have parent states that also decay, but with a longer half-life, can be produced in a generator system. In this case, the parent is first produced in a cyclotron and then slowly decays into the daughter positron emitter in the generator. Examples of generator-produced positron emitting radionuclides are ^{68}Ga ($t_{1/2} = 68$ min) and ^{82}Rb ($t_{1/2} = 75$ s). The parents of ^{68}Ga and ^{82}Rb are ^{68}Ge ($t_{1/2} = 271$ days) and ^{82}Sr ($t_{1/2} = 25$ days), respectively. Gallium-68 is used to assess blood-brain barrier integrity, as well as tumor localization (*7*). It is also widely used as a positron-emitting source for attenuation correction. Rubidium-82 is a myocardial perfusion PET tracer.

1.10.3 PET Tracer Design

There are a number of important considerations in PET tracer design (*1, 28*). Obviously, the availability of radionuclides that do not alter the biochemical behavior of the compound of interest is an enormous advantage. However, the half-life of some of these radionuclides is relatively short; therefore synthesis of the labeled product must be rapid. In practice, complex tracers are best labeled with either ^{18}F, ^{11}C, or ^{13}N. Oxygen-15 has a 2-minute half-life and the use of this radionuclide is therefore limited to simple tracers such as H_2O, CO, O_2, and CO_2. Another issue is whether to produce a tracer that is a direct radiolabeled version of a naturally occurring compound (e.g., substitution of ^{11}C for the stable ^{12}C atom in a compound), an analog of a natural compound (e.g., substitution of ^{18}F for the OH group on the second carbon of glucose), or a totally unique compound such as a radiolabeled drug. An analog is a compound whose chemical properties are slightly different from the natural compound to which it is related. The advantage of analogs is that they can be targeted and limited to interactions in a small section of complex biochemical reaction sequences (*28*). This can facilitate subsequent analysis and interpretation of the PET data.

The position at which the positron-emitting label is placed is also critical. The best labeling position is generally dictated by the biochemical result desired and that which minimizes the number and amount of labeled metabolites appearing in blood and tissue. Oftentimes, this requires a detailed knowledge of the biochemical reaction sequence for the tracer under consideration. Moreover, a PET tracer should have high target specificity, high membrane permeability to reach target areas, rapid blood pool clearance to reduce blood pool background at the target tissue (e.g., brain, heart, or tumor), little to no peripheral metabolism, high specific activity, and low non-specific binding (*1*).

1.10.4 Radiation Dosimetry

With positron-emitting radionuclides, the majority of the absorbed dose originates from ionization produced by the positively charged positron and not the 511 keV annihilation photons (*2*). For example, with ^{18}F-FDG PET, the dose to the brain is approximately 77% from positrons and 23% from the 511 keV annihilation photons (*2*). The effective dose to the patient from an administered activity of 10 mCi (370 MBq) of ^{18}F-FDG for a cerebral metabolic PET study is approximately 7.4 mSv (*15*). The three most highly exposed organs for ^{18}F-FDG are the bladder, heart, and brain (*15*). In general, approximately 10 to 20 mCi of ^{18}F-labeled tracers, 20 to 40 mCi of ^{11}C or ^{13}N-labeled tracers, and up to 180 mCi of ^{15}O-labeled tracers can be administered into the body while still staying within the recommended dose limits (*28*).

1.11 STATIC VS. DYNAMIC PET SCANS

The end point in most PET studies is to produce an image, from which diagnostic or quantitative parameters can be derived (*1*). These parameters can be as simple as a qualitative comparison of activity concentration in different tissue regions or more thorough measures of biologic function such as blood flow, metabolic rate, and receptor density. The information that is to be extracted from the image will dictate how the PET data are collected (i.e., as a single static snapshot of the organ of interest or as a dynamic sequence of multiple snapshots).

The most basic data acquisition protocol in PET is the collection of a single data set or static frame over a fixed length of time (*1*). The image reconstructed from such a data set represents the average tissue activity concentration during the acquisition. For some radiotracers, though, it is necessary to follow the dynamic changes in concentration to extract a particular parameter of interest. In these studies, the data are collected as a *sequence* of dynamic time frames, where the PET images provide information about the changes in activity concentration distribution over time (*1*). This information represents the tissue response to the time course of the radiotracer in the plasma following intravenous injection. The tissue time-activity curve can then be processed with a compartmental model to determine the parameters of interest. These types of studies also typically require additional data such as the plasma radioactivity concentration and the plasma concentration of labeled metabolites, which can be determined from blood samples (*1*).

1.12 TRACER KINETIC MODELING

Three things allow one to estimate the rate of a certain biological process in the body with PET: first, an input function taken from the plasma to represent the delivery of the labeled probe to the tissue; second, the PET measurement of the tissue concentration of the labeled probe and its labeled reaction products; and third, a compartment model.

1.12.1 Introduction

Compartmental modeling and tracer kinetic analysis form one of the cornerstones of PET (*53-55*). PET, at its core, is a tracer kinetic method and the goal of a PET study is to probe a certain physiologic or biochemical process in the body without perturbing that process. If the amount of radiotracer is very small in comparison to the amount of the native compound or its competitor, then the process will be perturbed very little (*7*). The distribution of a PET tracer within the body is not static over the course of the study, but varies with time, depending on the different processes that govern its uptake and subsequent biologic fate in the body (*7*). By acquiring a dynamic sequence of PET measurements (i.e., images taken of a region of interest at multiple time points), one can obtain information about the *in vivo* behavior of a particular radiotracer being imaged, which can be used to provide *quantitative* measurements of specific biologic functions. The common procedure of using imaging probes in PET is illustrated in Figure 1.10.

Compartmental modeling techniques are mathematical constructs that involve the concept of different spaces or compartments in which the tracer can reside plus a set of model rate constants or parameters that describe how rapidly the tracer moves between compartments (*7, 53*). Different compartments may represent either *distinct* physical spaces (such as blood plasma versus brain tissue) or different chemical forms (FLT vs. FLT-5-PO_4) or pharmacological states (bound vs. unbound) of the radiotracer that occupy the *same* physical space (*7*). With some knowledge of the radiotracer and the biological properties that govern its *in vivo* behavior, the rate constants in the compartmental model are then assumed to represent specific physiologic or biochemical processes such as blood flow, glucose metabolism, protein synthesis, enzyme activity, neurotransmitter level, and receptor or binding site density (*7*). The tracer kinetic models for ^{18}F-FDG and ^{18}F-FLT are shown in Figure 1.11.

1.12.2 Compartmental Models

A compartmental model consists of a finite number of interconnected compartments (*53, 54, 56-61*). The basic component of such a model is the compartment, which is defined as a pool or 3D space with volume V (in mL), within which the concentration C(t) of an imaging probe is spatially uniform. For radiolabeled probes, the concentration typically has units of Bq/mL, which indicates the number of radioactive disintegrations per second per mL. The clearance rate of the probe from a compartment is proportional to C(t). The proportional constant is called the transport rate constant and is usually not a function of time or C(t), although the value of the rate constant could be dependent on the concentration of competitive endogenous compounds (e.g., those following Michaelis-Menton kinetics) (*54*). The rate constants generally have units of inverse time (e.g., 1/min). The assumption of a constant value for the rate constants, however, is not always valid for the pharmacokinetic modeling of drugs (*54*). The efflux of the tracer from one compartment can be the influx to another compartment, and this is usually denoted with an arrow line between the two compartments. The mass flux is the amount of probe transported out of a compartment per unit time and is equal to the product of the rate constant and the amount of tracer in the originating compartment. Based on the law of conservation of mass, the amount or concentration of the radiotracer can be described as a function of time by a set of linear first-order ordinary differential equations, the solutions to which are quite simple (*1*). In tracer studies, it is assumed that the biologic system under study is effectively in steady state (i.e., it is not a function of time during the measurement time).

1.12.2.1 Types of Compartmental Models

There are two classes of compartmental model configurations that are frequently used to interpret tracer kinetic data: catenary and mammillary. The catenary model consists of a series of compartments joined to each other like links in a chain (Figure 1.12). By contrast, the mammillary model consists of one or more peripheral compartments connected to a central compartment (Figure 1.13).

1.12.2.2 Input Function, Compartmental Model Structure, and Tissue Response Curve

The blood time-activity curve represents activity in whole-blood or plasma and serves as input into the tissue compartments (*1*). It is also referred to as the input function. The input function can be obtained from direct blood sampling or from PET images of the blood pool (e.g., the left ventricle of the heart). The tissue time-activity curve is obtained by placing a region of interest on a set of dynamic PET images and represents the tracer and its potential labeled metabolites. Usually, blood vessels also traverse the region of interest so that a fraction of the blood time-activity curve is superimposed on the tissue time-activity curve.

The shape of the tissue response curve is determined by the compartment model structure and the input function (*53*). Both must be known to obtain the tissue response. The radiotracer delivered to the tissue represents the input or excitation; the data measured with the PET scanner represents the output or the response of the tissue to the excitation (i.e., the input function). In all cases, the tissue response is obtained by convolving the input function with the solution to the model equations for a unit impulse input function (*1*).

1.12.2.3 Differential Equations for a Compartmental Model

As mentioned previously, the rate of transfer from one compartment to another is proportional to the concentration in the compartment of origin and to a first-order rate constant. In general, a compartmental model is described by a system of linear first-order ordinary differential equations, where each equation corresponds to the sum of all transfer rates to and from a specific compartment, i:

$$\frac{d}{dt}C_i(t) = \sum_{\substack{j=1 \\ j \neq i}}^{N} \left(k_{ij} C_j(t) - k_{ji} C_i(t) \right) \qquad \text{Eq. 1.5}$$

$$i = 1 \ldots N$$

where $C_i(t)$ is the tracer concentration in compartment i at time *t*, N is the number of compartments in the model, and k_{ij} is the rate constant for transfer *to* compartment i *from* compartment j. In the field of nuclear medicine, however, a single-index nomenclature is often used to denote the rate constants. The rate constants for transfer from the vascular compartment to the tissue compartment and from the tissue compartment back to the vascular compartment are called K_1 and k_2, respectively. Additional rate constants in the model are called k_3, k_4, and so on. Traditionally, a capital K is used for K_1, while the other rate constants are denoted with a lower case k. A rate constant generally has units of reciprocal time (min^{-1}) and describes the fraction of radiotracer leaving a compartment in a given amount of time. For example, a rate constant of 0.05 min^{-1} indicates that an amount of tracer equal to 5% of that in the compartment will be transported out of the compartment every minute.

The differential equations for the 3-compartment, 2-tissue model shown in Figure 1.14 can be written as:

$$\frac{dC_E}{dt} = K_1 C_P - (k_2 + k_3) C_E + k_4 C_M \qquad \text{Eq. 1.6}$$

$$\frac{dC_M}{dt} = k_3 C_E - k_4 C_M \qquad \text{Eq. 1.7}$$

Solutions to these differential equations can be computed with the use of Laplace transforms and are shown below:

$$C_E(t) = \frac{K_1}{\alpha_2 - \alpha_1}[(k_4 - \alpha_1)e^{-\alpha_1 t} + (\alpha_2 - k_4)e^{-\alpha_2 t}] \otimes C_P(t) \qquad \text{Eq. 1.8}$$

$$C_M(t) = \frac{K_1 k_3}{\alpha_2 - \alpha_1}[e^{-\alpha_1 t} - e^{-\alpha_2 t}] \otimes C_P(t)$$ Eq. 1.9

where

$$\alpha_1, \alpha_2 = \frac{(k_2 + k_3 + k_4) \mp \sqrt{(k_2 + k_3 + k_4)^2 - 4k_2 k_4}}{2}$$

Eq. 1.10

The symbol ⊗ denotes the convolution operator. It is important to keep in mind that the compartment that represents the blood pool does not need an explicit equation because the blood time-activity curve is already available as the input function to the model.

The measured tissue time-activity curve from the PET image can be defined in terms of the model solutions for each compartment as shown below:

$$C_{TISSUE}(t) = C_E(t) + C_M(t) + V_b C_B(t)$$ Eq. 1.11

where V_b is the vascular volume and C_B is the whole-blood radioactivity, which includes the authentic tracer and its labeled metabolites. The parameters in the model solution for the tissue time-activity curve are optimized until the sum of squared differences between the model solution and the measured tissue time-activity curve from the dynamic PET image is minimized. The estimated model parameters are then outputted and analyzed. Various software packages have been developed over the years to perform tracer kinetic analysis (*62-66*); among them include KIS, SAAM II, ADAPT, COMKAT, and PMOD.

1.12.2.4 Data Acquisition Considerations for Compartmental Modeling

In general, compartmental modeling and tracer kinetic analysis requires the acquisition of two sets of data to yield estimates of physiologic parameters: (1) the radioactivity time course of the authentic tracer in blood, and (2) the radioactivity time course of the authentic tracer in tissue. Measurement of the amount of radioactivity delivered to the tissue is typically accomplished by acquiring discrete arterial plasma samples and measuring the radioactivity in a well counter. For cardiac applications, it is possible to derive the radioactivity time course of the authentic tracer in blood from the PET images themselves by drawing a volume of interest on the left-ventricle blood pool. The second set of data required for kinetic modeling is obtained from the reconstructed PET image.

In addition, it is important to keep in mind that there can be and generally is a difference between the whole-blood and plasma concentration of a particular tracer (*1*). A tracer kinetic model generally uses the plasma component of the blood time-activity curve to feed into the other compartments of the model (*1*). Only the tracer in the plasma has the potential to directly leave the intravascular space. Tracers in blood cells would have to first come out of the cells and into the plasma before exiting the vascular space. It is, therefore, important to determine the whole-blood and plasma concentrations of the tracer as a function of time and to use the plasma concentration in the tracer kinetic model. If a relatively fixed ratio exists between whole-blood and plasma (independent of time), then one can use a non-invasive image-based approach to obtain the whole-blood value and correct it to obtain the plasma value (based on the hematocrit) (*1*).

1.12.3 Identifiability of Compartmental Models

An important step in defining a model is to determine whether it is identifiable (i.e., if the parameters of the model can be uniquely determined from the measured data) (*47, 56, 57, 67*). In some cases, the structure of the model itself does not permit the unique definition of parameter values, even with noise-free data. A more significant problem in many applications is that of numerical identifiability (*47*). Here, parameter estimation can be successfully performed with low-noise data, but when the model is inputted with realistic noise levels, the uncertainties in the resulting parameter estimates are large. It may be that in theory a model is structurally identifiable but the data is such that, in practice, the parameters of the model cannot be estimated reliably (*67*). If a model is not structurally identifiable, then a model will not be numerically identifiable (*67*). Similarly, a model that is numerically identifiable does not necessarily mean the model is structurally identifiable (*67*). A stringent criteria for identifiability is that the model is strongly connected (i.e., starting in any compartment, material can pass to any other compartment by some path) (*67*).

Having understood the problem, a more formal definition of model identifiability can now be made. A compartmental model is structurally identifiable (also sometimes referred to as globally identifiable) if every variable parameter in the model is uniquely identifiable everywhere in parameter space (*67*). A model is locally identifiable if a parameter is identifiable in a constrained region of the parameter space (*67*). The solution of the identifiability problem is, in general, a difficult one because it involves the solution of a system of non-linear algebraic equations, which increases in the number of terms and non-linearity degree with model order (i.e., the number of compartments in the model) (*57*). No general solution is available except for the one, two, some three compartment models, and certain catenary and mammillary models (*57*).

A catenary compartmental model which is either closed (i.e., there is no irreversible loss to the environment so $k_{0i} = 0$, $i = 1, \ldots, n$) or almost closed (i.e., there is only one non-zero k_{0i} which can be from any compartment) is globally identifiable if the accessible compartment (for input and measurement) is an external compartment (i.e., compartment 1 or n in Figure 1.12) (*57*). If the accessible compartment is an intermediate compartment (i.e., 2, 3, • • •, or $n - 1$), the k_{ij} are only non-uniquely identifiable and the number of different solutions increases with the distance of the accessible compartment from either end of the chain (*57*). More precisely, if the accessible compartment is j, the number of solutions for the k_{ij} is $\frac{(n-1)!}{(n-j)!(j-1)!}$ (*57*). If the irreversible loss is from compartment j, then k_{0j} is uniquely identifiable (*57*). For the three-compartment ^{18}F-FDG (or ^{18}F-FLT) model, since $n = 3$ and $j = 1$, the number of solutions for k_{ij} $= \frac{(2)!}{(2)!(0)!} = 1$ and thus, the model is uniquely identifiable.

1.12.4 Distribution Volume

Distribution volume (also called the volume of distribution) can be best understood by doing a tracer thought experiment (*1*). If one intravenously injects a tracer with mass M into a patient and then waits a sufficient period of time and samples the tracer concentration in blood, then one can estimate the volume of distribution as $V_d = M/C$. Obviously, if the tracer never leaves the vascular system and is not metabolized, then V_d will equal the blood volume. At the other extreme, if no tracer remains in the blood, then V_d becomes infinitely large. The larger the volume of distribution is for a given tracer, the more it is distributed throughout the body tissues. Mathematically, the volume of distribution is defined as the equilibrium ratio and has units of volume per mass:

$$V_d = (\text{g of tracer/g of tissue})/(\text{g of tracer/mL of blood}) \qquad \text{Eq. 1.12}$$

1.12.5 Standardized Uptake Value

The standardized uptake value (SUV) is a semi-quantitative measure that is often used for describing PET data. The formula for the SUV is given by Equation 1.13.

$$\text{SUV}=\frac{\text{measured activity per mL within region of interest }(\text{Bq/mL})}{\left[\dfrac{\text{injected activity }(\text{Bq})}{\text{body weight }(\text{in grams})}\right]} \qquad \text{Eq. 1.13}$$

The value of SUV would be equal to 1.0 if the tracer is distributed uniformly throughout the body. If the value is higher (or lower) than 1.0 in a tissue region, then the tracer uptake in that tissue is more (or less) than the whole-body average.

1.13 IMAGE REGISTRATION

"Information is the resolution of uncertainty." – Claude Shannon

1.13.1 Introduction

Image registration is the process of aligning images so that corresponding features can easily be related (*68, 69*). Image registration is finding increased clinical use both in aiding diagnosis and guiding therapy (*68*). There are numerous algorithms for registration, all of which involve optimizing a similarity metric between a transformed source image and a reference image. Algorithms for registration are loosely classified by the number of transformations allowed, similarity metric, and optimization procedure used (*70*). To register two images, an optimization procedure tries different transformations and evaluates each of these parameters using a similarity metric (*70*). Similarity metrics quantitatively score the "goodness-of-fit" of two images related by a transformation. Depending on the similarity metric, the optimization process tries to find the global minimum or maximum. The transformation at that global minimum or maximum should bring the two images into alignment. Image registration may be intra-subject (within the same subject), inter-subject (across different subjects), intra-modality (using images from the same modality), and/or inter-modality (using images from multiple modalities).

Rigid-body registration is one of the simplest forms of image registration (Figure 1.15). Rigid-body transformations allow rotation and translation, but no scaling or deformation (*71*). A rigid-body transformation in three dimensions is defined by six parameters (i.e., three translations along the x, y, and z axes, and three rotations around each of the respective axes). Affine transformations add scaling and shearing to rigid-body transformations and are useful for inter-subject registration (*71*). Oftentimes, registration using an affine transformation is used as input to high-dimensional deformable transformation registration. Deformable transformations allow many possible deformations of one image into another (Figure 1.16). Deformable transforms can be applied inter-subject and intra-subject.

1.13.2 Mutual Information

A similarity metric called mutual information (MI) has found considerable success in medical imaging, especially with multi-modality image registration (*7, 72-74*). MI is a basic concept from information theory that measures the statistical dependence between two random variables or, for our purposes, between two images. The assumption is that there is maximal dependence between the grey values of the images when they are correctly aligned (Figure 1.17). Misregistration will result in a decrease in the measure. Thus, MI quantifies the amount of information that one image from one modality contains about the other image from another modality (i.e., knowing the value of a voxel in image A reduces the uncertainty [and hence entropy] for the value of the corresponding location in image B when the images of the same object are correctly aligned). Because there are no assumptions made regarding the relationship between the voxel values of the two image sets, the method is general and can be applied automatically. For these reasons, MI offers great flexibility. The algorithm also requires little to no preprocessing and minimal user interaction.

The MI between two random variables (or two images) X and Y is defined as:

$$I(X,Y) = \sum_{x} \sum_{y} p_{XY}(x,y) \log\left(\frac{p_{XY}(x,y)}{p_X(x)\, p_Y(y)} \right) \qquad \text{Eq. 1.14}$$

where p_X and p_Y are the probability density functions of X and Y, respectively, and p_{XY} is their joint probability function. MI is also related to entropy by the following formula:

$$I(X,Y) = H(X) + H(Y) - H(X,Y) \qquad \text{Eq. 1.15}$$

where H(X) and H(Y) give the entropy of X and Y, respectively, and H(X,Y) gives their joint entropy.

$$H(X) = -\sum_{x} p_X(x)\log\left[p_X(x)\right]$$
$$H(Y) = -\sum_{y} p_Y(y)\log\left[p_Y(y)\right] \qquad \text{Eq. 1.16}$$
$$H(X,Y) = -\sum_{x}\sum_{y} p_{XY}(x,y)\log\left[p_{XY}(x,y)\right]$$

1.14 MULTI-MODALITY IMAGING SYSTEMS

1.14.1 PET/CT

The development of the combined PET/CT scanner was an important evolution in imaging technology and made a significant impact on several aspects of PET imaging (*4, 31, 32, 75, 76*). The addition of the CT allowed a dramatic reduction in the overall scan time, for some protocols by a factor of two (*32*). With the latest generation of multi-detector CT systems, a whole-body transmission scan only takes a few seconds as opposed to 15-20 minutes with PET transmission sources. The potential noise contamination from the transmission scan into the emission data has been eliminated when using the CT images for attenuation correction. The greatest advantage of a combined PET/CT scanner is that by acquiring the image data on the same system under the same imaging conditions, fusion of functional PET images and anatomical CT images can be made with very high accuracy. Imaging anatomy and function in the same scanner is advantageous to both the patient and physician. For the patient, it is a convenient and straightforward procedure, while for the physician it provides accurately aligned images of function and anatomy from which tissue abnormalities can be precisely localized and non-specific radiotracer uptake in normal structures can be distinguished from disease (*4*). Clinical cases have shown that the merging of the two imaging modalities into one imaging procedure has resulted in a higher diagnostic accuracy compared to PET imaging alone (*4*). PET/CT also provides advantages in the drug discovery process (*48, 77*), with PET providing information about the distribution and functional effects of the drug and CT helping to define the anatomical structures in which the drug's actions take place, both at the disease target and throughout the organ systems of the body.

The first proposal to combine PET with CT was made in the early 1990s by David Townsend, Ronald Nutt, and colleagues (*78*). The first combined PET/CT prototype scanner was completed in 1998 (*26*). The PET/CT scanner was heralded as the "Medical Invention of the Year" by TIME magazine in 2000 and was called by some in the medical imaging community as "a technical *evolution* that lead to a medical *revolution*."

Interestingly, the first PET/CT grant proposal to the National Institutes of Health (NIH) was rejected in 1994 and many physicians opposed PET/CT in the early days. It took three years for Townsend and his team to obtain sufficient research funding to build a prototype scanner. Their persistence paid off and patients today benefit from the existence of PET/CT on a daily basis.

1.14.2 PET/MRI

Although PET/CT is already an established clinical tool, it still bears some limitations. A major drawback is that CT provides only limited soft tissue contrast and exposes the patient or animal being studied, to a significant radiation dose (*35*). Since the PET and CT components are attached back-to-back, the PET/CT scanner does not allow simultaneous data acquisition. This temporal mismatch can cause image artifacts by patient movement between the two scans or by respiratory motion. To overcome these limitations, recent research has concentrated on the combination of PET and MRI into one machine. The goal of this development is to integrate the PET detectors into the MRI scanner which would allow *simultaneous* data acquisition (instead of sequential as is done with PET/CT), resulting in combined functional and morphological images with excellent soft tissue contrast, very good spatial resolution of the anatomy, and accurate temporal and spatial image fusion. Additionally, since MRI provides functional information such as spectroscopy or blood oxygenation level dependant (BOLD) imaging, PET/MRI could even provide multi-functional information of physiological processes *in vivo (35)*. First experiments with PET/MRI systems have showed promising results (*36, 79, 80*), indicating its great potential for clinical and preclinical imaging. The first simultaneous PET/MRI brain study in a healthy volunteer is shown in Figure 1.18.

An important advantage of PET/CT over PET/MRI is that the CT information can be used for PET attenuation correction. The main problem in MR-based PET attenuation correction is that the photon attenuation in PET is not directly correlated to the signal measured by the MRI scanner. Although several MR-based PET attenuation correction methods have shown promising results (*81, 82*), more work still needs to be done in this field.

It has to be mentioned that PET/MRI is unlikely to replace PET/CT as a molecular imaging modality. Both imaging systems are here to stay because both platforms incorporate the diagnostic power of PET. The choice of using PET/MRI or PET/CT will most likely depend on the clinical question being investigated and any contraindications that the patient may have for performing either imaging procedure. A side-by-side comparison of images from an ^{18}F-FDG-PET/CT scan and an ^{18}F-FDG-PET/MRI scan in a patient with a large left lung legion is shown in Figure 1.19.

1.15 BASICS OF CANCER

In its most basic form, cancer is a failure in tissue homeostasis (cell growth vs. cell death) (*83-91*). Cancer cells do not respond to signals that usually regulate cell growth and cell division. These cells grow unchecked, producing more and more cancer cells that can invade and colonize territories normally reserved for other cells. The more widely the cancer cells spreads, the harder it becomes to eradicate, and it is generally the metastases that kill the cancer patient (*88*). Some of the biological hallmarks of cancer (*85, 86*) are listed in Table 1.3.

Cancer can be caused by external factors (e.g., infectious organisms, tobacco, chemicals, and radiation) as well as internal factors (e.g., inherited genetic mutations, hormones, immune conditions, and mutations that occur from metabolism) (*92*). These factors may act together or in sequence to initiate or promote the development of cancer.

Cancer statistics are shocking. Approximately 25% of people in the United States will get cancer during their lifetime, and 15% will die of the disease (*93*). Cancer can be treated more effectively when metastatic disease can be localized or excluded; it often can be cured if detected early (*92, 93*). Imaging technologies play an important role in the detection of malignant disease and in the management of the patient with known or suspected cancer.

1.16 ANATOMY OF THE BRAIN

> *"The brain is the last and grandest biological frontier,*
> *the most complex thing we have yet discovered in our universe.*
> *It contains hundreds of billions of cells interlinked through trillions of*
> *connections. The brain boggles the mind."* – James D. Watson
>
> *"It is essential to understand our brains in some detail if*
> *we are to assess correctly our place in this vast and complicated*
> *universe we see all around us."* – Francis H.C. Crick

The brain and spinal cord constitute the central nervous system (CNS). The principal roles of the CNS are to:

- Integrate and coordinate incoming and outgoing neural signals
- Carry out high mental functions such as thinking and learning

The brain contains billions of neurons arranged in a vast array of synaptic connections that provide a seemingly unfathomable circuitry. Through this circuitry, the brain integrates and processes sensory information and provides motor output. In this section, we will give a brief overview of the anatomy of the human brain. Our coverage is meant to be basic and not comprehensive. For an in-depth review, the reader is directed to anatomy textbooks written by Tortora (*94*), Marieb *et al.* (*95*), and Moore *et al. (96)*.

1.16.1 Nervous Tissue

Nervous tissue consists of two main types of cells: neurons (nerve cells) and neuroglia (also called glial cells). Neurons are the structural and functional units of the nervous system that are specialized for rapid communication (*96*). The neuron is composed of a cell body and its processes, dendrites and axons, which carry impulses *to* and *away* from the cell body, respectively. The dendrites are the main receiving or input regions of a neuron. The output part typically is a single axon, which propagates nerve impulses toward another neuron, a muscle fiber, or a gland cell. Layers of lipid and protein substances called myelin form a sheath around some axons, greatly increasing the velocity of impulse conduction. Neurons communicate with each other at synapses (i.e., points of contact between neurons). The communication occurs by means of neurotransmitters (chemical agents released or secreted by one neuron), which may excite or inhibit another neuron, continuing or terminating the relay of impulses or the response to them.

Neuroglia are non-neuronal cells that form a major component of nervous tissue (*96*). In contrast to neurons, neuroglia do not generate or propagate action potentials and they can undergo cell division in the mature nervous system. Neuroglia provide support and nourishment for neurons. A collection of nerve cell bodies in the CNS is called a nucleus. A bundle of nerve fibers (axons) connecting neighboring or distant nuclei of the CNS is called a tract.

1.16.1.1 White and Gray Matter

The brain contains white and gray matter. White matter is primarily composed of myelinated axons. Gray matter consists of neuron cell bodies, dendrites, axon terminals, unmyelinated axons, and neuroglia. Blood vessels are present in both white and gray matter (*94*).

1.16.2 Divisions of the Brain

The brain can generally be classified into four parts: (1) the cerebrum (which is composed of two cerebral hemispheres), (2) the diencephalon, (3) the brainstem (midbrain, pons, and medulla oblongata), and (4) the cerebellum. The basic parts of the brain are illustrated in Figure 1.20.

1.16.2.1 Cerebrum

The cerebrum is the "seat of intelligence" and serves as the control site of the nervous system, enabling us to possess the qualities associated with consciousness such as perception, communication, understanding, and memory (*94*). The right and left halves of the cerebrum, called cerebral hemispheres, are separated by a deep groove called the longitudinal fissure. The two hemispheres are connected internally by the corpus callosum, a broad band of white matter containing axons that extend between the hemispheres. The hemispheres consist of an outer rim of gray matter, an internal region of cerebral white matter, and gray matter nuclei deep within the white matter (Figure 1.21). The outer rim of gray matter is called the cerebral cortex.

Moreover, the cerebral hemispheres consist of gyri (elevations) and sulci (valleys). Each cerebral hemisphere can be further subdivided into four lobes (Figure 1.22):

1. **Frontal Lobe.** A major part of the frontal lobe is concerned with planning ahead, prediction, and programming for an individual's needs (*97*). The central sulcus divides the frontal lobe from the parietal lobe in the coronal plane. The gyrus anterior to the central sulcus is called the precentral gyrus and serves as the primary motor area of the brain. The remainder of the frontal lobe is used in modifying motor

actions. The lower portion of the frontal lobe, primarily on the left side, is specialized for the articulation of speech.

2. **Parietal Lobe.** The parietal lobe interprets sensations from the body. The gyrus posterior to the central sulcus, the postcentral gyrus, is the primary area for receipt of these sensations.

3. **Occipital lobe.** Visual information is processed in the occipital lobe; damage to this area results in partial or complete blindness.

4. **Temporal lobe.** The uppermost part of the temporal lobe is concerned with the sense of hearing. Damage to this part of the brain results in impaired hearing or deafness. The inner surface of the temporal lobe plays a role in memory processing. Much of the remaining temporal lobe may be involved with the integration of multiple sensory functions (*97*).

Functional areas of the cerebral cortex are shown in Figure 1.23. An MRI of the human brain is shown in Figure 1.24.

1.16.2.2 Diencephalon

The diencephalon consists of the thalamus, hypothalamus, and epithalamus, and is situated between the cerebrum and the brainstem. The diencephalon serves as the main processing center for information destined to reach the cerebral cortex from the ascending pathways (*98*).

1.16.2.3 Brainstem

The brainstem consists of the midbrain, pons, and medulla oblongata. The brainstem manages basic life support functions such as breathing, heart rate, blood pressure, and sleep cycles.

1.16.2.4 Cerebellum

The cerebellum, second only to the cerebrum in size, occupies the inferior and posterior aspects of the cranial cavity. It accounts for about one-tenth of the brain mass yet contains nearly half of the neurons in the brain (*94*). The primary function of the cerebellum is to evaluate how well movements initiated by motor areas in the cerebrum are actually being carried out (*94*). The cerebellum coordinates contractions of skeletal muscles and maintains normal muscle tone, posture, and balance.

1.16.3 Ventricular System of the Brain

The ventricular system of the brain is a set of four chambers within the brain and is continuous with the central canal of the spinal cord (*98*). Cerebrospinal fluid (CSF) flows within these chambers and serves as a liquid cushion, providing buoyancy to the brain and spinal cord.

1.16.4 Blood Supply of the Brain

The four main arteries that supply the brain are the two internal carotid arteries that ascend anteriorly in the neck and the two vertebral arteries that ascend posteriorly in the neck (Figure 1.25). The cerebral arterial circle (of Willis) at the base of the brain is an important anastomosis (i.e., communication) between the four arteries that supply the brain. It is formed by the posterior cerebral, posterior communicating, internal carotid, anterior cerebral, and anterior communicating arteries. The cerebral arterial circle is an important means of collateral circulation in the event one of the arteries forming the circle is obstructed.

1.16.5 Protection of the Brain

The brain is protected by the bones of the skull, the meninges (membranes enveloping the brain and spinal cord: dura mater, arachnoid mater, and pia mater), the CSF, and the blood-brain barrier (BBB). The BBB protects brain cells from harmful substances and pathogens by preventing passage of many substances from the blood into brain tissue. The BBB helps to maintain a stable environment for the brain. No other body tissue is as dependent on a constant internal environment as is the brain.

1.16.6 Miscellaneous Facts about the Human Brain

1. The average adult human brain weighs about 1500 g (or 3.3 pounds).
2. Albert Einstein’s brain weighed about 1230 g.
3. The first mention of the brain as an organ occurred in the papyri of ancient Egypt.
4. The brain contains about 100 billion neurons.
5. The cerebral cortex, although only 2-4 mm thick, contains billions of neurons arranged in six layers.
6. Twelve pairs of cranial nerves (left and right) emerge from the base of the brain.
7. Neuroglia make up about half the volume of the CNS and are approximately 5 to 50 times more numerous than neurons.

8. Although the adult brain represents about 2% of the total body weight, it receives approximately 15% of the cardiac output, 20% of the total body oxygen consumption, and 25% of the total body glucose utilization.
9. Glucose supplies approximately 95% to 99% of the brain's energy in normal physiologic states.
10. Every part of the brain that communicates with the cerebral cortex must relay its signals through a nucleus of the thalamus; the thalamus is thus sometimes called the "gateway" to the cerebral cortex.
11. The brain is unique, compared with other tissues in the human body, in having virtually no means of storing energy.
12. Each hemisphere of the brain is chiefly concerned with the sensory and motor functions of the opposite (contralateral) side of the body (i.e., there is left/right governance).
13. Eleven of the twelve paired cranial nerves arise from the brainstem.

1.17 DISEASES OF THE BRAIN

The brain, like other important organs of the body, is subject to a wide assortment of diseases, many of which can have serious consequences. Diseases of the brain can result from errors introduced into its chemical systems by viruses, bacteria, genetic abnormalities, drugs, trauma, environmental factors, aging, and behavior (*2*). This section reviews two neurological disorders: Alzheimer's disease and brain tumors.

1.17.1 Alzheimer's Disease

Alzheimer's disease (AD) is a type of dementia that afflicts about 11 percent of the population over the age of 65 (*99*). It was originally described in 1907 by the German psychiatrist and neuro-pathologist, Alois Alzheimer. AD is the most common cause of dementia worldwide. In the United States, more than 4 million people are afflicted with this tragic disease (*99*). AD results in the loss of reasoning and the ability to care for oneself. Claiming over 100,000 lives a year, AD is the fourth leading cause of death among the elderly, after heart disease, cancer, and stroke (*99*). The present financial burden exceeds $100 billion annually in the United States alone (*100*).

The cause of most AD cases is still unknown, but evidence suggests it is due to a combination of genetic factors, environmental or lifestyle factors, and the aging process. Onset of AD is usually late in life. Mutations in three different genes (coding for presenilin-1, presenilin-2, and amyloid precursor protein) can lead to early-onset forms of AD in afflicted families but account for less than 1 percent of all cases. An environmental risk factor for developing AD is a history of head injury.

In normal aging, nerve cells in the brain are not lost in large numbers. However, in AD, many nerve cells stop functioning, lose connections with other nerve cells, and die. At first, AD destroys neurons in parts of the brain that control memory, including the hippocampus (a structure deep in the brain that helps to encode short-term memories) and related structures (*101*). As nerve cells in the hippocampus stop working properly, short-term memory fails, and often, a person's ability to do easy and familiar tasks begins to decline. AD later attacks the cerebral cortex, particularly the areas responsible for language and reasoning (*101*). At this point, AD begins to take away language skills and changes a person’s ability to make judgments. Personality changes also may occur. Emotional outbursts and disturbing behaviors, such as wandering and agitation, begin to take place and become more and more frequent as the disease progresses. Eventually, many other areas of the brain are involved and most, if not all, of these brain regions atrophy (i.e., they shrink and lose function). A person with AD usually dies of some complication that afflicts bedridden patients, such as pneumonia. A comparison of the brains of a non-demented, normal aging individual and an AD patient is shown in Figure 1.26.

At autopsy, the brains of AD patients show three distinct structural abnormalities:

1. **Loss of neurons that liberate acetylcholine.** A major center of neurons that liberate acetylcholine is the nucleus basalis, a group of large cells below the globus pallidus. Axons of these neurons project widely throughout the cerebral cortex and limbic system. Their destruction is one of the hallmarks of AD. Drugs that inhibit acetylcholinesterase, the enzyme that breaks down acetylcholine and thereby terminates its action, can improve alertness and behavior in about 5 percent of AD patients. Although acetylcholinesterase inhibitors such as donepezil (Aricept), rivastigmine (Exelon), and galantamine (Reminyl) may help prevent some of the symptoms from becoming worse for a limited time, there is still no cure for AD at this moment.

2. **Beta-amyloid plaques.** Beta-amyloid plaques are clusters of abnormal proteins deposited *outside* of neurons. AD has been identified as a protein misfolding disease due to the accumulation of these abnormally folded proteins in the brains of AD

patients. Researchers still do not know whether amyloid plaques themselves cause AD or whether they are a by-product of the AD process.

3. **Neurofibrillary tangles (NFTs).** The severity of the dementia in AD is well correlated with the number and distribution of what are now commonly known as NFTs, the "tombstones" of dead and dying neurons (*102*). NFTs are abnormal bundles of filaments located *inside* of neurons in affected brain regions. These filaments consist of a protein called *tau* which has been hyper-phosphorylated (i.e., too many phosphate groups have been added to it). In healthy neurons, microtubules form structures like train tracks, which guide nutrients and molecules from the cell bodies down to the ends of the axon. Tau normally holds together the "railroad ties" or connector pieces of the microtubule tracks. However, in AD, the altered tau no longer holds the railroad tracks together and the microtubules fall apart. This collapse of the transport system may first result in malfunctions in communication between nerve cells and may later lead to neuronal death that contributes to the development of dementia (*101*).

There has been much discussion in the AD research community on whether amyloid or NFTs may be "primary" in disease causality. While both pathological cascades are the target of intense research interest and study, it must be noted that the relationship between neuritic plaques and NFTs is still unknown at this time (*14*).

The deposition of beta-amyloid plaques and NFTs in the brains of AD patients has been studied extensively (*100*). NFTs are most abundant in the limbic and temporal lobes followed by the frontal and parietal lobes and then the occipital lobe (*100*). Primary sensory areas are relatively spared. Beta-amyloid plaque pathology, on the other hand, develops in a pattern different from NFT distribution and predominantly affects neocortical regions. Beta-amyloid plaques are distributed more uniformly with temporal, parietal, and occipital lobes being higher than frontal lobe and much higher than the limbic lobe (*100*). There is, again, relative sparing of primary sensory-motor areas. ^{18}F-FDG-PET scans in AD patients typically show biparietal and bitemporal hypometabolism, with characteristic sparing of the sensorimotor cortex (*1, 14*).

^{18}F-FDDNP was the first radiolabeled PET molecular imaging probe to be successfully applied to the *in vivo* visualization of beta-amyloid plaques and NFTs in AD patients (*100*). It is a hydrophobic molecule and contains a naphthalene ring system (i.e., two benzene rings fused together) in its structure. ^{18}F-FDDNP is short for its full chemical name: 2-(1-{6-[(2-^{18}F-fluoroethyl)(methyl)amino]-2-naphthyl}-ethylidene)malononitrile). It was developed by Jorge R. Barrio and colleagues at UCLA (*100*). A neat piece of trivia about ^{18}F-FDDNP is that it appeared on the hit TV show House M.D. (Season 1, Episode 22 - "Honeymoon").

1.17.2 Brain Tumors

1.17.2.1 Introduction

Glial cells are non-neuronal cells that provide support and protection for neurons in the brain. Glial cells do not generate or propagate nerve impulses like neurons. However, unlike neurons, they do have the ability to multiply and divide in the mature nervous system. Malignant glioma, a type of tumor that arises in the glial cells of the brain, remains a difficult and sometimes intractable problem for physicians.

According to the National Cancer Institute and the American Cancer Society, there will be an estimated 23,130 new cases of malignant primary brain tumors in the United States in 2013, and there will be an estimated 14,080 deaths (*92, 103*). Gliomas comprise 80% of malignant brain tumors, with approximately 14,000 new cases each year in the United States (*104*). The incidence of glioblastoma (GBM), the most common malignant glioma, increases with age, with the highest rates in the 75-84 year age group (*104*). GBMs are 1.6 times more common in males than females and more than twice as common among white than black people (*104*). The majority of malignant gliomas are comprised of GBM (60-70%, World Health Organization [WHO] grade IV), anaplastic astrocytoma (10-15%, WHO grade III), and anaplastic oligoastrocytoma and anaplastic oligodendroglioma (10%, WHO grade III) (*104*). Though gliomas can manifest in any area of the central nervous system, they are located supratentorially (i.e., above the tentorium cerebelli, which separates the cerebrum from the cerebellum) in 70% of affected adults (*104*). In children, however, 70% are infratentorial (i.e., below the tentorium cerebelli).

In addition to gliomas initially being diagnosed as grade III or IV, also called de novo or primary high-grade glioma, some lower grade gliomas (typically grade II) may transform into a higher grade tumor over time (*104, 105*). These tumors are referred to as secondary high-grade gliomas (*104*). Primary GBMs typically present with a rapid progression of symptoms, while secondary GBMs can present more slowly and are more often seen in younger patients (*104*).

The standard of care for GBM includes maximal surgical resection followed by radiotherapy with concurrent and adjuvant temozolomide (TMZ) therapy (*104-106*). TMZ is a DNA methylating agent that produces cross-links in the DNA strands such that they disrupt replication or transcription (*107*). Even with aggressive therapy, prognosis for malignant glioma remains poor, with a median survival of 15 months for patients with a GBM (*104*). The relative survival estimates for GBM are quite low; less than 5% of patients diagnosed between 1995 and 2006 survived 5 years after diagnosis (*104*).

The biology of malignant glioma is unique (*108, 109*). Although systemic metastases occur, they are relatively rare. The vast majority of glioblastomas recur within two centimeters of their original margin (*110*). The tumors are extremely aggressive in a locally invasive fashion. Morphologically, malignant gliomas are histologically heterogeneous and highly vascular tumors that often have extensive areas of necrosis and hypoxia (*104, 106*). GBMs have a predilection for the white matter of the cerebral hemispheres, especially the frontal lobes, and frequently infiltrate extensively into adjacent lobes and deep structures (*111*) (see Figure 1.27). Some of the acquired genetic mutations found in GBM are shown in Table 1.4.

Imaging of brain tumors was one of the first clinical applications of PET in oncology. In these early studies, 2-deoxy-2-[^{18}F]-fluoro-D-glucose (^{18}F-FDG) was used to image glucose metabolism in tumor cells. One of the drawbacks of ^{18}F-FDG for studying brain tumors is that due to the high physiologic glucose metabolism of normal gray matter, the detectability of tumors with only modest increases in glucose metabolism (such as in low-grade tumors and in some cases recurrent high-grade tumors) has proved to be difficult (*112, 113*). Therefore, researchers have turned to other tracers that have a much higher tumor-to-background ratio such as 3′-deoxy-3′-[^{18}F]-fluorothymidine (^{18}F-FLT) (*114-116*), which images cellular proliferation and 3,4-dihydroxy-6-[^{18}F]-fluoro-L-phenylalanine (^{18}F-FDOPA) (*117, 118*), which images the transport of large neutral amino acids in tumors (Figure 1.28).

1.17.2.2 Recurrent Disease

Tumor recurrence is nearly universal, and treatment at recurrence depends both on the prior treatment received and on the patient's physical condition and goals (*104, 105*). The median time to progression for GBM after treatment with radiotherapy and TMZ was shown to be 6.9 months in a phase III clinical trial (*104*). The anti-angiogenic agent bevacizumab was granted accelerated approval by the U.S. Food and Drug Administration in May 2009 for use in recurrent GBM. Bevacizumab improved the 6-month progression-free survival in recurrent GBM as compared to patients treated with TMZ. Repeat surgery and implantation of carmustine-impregnated wafers is another approved treatment that may prolong survival in selected patients.

1.17.2.3 Pseudoprogression and Pseudoresponse

Assessment of treatment response is of paramount importance to routine patient care and for clinical trials. Traditionally, response assessment in neuro-oncology is done with contrast-enhanced T1-weighted MRI. However, this technique does not provide a specific measure of tumor size and activity, but is mainly influenced by vascular leakage of the contrast agent at sites where the BBB is disrupted (*119*). In many situations, changes in enhancement do not correlate with response. One example of this occurrence is pseudoprogression, in which an increase in contrast uptake does not reflect tumor progression (*104, 119*). Another example is the reverse effect, called pseudoresponse, in which a decrease in contrast enhancement does not reflect tumor regression in patients treated with anti-angiogenic agents. Pseudoprogression can occur after radiotherapy with or without TMZ (*119*). Pseudoresponse in the setting of anti-angiogenic treatment is likely due to a normalization of the abnormally permeable tumor vasculature (*119*).

This can lead to a rapid decrease in contrast enhancement on gadolinium T1-weighted MRI, but does not reflect a real decrease in tumor size or biological activity (*119*).

1.17.2.4 Response Assessment in Neuro-Oncology Criteria

The Macdonald criteria have been the standard for response evaluation in neuro-oncology for many years (*120, 121*). In short, they consist of a 2-dimensional measurement of contrast enhancement, with attention paid to steroid dosing and the clinical status of the patient as well. These criteria represented a significant advance, but over time, neuro-oncologists have come to appreciate the complexity of imaging interpretation, and so a multidisciplinary task force was formed to update the response criteria. While still a work in progress, the Response Assessment in Neuro-Oncology (RANO) criteria have been published (*122*) and are becoming the new standard for the field of neuro-oncology.

The RANO criteria encompass some important modifications of the Macdonald criteria. A major impetus for this update was the widespread adoption of anti-angiogenic therapies for the treatment of malignant gliomas. These treatments have a pronounced anti-permeability effect, which can cause marked diminishment of tumor enhancement, even when overall tumor size is unchanged or even when tumor growth is apparent. This increased “decoupling” of enhancement from an accurate measure of tumor burden made the Macdonald criteria, which are based on bi-dimensional measurements of enhancing lesions only, no longer tenable (*123*). The major modification proposed by the RANO guidelines is the assessment of increasing fluid-attenuated inversion recovery (FLAIR) signal intensity change as evidence of tumor progression. In short, the RANO criteria have therefore been referred to as Macdonald plus FLAIR. The incorporation of FLAIR imaging into the RANO guidelines improves the accuracy of determining tumor progression in the setting of anti-angiogenic therapy, because it allows the inclusion of non-enhancing tumor into the determination of overall tumor burden (*123*). As imaging technology moves forward, these response criteria will continue to be refined.

1.18 ORGANIZATION OF THE DISSERTATION

This dissertation consists of five chapters, the first of which has already been covered. A major theme that resonates through these chapters is the usefulness of PET as an imaging and analytical tool for measuring biological processes in the brain in a quantitative and non-invasive manner.

In Chapter 1, we presented a general overview of PET, tracer kinetic modeling, image registration, multi-modality imaging systems (specifically, PET/CT and PET/MRI), human brain anatomy, and diseases of the brain such as Alzheimer's disease and malignant brain tumors. In Chapter 1, we learned that diseases are biological processes in which molecular errors cause failure of the normal, well-regulated function of cells, and molecular imaging with PET is sensitive to and informative of these processes. Moreover, we learned that the use of PET to obtain quantitative measurements of physiologic, biochemical, and pharmacokinetic processes *in vivo* requires the integration of three major components: (1) the PET scanner, (2) compounds labeled with cyclotron produced positron-emitting radioisotopes, and (3) tracer kinetic models that represent mathematical descriptions of transport or biochemical reaction sequences. A major goal of PET imaging for clinical brain applications is the early detection of neurological disease and the monitoring of neuroprotective/neurorestorative interventions. As we move forward from Chapter 1, we will cover three projects that form the basis of this dissertation.

In Chapter 2, we will describe a retrospective image-based movement correction method and evaluate its implementation on dynamic ^{18}F-FDDNP PET images of cognitively intact controls and patients with Alzheimer's disease, each with varying degrees of head movement. We will see that head movement during a PET scan (especially a dynamic scan) can cause incorrect attenuation correction factors to be applied to the emission data because it induces misalignments between the transmission scan that is acquired at the start of the study and the serial emission scans that are acquired afterwards. Without a method to properly correct for head movement, a distorted view of the true activity distribution in the reconstructed images will result; furthermore, the PET images will not be quantitatively correct.

In Chapters 3 and 4, we will examine the quantitative capability of PET for studying human brain tumors. In Chapter 3, we will investigate whether changes in tumor ^{18}F-FLT kinetic parameters, taken early after the start of therapy, can predict overall survival and progression-free survival in patients with recurrent malignant glioma undergoing treatment with an angiogenesis inhibitor and a chemotherapeutic agent. Kinetic parameter values before and after the start of treatment as well as their changes will be incorporated into a linear discriminant function for predicting membership into one of two groups: those that lived less than 1 year and those that lived greater than or equal to 1 year. This method has the potential to help physicians provide more personalized treatment regimens by giving them an early indicator on whether to discontinue ineffective therapies or switch the patient to more advanced treatment regimens that could help improve patient outcome.

In Chapter 4, we will expand on what we did in Chapter 3, except that we will acquire longitudinal ^{18}F-FDOPA PET scans in addition to ^{18}F-FLT PET scans. We will also try to predict overall survival as a continuous outcome variable using multiple linear regression as opposed to a dichotomous categorical variable with discriminant analysis from before. Lastly, in Chapter 5, we will conclude with a summary of the work described in this dissertation and share some final thoughts on future research directions.

1.19 FIGURES

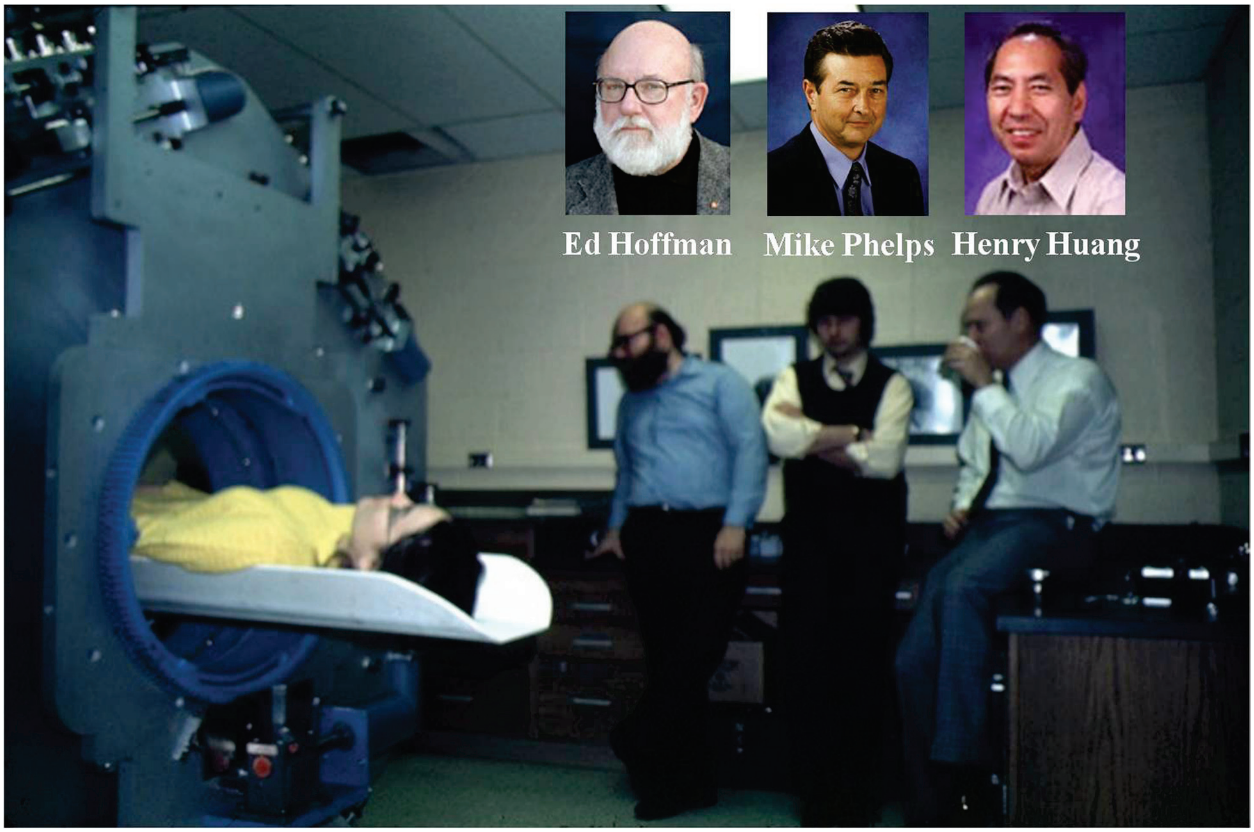

Figure 1.1 Michael E. Phelps, Edward J. Hoffman, and Sung-Cheng (Henry) Huang during the early days of PET at UCLA. It is difficult to put into words the extraordinary impact of their visionary efforts in developing an imaging technology that has revolutioned the field of modern medicine. This picture was taken at UCLA Medical Center circa 1977. The National Institutes of Health would go on to fund seven PET centers in 1979 under a program grant, initiating PET as a discipline. (Background photograph courtesy of Dr. Simon Cherry, UC Davis)

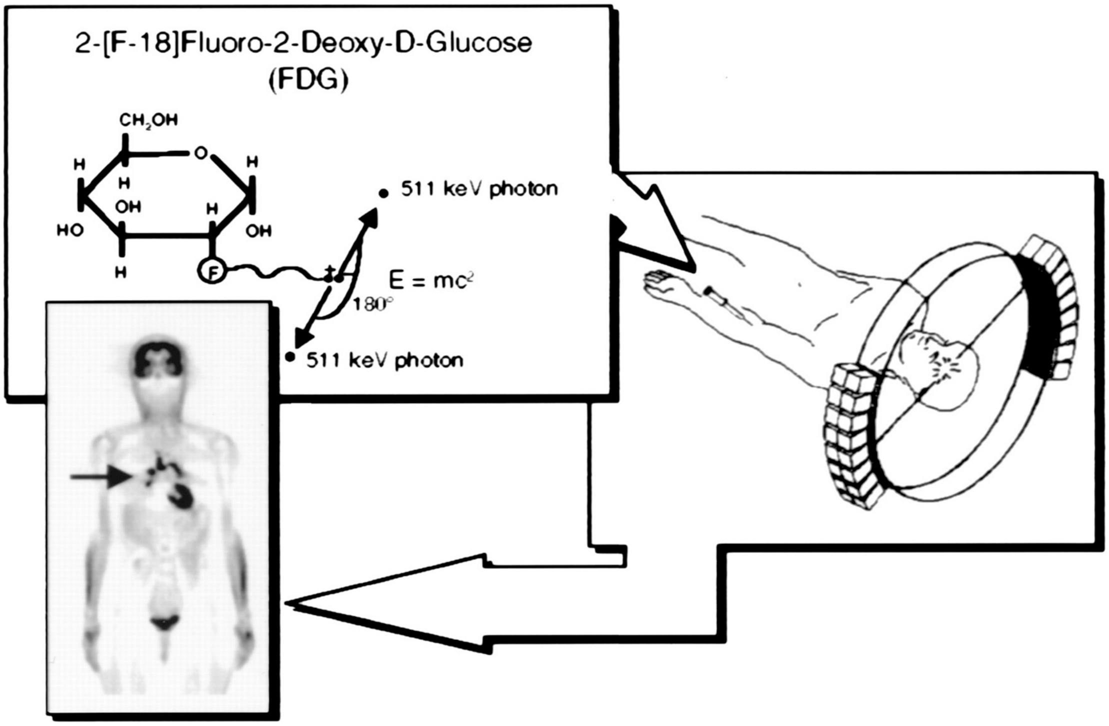

Figure 1.2 Principles of PET. To perform a PET study, one needs to first label a biologically active molecule with a positron-emitting radionuclide such as C-11, N-13, O-15 or F-18. The labeled compound (typically 10^{13}-10^{15} labeled molecules) is then introduced into the body, typically by intravenous injection, and is distributed in tissues in a manner that is determined by the biochemical properties of the radiolabeled tracer and the physiologic state of the subject. A positron (which has the same mass as an electron but the opposite electric charge) is emitted from the unstable nucleus of the radionuclide and travels a short distance before it annihilates with an electron. Annihilation is a process whereby the masses of the positron and electron are converted into their energy equivalent ($E = mc^2$) through the emission of two 511-keV photons that are approximately 180° apart. The two 511-keV photons are electronically detected as a coincidence event when they strike opposing detectors simultaneously. The location of the radioactive decay is assumed to have occurred somewhere along the line connecting the two detectors. In a PET scanner, a large number of detectors are arranged around the object to be imaged. By collecting a large number of coincidence events between the detector pairs in the imaging system, the distribution of the activity can be reconstructed. In the figure shown above, 2-deoxy-2-[^{18}F]-fluoro-D-glucose (^{18}F-FDG) is administered into a patient to image the glucose metabolism in the body. ^{18}F-FDG is an *analog* of glucose and is transported across the cell membrane via GLUT transporters, which operate by facilitated diffusion. ^{18}F-FDG is trapped within cells after it is phosphorylated by hexokinase. The formation of the negatively charged ^{18}F-FDG-monophosphate results in intracellular trapping and accumulation of radioactivity. Importantly, PET tracers are administered at a non-pharmacological dose (micrograms or less), so they neither disturb the underlying system nor cause pharmacological or behavioral effects. The above figure shows a coronal image of a woman with bilateral metastasis to the lung (arrow) from a previous ovarian cancer that was surgically resected. Regions with a high metabolic rate of glucose are shown in black. (Figure is reprinted from Phelps (*12*), with permission from the Journal of Nuclear Medicine)

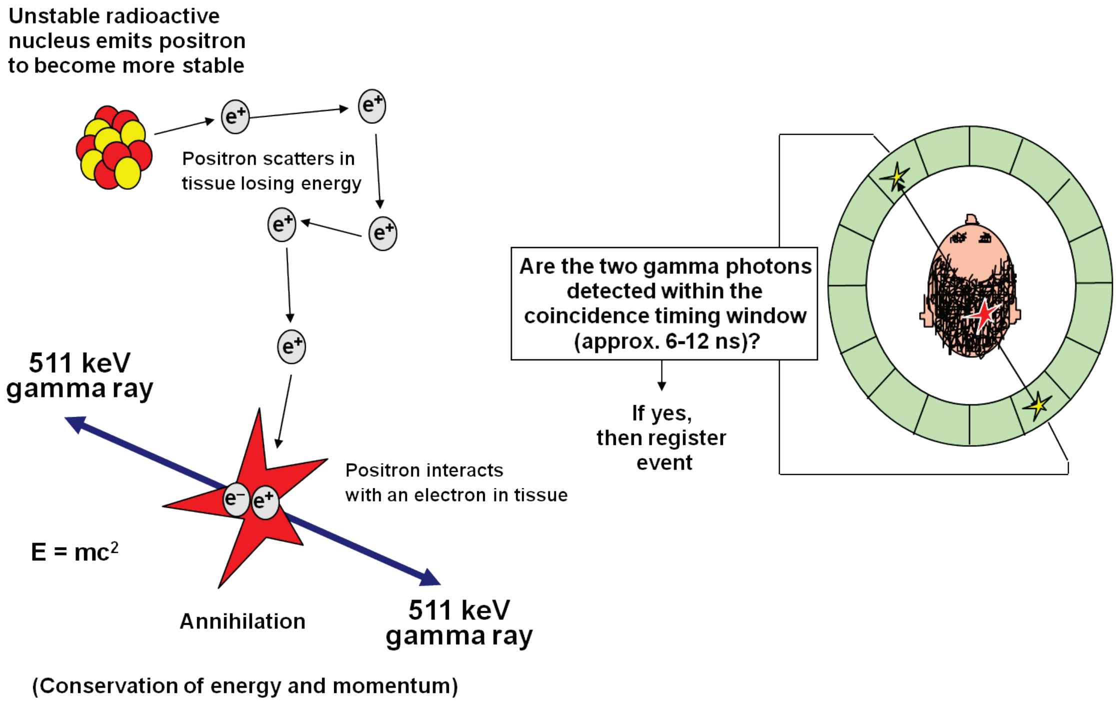

Figure 1.3 A PET scanner is a sophisticated imaging system which provides analytical tomographic measurements of the tissue concentration of compounds labeled with a positron emitter. The radionuclide is attached to a molecular probe that is designed to trace some biologic process in the body. After the positron is emitted from the *nucleus* of the unstable radionuclide, it loses energy by scattering from electrons in tissue before annihilating with an electron to produce two 511 keV gamma rays, which are emitted at approximately 180 degrees to each other. The annihilation event is usually very close to the site of positron emission because the emitted positrons rapidly lose their energy in tissue. The distance the positron travels before annihilation is small, typically less than 2 mm. In a typical PET scan, millions of these photon pairs will be detected from the radiolabeled molecules which have been injected into the body. A PET scanner consists of a circumferential array of scintillation detectors which register a signal when a gamma ray interacts in them. Scintillation detectors are widely used gamma ray detectors for almost all PET scanners in use today. These detectors consist of a dense crystalline scintillator material that serves as an interacting medium for gamma rays and high-energy photons and which emits *visible light* when energy is deposited in them. This light is then detected by a photon detector and converted into an electrical current. The detectors are connected with fast timing circuits which look for two simultaneous or “coincident” events on opposite sides of the head. Detection of the two coincident gamma rays defines a line which intersects the position of the annihilation event (and thus the positron-emitting probe).

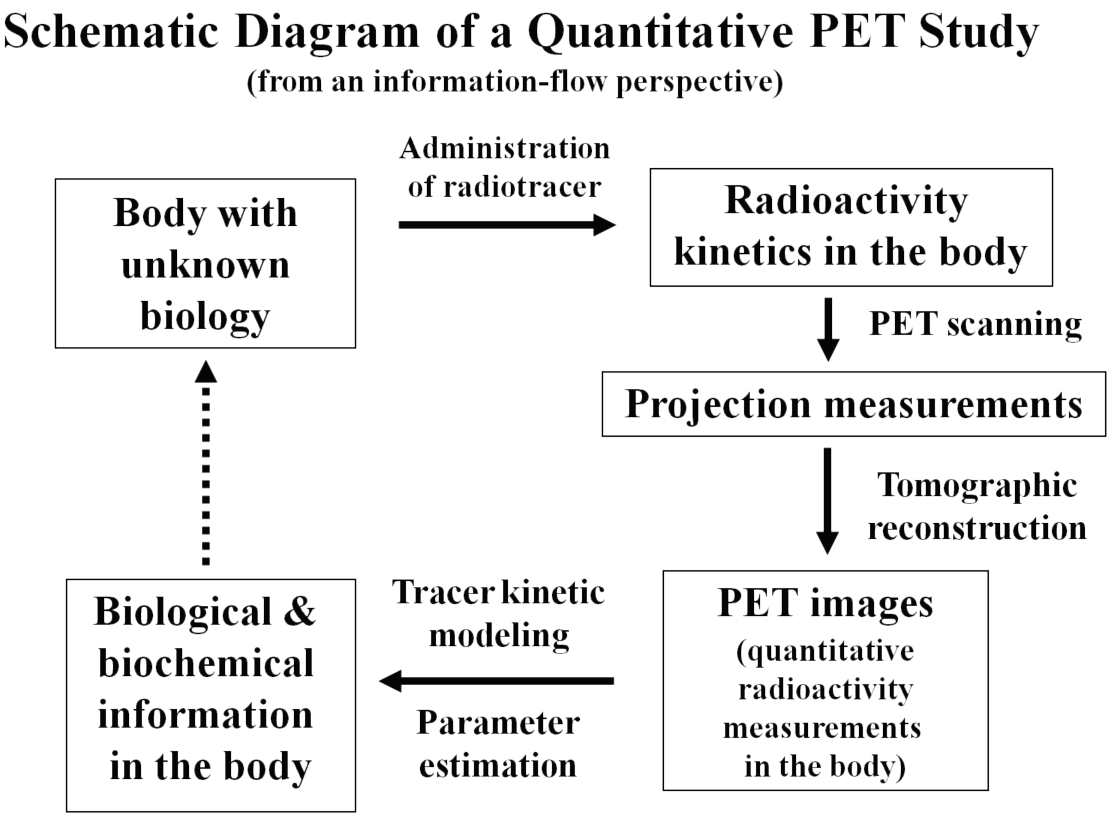

Schematic Diagram of a Quantitative PET Study

(from an information-flow perspective)

Figure 1.4 Schematic diagram of a quantitative PET study from an information-flow perspective. The dashed arrow indicates the interpretation of the images obtained from PET imaging after a radiotracer has been administered to the subject. The interpretation is accomplished by kinetic modeling of the tracer distribution in the body and by estimation of the model parameters best matching the biological functions in the body of the subject being studied. (Figure courtesy of Dr. Henry Huang, UCLA)

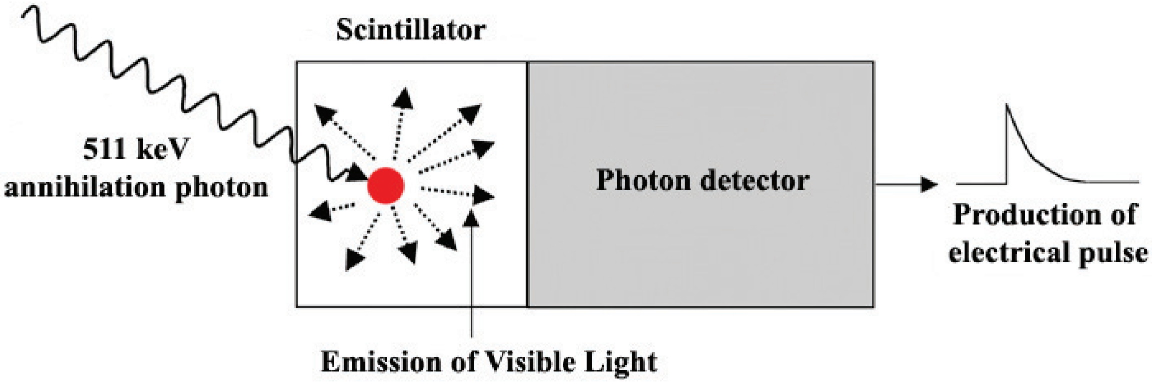

Figure 1.5 Basic components of a scintillation detector. The incident annihilation photon interacts in the scintillator (either by photoelectric or Compton interaction). Each annihilation photon that interacts in the scintillator produces a single electrical pulse in the detector, with the amplitude of the pulse being determined by the number of scintillation photons reaching the photon detector and any amplification inherent in the photon detector. One of the desirable characteristics of a detector material for PET is that the primary interaction type is photoelectric interaction. This will ensure that the photon energy is absorbed in a small detector volume. The ideal detector material for PET should therefore have a high effective Z. In addition, a suitable detector for PET should have a fast scintillation decay time, a high density, a high linear attenuation coefficient, and a high light output. The wavelength of the emitted scintillation light should also be well matched to the spectral response of the photon detector. The detector material should preferably not be hygroscopic (i.e., it does not readily absorb or retain moisture). The material should also be relatively rugged to allow it to be cut into suitable detector dimensions.

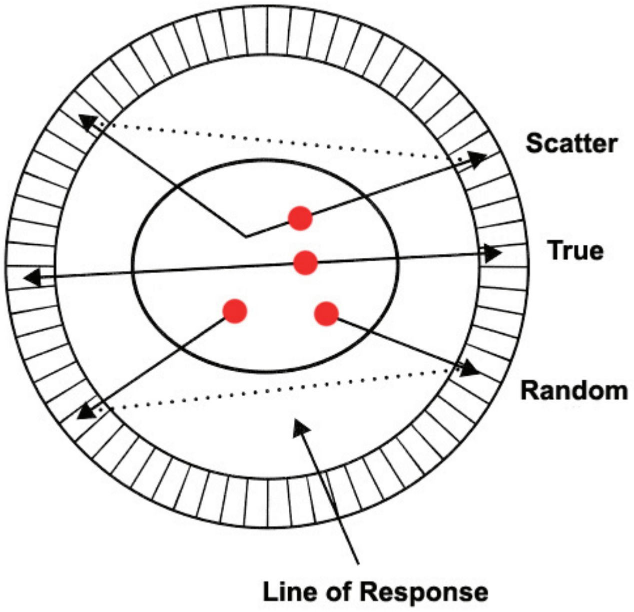

Figure 1.6 True, scattered, and random coincidence events. A true coincidence occurs when both annihilation photons escape the body and are recorded by a pair of detectors. Only the true coincidences carry spatial information regarding the distribution of the radiotracer. In a scattered coincidence, one or both of the annihilation photons interacts in the body prior to detection. This results in a mispositioning of the event. A random coincidence is generated by two photons originating from two separate annihilations. These events form a background in the data that needs to be subtracted. Corrections for random and scattered coincidence events must be applied to maximize quantitative accuracy. A fourth type of coincidence event called multiple coincidence (not shown above) may also occur. In a multiple coincidence event, three or more photons are detected simultaneously. However, due to the ambiguity of where to position the multiple events, these events are normally discarded.

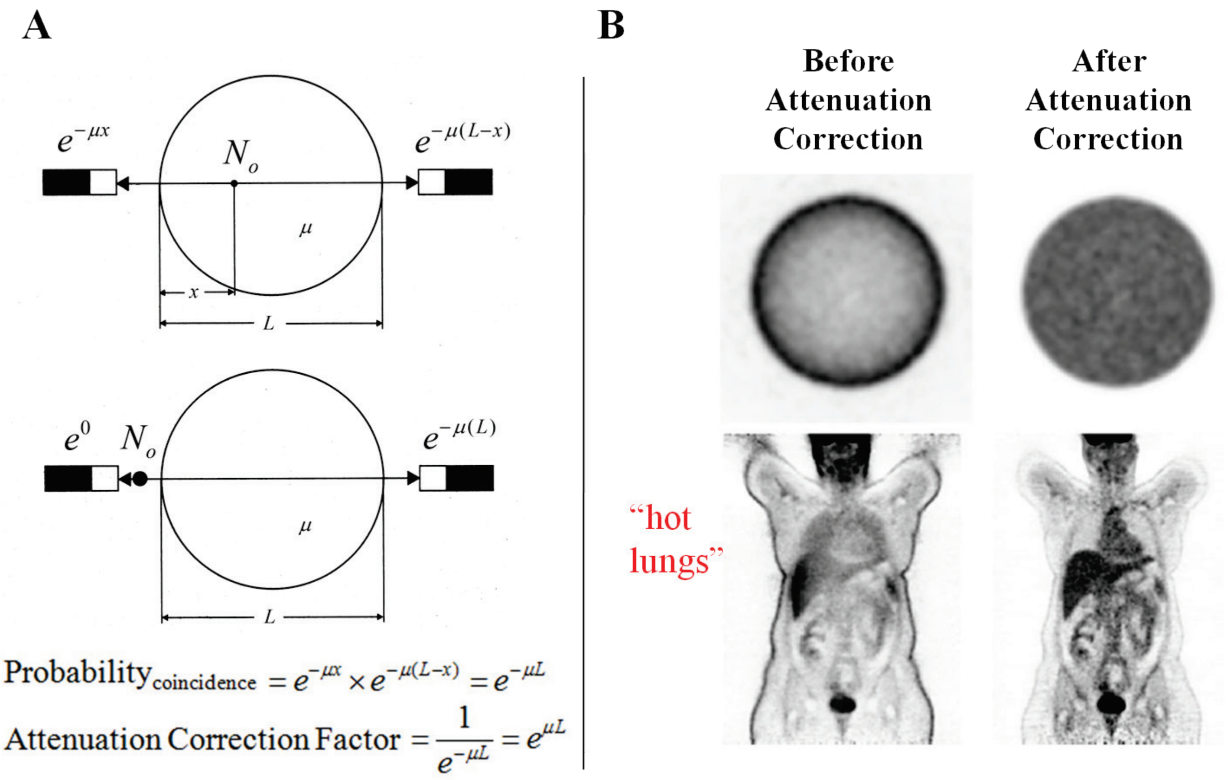

Figure 1.7 Illustration of the effect of photon attenuation in PET. Attenuation is the loss of coincidence events through scatter or absorption of one or both of the annihilation photons in the body. In subpanel A, we see that the attenuation of two annihilation photons is independent of the location from which the two photons were produced along the line of response, since the photon pair must always travel the same distance within the body and escape without interaction in order to be detected as a true event. Even if the annihilation event happens outside the body, the attenuation is the same. It is, therefore, possible to use an external positron-emitting source (usually a rod source orbiting just inside the field of view) to measure the attenuation correction factors. In subpanel B, the left images were reconstructed without attenuation correction. The cross section of the uniform cylinder (top) appears to have suppressed activity in the center and a progressive underestimation of the true radioactivity from the edge to the center. The coronal cross-section of the patient (bottom) shows an apparent high uptake in the skin and lungs. Large organs in the abdomen, such as the liver, appear to have a very heterogeneous uptake. The images on the right in subpanel B were reconstructed with attenuation correction. After attenuation correction, the image of the cylinder and the image of the internal organs of the patient show a more uniform uptake. In the patient image after attenuation correction, there is also no more "hot lung" artifact. (Figure 1.7B is reprinted from Dahlbom (*32*), with permission from Springer)

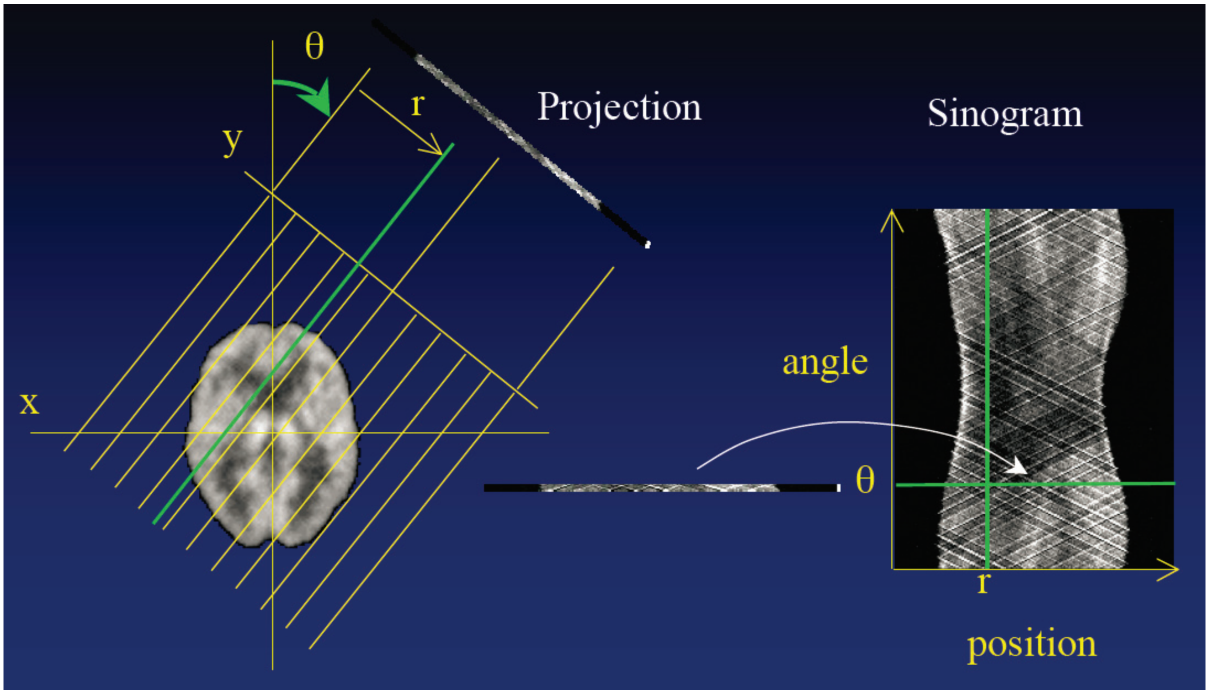

Figure 1.8 PET projection data are conventionally stored in the form of a 2D matrix known as a sinogram. The relation between the projection line and its position in the sinogram is shown above. Each element in the sinogram represents the number of counts detected by a particular detector pair (i.e, the projection or sum of all the activity along the line joining the two detectors). By convention, the vertical axis of the sinogram represents the angle of the line of response and the horizontal axis represents the displacement from the center of the field of view. Tomography is the process of taking projection data from multiple views and converting the data into cross-sectional images of the original object. Simple backprojection of all the projection data into image space leads to a blurred representation of the original object. To obtain a more faithful representation of the true image, the projections must be filtered before the backprojection process. (Figure courtesy of Dr. Carl Hoh, UCSD)

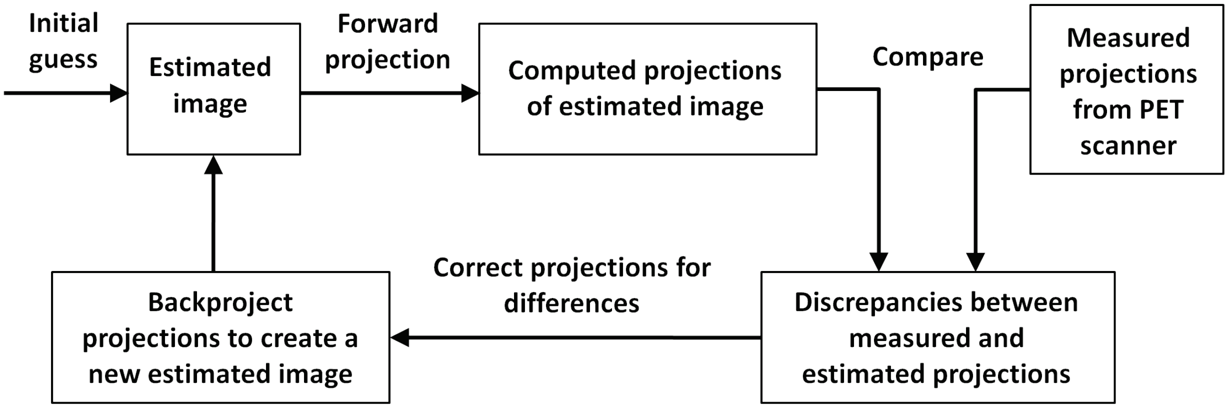

Figure 1.9 Diagram of the iterative image reconstruction process. Following an initial guess of the activity distribution, the estimated image is forward projected to calculate a sinogram, which is then compared with the measured sinogram from the PET scanner. Based on the difference between the calculated and measured sinograms, the image is updated. This updated image is then the starting point for the next iteration. This process is repeated until the difference between the measured and forward projected data has reached a specific threshold (i.e., convergence has occurred). One of the advantages of the iterative reconstruction method is its ability to model various aspects of the imaging chain (e.g., attenuation, scatter, and detector normalization) during the reconstruction process.

Tracer kinetic modeling and parameter estimation

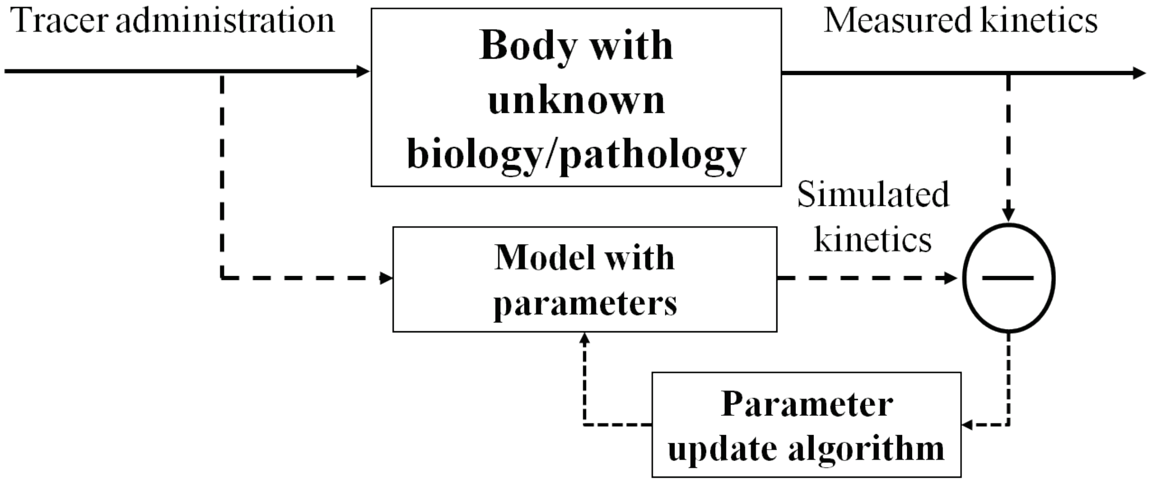

Figure 1.10 Sketch diagram illustrating the role of pharmacokinetic modeling in PET imaging. After an imaging probe is injected into the body, the probe is distributed in the body over time according to the biologic state in the body. The distribution kinetics are measured by the PET scanner. A pharmacokinetic model imitates the body state and simulates the pharmacokinetics of the probe. Deviation between the simulated pharmacokinetics and those measured with PET imaging is used to adjust the parameters in the model, until the two are in agreement. (Figure courtesy of Dr. Henry Huang, UCLA)

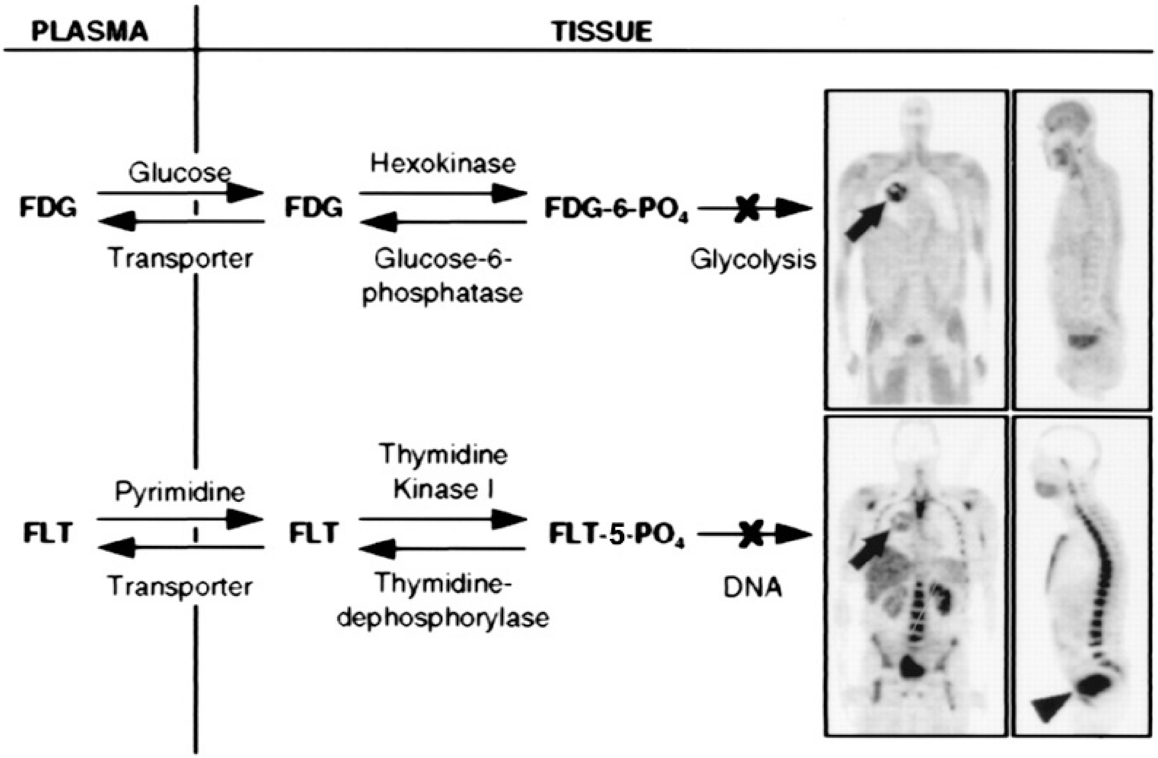

Figure 1.11 Tracer kinetic models for ^{18}F-FDG and ^{18}F-FLT. Arrows show forward and reverse transport between plasma and tissue as well as phosphorylation and dephosphorylation reactions in tissue. Compartmental models in PET provide the mathematical framework for calculating various rates of biological processes, based on the time course of tracer distribution in a dynamic series of PET images and the plasma concentration of the molecular PET probe. Images on the far right are coronal and sagittal views of a patient with a non-small lung carcinoma with high glucose metabolism (top) and high DNA replication (bottom). In the ^{18}F-FLT image, notice the normal high DNA replication for cell proliferation in the skeletal system and the clearance of ^{18}F-FLT to the bladder. The high activity in the liver is due to glucuronidation of ^{18}F-FLT. (Figure adapted from Phelps (*13*), with permission from the National Academy of Sciences, U.S.A.)

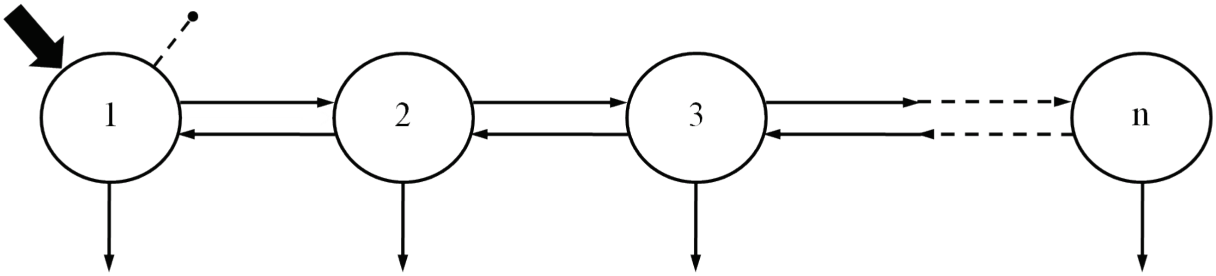

Figure 1.12 The general *n* compartment catenary model, where compartment 1 is shown as the accessible compartment (for input and measurement). A catenary model consists of compartments joined to one another like the compartments of a train. Compartmental models are simplified representations of biologic systems. The aim of modeling is to create a mathematical "likeness" of the system so that the model behaves in the same way as the system.

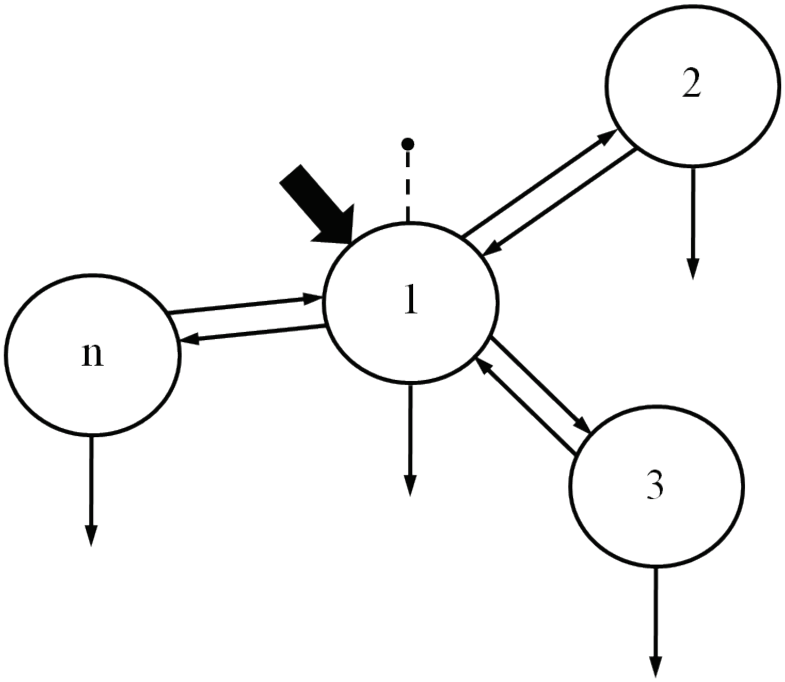

Figure 1.13 The general *n* compartment mammillary model. The mammillary model consists of a central compartment that is surrounded by one or more peripheral compartments.

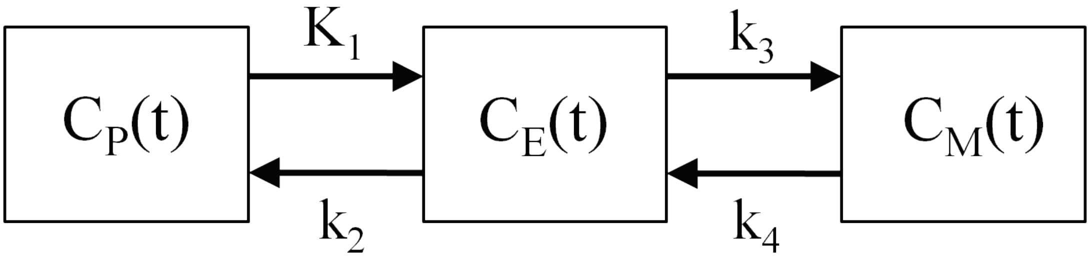

Figure 1.14 Illustration of a three compartment tracer kinetic model, where C_P represents the radiotracer in the plasma compartment, C_E represents the radiotracer in the exchangeable (or free) tissue compartment, and C_M represents the radiotracer in the metabolized (or trapped) tissue compartment. Note that the two tissue compartments represent the radiotracer in the same physical space but in two different chemical forms. K_1, k_2, k_3 and k_4 are the fractional rate constants that describe how rapidly the radiotracer moves between the interconnected compartments. While k_i (for $i \geq 2$) are expressed in units of (min^{-1}), K_1 is expressed in the same units as blood flow (i.e., $\text{mL} \bullet \text{cm}^{-3} \bullet \text{min}^{-1}$).

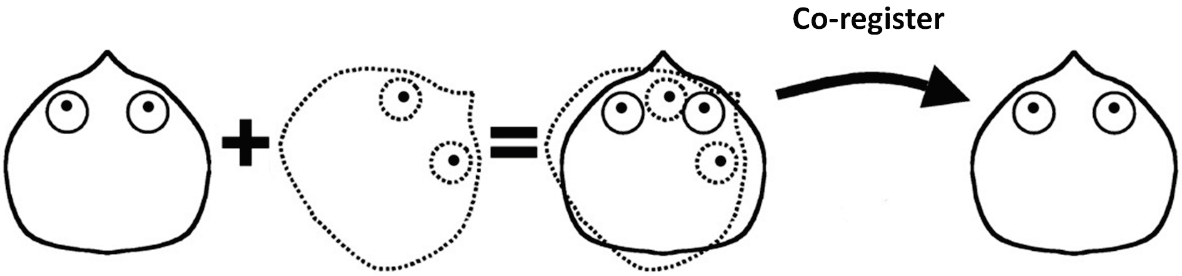

Figure 1.15 Example of a rigid-body registration. Rigid-body registration is useful for images of structures that do not deform substantially (e.g., the brain); it would not work well for structures that move, like the heart.

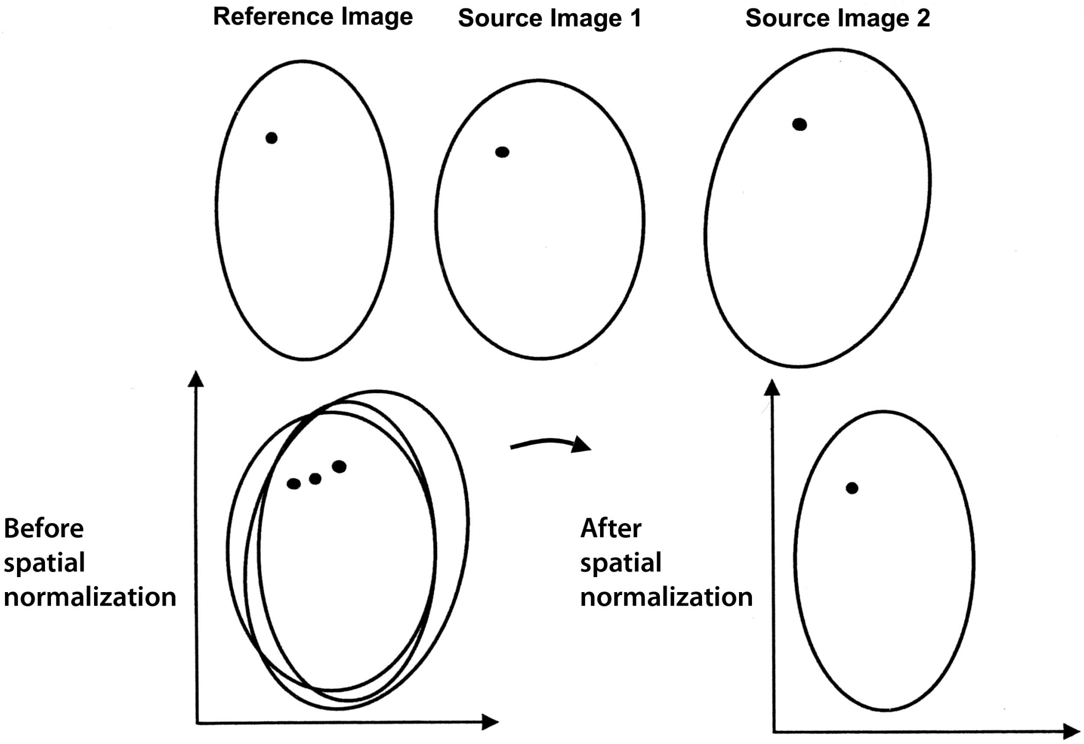

Figure 1.16 Warping of two images into a common space. Spatial normalization is a type of non-rigid registration that transforms an image into a common standardized space. The purpose of spatial normalization is to be able to compare data from one subject with those from the same subject studied at a different time, or against other subjects.

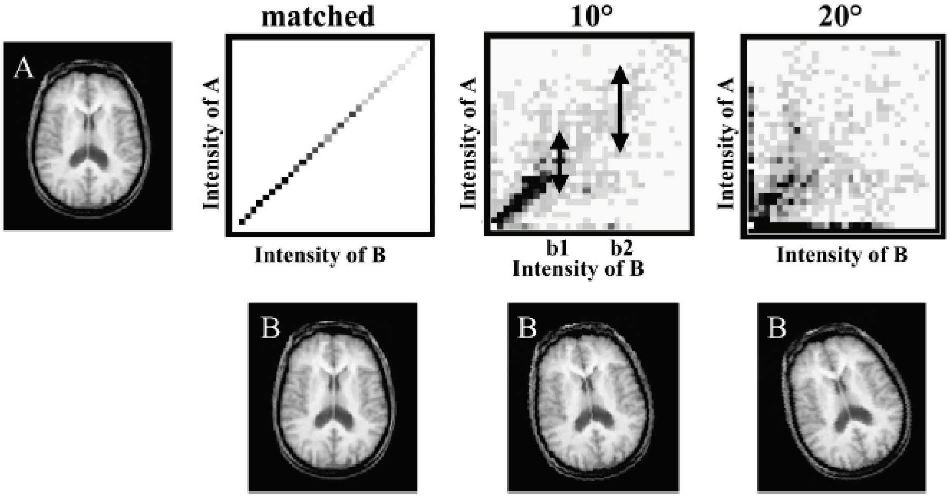

Figure 1.17 Registration of two images by maximization of mutual information. For two images, a joint intensity histogram is constructed by plotting the relative frequency of each pair of intensities. The histogram approximates the joint probability density function and, therefore, the value in each cell estimates the probability of occurrence of a particular pair of intensities in the two images. For the special case of identical images (as illustrated above), the joint histogram forms a single line when the images are aligned, but disperses from this line as image B is reoriented by 10 and 20 degrees. (Figure reprinted from Hutton *et al.* (*73*), with permission from Elsevier)

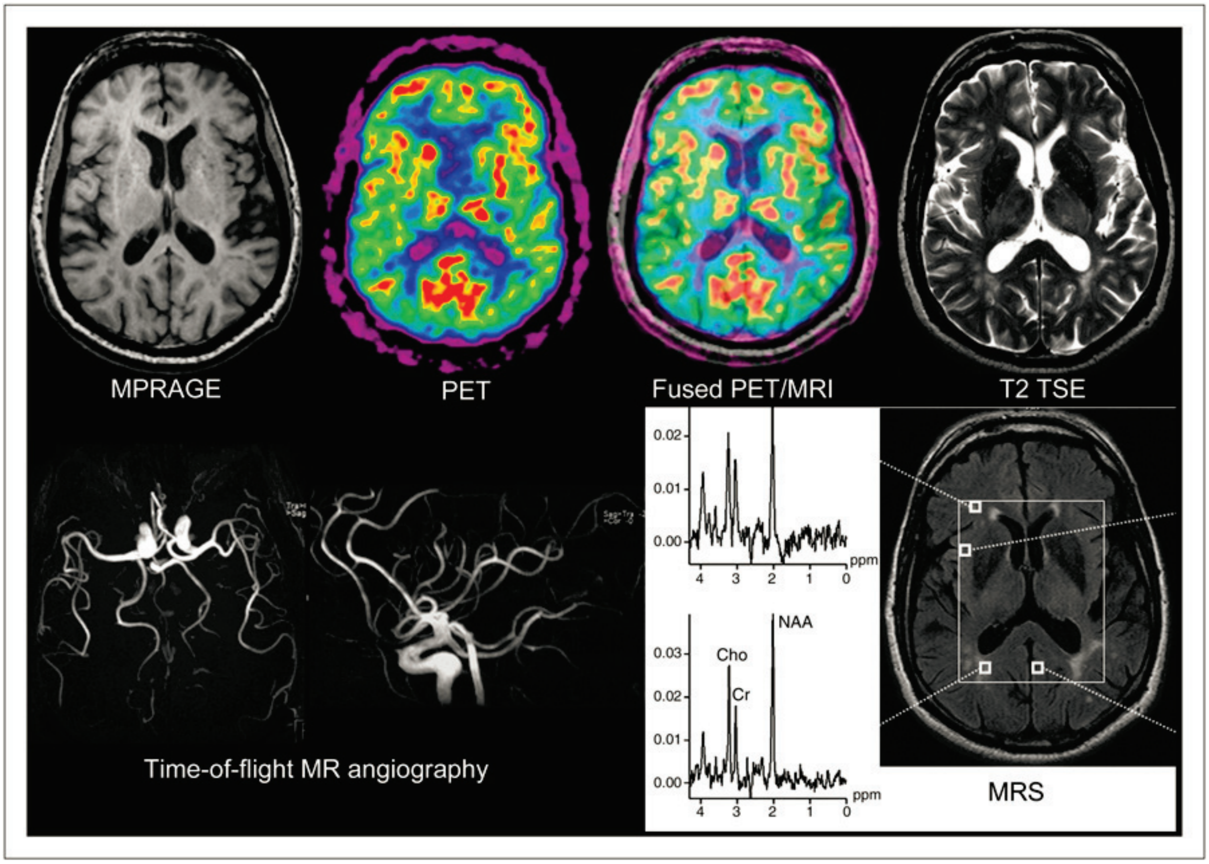

Figure 1.18 First simultaneous PET/MRI brain study in a 66-year old healthy volunteer that was performed on the BrainPET prototype (Siemens Healthcare). PET/MRI combines the biochemical information from PET with the excellent soft-tissue contrast information from MRI, and allows advanced MRI techniques to be performed such as time-of-flight MR angiography, diffusion-weighted MR imaging, and MR spectroscopy. (Figure reprinted from Schlemmer *et al.* (*79*), with permission from the Radiological Society of North America)

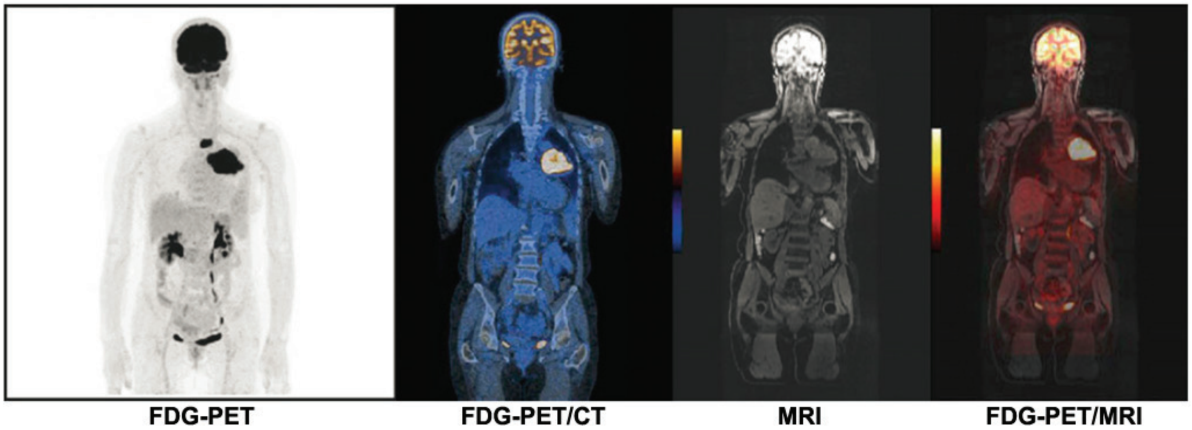

Figure 1.19 ^{18}F-FDG-PET/CT and ^{18}F-FDG-PET/MR whole-body images of a patient with a large left lung legion. Note how the tumor lights up on the PET image, and how bone shows up bright on the CT image but is essentially absent on the MR image. Images are displayed in radiological view, where the right side of the subject is on the left side of the image and vice versa. Regions with a high metabolic rate of glucose are shown in black. (Figure reprinted from Ratib *et al.* (*6*), with permission from Springer)

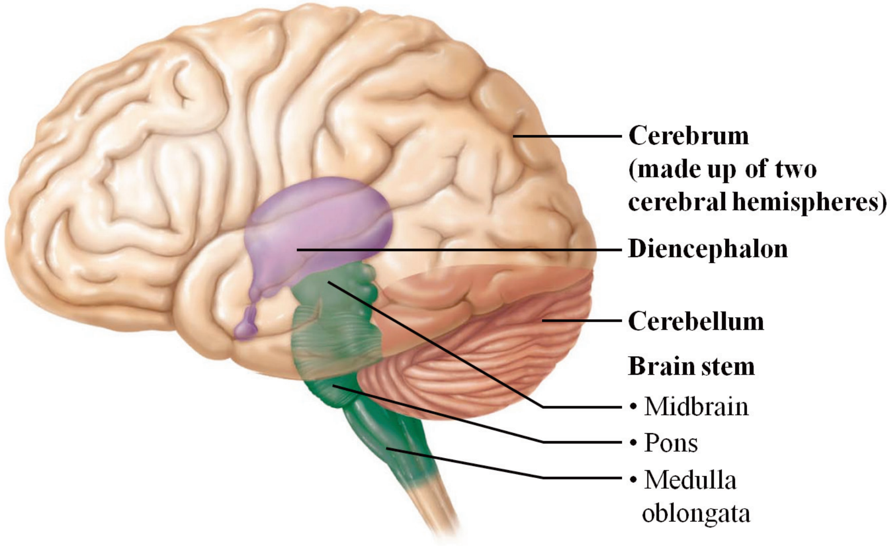

Figure 1.20 Divisions of the human brain. (Figure adapted from Marieb *et al. (95)*, with permission from Pearson Education, Inc.)

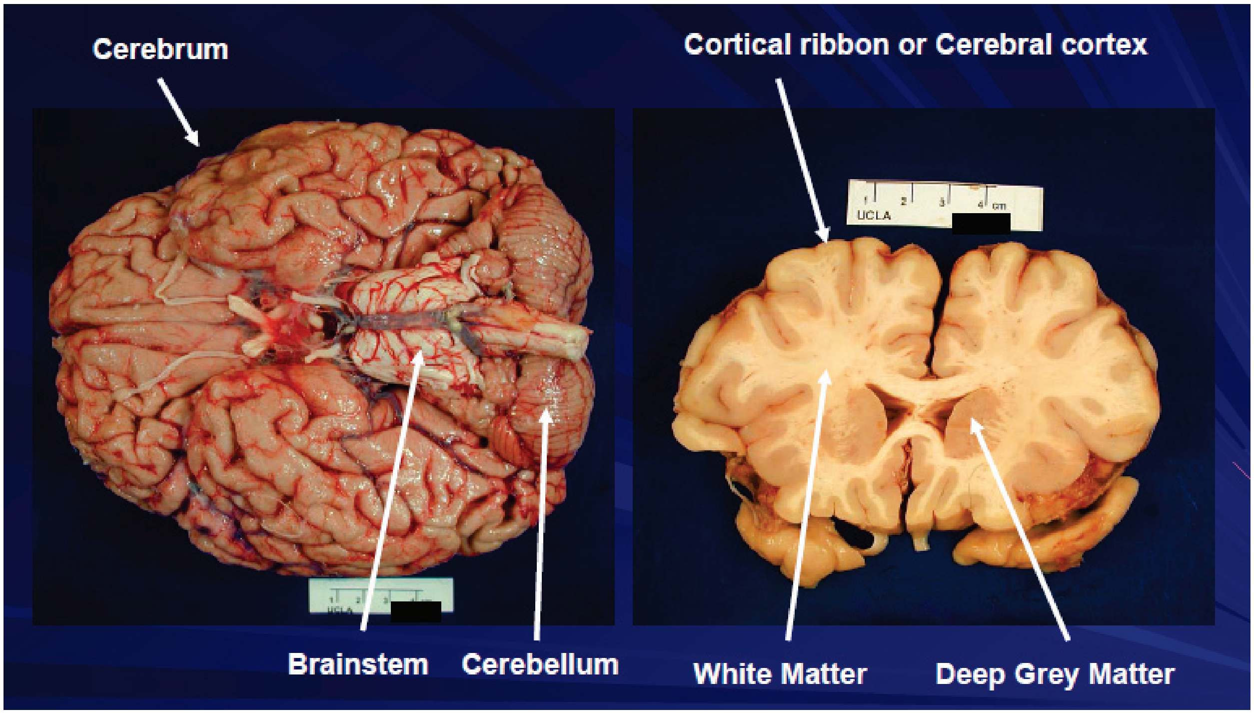

Figure 1.21 Gross anatomy of the human brain. (Figure courtesy of Dr. William Yong, UCLA)

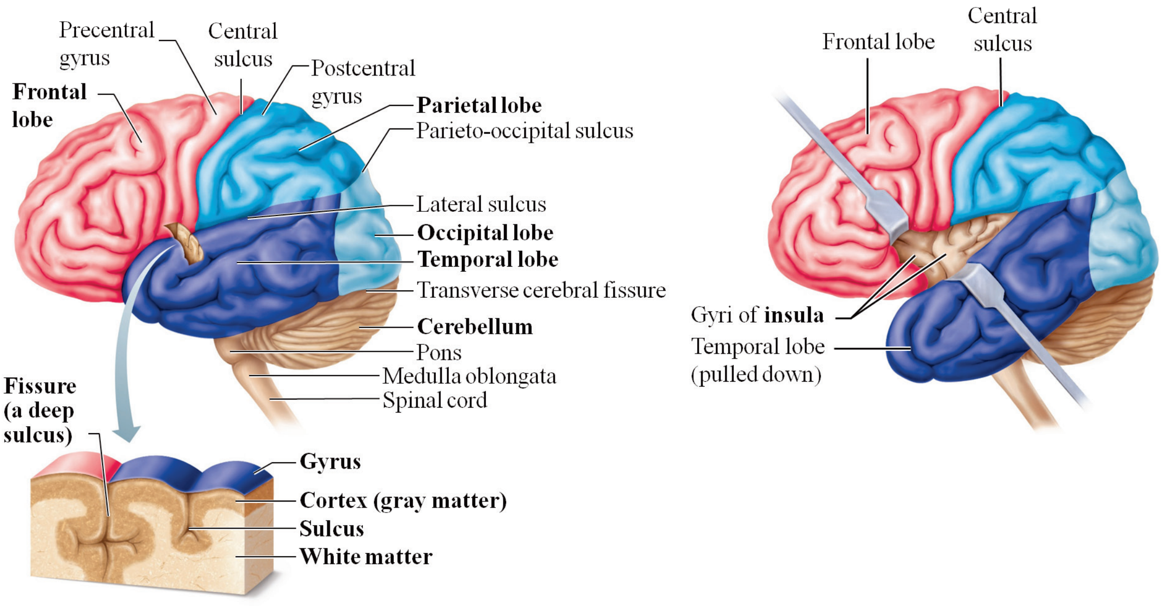

Figure 1.22 Major structural areas of the brain as seen from the left lateral view. (Figure adapted from Marieb *et al. (95)*, with permission from Pearson Education, Inc.)

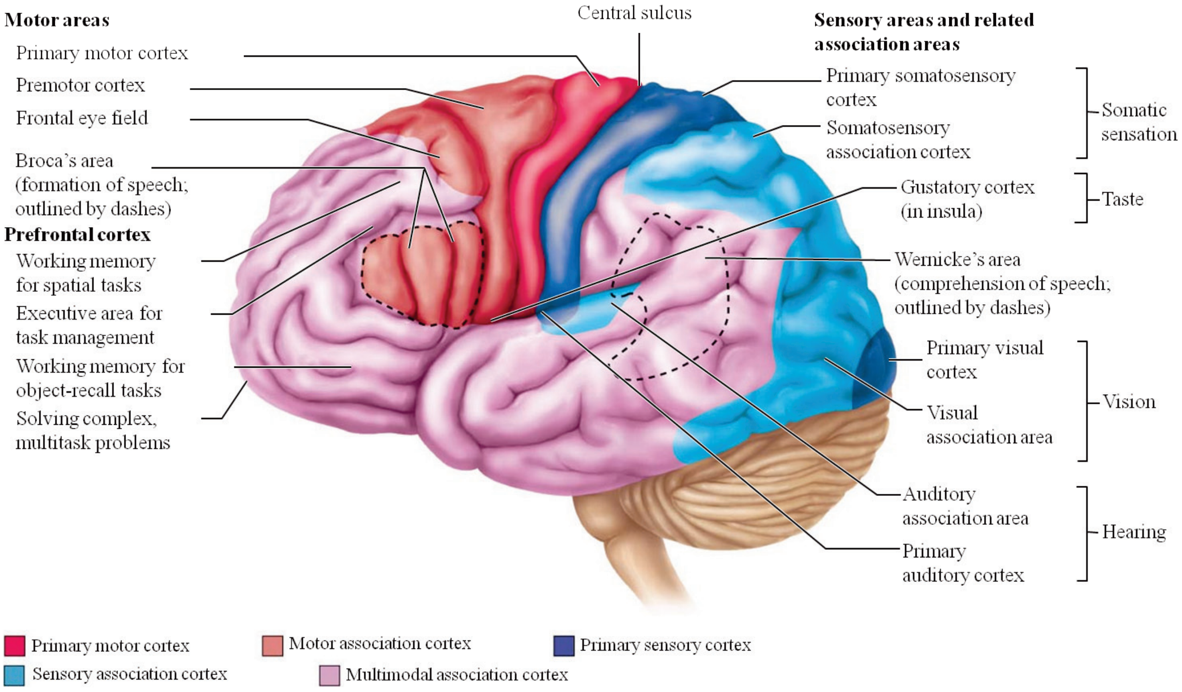

Figure 1.23 Functional areas of the cerebral cortex as seen from the left lateral view of the cerebral hemisphere. (Figure adapted from Marieb *et al. (95)*, with permission from Pearson Education, Inc.)

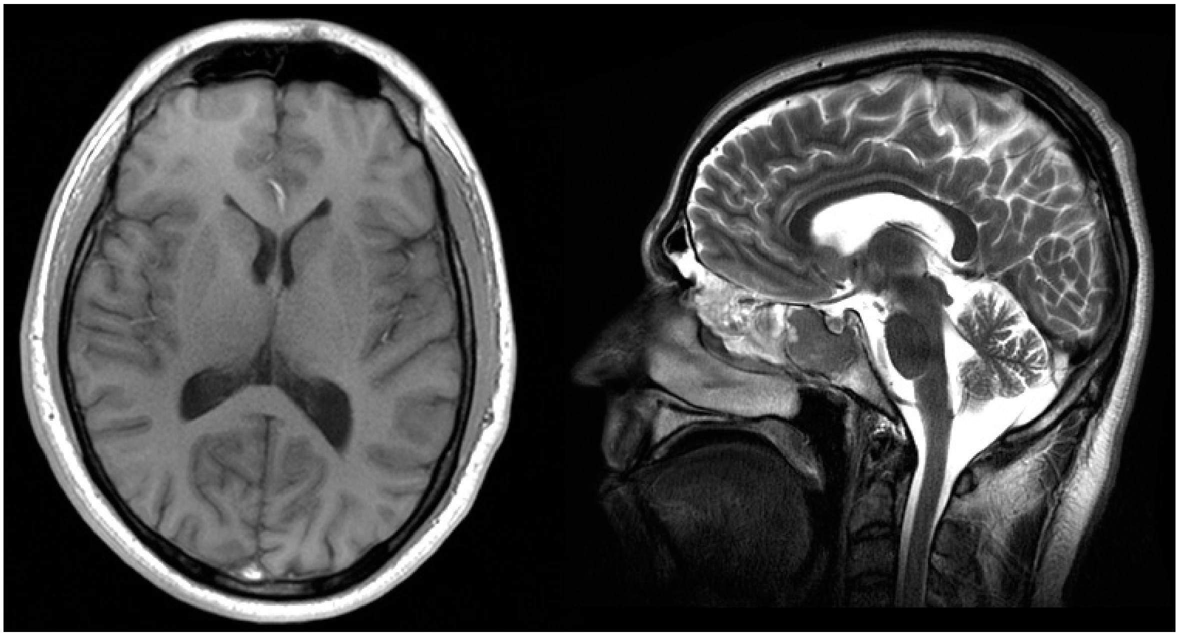

Figure 1.24 Axial T1-weighted (left) and sagittal T2-weighted MR images (right) of the human brain. Note that on the T1-weighted MR image, cerebrospinal fluid (CSF) is dark and the fatty myelin sheaths of white matter appear brighter than gray matter. On the T2-weighted MR image, CSF is bright and white matter appears darker than gray matter. T1-weighted images are best at defining anatomy. T2-weighted images are often the best MR pulse sequence for evaluating pathology; this is because pathological lesions like tumors often contain water and are therefore bright and easily seen on T2-weighted images (*124*). Another acquisition sequence used in MRI is called fluid-attenuated inversion recovery (FLAIR) (not shown here), which produces images similar to those formed by T2-weighted pulse sequences except that the bright signal from the CSF is suppressed; this allows clearer evaluation of T2-bright lesions, especially those near CSF-filled spaces (e.g., the ventricles). Each of these MR sequences demonstrates different patterns of tissue signal characteristics, which commonly forms the basis of interpretation and diagnosis (*124*). Advantages of MRI are that it uses non-ionizing radiation (unlike PET and CT), provides excellent soft tissue contrast with high spatial resolution, acquires a signal that is *intrinsic* to the tissue (unlike in PET where the signal is from the administered radiopharmaceutical), produces no bony artifacts since there is no signal from bone, and can visualize blood vessels without the use of contrast agents (*70*). Disadvantages of MRI are that it provides limited functional information, produces poor images of the lung, is not able to show calcification, and is contraindicated in patients with pacemakers or metallic foreign bodies (*70*).

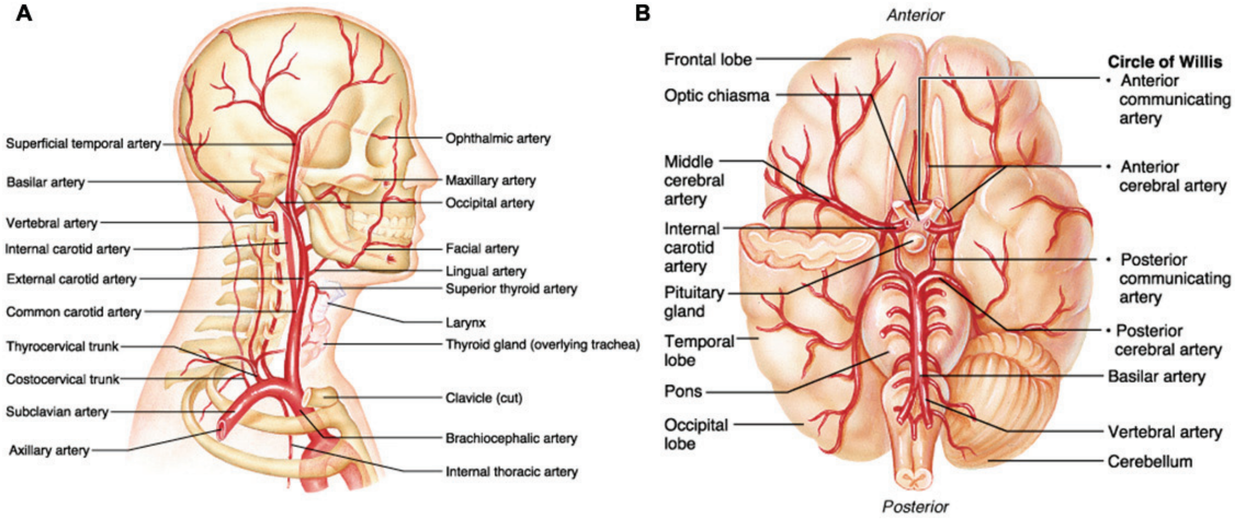

Figure 1.25 (A) Arteries of the head and neck (right aspect). (B) Major arteries serving the brain as seen from the inferior view (right side of cerebellum and part of the right temporal lobe has been removed). (Figure adapted from Marieb *et al. (95)*, with permission from Pearson Education, Inc.)

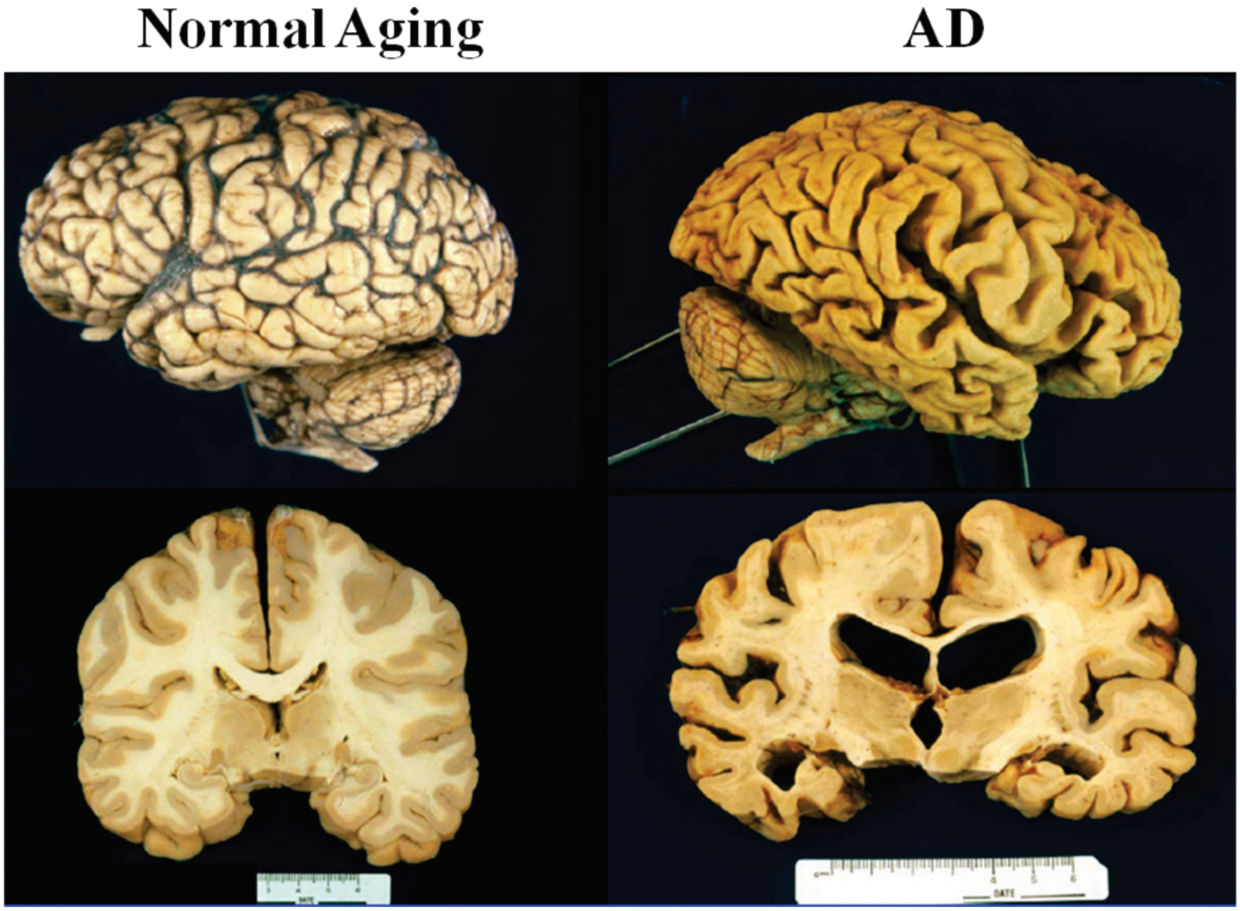

Figure 1.26 Neuronal cell loss leads to extensive neurodegeneration as shown on the right in a brain of a severely affected AD patient. For comparison, a non-demented normal aging human brain is shown on the left. (Figure courtesy of Dr. Harry Vinters, UCLA)

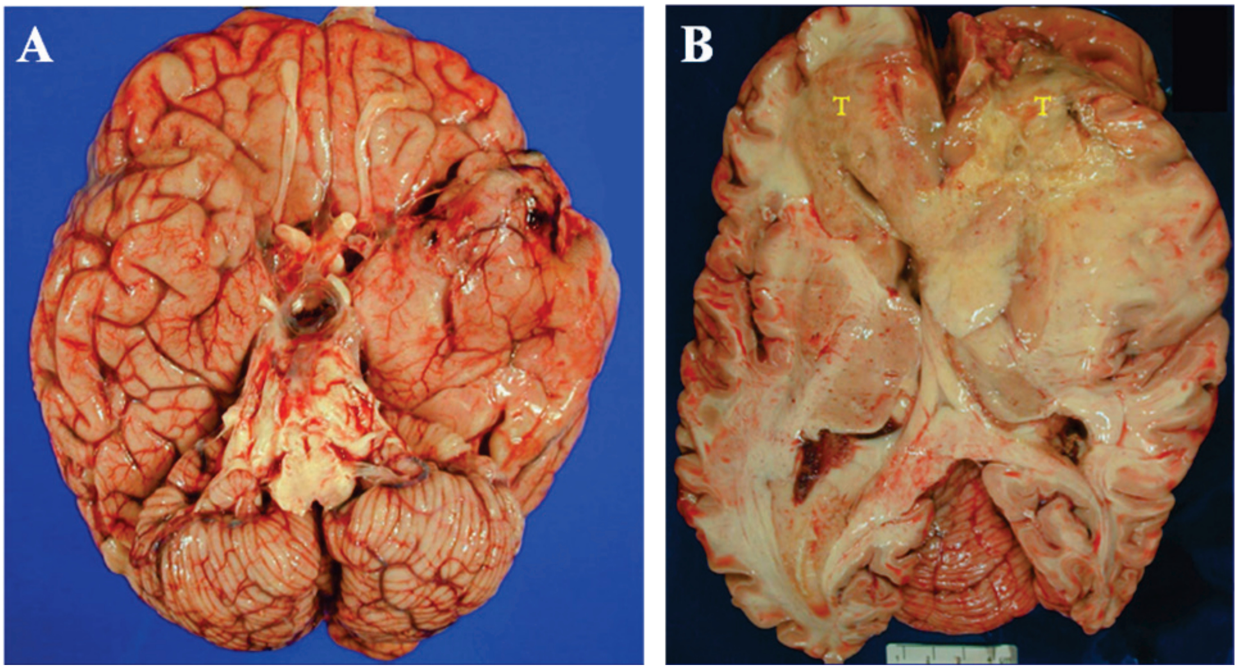

Figure 1.27 Shown in (A) is a brain tumor that occupies the majority of the left temporal region and shown in (B) is a brain tumor involving both cerebral hemispheres. (Figure courtesy of Dr. William Yong, UCLA)

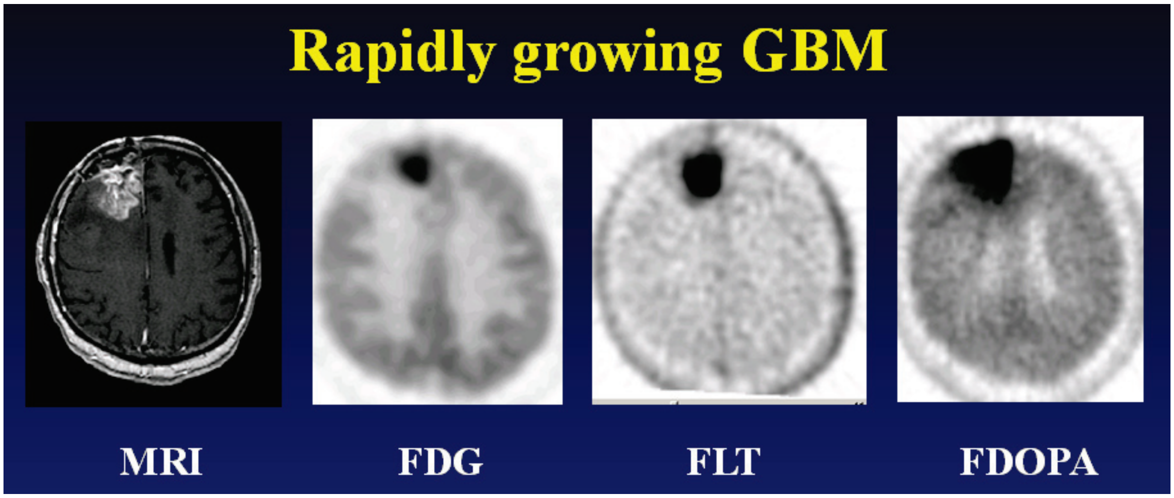

Figure 1.28 MRI and multi-tracer PET images (^{18}F-FDG, ^{18}F-FLT, and ^{18}F-FDOPA) of a patient with a rapidly growing GBM. Note the high background signal of normal cortical gray matter in the ^{18}F-FDG PET image and the lower background activity in the ^{18}F-FLT and ^{18}F-FDOPA PET images. (Figure courtesy of Dr. Christiaan Schiepers and Dr. Wei Chen, UCLA)

1.20 TABLES

Table 1.1 Positron-emitting radionuclides commonly used in PET.

Positron Emitting Radionuclide	Half-Life*	Decay Modes	Maximum Positron Energy (MeV) in Water	Mean Positron Range (mm) in Water†	Production Method‡
Fluorine-18	110.0 min	β^+ (97%), EC (3%)	0.63	0.6 (2.4)	$^{18}O(p,n)^{18}F$ $^{20}Ne(d,\alpha)^{18}F$
Carbon-11	20.4 min	β^+ (100%)	0.96	1.1 (4.1)	$^{14}N(p,\alpha)^{11}C$
Nitrogen-13	10.0 min	β^+ (100%)	1.20	1.5 (5.1)	$^{16}O(p,\alpha)^{13}N$
Oxygen-15	2.0 min	β^+ (100%)	1.74	2.5 (7.3)	$^{15}N(p,n)^{15}O$ $^{14}N(d,n)^{15}O$

β^+: positron; β^-: electron; EC: electron capture; p: proton; n: neutron; α: alpha particle (i.e., a helium nucleus); d: deuteron (made up of one proton and one neutron; a deuteron is the nucleus of deuterium, which is also known as heavy hydrogen).

1 eV = 10^{-6} MeV = 1.6×10^{-19} J.

[*] The half-life of a radionuclide is the time required for it to decay to half of its initial activity level.

[†] Maximum positron range is shown in parentheses.

[‡] The nomenclature for a nuclear reaction is $^{18}_{8}O\ (p,n)\ ^{18}_{9}F$, where ^{18}O is the target material (i.e., H_2O enriched in ^{18}O), p is the energetic proton that enters the target and reacts with ^{18}O by expelling a neutron (n) to yield radioactive ^{18}F. The subscript refers to the atomic number (i.e., the number of protons in the nucleus of the atom) and the superscript refers to the mass number (i.e., the total number of protons and neutrons in the atomic nucleus). The atomic number determines the chemical element to which the atom belongs.

Table 1.2 Properties of scintillator materials used for gamma-ray detection at 511 keV.

Scintillator	**Density (g/cc)**	**Decay Time (ns)**	**Effective Atomic Number**	**Relative Light Yield (with respect to NaI)**	**Linear Attenuation Coefficient (cm^{-1})**
NaI[*]	3.67	230	51	100%	0.34
BGO	7.13	300	74	15%	0.95
LSO	7.40	40	66	75%	0.88
GSO	6.71	60	59	25%	0.70

[*] Sodium iodide crystal contains a trace amount of thallium.

Table 1.3 Biological hallmarks of cancer.

	Hallmarks of Cancer
1.	Self-sufficiency in proliferative growth signals
2.	Insensitivity to growth inhibitory signals
3.	Resisting cell death
4.	Enabling replicative immortality
5.	Inducing angiogenesis (formation of new blood vessels)
6.	Activating invasion and metastasis
7.	Reprogramming of energy metabolism *(emerging hallmark)* (a prime example of this emerging hallmark is that, unlike normal cells, cancer cells carry out glycolysis even in the presence of oxygen)
8.	Avoiding destruction by the immune system *(emerging hallmark)*
9.	Genome instability and mutation *(an enabling characteristic)*
10	Tumor-promoting inflammation *(an enabling characteristic)*

Table 1.4 Acquired genetic mutations in glioblastoma.

Genetic Mutation	Normal Function	Seen in Primary Glioblastoma?	Seen in Secondary Glioblastoma?
Tumor suppressor protein 53 (p53); also called the "guardian of the genome"	DNA repair, apoptosis regulation	Yes	Yes
Phosphatase and tensin homolog (PTEN)	Assists in cell destruction	Yes	Yes
Epidermal growth factor receptor (EGFR) overexpression	Cell proliferation	Yes	Yes
Loss of heterozygosity on chromosome 10q (most frequent genetic alteration in GBM)	Location of several tumor suppressor genes	Yes	Yes
p16 deletion/mutation	Cyclin dependent kinase 4 inhibitor	Yes	Yes
Overexpression of platelet derived growth factor receptor (PDGFR)	Glial cell development	--	Yes
Retinoblastoma (Rb)	Tumor suppressor	--	Yes
Isocitrate dehydrogenase (IDH) 1 and 2 (associated with a more favorable prognosis; IDH mutation and improved survival has been observed in low grade tumors as well)	Cellular intermediate metabolism	--	Yes

1.21 REFERENCES

1. Phelps ME. *PET : molecular imaging and its biological applications*. New York: Springer; 2004.

2. Mazziotta JC, Gilman S. *Clinical brain imaging : principles and applications*. Philadelphia: F.A. Davis; 1992.

3. Bushberg JT, Seibert JA, Leidholdt EM, Boone JM, Mahesh M. The essential physics of medical imaging, third edition. *Med Phys.* Jul 2013;40(7):077301.

4. Czernin J. *Atlas of PET/CT imaging in oncology*. Berlin ; New York: Springer; 2004.

5. Shreve P, Townsend DW. Clinical PET-CT in radiology : integrated imaging in oncology. New York ; London: Springer; 2011.

6. Ratib O, Schwaiger M, Beyer T. Atlas of PET/MR imaging in oncology. Berlin ; New York: Springer; 2013.

7. Wahl RL. *Principles and practice of positron emission tomography*. Philadelphia: Lippincott Williams & Wilkins; 2002.

8. Sandler MP, Coleman RE, Patton JA. *Diagnostic nuclear medicine*. 4th ed. Philadelphia, Pa.: Lippincott Williams & Wilkins; 2003.

9. Cherry SR, Sorenson JA, Phelps ME. *Physics in nuclear medicine*. 4th ed. Philadelphia: Elsevier/Saunders; 2012.

10. Webb AR, IEEE Engineering in Medicine and Biology Society. *Introduction to biomedical imaging*. Hoboken, N.J.: Wiley; 2003.

11. Wagner HN, Szabo Z, Buchanan J. *Principles of nuclear medicine*. 2nd ed. Philadelphia: Saunders; 1995.

12. Phelps ME. PET: the merging of biology and imaging into molecular imaging. *J Nucl Med.* Apr 2000;41(4):661-681.

13. Phelps ME. Positron emission tomography provides molecular imaging of biological processes. *Proc Natl Acad Sci U S A.* Aug 1 2000;97(16):9226-9233.

14. Daroff RB, Fenichel GM, Jankovic J, Mazziotta JC. *Bradley's neurology in clinical practice*. 6th ed. Philadelphia, PA: Elsevier/Saunders; 2012.

15. Ell PJ, Gambhir SS. *Nuclear medicine in clinical diagnosis and treatment*. 3rd ed. Edinburgh ; New York: Churchill Livingstone; 2004.

16. Phelps ME, Hoffman EJ, Mullani NA, Ter-Pogossian MM. Application of annihilation coincidence detection to transaxial reconstruction tomography. *J Nucl Med.* Mar 1975;16(3):210-224.

17. Ter-Pogossian MM, Phelps ME, Hoffman EJ, Mullani NA. A positron-emission transaxial tomograph for nuclear imaging (PETT). *Radiology.* Jan 1975;114(1):89-98.

18. Phelps ME, Hoffman EJ, Huang SC, Kuhl DE. ECAT: a new computerized tomographic imaging system for positron-emitting radiopharmaceuticals. *J Nucl Med.* Jun 1978;19(6):635-647.

19. Nutt R. The history of positron emission tomography. *Mol Imaging Biol.* Jan 2002;4(1):11-26.

20. Wacholtz E. History and Development of PET. CEwebsource.com; 2011.

21. Toga AW, Mazziotta JC. *Brain mapping : the systems*. San Diego: Academic Press; 2000.

22. Delbeke D. Practical FDG imaging a teaching file. New York: Springer,; 2002:xviii, 435 p. ill. (some col.).

23. Phelps M. In tribute of Edward J. Hoffman, PhD (1942-2004). *Mol Imaging Biol.* Sep-Oct 2004;6(5):271-274.

24. Hoh CK, Hawkins RA, Dahlbom M, et al. Whole body skeletal imaging with [^{18}F]fluoride ion and PET. *Journal of computer assisted tomography.* Jan-Feb 1993;17(1):34-41.

25. Dahlbom M, Hoffman EJ, Hoh CK, et al. Whole-body positron emission tomography: Part I. Methods and performance characteristics. *J Nucl Med.* Jun 1992;33(6):1191-1199.

26. Beyer T, Townsend DW, Brun T, et al. A combined PET/CT scanner for clinical oncology. *J Nucl Med.* Aug 2000;41(8):1369-1379.

27. Cherry SR, Phelps ME. Imaging Brain Function with Positron Emission Tomography. In: Toga AW, Mazziotta JC, eds. *Brain mapping : the methods*. San Diego: Academic Press; 1996.

28. Cherry SR, Phelps ME. Positron Emission Tomography: Methods and Instrumentation. In: Sandler MP, Coleman RE, Patton JA, eds. *Diagnostic nuclear medicine*. 4th ed. Philadelphia, Pa.: Lippincott Williams & Wilkins; 2003.

29. Phelps ME, Mazziotta JC, Schelbert HR. *Positron emission tomography and autoradiography : principles and applications for the brain and heart*. New York: Raven Press; 1986.

30. Lima JJPd. *Nuclear medicine physics*. Boca Raton, FL: CRC Press; 2011.

31. Kim EE. Clinical PET and PET/CT principles and applications. 2nd ed ed. New York: Springer; 2013.

32. Dahlbom M. PET Imaging: Basics and New Trends. In: Grupen C, Buvat I, eds. *Handbook of particle detection and imaging*. Berlin ; New York: Springer; 2012.

33. Barrington SF, Wahl RL, Maisey M. *Atlas of clinical positron emission tomography*. 2nd ed. London New York: Hodder Arnold ; Distributed in the United States of America by Oxford University Press; 2006.

34. Brix G, Zaers J, Adam LE, et al. Performance evaluation of a whole-body PET scanner using the NEMA protocol. National Electrical Manufacturers Association. *J Nucl Med.* Oct 1997;38(10):1614-1623.

35. Semmler W, Schwaiger M. *Molecular imaging*. Berlin: Springer; 2008.

36. Judenhofer MS, Wehrl HF, Newport DF, et al. Simultaneous PET-MRI: a new approach for functional and morphological imaging. *Nature medicine.* Apr 2008;14(4):459-465.

37. Schiepers C, Dahlbom M. Molecular imaging in oncology: the acceptance of PET/CT and the emergence of MR/PET imaging. *Eur Radiol.* Mar 2011;21(3):548-554.

38. Henkin RE. *Nuclear medicine*. 2nd ed. Philadelphia: Mosby Elsevier; 2006.

39. Jadvar H, Parker JA. Clinical PET and PET/CT. London ; New York: Springer; 2005.

40. Saha GB. *Basics of PET imaging : physics, chemistry, and regulations*. New York, NY: Springer; 2005.

41. Cherry SR, Dahlbom M. *PET : physics, instrumentation, and scanners*. New York: Springer; 2006.

42. Cho ZH, Jones JP, Singh M. *Foundations of medical imaging*. New York: Wiley; 1993.

43. Hsieh J. *Computed tomography : principles, design, artifacts, and recent advances*. Bellingham, WA: SPIE Optical Engineering Press; 2003.

44. Zeng GL. *Medical image reconstruction : a conceptual tutorial*. New York: Springer; 2010.

45. Kak AC, Slaney M, IEEE Engineering in Medicine and Biology Society. *Principles of computerized tomographic imaging*. New York: IEEE Press; 1988.

46. Phelps ME, Mazziotta JC. Positron emission tomography: human brain function and biochemistry. *Science.* May 17 1985;228(4701):799-809.

47. Bailey DL. *Positron emission tomography : basic sciences*. New York: Springer; 2005.

48. Weissleder R. *Molecular imaging : principles and practice*. Shelton, Conn.: People's Medical Pub. House-USA; 2009.

49. Bryan RN. *Introduction to the science of medical imaging*. Cambridge: Cambridge University Press; 2010.

50. Phelps ME, Huang SC, Hoffman EJ, Selin C, Sokoloff L, Kuhl DE. Tomographic measurement of local cerebral glucose metabolic rate in humans with (F-18)2-fluoro-2-deoxy-D-glucose: validation of method. *Ann Neurol.* Nov 1979;6(5):371-388.

51. Huang SC, Phelps ME, Hoffman EJ, Sideris K, Selin CJ, Kuhl DE. Noninvasive determination of local cerebral metabolic rate of glucose in man. *Am J Physiol.* Jan 1980;238(1):E69-82.

52. Padgett HC, Schmidt DG, Luxen A, Bida GT, Satyamurthy N, Barrio JR. Computer-controlled radiochemical synthesis: a chemistry process control unit for the automated production of radiochemicals. *Int J Rad Appl Instrum A.* 1989;40(5):433-445.

53. Huang S-C, Phelps ME. Principles of Tracer Kinetic Modeling. *Positron emission tomography and autoradiography : principles and applications for the brain and heart*. New York: Raven Press; 1986:287-346.

54. Huang S-C. Pharmacokinetic modeling. In: Weissleder R, ed. *Molecular imaging : principles and practice*. Shelton, Conn.: People's Medical Pub. House-USA; 2009.

55. Huang SC. Role of Kinetic Modeling in Biomedical Imaging. *J Med Sci.* 2008;28(2):57-63.

56. Godfrey K. *Compartmental models and their application*. London ; New York: Academic Press; 1983.

57. Cobelli C, Foster D, Toffolo G. *Tracer kinetics in biomedical research : from data to model*. New York: Kluwer Academic/Plenum; 2000.

58. Gibaldi M, Perrier D. *Pharmacokinetics*. 2nd ed. New York: M. Dekker; 1982.

59. Schoenwald RD. *Pharmacokinetics in drug discovery and development*. Boca Raton: CRC Press; 2002.

60. Wastney ME. *Investigating biological systems using modeling : strategies and software*. San Diego: Academic Press; 1999.

61. Jacquez JA. *Compartmental analysis in biology and medicine*. 2nd ed. Ann Arbor: University of Michigan Press; 1985.

62. Muzic RF, Jr., Cornelius S. COMKAT: compartment model kinetic analysis tool. *J Nucl Med.* Apr 2001;42(4):636-645.

63. Huang SC, Truong D, Wu HM, et al. An internet-based "kinetic imaging system" (KIS) for MicroPET. *Mol Imaging Biol.* Sep-Oct 2005;7(5):330-341.

64. Barrett PH, Bell BM, Cobelli C, et al. SAAM II: Simulation, Analysis, and Modeling Software for tracer and pharmacokinetic studies. *Metabolism.* Apr 1998;47(4):484-492.

65. D'Argenio DZ, Schumitzky A, Wang X. ADAPT 5 User's Guide: Pharmacokinetic/Pharmacodynamic Systems Analysis Software. Los Angeles: Biomedical Simulations Resource; 2009.

66. User's Guide: PMOD Kinetic Modeling (PKIN). Zurich: PMOD Technologies Ltd.; 2012.

67. Bonate PL. *Pharmacokinetic-pharmacodynamic modeling and simulation*. New York: Springer; 2011.

68. Hajnal JV, Hawkes DJ, Hill DLG. *Medical image registration*. Boca Raton: CRC Press; 2001.

69. Bui AAT, Taira RK. Medical imaging informatics. Dordrecht: Springer; 2010.

70. Branstetter BF, Society for Imaging Informatics in Medicine. Practical imaging informatics foundations and applications for PACS professionals. New York: Springer; 2009.

71. Friston KJ. *Statistical parametric mapping : the analysis of funtional brain images*. 1st ed. Amsterdam ; Boston: Elsevier/Academic Press; 2007.

72. Maes F, Collignon A, Vandermeulen D, Marchal G, Suetens P. Multimodality image registration by maximization of mutual information. *IEEE Trans Med Imaging.* Apr 1997;16(2):187-198.

73. Hutton BF, Braun M. Software for image registration: algorithms, accuracy, efficacy. *Semin Nucl Med.* Jul 2003;33(3):180-192.

74. Maes F, Vandermeulen D, Suetens P. Medical image registration using mutual information. *Proceedings of the IEEE.* 2003;91(10):1699-1722.

75. Townsend DW, Carney JP, Yap JT, Hall NC. PET/CT today and tomorrow. *J Nucl Med.* Jan 2004;45 Suppl 1:4S-14S.

76. Townsend DW. Dual-modality imaging: combining anatomy and function. *J Nucl Med.* Jun 2008;49(6):938-955.

77. Wahl RL, Wagner HN. *Principles and practice of PET and PET/CT*. 2nd ed. Philadelphia: Lippincott Williams & Wilkins; 2009.

78. Townsend DW. Combined positron emission tomography-computed tomography: the historical perspective. *Semin Ultrasound CT MR.* Aug 2008;29(4):232-235.

79. Schlemmer HP, Pichler BJ, Schmand M, et al. Simultaneous MR/PET imaging of the human brain: feasibility study. *Radiology.* Sep 2008;248(3):1028-1035.

80. Drzezga A, Souvatzoglou M, Eiber M, et al. First clinical experience with integrated whole-body PET/MR: comparison to PET/CT in patients with oncologic diagnoses. *J Nucl Med.* Jun 2012;53(6):845-855.

81. Wagenknecht G, Kaiser HJ, Mottaghy FM, Herzog H. MRI for attenuation correction in PET: methods and challenges. *MAGMA.* Feb 2013;26(1):99-113.

82. Keereman V, Mollet P, Berker Y, Schulz V, Vandenberghe S. Challenges and current methods for attenuation correction in PET/MR. *MAGMA.* Feb 2013;26(1):81-98.

83. Gambhir SS. Molecular imaging of cancer: from molecules to humans. Introduction. *J Nucl Med.* Jun 2008;49 Suppl 2:1S-4S.

84. Weinberg RA. *The biology of cancer*. Second ed. New York: Garland Science; 2013.

85. Hanahan D, Weinberg RA. The hallmarks of cancer. *Cell.* Jan 7 2000;100(1):57-70.

86. Hanahan D, Weinberg RA. Hallmarks of cancer: the next generation. *Cell.* Mar 4 2011;144(5):646-674.

87. Pecorino L. *Molecular biology of cancer : mechanisms, targets, and therapeutics*. Third edition. ed; 2012.

88. Alberts B. *Molecular biology of the cell*. 5th ed. New York: Garland Science; 2008.

89. Lodish HF, Storrie B. *Molecular cell biology*. 4th ed. New York: W.H. Freeman; 2000.

90. New Answers for Cancer. *Scientific American (Special Edition).* Vol 18; 2008.

91. Dunn B. Cancer: Solving an age-old problem. *Nature.* Mar 1 2012;483(7387):S2-6.

92. American Cancer Society. Cancer facts & figures. Atlanta, GA: The Society; 2013.

93. Alazraki NP, Shumate MJ, Kooby DA, Society of Nuclear Medicine (1953-). *A clinician's guide to nuclear oncology : practical molecular imaging and radionuclide therapies*. Reston, VA: SNM; 2007.

94. Tortora GJ. *Principles of human anatomy*. 10th ed. Hoboken, NJ: J. Wiley; 2005.

95. Marieb EN, Wilhelm PB, Mallatt J. *Human anatomy*. 6th ed. San Francisco, California: Pearson Benjamin Cummings; 2010.

96. Moore KL, Agur AMR. *Essential clinical anatomy*. 2nd ed. Philadelphia: Lippincott Williams & Wilkins; 2002.

97. Diamond MC, Scheibel AB, Elson LM. *The human brain coloring book*. 1st ed. New York: Barnes & Noble Books; 1985.

98. Morton DA, Foreman KB, Albertine KH. Gross anatomy the big picture. New York: McGraw-Hill; 2011.

99. Tortora GJ. *Principles of anatomy and physiology*. 11th ed. Hoboken, NJ: J. Wiley; 2006.

100. Silverman DHS. PET in the evaluation of Alzheimer's disease and related disorders. New York ; London: Springer; 2009.

101. Bennington TV. *Alzheimer's disease : overview and bibliography*. New York: Nova Science Pub.; 2003.

102. Bear MF, Connors BW, Paradiso MA. *Neuroscience : exploring the brain*. 3rd ed. Philadelphia, PA: Lippincott Williams & Wilkins; 2007.

103. SEER Cancer Statistics Review, 1975-2010, National Cancer Institute. http://seer.cancer.gov/csr/1975_2010/, based on November 2012 SEER data submission, posted to the SEER web site, April 2013.

104. Ivan M, Tate M, Clarke JL. Malignant Gliomas in Adulthood. In: Packer RJ, Schiff D, eds. *Neuro-oncology* First ed. Oxford: Blackwell Publishing Ltd.; 2012.

105. Adamson C, Kanu OO, Mehta AI, et al. Glioblastoma multiforme: a review of where we have been and where we are going. *Expert Opin Investig Drugs.* Aug 2009;18(8):1061-1083.

106. Schiff D, O'Neill B. *Principles of neuro-oncology*. New York: McGraw-Hill Medical Pub. Division; 2005.

107. Patrick GL. *An introduction to medicinal chemistry*. 3rd ed. Oxford ; New York: Oxford University Press; 2005.

108. Kanu OO, Mehta A, Di C, et al. Glioblastoma multiforme: a review of therapeutic targets. *Expert Opin Ther Targets.* Jun 2009;13(6):701-718.

109. Carrillo JA, Lai A, Nghiemphu PL, et al. Relationship between tumor enhancement, edema, IDH1 mutational status, MGMT promoter methylation, and survival in glioblastoma. *AJNR Am J Neuroradiol.* Aug 2012;33(7):1349-1355.

110. Markert J. *Glioblastoma Multiforme*. 1st ed. Sudbury, Mass.: Jones and Bartlett Publishers; 2005.

111. Kim EE. *Clinical PET : principles and applications*. New York: Springer; 2004.

112. Chen W. Clinical applications of PET in brain tumors. *J Nucl Med.* Sep 2007;48(9):1468-1481.

113. Heiss WD, Raab P, Lanfermann H. Multimodality assessment of brain tumors and tumor recurrence. *J Nucl Med.* Oct 2011;52(10):1585-1600.

114. Shields AF, Grierson JR, Dohmen BM, et al. Imaging proliferation in vivo with [F-18]FLT and positron emission tomography. *Nature medicine.* Nov 1998;4(11):1334-1336.

115. Schiepers C, Chen W, Dahlbom M, Cloughesy T, Hoh CK, Huang SC. ^{18}F-fluorothymidine kinetics of malignant brain tumors. *European journal of nuclear medicine and molecular imaging.* Jul 2007;34(7):1003-1011.

116. Schiepers C, Dahlbom M, Chen W, et al. Kinetics of 3'-deoxy-3'-^{18}F-fluorothymidine during treatment monitoring of recurrent high-grade glioma. *J Nucl Med.* May 2010;51(5):720-727.

117. Heiss WD, Wienhard K, Wagner R, et al. F-Dopa as an amino acid tracer to detect brain tumors. *J Nucl Med.* Jul 1996;37(7):1180-1182.

118. Schiepers C, Chen W, Cloughesy T, Dahlbom M, Huang SC. ^{18}F-FDOPA kinetics in brain tumors. *J Nucl Med.* Oct 2007;48(10):1651-1661.

119. Dhermain FG, Hau P, Lanfermann H, Jacobs AH, van den Bent MJ. Advanced MRI and PET imaging for assessment of treatment response in patients with gliomas. *Lancet neurology.* Sep 2010;9(9):906-920.

120. Macdonald DR, Cascino TL, Schold SC, Jr., Cairncross JG. Response criteria for phase II studies of supratentorial malignant glioma. *J Clin Oncol.* Jul 1990;8(7):1277-1280.

121. Clarke JL, Chang SM. Neuroimaging: diagnosis and response assessment in glioblastoma. *Cancer J.* Jan-Feb 2012;18(1):26-31.

122. Wen PY, Macdonald DR, Reardon DA, et al. Updated response assessment criteria for high-grade gliomas: response assessment in neuro-oncology working group. *J Clin Oncol.* Apr 10 2010;28(11):1963-1972.

123. Pope WB, Hessel C. Response assessment in neuro-oncology criteria: implementation challenges in multicenter neuro-oncology trials. *AJNR Am J Neuroradiol.* May 2011;32(5):794-797.

124. Chowdhury R. *Radiology at a glance*. Chichester, West Sussex ; Hoboken, NJ: John Wiley; 2010.

Chapter 2

Movement Correction Method for Human Brain PET Images: Application to Quantitative Analysis of Dynamic ^{18}F-FDDNP Scans

2.1 ABSTRACT

Purpose:

Head movement during a PET scan (especially a dynamic scan) can affect both the qualitative and the quantitative aspects of an image, making it difficult to accurately interpret the results. The primary objective of this study was to develop a retrospective image-based movement correction (MC) method and evaluate its implementation on dynamic 2-(1-{6-[(2-^{18}F-fluoroethyl)(methyl)amino]-2-naphthyl}ethylidene)malononitrile (^{18}F-FDDNP) PET images of cognitively intact controls and patients with Alzheimer's disease (AD).

Materials and Methods:

Dynamic ^{18}F-FDDNP PET images, used for *in vivo* imaging of β-amyloid plaques and neurofibrillary tangles, were obtained from 12 AD patients and 9 age-matched controls. For each study, a transmission scan was first acquired for attenuation correction. An accurate retrospective MC method that corrected for transmission-emission misalignments as well as emission-emission misalignments was applied to all studies. No restriction was assumed for zero

movement between the transmission scan and the first emission scan. Logan analysis, with the cerebellum as the reference region, was used to estimate various regional distribution volume ratio (DVR) values in the brain before and after MC. Discriminant analysis was used to build a predictive model for group membership, using data with and without MC.

Results:

MC improved the image quality and quantitative values in ^{18}F-FDDNP PET images. In this subject population, no significant difference in DVR value was observed in the medial temporal (MTL) region of controls and patients with AD before MC. However, after MC, significant differences in DVR values in the frontal, parietal, posterior cingulate, MTL, lateral temporal (LTL), and global regions were seen between the 2 groups ($P < 0.05$). In controls and patients with AD, the variability of regional DVR values (as measured by the coefficient of variation) decreased on average by more than 18% after MC. Mean DVR separation between controls and patients with AD was higher in frontal, MTL, LTL, and global regions after MC. Group classification by discriminant analysis based on ^{18}F-FDDNP DVR values was markedly improved after MC.

Conclusions:

The streamlined and easy-to-use MC method presented in this work significantly improves the image quality and the measured tracer kinetics of ^{18}F-FDDNP PET images. The proposed MC method has the potential to be applied to PET studies on patients having other disorders (e.g., Down syndrome and Parkinson's disease) and to brain PET scans with other molecular imaging probes.

2.2 INTRODUCTION

Head movement in PET is an issue that clinicians and research scientists have to address if they want to accurately quantify the pharmacokinetic analysis of metabolic information contained in a PET image. This is particularly true in the elderly, with increased significance in patients with dementia or movement disorders. The development of methods to correct for head movement in PET data is also especially important as the spatial resolution of PET cameras continues to improve, and movement artifacts become more evident (*1*).

Typical dynamic PET scans with molecular imaging probes usually last for at least an hour, a lengthy procedure for elderly patients but one that is necessary for accurate brain pharmacokinetics. Head movement during the scan can not only introduce a loss in spatial resolution in the image but may also lead to a loss of information and even useless data (*2*). Part of the problem is movement-induced misalignment between transmission and emission scans as the subject moves from his or her initial position at the start of the study, which is when the transmission scan is acquired. This movement will cause an incorrect attenuation correction factor (ACF) matrix to be applied to each uncorrected emission frame of the dynamic image. The integrity of the reconstructed PET data will hence be compromised (*3*).

Moreover, when dynamic images are acquired, movement within an emission frame and movement between emission frames can cause additional complications. Classical compartmental model analysis, along with its linearized or graphical counterparts (*4*), may give erroneous values for physiologic parameters (e.g., distribution volume ratio [DVR] or metabolic flux) derived from such methods, because movement between frames can alter the validity of image-derived blood and tissue time-activity curves. The motivation to address such a continuing problem in PET is thus greatly merited.

One way to reduce head movement during a PET scan is to use a stereotactic head restraint or thermoplastic mask. However, these devices are not able to completely eliminate head movement (*5*) and could produce significant discomfort or claustrophobia in elderly patients, which would compromise the studies. Therefore, a better solution is needed.

The primary purpose of this work was to develop a retrospective image-based head movement correction (MC) method and then evaluate its validity on 2-(1-{6-[(2-^{18}F-fluoroethyl)(methyl)amino]-2-naphthyl}ethylidene)malononitrile (^{18}F-FDDNP) PET images of cognitively intact controls and patients with Alzheimer's disease (AD). ^{18}F-FDDNP is a hydrophobic molecular probe used for *in vivo* imaging of β-amyloid plaques and neurofibrillary tangles (*6, 7*), the neuropathologic hallmarks of AD. The MC method would have to not only correct for transmission-emission misalignment but also correct for emission-emission misalignment if present in these PET studies. In addition, the MC method has to be easy to use to make it practical for common use. The effects of head movement on tissue time-activity curves and parametric DVR images would also have to be addressed.

2.3 MATERIALS AND METHODS

2.3.1 Clinical Assessments

The retrospective MC method was evaluated and validated on 12 AD patients and 9 controls. Table 2.1 summarizes the clinical characteristics in this subject population. All subjects underwent comprehensive neurologic and psychiatric evaluations as previously reported

(*6*). The Mini-Mental State Examination (MMSE) (*8*) was used as one of the clinical tools for detecting cognitive impairment and assessing its severity. Subjects with AD met the standard diagnostic criteria for AD (*9*). Control subjects had normal cognitive functioning for their age and did not meet the diagnostic criteria for AD. In accordance with the procedures of the Human Subjects Protection Committee at UCLA, written informed consent was obtained from all subjects or their legal representatives.

2.3.2 ^{18}F-FDDNP PET Protocol

Dynamic ^{18}F-FDDNP PET scans were acquired with an ECAT EXACT HR+ scanner (Siemens/CTI). A curved head-holder made of carbon fiber was attached to the patient bed. The intrinsic spatial resolution of the scanner was 4.5 mm in full width at half maximum in the center of the field of view. Using a set of external rotating ^{68}Ge rod sources, we first acquired a transmission scan for 20 min in 2-dimensional mode to correct for photon attenuation occurring along each line of response in the emission scan. ^{18}F-FDDNP (382.95 ± 27.07 MBq), as synthesized by methods previously reported (*10*), was injected intravenously as a bolus, and a dynamic emission scan (6×30 s, 4×3 min, 5×10 min, and 3×20 min) was initiated. Dynamic images were reconstructed using filtered backprojection with a Hann filter at a cutoff frequency of $0.3 \times$ Nyquist and a zoom factor of 3.5. The final reconstructed volume had a spatial resolution of 9 mm in full width at half maximum and a matrix size of 128×128 that consisted of 63 planes, resulting in a voxel size of $1.47 \times 1.47 \times 2.43$ mm^3. The same reconstruction parameters were used in the MC method.

2.3.3 Movement Correction Procedure

The head MC method consists of 2 major parts (Fig. 2.1). The first part properly corrects for the attenuation in each of the emission frames of the dynamic image. The second part then aligns each of the properly attenuation-corrected (AC) emission frames to a common reference frame. The MC method involves stepping back and forth between projection space and image space, because the rigid-body alignment routine in the freely available SPM2 software (*11*) must be done in image space. The reslicing of image volumes was also done in SPM2 using trilinear interpolation. The Clinical Applications Programming Package (CAPP; Siemens) was used to reconstruct images. The full procedure, which has been streamlined and made easy to use, consists of the following steps:

1. The first part of the MC method starts by segmenting out the head-holder from the transmission image because the head-holder stayed stationary when the patient's head moved. This is done by manually drawing a contour around the head-holder in ImageJ (*12*) and then masking it out. This is the only user-dependent task within the MC method, although an easy one.

2. The original transmission image without the head-holder ($TX_{ORIGINAL}$) is then co-registered (as a rigid body) to a preselected non-attenuation corrected (non-AC) emission frame, which serves as our reference frame (e.g., frame 11 was used in this study). This will produce a resliced transmission image (TX_{REF}) that is aligned to the reference non-AC emission frame. $TX_{ORIGINAL}$ does not undergo any further co-registrations with emission frames other than to the reference frame. The reference non-AC emission frame has to have a relatively high signal-to-noise ratio for the

normalized mutual information (*13*) matching criterion in SPM2 to work well. No additional preprocessing (besides removing the head-holder) such as filtering or thresholding of the transmission image or the reference non-AC emission frame needs to be done for the registration to work well.

3. The reference non-AC emission frame is then individually co-registered to the other non-AC emission frames to derive $(n-1)$ transformation matrices, where n is the total number of frames in the dynamic image. Non-AC emission images were used because they are not corrupted by any transmission-emission misalignment. It is also at this step that 3 translational and 3 rotational parameters are extracted from each of the $(n-1)$ transformation matrices.

4. TX_{REF} is then separately resliced $(n-1)$ times based on the transformation matrices derived in step 3. It is only after this step that there is an aligned transmission image that matches each of the non-AC emission frames.

5. The attenuation due to the head-holder, which was taken out in step 1, is then added back to each frame of the dynamic transmission image obtained in step 4.

6. The measured ACF matrix for each emission frame is generated based on the aligned transmission images and is applied to the measured non-AC emission sinogram. The properly AC emission image for each frame is then reconstructed.

7. The second part of the MC method is now initiated, whereby each of the properly AC emission frames is individually co-registered to the reference frame.

2.3.4 Logan Plot and Region-of-Interest (ROI) Analysis

To quantify ^{18}F-FDDNP binding, Logan graphical analysis (*4*) was applied to generate DVR parametric images, using the time-activity curve derived from the cerebellar cortex as the reference input for time points between 15 and 125 min. The slope of the linear portion of the Logan plot is the DVR, which is equal to the distribution volume of the tracer in an ROI divided by the distribution volume of the tracer in the reference region (*4*).

ROIs were separately drawn before and after MC on the early summed ^{18}F-FDDNP image (frames 1-7), which resembled tracer perfusion (*14*), and then applied to the DVR image to calculate various regional DVR values in the brain. The volume of the ROIs ranged from 0.2 to 2.0 cm^3. Image visualization and ROI analyses were performed using CAPP software. Regions included in the analysis were (left and right) frontal, parietal, posterior cingulate, medial temporal (MTL), lateral temporal (LTL), subcortical white matter, and cerebellum. Furthermore, each regional DVR value was expressed as a volume-weighted average of the left and right regions, and global DVR values were then calculated as straight averages for all these regional values (*6*), excluding the cerebellum and subcortical white matter. The effects of head movement on tracer time-activity curves were also assessed.

2.3.5 Statistical Analysis

All statistical analyses were performed using SPSS, version 17.0 (SPSS Inc.) for Windows (Microsoft). The results are reported as the mean ± SD (unless otherwise noted) and are regarded as statistically significant if the *P*-value was less than 0.05.

2.3.5.1 Group Comparisons

Group differences in regional DVR values between controls and patients with AD were tested with the Mann-Whitney test (two-tailed). A nonparametric test was chosen because of our small group size and because this type of test makes fewer assumptions about the sample data characteristics (i.e., samples do not have to be drawn from normally distributed populations with equal variance).

2.3.5.2 Discriminant Analysis

Discriminant analysis was used to build a predictive model for group membership (*15*). Given a set of variables, discriminant analysis attempts to find linear combinations of those variables that best separate the two or more groups of individuals. These combinations are called discriminant functions and have the form displayed in the following equation:

$$D = b_1x_1 + b_2x_2 + \ldots + b_nx_n + C \qquad \text{Eq. 2.1}$$

where D is the discriminant score formed by the discriminant function, b_n are the discriminant coefficients, x_n are the predictor variables, and C is a constant. The number of functions equals the minimum of either the number of groups minus one, or the number of predictors.

Moreover, the discriminant function is generated from a sample of cases for which group membership is known and can then be applied to new cases that have measurements for the predictor variables but have unknown group membership (*15*). To assess the predictive performance of the discriminant function, a classification table was generated summarizing the percentage and number of subjects classified correctly and incorrectly. Although the classifications based on the cases used to create the model may be looked upon as too optimistic, in the sense that their classification rate is inflated, a cross-validated section of the table attempts to correct this by classifying each subject while leaving it out of the model calculations (*15*). Cross-validation thus gives an approximately unbiased estimate of the true error rate, although a relatively noisy one (*16*).

2.4 RESULTS

2.4.1 Group Characteristics

The groups were shown to be statistically matched for age ($P > 0.05$). The mean MMSE scores for the control and AD groups were 29.4 ± 0.7 and 17.8 ± 6.8, respectively ($P < 0.001$).

2.4.2 Image Processing and Analysis

Figure 2.2 illustrates how head movement during a dynamic brain PET can cause misalignment between the transmission and the emission scans. The first part of the MC procedure described in this article corrects for this problem. Qualitative differences in ^{18}F-FDDNP DVR images before and after MC are shown in Figure 2.3. The DVR image of an AD patient with considerable head movement (e.g., AD patient 2 in Table 2.2) before MC was subject to image artifacts (i.e., increased scalp uptake and asymmetric ^{18}F-FDDNP binding near the top of the head as seen in the coronal view) because of transmission-emission misalignment. Scalp uptake of ^{18}F-FDDNP, in general, is patient-specific, but it should not be abnormally high and asymmetric as seen in the DVR image before MC. However, after the MC procedure was applied, the image quality of the DVR image was improved, and ^{18}F-FDDNP signal was more clearly defined in frontal, striatal, thalamic, and temporal regions. For a control subject with minor head movement (e.g., Control subject 1 in Table 2.2), the MC procedure did not introduce any artifacts or image degradation to the DVR image. As a result, the image integrity of the original DVR image was maintained.

Transformation parameters (3 translations, 3 rotations) for Control subject 1 and AD patient 2 are shown in Supplementary Figure S2.1. A left-handed coordinate system (*11*) was used to describe the transformation parameters. The severity of the head movement for all subjects in this study was determined by not only examining the transformation parameters but also looking at the fused images of $TX_{ORIGINAL}$, compared with each of the non-AC emission frames. The primary translational direction affected by head movement for both controls and patients with AD was the longitudinal z-axis (i.e., the patient’s superior-inferior axis).

Displacement maps in Figure 2.4 show the individual displacement of each voxel in the reference non-AC emission frame as it is co-registered to a late non-AC emission frame. The displacement is defined as:

$$\text{Displacement}=\sqrt{\text{trans}_x^2+\text{trans}_y^2+\text{trans}_z^2} \qquad \text{Eq. 2.2}$$

where trans_x, trans_y, and trans_z are the absolute translations undergone by a voxel in each directional axis (i.e., a patient’s left-right, anterior-posterior, and superior-inferior axes, respectively) during the registration process. For Control subject 1 (Fig. 2.4A), the displacements were small (< 4 mm). As a result, regional time-activity curves and Logan plots for this subject showed no noticeable changes before and after MC (Supplementary Figs. S2.2A - S2.2D). For AD patient 2 (Fig. 2.4B), the displacements were as large as 24 mm, with increasing regional displacements occurring in the following order: (cerebellum, parietal, and posterior cingulate) (~12-13 mm) < (striatum, thalamus, MTL, and LTL) (~14-15 mm) <

(frontal) (~17-18 mm). As a result, regional time-activity curves before MC were distorted for this subject, and regional DVR values from the Logan plots differed before and after MC (Supplementary Figs. S2.2E - S2.2H). The displacement pattern for each subject in each group was dependent on the subject's individual head movements during the scan and might not necessarily mirror what is shown in Figure 2.4.

The mean displacement (calculated from all the voxels in the head) of the reference non-AC emission frame as it is co-registered to each of the remaining frames in the dynamic image is plotted in Figure 2.5 for Control subject 1 and AD patient 2. The maximum of the mean displacement between the reference frame and any non-AC emission frame is shown in Table 2.2 for all subjects. The maximum of the maximum displacement (undergone by a single voxel in the head) between the reference frame and any non-AC emission frame is also shown in Table 2.2 for all subjects.

2.4.3 Group Comparisons

The results of the group comparisons in regional DVR values before and after MC are summarized in Table 2.3 and plotted in Supplementary Figure S2.3. In this subject population, significant differences between controls and patients with AD were found in frontal, parietal, posterior cingulate, LTL, and global regions before MC ($P < 0.05$). MTL and subcortical white matter regions did not show significant differences before MC. By contrast, all regions showed significant differences between control subjects and AD patients after MC ($P < 0.05$), except for subcortical white matter. Additionally, the P-values from the Mann-Whitney test for frontal, parietal, posterior cingulate, MTL, LTL, and global DVR values decreased after MC, with the MTL region having the most prominent decrease (a decrease of more than 90% in the P-value).

In control subjects, the variability of DVR values [as measured by the coefficient of variation (CV)] in frontal, parietal, posterior cingulate, MTL, LTL, subcortical white matter, and global regions decreased on average by 18% after MC. In subjects with AD, the variability of DVR values in frontal, MTL, LTL, and subcortical white matter regions decreased on average by 36% after MC. The decrease in the CV for subcortical white matter was especially apparent in the AD group, with a decrease of more than 70% from its original value. The DVR separation between controls and patients with AD (as measured by the separation in the means of the 2 groups) was higher in frontal, MTL, LTL, and global regions after MC than before MC.

2.4.4 Discriminant Analysis

Supplementary Figure S2.4 shows the scatter plots of the discriminant scores (before and after MC) for the control and AD groups using frontal, parietal, posterior cingulate, MTL, and LTL collectively as predictor regions in the discriminant function. Note the complete separation between the 2 groups after MC, which leads to 100% overall accuracy in the classification performance by the discriminant function when cross-validation is not applied.

Table 2.4 summarizes the overall accuracy, sensitivity, and specificity in group classification performance (with and without cross-validation) for various combinations of predictor regions before and after MC. The overall accuracy in addition to the sensitivity and specificity improved after MC.

2.5 DISCUSSION

A retrospective image-based head MC method that corrected for transmission-emission and emission-emission misalignments was proposed and investigated in this study. To make it practical for common use, the MC method had to be easy to use and not add tremendous burden to any human brain PET study. The shape of a human head changes little with movement, so rigid-body transformations were used to model the relative positions during a dynamic PET scan (*11*). Two images were matched by finding the translations and rotations that optimized some matching function of the images (*11*). This type of MC method is of value to those who want to extract the fine details of tracer behavior in a PET image but are restricted in doing so because of the degradation present in the image caused by patient movement. With the proposed MC method presented in this article, valuable data once hidden in a brain PET image can come to light, making otherwise questionable studies useful.

Various strategies have been used to address the problems of patient head movement in PET (*1, 2, 17-22*). An attractive method of late has been the acquisition of PET data in list-mode while simultaneously tracking the patient's head movement with an optical motion-tracking system (*1, 22*). The optical motion-tracking system emits infrared light and detects the translational and rotational information of the head during image acquisition from the light that is reflected back from markers positioned on the patient's head. Each detected event in the list-mode data is then corrected for by the movement information provided by the motion-tracking system, and the image is reconstructed thereafter (*1*). A big advantage of this method is its tracer independence (i.e., there is no reliance on the PET data for determining the head movement). However, there are technical issues with this method that still need to be addressed (*1, 19*). Also, optical-tracking systems are of no help in trying to retrospectively correct for head movement in PET images previously acquired. For these cases, image-based methods would offer a more practical solution.

One of the limitations of image-based methods (besides their susceptibility to the quality of the PET data) is that they do not account for motion within a frame. However, this problem can be minimized by shortening the frame duration in the PET protocol. It must be cautioned, though, that excessive shortening of the frame duration might also increase the noise due to lower counting statistics. Furthermore, in the MC method presented in this article, there is no assumption or restriction set on having no movement between the transmission scan and the first emission scan, as is required by some other methods (*18, 19, 21*). This restriction was removed by the alignment of the transmission image to the non-AC emission frames using the mutual information maximization criterion. Although mutual information is a powerful algorithm for the registration of multimodality images (and that worked well in our study), the optimization of other cost functions may be more appropriate for other tracers for which there is too little "mutual information" between the transmission image and the reference emission frame or between the emission frames themselves.

Recently, Costes *et al.* (*20*) investigated a co-registration-based frame-realignment method for dynamic PET images using simulated ^{11}C-raclopride PET data. Upon optimizing the choice of target volume and similarity criterion, a correction strategy was designed that took into account transmission-emission misalignment and the realignment of the individual time frames. Their optimal method consisted of using non-AC emission images and the cross-correlation criterion.

Moreover, Mourik *et al.* (*21*) evaluated 4 different "offline" frame-by-frame MC methods. Their optimal method (based on simulated ^{11}C-flumazenil and (*R*)-^{11}C-PK11195 studies) consisted of aligning non-AC emission frames to a summed image of the early non-AC frames (0-3 min). They then used a common attenuation map to reconstruct a series of aligned AC emission images. The study assumed there was no patient motion during the early emission frames or between the transmission scan and the start of the emission scan. Although both of these studies mirrored our study in certain respects, there were some important differences: our method was derived from real patient data, not simulated data; our method specifically accounted for the attenuation due to the head-holder; normalized mutual information was the matching criterion used in our study; our method did not necessarily assume no mismatch between the transmission scan and the early frames of the emission scan; and we worked with ^{18}F instead of ^{11}C-radiolabeled probes.

With regard to the results reported in this paper, we saw that in Supplementary Figure S2.1 the head movements of Control subject 1 were relatively negligible, whereas the head movements of AD patient 2 could not be ignored, especially along the longitudinal z-axis. The DVR images of Control subject 1 before and after MC were similar (Fig. 2.3) and showed no apparent signs of image degradation that might have been introduced by the MC procedure. This should be the case if the MC procedure worked as it should, because the subject had relatively little head movement to begin with. However, this does not mean that all control subjects will have negligible head movement. For example, there were control subjects in this study whose head movements were substantial and could not be ignored (e.g., Control subject 3 in Table 2.2). The MC procedure should thus be applied to all subjects in a brain PET study, regardless of whether head movements were apparent during the scan.

Previous PET studies have shown significantly higher ^{18}F-FDDNP binding in the frontal, parietal, and temporal regions of the brain in patients with AD than in older control subjects without cognitive impairment (*6*). After MC, the image quality of the ^{18}F-FDDNP DVR images in subjects who moved was improved, and ^{18}F-FDDNP binding in the aforementioned regions was more clearly defined. Quantitatively, this can be seen in the increased separation of the mean DVR values between controls and patients with AD in frontal, MTL, LTL, and global regions (Table 2.3; Supplementary Fig. S2.3). This increased separation explained in part why the discriminant analysis performed better after MC. Another reason for the improved performance was the considerable decrease (ranging from 42% to 91%) in the *P*-values after MC for frontal, parietal, posterior cingulate, MTL, LTL, and global regions. These 2 reasons allowed for the calculation of a more refined discriminant function that was used to correctly classify individuals from the sampled population. The resulting discriminant function can thus be of significant help to diagnose new AD cases based on ^{18}F-FDDNP DVR images.

Additionally, before MC, we saw that the MTL and subcortical white matter regions did not show significant differences between control subjects and AD patients. Because the MTL lobe is the brain region affected the earliest in AD (*23*), these results can be interpreted on the basis of the possibility that elderly control subjects may already have significant pathology present, even in the absence of neuropsychiatric symptoms. However, and even though it is possible that control subjects may have elevated MTL lobe signal with ^{18}F-FDDNP PET, we saw that after MC the MTL region did show a significant difference ($P = 0.0077$) between control subjects and AD patients whereas differences in subcortical white matter remained insignificant between the 2 groups. The MTL region is thus sensitive to head movement. The fact that DVR values in subcortical white matter did not differ significantly between the 2 groups also offers the possibility of using subcortical white matter as a reference region for ^{18}F-FDDNP Logan analysis.

Moreover, the variability in regional DVR values decreased after MC. This decrease was most apparent in subcortical white matter in the AD group. MC should be considered if subcortical white matter is used as a reference region for Logan analysis, because its DVR is highly variable without MC in AD. The reduction in within-group CV would affect the design considerations of an experiment and the costs involved, because the sample size needed for detecting a given percentage of change between means is a function of the CV (*16*). In addition, regional time-activity curves were distorted in subjects with large head movement when compared with the kinetic data after MC. This is a problem because the Logan plots of distorted time-activity curves would yield less reliable DVR values. The proposed MC method would thus be a significant contributor to the precision of the data.

2.6 CONCLUSIONS

The retrospective image-based MC method described in this article significantly improves the image quality and the measured tracer kinetics of ^{18}F-FDDNP PET images. Reliable DVR estimations and increased mean DVR separation in frontal, MTL, LTL, and global regions between control subjects and AD patients are the results of using such a method. The refined discriminant functions derived from movement-corrected data add value to clinicians and researchers who want to use ^{18}F-FDDNP PET to assist with the early diagnosis of AD and to facilitate its use in the monitoring of the efficacy of new treatments for AD. Although validation of the accuracy will need to be separately performed, the proposed MC method can be applied to PET studies of patients with other disorders (e.g., Down syndrome and Parkinson’s disease) and to brain PET scans with other molecular imaging probes.

2.7 FIGURES

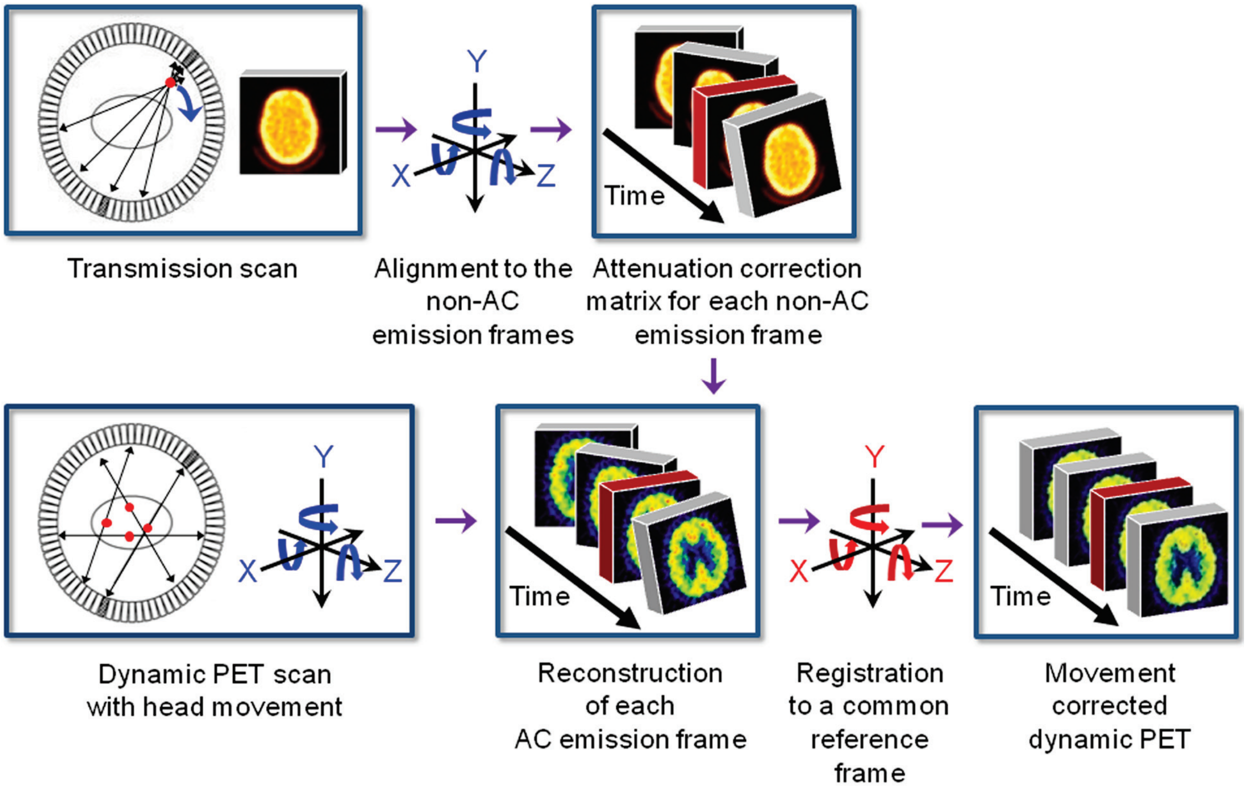

Figure 2.1 Illustrated overview of the retrospective MC method proposed in this study.

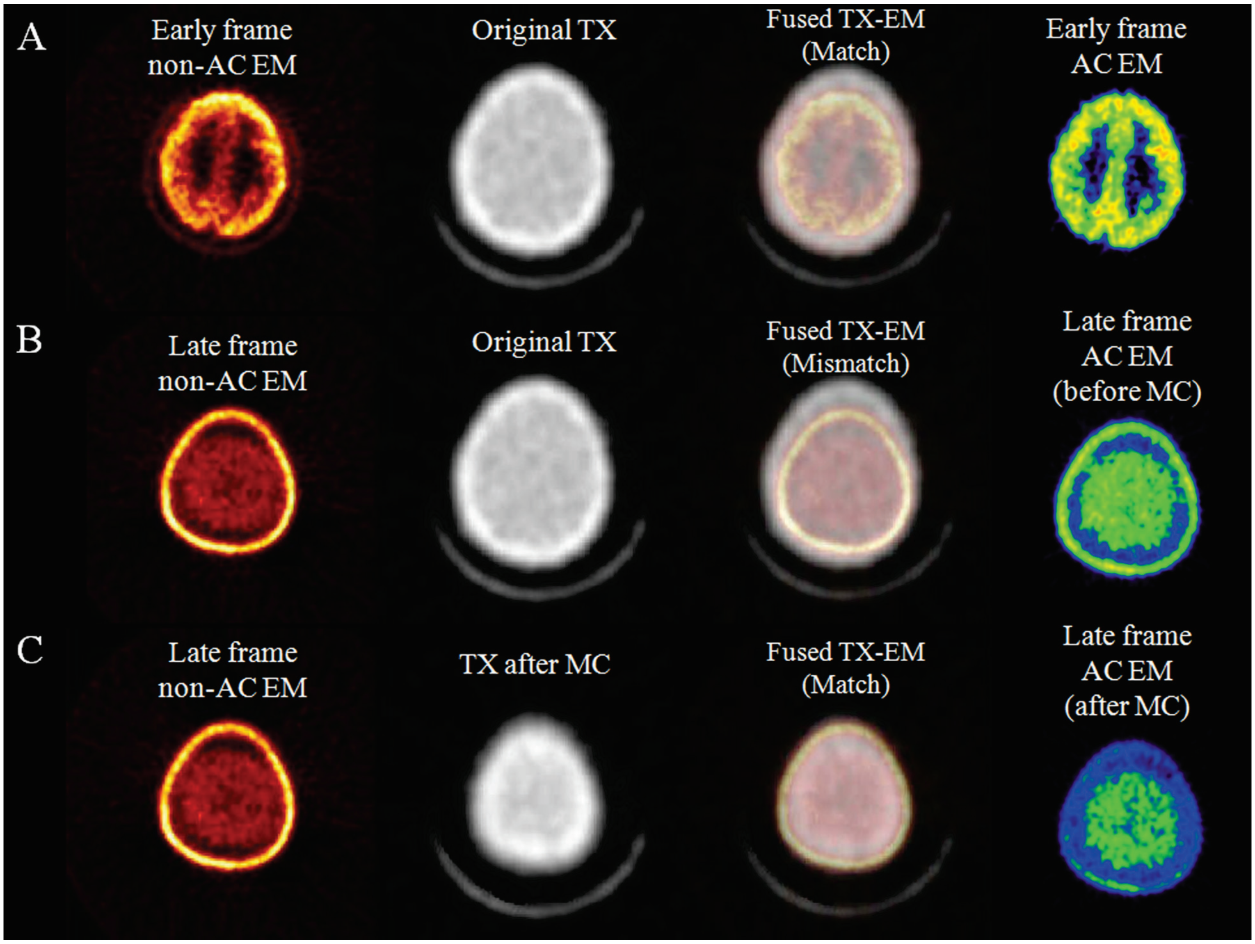

Figure 2.2 Head movement can cause transmission-emission misalignment during dynamic brain PET. (A) Early non-AC emission frame is shown to be fused well with transmission image taken at the start of the study. Both images are shown at the same transaxial plane. (B) Late non-AC emission frame is now fused with original transmission image at the same transaxial plane as before. Because the subject's head moves away from the PET gantry after acquisition of early non-AC emission frame, the mismatched transmission-emission scans would cause an incorrect ACF matrix to be applied to the late non-AC emission frame. (C) After the first part of the MC method has been applied, the original transmission image is matched to the late emission image, producing an accurate ACF matrix that can be used to properly reconstruct the late emission frame.

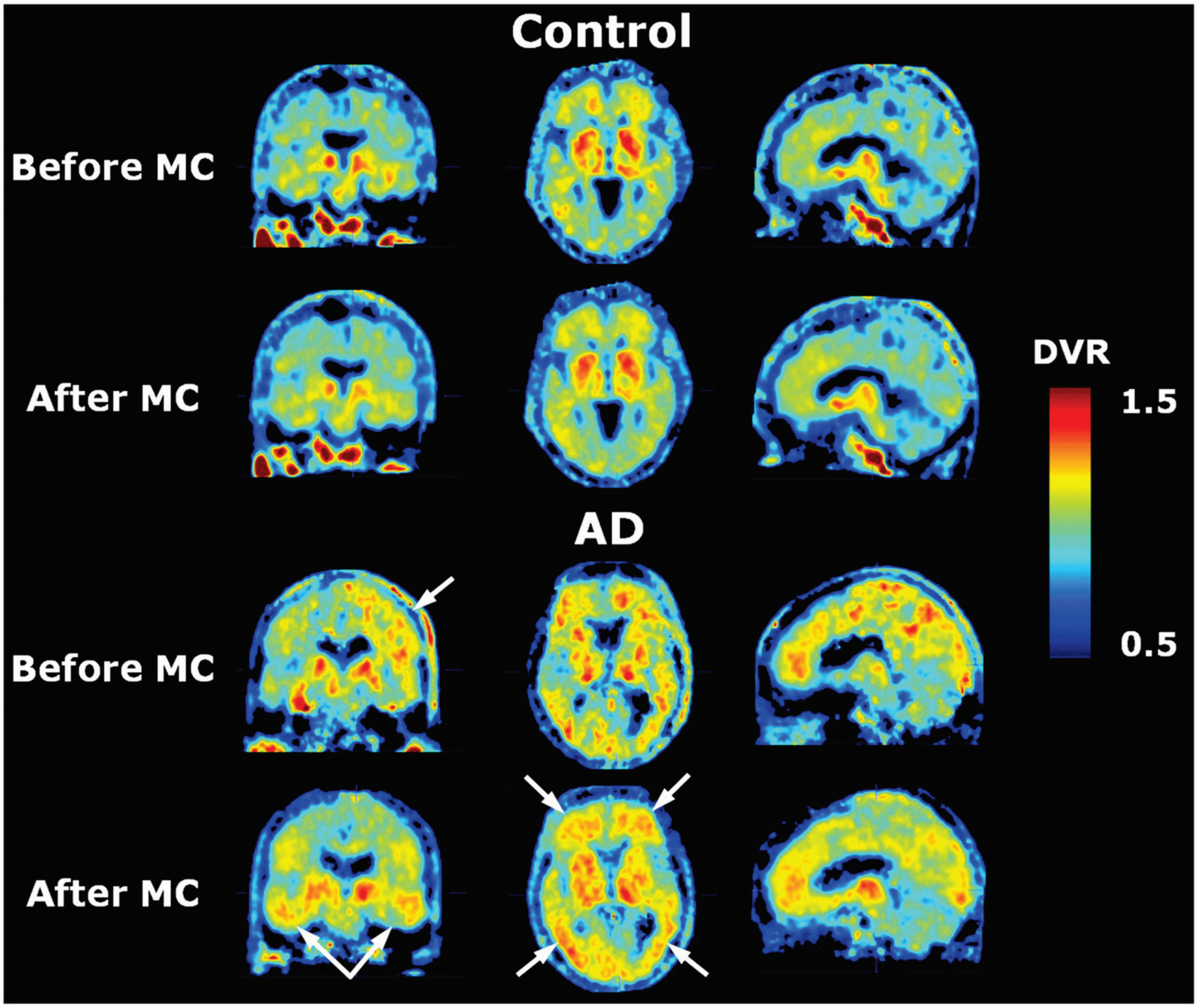

Figure 2.3 For a control subject with negligible head movement, the MC method did not introduce any apparent image degradation to the ^{18}F-FDDNP DVR image. Before MC, the DVR image of an AD patient with considerable head movement was subject to image artifacts (e.g., abnormally high scalp uptake and asymmetric ^{18}F-FDDNP binding near the top of the head as seen in the coronal view) due to transmission-emission misalignment. However, after MC, the image quality of the DVR image was improved. All images correspond approximately to the same cross-sectional locations in their respective coronal, transaxial, and sagittal views.

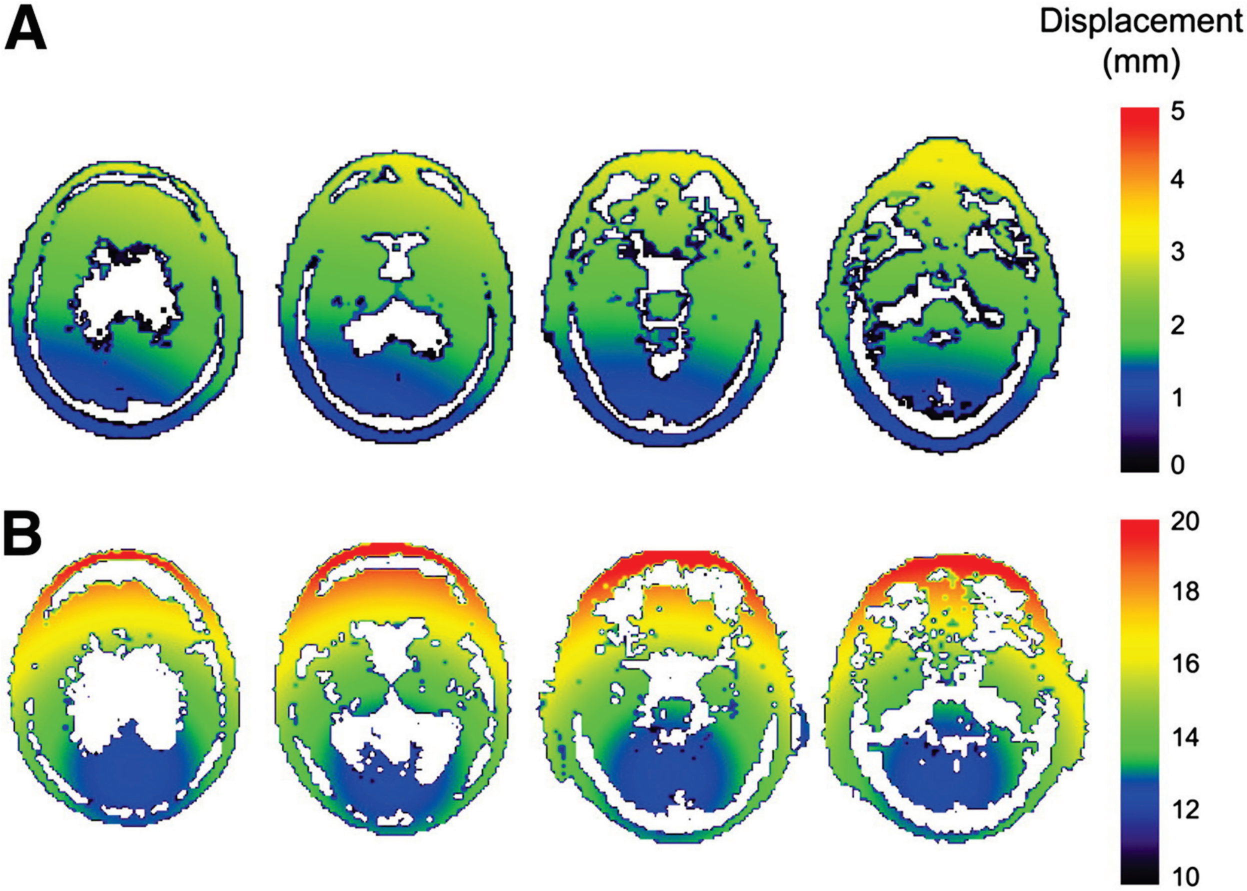

Figure 2.4 Displacement maps for a control subject with minor head movement (A) and an AD patient with significant head movement (B). Each map shows the displacement undergone by each voxel in the reference non-AC emission frame as it is co-registered to the last non-AC emission frame in the dynamic image. Note difference in scale for both color bars.

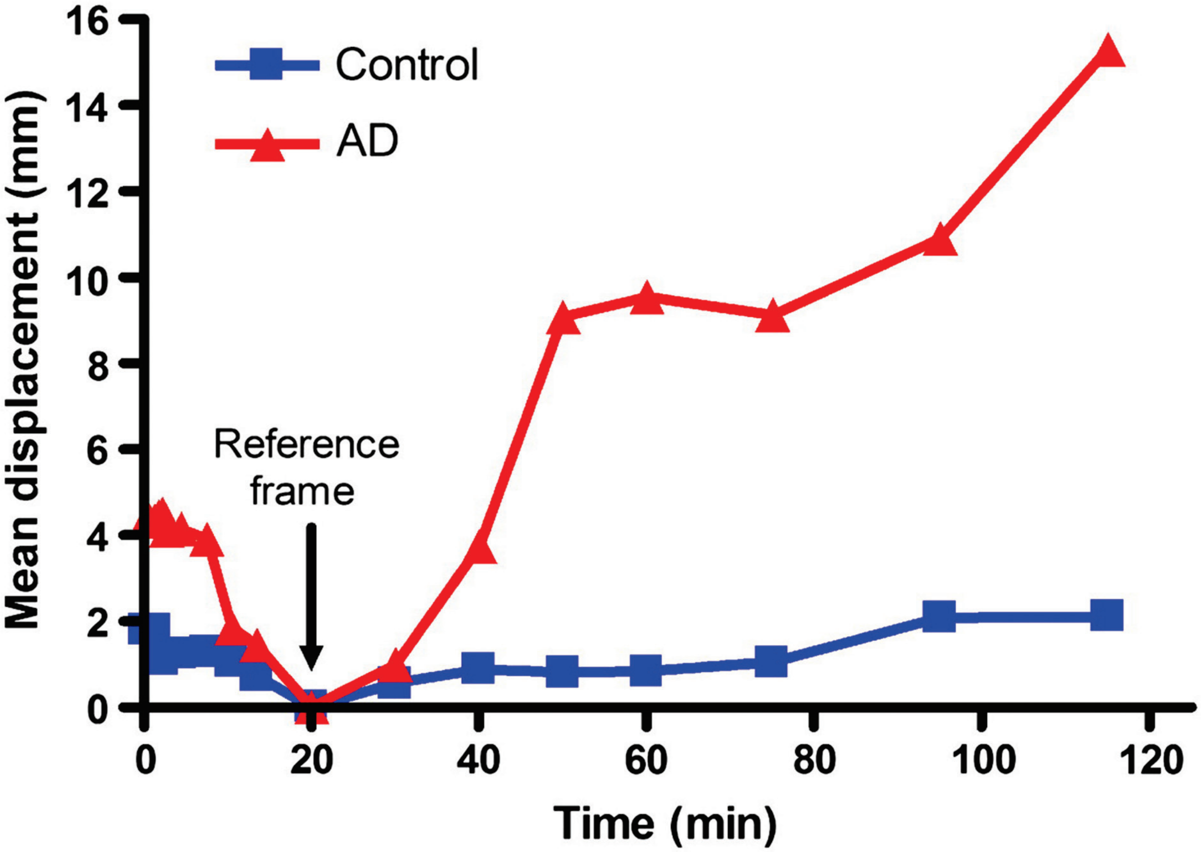

Figure 2.5 Mean displacement of the reference non-AC emission frame as it is co-registered to each remaining frame of the dynamic image as shown for a control subject with negligible head movement and an AD patient with large head movement. The mean was calculated from the displacements of all voxels in the head.

2.8 TABLES

Table 2.1 Clinical characteristics of patients in control and AD groups.

Parameter	Control	AD
n	9	12
Sex (male/female)	6/3	6/6
Age (y)	69 ± 8 (62-85)	74 ± 8 (61-85)
MMSE[*]	29.4 ± 0.7 (28-30)	17.8 ± 6.8 (4-25)
Injected dose (MBq)	383.3 ± 24.2 (351.5-418.1)	382.6 ± 29.9 (318.2-421.8)

[*] Scores range from 0 to 30, with higher scores indicating better cognitive functioning.

Values are mean ± SD, with range in parentheses.

Table 2.2 Displacement during dynamic ^{18}F-FDDNP PET studies in control subjects and AD patients.

	Displacement (mm)	
Control subjects	Maximum of Mean[*]	Maximum of Maximum[†]
1	2.10 (frame 18)	3.53 (frame 18)
2	2.32 (frame 18)	3.73 (frame 4)
3	12.42 (frame 17)	18.10 (frame 17)
4	4.13 (frame 18)	8.90 (frame 17)
5	2.27 (frame 17)	5.01 (frame 5)
6	4.62 (frame 15)	9.45 (frame 15)
7	2.60 (frame 18)	5.68 (frame 5)
8	2.20 (frame 5)	4.98 (frame 5)
9	2.45 (frame 4)	5.99 (frame 4)
AD patients	Maximum of Mean[*]	Maximum of Maximum[†]
1	6.29 (frame 3)	10.80 (frame 3)
2	15.30 (frame 18)	23.59 (frame 18)
3	15.89 (frame 18)	30.58 (frame 18)
4	4.73 (frame 13)	10.97 (frame 15)
5	2.66 (frame 15)	4.54 (frame 15)
6	2.60 (frame 17)	3.70 (frame 3)
7	8.68 (frame 18)	15.73 (frame 18)
8	3.66 (frame 18)	8.03 (frame 18)
9	4.60 (frame 18)	6.63 (frame 18)
10	2.98 (frame 18)	7.09 (frame 18)
11	2.44 (frame 18)	5.42 (frame 17)
12	15.11 (frame 18)	20.18 (frame 18)

[*] Maximum of mean displacement (for which the mean is taken over all voxels in the brain) between the reference frame and any non-AC emission frame.

[†] Maximum of maximum displacement (undergone by a single voxel in the brain) between the reference frame and any non-AC emission frame.

Non-AC emission frames for which the maximum occurs are shown in parentheses.

Table 2.3 Logan DVR values and CVs for various regions in control and AD groups before and after MC.

	Before MC					After MC				
	Control		AD			Control		AD		
Regions	Mean DVR	% CV*	Mean DVR	% CV*	*P*-value†	Mean DVR	% CV*	Mean DVR	% CV*	*P*-value†
FRT	1.032	4.55	1.148	5.11	0.0003	1.029	3.69	1.153	3.83	0.0001
PAR	1.078	3.90	1.173	3.13	0.0016	1.072	3.17	1.161	3.60	0.0006
PCG	1.112	5.03	1.212	3.65	0.0012	1.088	4.18	1.185	4.04	0.0007
MTL	1.151	5.80	1.218	5.63	0.0817	1.127	4.44	1.207	4.83	0.0077
LTL	1.100	5.60	1.177	4.42	0.0142	1.088	4.60	1.172	2.86	0.0012
SWM	1.004	3.73	0.989	11.13	0.6441	1.010	3.64	1.008	3.25	0.9151
GLOBAL	1.095	4.19	1.186	2.57	0.0010	1.082	3.07	1.176	2.97	0.0002

* CV = ratio of SD to mean.

† *P*-values are from the two-tailed Mann-Whitney test.

FRT = frontal; PAR = parietal; PCG = posterior cingulate; MTL = medial temporal; LTL = lateral temporal; SWM = subcortical white matter.

Table 2.4 Overall accuracy, sensitivity, and specificity in classification performance before and after MC using various combinations of predictor regions.

	Before MC			After MC		
Predictor Regions	Overall accuracy (%)	Sensitivity (%)	Specificity (%)	Overall accuracy (%)	Sensitivity (%)	Specificity (%)
FRT+PAR+PCG+MTL+LTL	95 (91)	92 (92)	100 (89)	100 (95)	100 (92)	100 (100)
FRT+MTL+PAR	95 (86)	100 (92)	89 (78)	100 (95)	100 (92)	100 (100)
FRT+MTL+PCG	95 (91)	100 (100)	89 (78)	100 (95)	100 (92)	100 (100)
FRT+PAR+PCG	91 (91)	92 (92)	89 (89)	100 (95)	100 (92)	100 (100)
FRT+MTL+LTL	91 (91)	92 (92)	89 (89)	100 (95)	100 (92)	100 (100)
MTL+LTL	76 (71)	83 (75)	67 (67)	86 (86)	92 (92)	78 (78)

Data in parentheses are cross-validated results.

FRT = frontal; PAR = parietal; PCG = posterior cingulate; MTL = medial temporal; LTL = lateral temporal.

2.9 SUPPLEMENTARY FIGURES

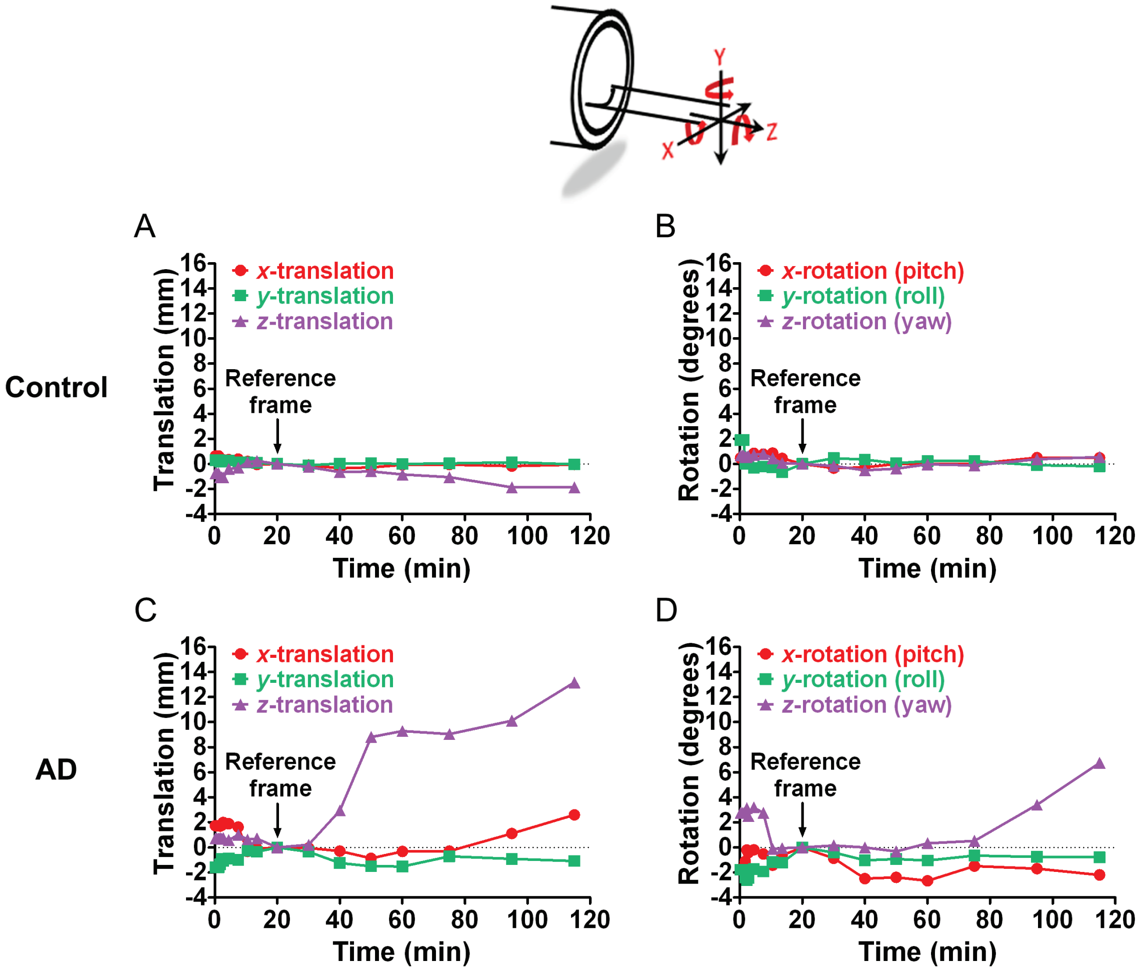

Supplementary Figure S2.1 Translational and rotational parameters when the reference non-AC emission frame is co-registered to other frames in the dynamic image. This is shown for a control subject with negligible head movement (upper panel A-B) and for an AD patient with large head movement (lower panel C-D). A positive translation parameter here indicates that the *voxel at the center of the reference frame* (located at 64, 64, 32) has been shifted along the x-, y-, or z-axis by so many millimeters in the *positive* direction (shown by the direction of the left-handed coordinate system arrows at the top of the figure) as the reference frame is co-registered to another frame within the dynamic image. Similarly, a positive rotation parameter indicates that the *voxel at the center of the reference frame* has been rotated around the axis of interest by so many degrees in a *clockwise* direction as the reference frame is co-registered to another frame within the dynamic image. A negative rotation parameter indicates a *counterclockwise* rotation.

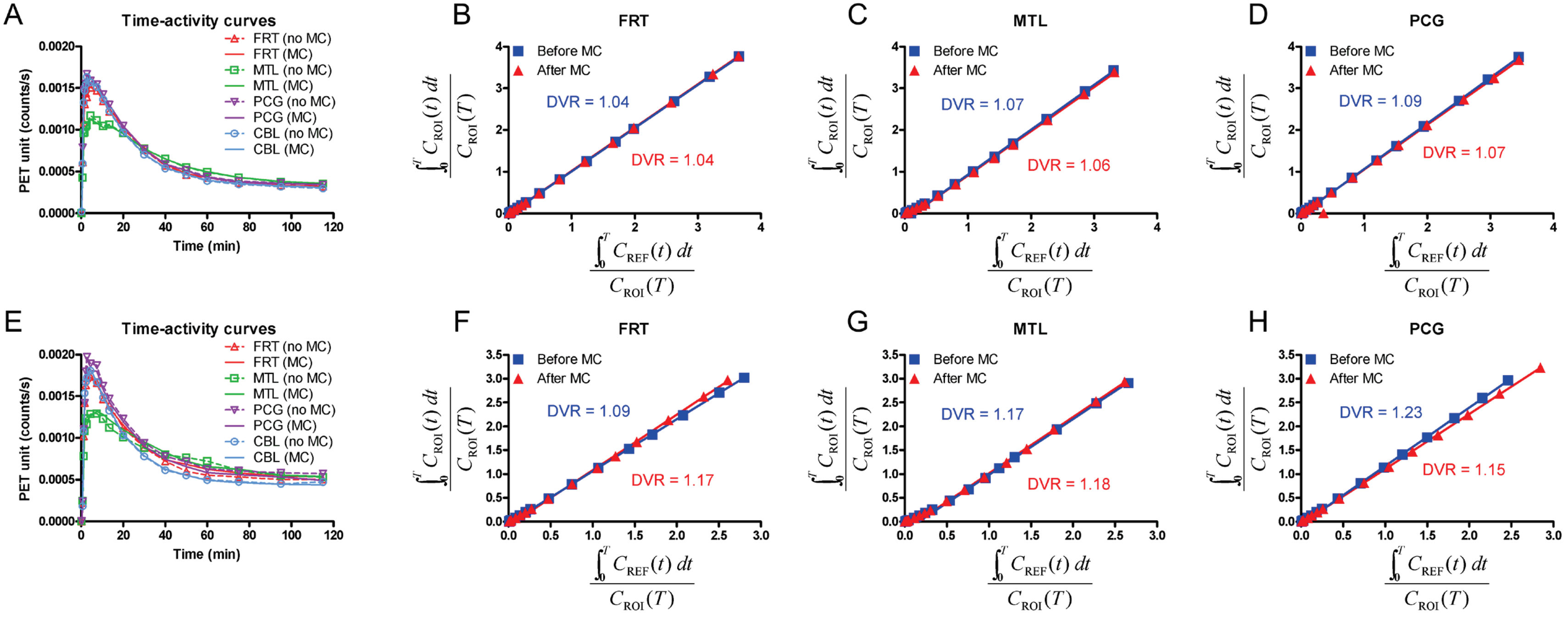

Supplementary Figure S2.2 Regional time-activity curves (TACs) and Logan plots for a control subject with negligible head movement (upper panel A-D) and for an AD patient with large head movement (lower panel E-H). The slope of the linear portion of the Logan plot is the distribution volume ratio (DVR), which is equal to the distribution volume of the tracer in the region of interest divided by the distribution volume of the tracer in the reference region. The control subject showed no noticeable changes in regional TACs and DVR values before and after movement correction. However, note the changes in the TACs and DVR values for the AD patient before and after movement correction. The x and y axes of the Logan plot are given in units of time (minutes). By dimensional analysis, the DVR is thus a unitless physiological parameter.

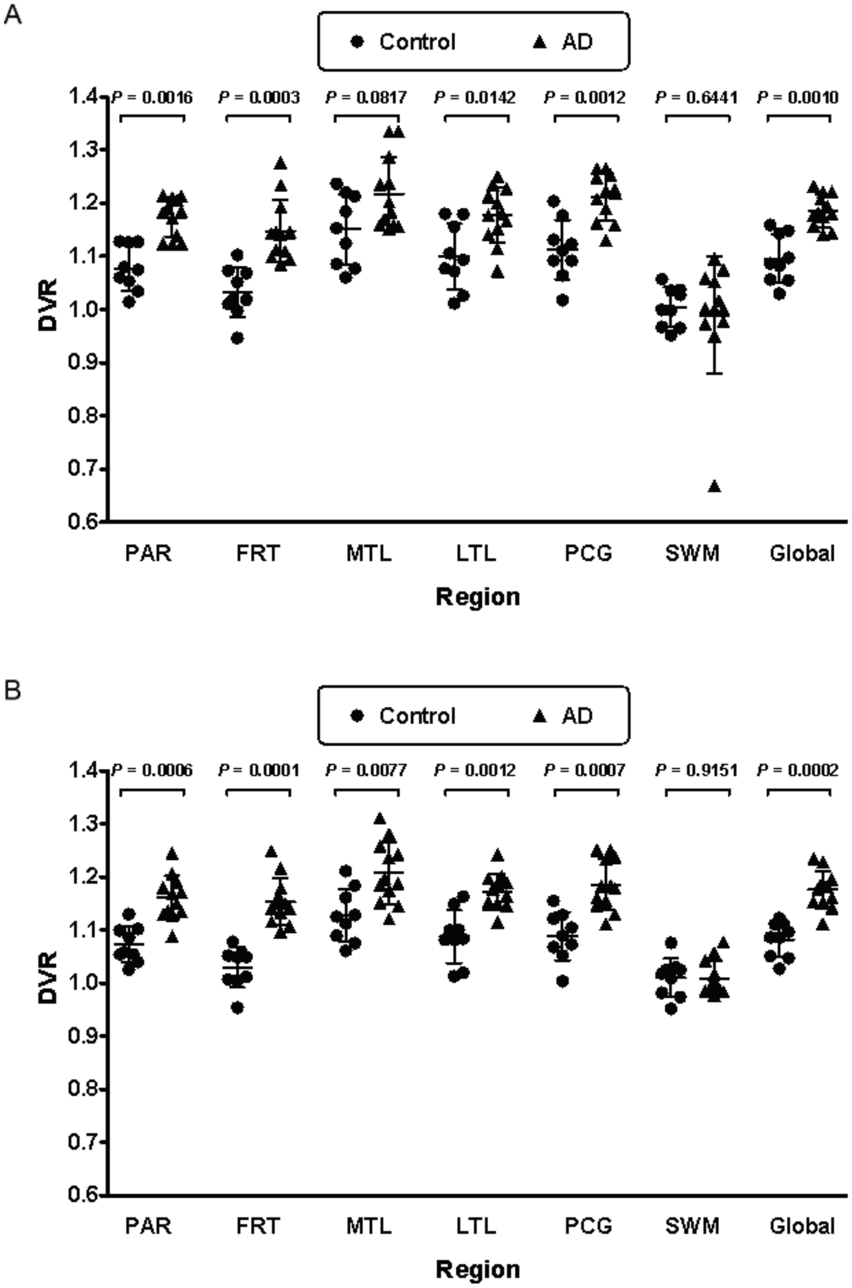

Supplementary Figure S2.3 Group comparisons in regional ^{18}F-FDDNP distribution volume ratios before (A) and after (B) movement correction. Regions included are parietal, frontal, medial temporal (MTL), lateral temporal (LTL), posterior cingulate (PCG), subcortical white matter (SWM) and global. *P*-values from the two-tailed Mann-Whitney test are shown. Note that MTL and SWM before movement correction were not shown to be statistically significant between control subjects and AD patients. Note also that parietal, frontal, MTL, LTL, PCG, and global regions had their *P*-values reduced after movement correction. This was especially apparent in the MTL region (a decrease of over 90% in *P*-value). All regions after movement correction were shown to be significant between controls and AD ($P < 0.05$), except for SWM.

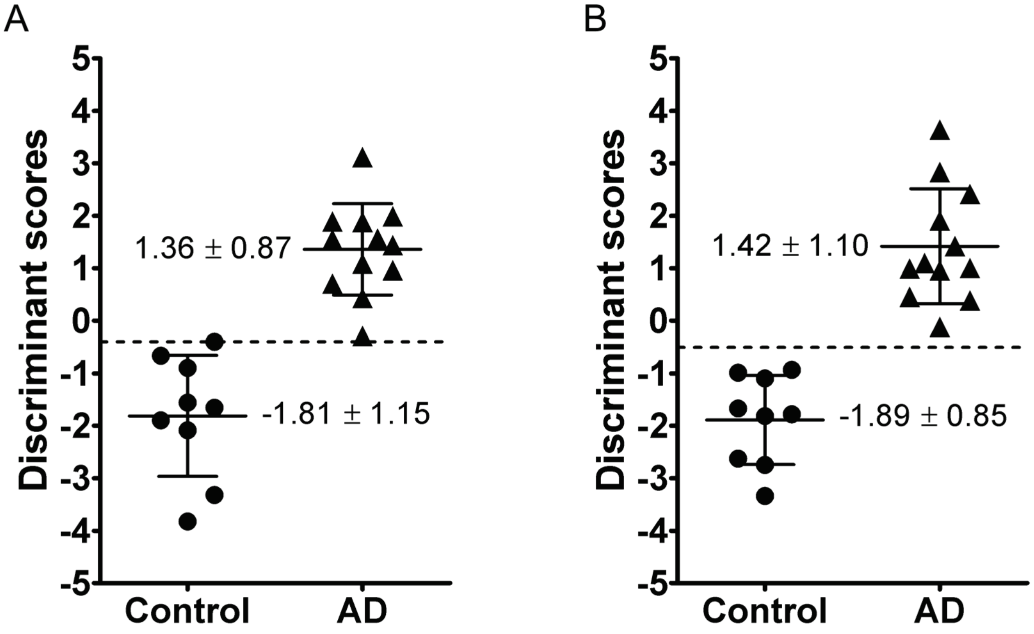

Supplementary Figure S2.4 Sample scatter plots of discriminant scores for the control and AD groups using frontal, parietal, posterior cingulate, medial temporal and lateral temporal collectively as predictor regions in the discriminant function before (A) and after (B) movement correction. Note the complete separation between the two groups after movement correction.

2.10 REFERENCES

1. Buhler P, Just U, Will E, Kotzerke J, van den Hoff J. An accurate method for correction of head movement in PET. *IEEE Trans Med Imaging.* Sep 2004;23(9):1176-1185.

2. Herzog H, Tellmann L, Fulton R, et al. Motion artifact reduction on parametric PET images of neuroreceptor binding. *J Nucl Med.* Jun 2005;46(6):1059-1065.

3. Huang SC, Hoffman EJ, Phelps ME, Kuhl DE. Quantitation in positron emission computed tomography: 2. Effects of inaccurate attenuation correction. *J Comput Assist Tomogr.* Dec 1979;3(6):804-814.

4. Logan J, Fowler JS, Volkow ND, Wang GJ, Ding YS, Alexoff DL. Distribution volume ratios without blood sampling from graphical analysis of PET data. *J Cereb Blood Flow Metab.* Sep 1996;16(5):834-840.

5. Ruttimann UE, Andreason PJ, Rio D. Head motion during positron emission tomography: Is it significant? *Psychiatry Res: Neuroimaging.* 1995;61:43-51.

6. Small GW, Kepe V, Ercoli LM, et al. PET of brain amyloid and tau in mild cognitive impairment. *N Engl J Med.* Dec 21 2006;355(25):2652-2663.

7. Shin J, Lee SY, Kim SH, Kim YB, Cho SJ. Multitracer PET imaging of amyloid plaques and neurofibrillary tangles in Alzheimer's disease. *Neuroimage.* Nov 1 2008;43(2):236-244.

8. Folstein MF, Folstein SE, McHugh PR. "Mini-mental state". A practical method for grading the cognitive state of patients for the clinician. *J Psychiatr Res.* Nov 1975;12(3):189-198.

9. McKhann G, Drachman D, Folstein M, Katzman R, Price D, Stadlan EM. Clinical diagnosis of Alzheimer's disease: report of the NINCDS-ADRDA Work Group under the auspices of Department of Health and Human Services Task Force on Alzheimer's Disease. *Neurology.* Jul 1984;34(7):939-944.

10. Liu J, Kepe V, Zabjek A, et al. High-yield, automated radiosynthesis of 2-(1-{6-[(2-[^{18}F]fluoroethyl)(methyl)amino]-2-naphthyl}ethylidene)malononitrile ([^{18}F]FDDNP) ready for animal or human administration. *Mol Imaging Biol.* Jan-Feb 2007;9(1):6-16.

11. Friston KJ. *Statistical parametric mapping : the analysis of functional brain images*. 1st ed. Amsterdam ; Boston: Elsevier/Academic Press; 2007.

12. Abramoff M, Magelhaes P, Ram S. Image processing with ImageJ. *Biophotonics International.* 2004;11(7):36-42.

13. Bankman IN. *Handbook of medical image processing and analysis*. 2nd ed. Amsterdam: Elsevier/Academic Press; 2009.

14. Wong KP, Wardak M, Shao W, et al. Quantitative analysis of [^{18}F]FDDNP PET using subcortical white matter as reference region. *Eur J Nucl Med Mol Imaging.* Mar 2010;37(3):575-588.

15. SPSS, Inc. *SPSS Base User's Guide 17.0.* Chicago: Prentice Hall; 2007.

16. Van Belle G, Fisher L. *Biostatistics : a methodology for the health sciences*. 2nd ed. Hoboken, N.J.: Wiley-Interscience; 2004.

17. Tellmann L, Fulton R, Bente K, et al. Motion correction of head movements in PET: realisation for routine usage. *IEEE Nuclear Science Symposium Conference Record.* 2003;5:3105-3107.

18. Andersson JL, Vagnhammar BE, Schneider H. Accurate attenuation correction despite movement during PET imaging. *J Nucl Med.* Apr 1995;36(4):670-678.

19. Picard Y, Thompson CJ. Motion correction of PET images using multiple acquisition frames. *IEEE Trans Med Imaging.* Apr 1997;16(2):137-144.

20. Costes N, Dagher A, Larcher K, Evans AC, Collins DL, Reilhac A. Motion correction of multi-frame PET data in neuroreceptor mapping: Simulation based validation. *Neuroimage.* May 27 2009.

21. Mourik JE, Lubberink M, van Velden FH, Lammertsma AA, Boellaard R. Off-line motion correction methods for multi-frame PET data. *Eur J Nucl Med Mol Imaging.* Jul 8 2009.

22. Bloomfield PM, Spinks TJ, Reed J, et al. The design and implementation of a motion correction scheme for neurological PET. *Phys Med Biol.* Apr 21 2003;48(8):959-978.

23. Mosconi L. Brain glucose metabolism in the early and specific diagnosis of Alzheimer's disease. *Eur J Nucl Med Mol Imaging.* Apr 2005;32(4):486-510.

Chapter 3

Discriminant Analysis of ^{18}F-Fluorothymidine Kinetic Parameters to Predict Survival in Patients with Recurrent High-Grade Glioma

3.1 ABSTRACT

Purpose:

The primary objective of this study was to investigate whether changes in 3′-deoxy-3′-[^{18}F]fluorothymidine (^{18}F-FLT) kinetic parameters, taken early after the start of therapy, could predict overall survival (OS) and progression-free survival (PFS) in patients with recurrent malignant glioma undergoing treatment with bevacizumab and irinotecan.

Experimental Design:

High-grade recurrent brain tumors were investigated in 18 patients (8 male and 10 female), ages 26 to 76 years. Each had 3 dynamic positron emission tomography (PET) studies as follows: at baseline and after 2 and 6 weeks from the start of treatment, ^{18}F-FLT (2.0 MBq/kg) was injected intravenously, and dynamic PET images were acquired for 1 hour. Factor analysis generated factor images from which blood and tumor uptake curves were derived. A three-compartment, two-tissue model was applied to estimate tumor ^{18}F-FLT kinetic rate constants using a metabolite- and partial volume-corrected input function. Different combinations of

predictor variables were exhaustively searched in a discriminant function to accurately classify patients into their known OS and PFS groups. A leave-one-out cross-validation technique was used to assess the generalizability of the model predictions.

Results:

In this study population, changes in single parameters such as standardized uptake value or influx rate constant did not accurately classify patients into their respective OS groups (<1 and ≥1 year; hit ratios ≤78%). However, changes in a set of ^{18}F-FLT kinetic parameters could perfectly separate these two groups of patients (hit ratio = 100%) and were also able to correctly classify patients into their respective PFS groups (<100 and ≥100 days; hit ratio = 88%).

Conclusions:

Discriminant analysis using changes in ^{18}F-FLT kinetic parameters early during treatment seems to be a powerful method for evaluating the efficacy of therapeutic regimens.

3.2 TRANSLATIONAL RELEVANCE

Conventional magnetic resonance imaging (MRI) techniques are commonly used in the diagnosis and follow-up of patients with malignant glioma. However, in many situations, changes in contrast enhancement on standard MRI do not correlate with treatment response. Advanced imaging methods are therefore needed to overcome the limitations of conventional MRI. In this positron emission tomography study, we investigated whether changes in 3′-deoxy-3′-[^{18}F]fluorothymidine kinetic parameters, at 2 and 6 weeks after the start of treatment, could predict overall survival and progression-free survival in patients with recurrent malignant glioma undergoing treatment with bevacizumab and irinotecan. This article shows that when a group of optimal kinetic parameter changes are incorporated into a linear discriminant function, one could accurately classify patients into their known survival groups. This method is advantageous because by reliably identifying short- and long-term survivors early during therapy, clinicians can discontinue ineffective treatment strategies and switch to more advanced treatment regimens that could improve patient outcome.

3.3 INTRODUCTION

In vivo imaging of cellular proliferation has tremendous potential for monitoring and predicting response to anticancer therapy. The thymidine nucleoside analogue 3′-deoxy-3′-[^{18}F]fluorothymidine (^{18}F-FLT) was developed as a molecular imaging probe to assess cellular proliferation *in vivo* with positron emission tomography (PET; ref. 1). Once ^{18}F-FLT is transported into the cell, it is phosphorylated by thymidine kinase-1 (TK-1) and subsequently trapped inside the cell (*2*). TK-1 is a cytosolic enzyme that is expressed during the DNA synthesis stage of the cell cycle (*2*). The rate-limiting step in ^{18}F-FLT accumulation is phosphorylation by TK-1, causing ^{18}F-FLT to accumulate in proportion to TK-1 activity (*3*). Compared with normal proliferating tissue, tumor cells have increased levels of TK-1, resulting in an increased ^{18}F-FLT uptake (*4*). The half-life of ^{18}F makes ^{18}F-FLT suitable for tracer kinetic analysis.

In a patient population with nontreated newly diagnosed high-grade gliomas, it was shown that kinetic modeling of ^{18}F-FLT enabled determination of tumor proliferation *in vivo* via the metabolic influx constant K_i (*4*). In their study, K_i strongly correlated with the proliferation index as measured by Ki-67 immunostaining, whereas uptake of methyl-^{11}C-L-methionine (^{11}C-MET) or ^{18}F-FLT failed to correlate with the *in vitro* proliferation marker Ki-67. Furthermore, a National Cancer Institute (NCI)–sponsored trial explored the capacity of ^{18}F-FLT PET to distinguish recurrence from radiation necrosis in previously treated gliomas (*5*). In the NCI trial, it was shown that K_i and the phosphorylation rate constant k_3 seemed to distinguish tumor recurrence from radiation necrosis, with the clinical diagnosis determined independently after the ^{18}F-FLT PET scan (*5*). Standardized uptake value (SUV) and visual analyses of ^{18}F-FLT or 2-

^{18}F-fluoro-deoxy-D-glucose (^{18}F-FDG) images did not significantly separate the 2 groups in the NCI trial. Kinetic modeling with ^{18}F-FLT and other molecular imaging probes in brain tumor patients has also been reported elsewhere (*6-10*).

In the evaluation of treatment response, ^{18}F-FLT was used in a group of patients with recurrent glioma who received a combination of antiangiogenic and chemotherapeutic agents (*11*). A reduction of more than 25% in tumor SUV, defined as a metabolic response, was found to be the threshold with the best predictive power for overall survival (OS; ref. 11). Treatment response in patients with brain tumors has also been assessed by other PET tracers (*12-14*) and with advanced magnetic resonance imaging (MRI) techniques (*15, 16*).

The primary purpose of this work was to investigate whether changes in ^{18}F-FLT kinetic parameters, taken early after the start of therapy, could predict OS and progression-free survival (PFS) in patients with recurrent malignant glioma undergoing treatment with bevacizumab and irinotecan. We hypothesized that there exists a group of kinetic parameter changes that when incorporated into a linear discriminant function would be able to accurately distinguish short-term survivors from long-term survivors. We also hypothesized that this set of parameter changes would provide more predictive information than ^{18}F-FLT uptake changes alone.

3.4 MATERIALS AND METHODS

3.4.1 Study Participants

The studied population consisted of 18 patients with recurrent high-grade glioma. Fifteen of the 18 patients were from our previous study (*10*) and 3 were newly enrolled. The time period during which the data were collected was from July 2005 to June 2009. There were 8 men and

10 women, with a mean age of 54 ± 15 years (range: 26-76 years) at the start of the study. All gliomas were confirmed by histopathology and graded according to the World Health Organization scheme. Sixteen patients had glioblastoma multiforme (GBM; grade IV), 1 patient had anaplastic astrocytoma (AA; grade III), and 1 patient had anaplastic mixed glioma (AMG; grade III). Each patient had previously undergone surgical resection followed by adjuvant treatment with chemotherapy and/or radiation. An overview of the population data is shown in Table 3.1. In accordance with the procedures of the Office of the Human Research Protection Program at UCLA, written informed consent was obtained from all subjects.

3.4.2 Treatment

Patients were treated off-label with biweekly cycles of bevacizumab (10 mg/kg) and irinotecan (125 or 350 mg/m^2 depending on concomitant use of enzyme-inducing antiepileptic drugs). Bevacizumab is a recombinant humanized monoclonal antibody that binds to and inhibits the activity of vascular endothelial growth factor. Irinotecan is a chemotherapeutic agent that inhibits topoisomerase I, an enzyme that helps unwind DNA during replication. All 18 enrolled patients finished the first course of 6 weeks. No patient was lost to follow-up.

3.4.3 Patient Outcome

Patients had regular follow-up at the Neuro-Oncology Clinic, and the date of progression was diagnosed by the neuro-oncologist on the basis of physical examination, clinical deterioration, and imaging. PFS was calculated from the date of baseline ^{18}F-FLT PET to the date of disease progression. In data pooled from 16 clinical trials that used various pharmaceuticals in treating patients for recurrent GBM (none of which included bevacizumab), the median PFS was 1.8 months (*17*). Because most tumors in our patient population were GBM

(16 of 18; 89%), we selected 100 days as a reasonable cutoff point for patients with rapid recurrence versus usual disease progression. OS was calculated from the date of baseline ^{18}F-FLT PET to the date of patient death. A cutoff value of 1 year for OS (*17*) was used to distinguish short-term survivors from long-term survivors.

3.4.4 ^{18}F-FLT Synthesis

^{18}F-FLT was synthesized according to the method developed by Walsh and colleagues (*18*). The chemical and radiochemical purities of ^{18}F-FLT were found to be more than 99%. The specific activity of ^{18}F-FLT was more than 1,000 Ci/mmol (>37 TBq/mmol). The final product was sterile and pyrogen free.

3.4.5 Imaging Protocol

The study protocol was approved by the UCLA Institutional Review Board, the UCLA Medical Radiation Safety Committee, and the UCLA Radioactive Drug Research Committee. A baseline ^{18}F-FLT PET [study 1 (S1)] was carried out within 1 week before the start of treatment, and follow-up ^{18}F-FLT scans were carried out at 2 weeks [study 2 (S2)] and then again at 6 weeks [study 3 (S3)] after the start of treatment. The experimental design is illustrated in Fig. 3.1. PET imaging was carried out with an ECAT EXACT HR+ scanner (Siemens/CTI). The intrinsic spatial resolution of the scanner was 4.5 mm full-width at half-maximum (FWHM) in the center of the field of view. Using a set of external rotating ^{68}Ge/^{68}Ga rod sources, a transmission scan was first acquired for 5 minutes in 2-dimensional mode to correct for photon attenuation. Subsequently, ^{18}F-FLT (2.0 MBq/kg of patient weight) was injected intravenously as a bolus, and a dynamic emission scan with 23 frames (8×15, 2×30, and 2×60 seconds and 11×5 minutes) was acquired in 3-dimensional mode. PET emission data were reconstructed using ordered subset expectation maximization (6 iterations and 16 subsets) with a zoom factor of 2.5. A Gaussian kernel of 5-mm FWHM was used as a post-reconstruction smoothing filter. The spatial resolution of the final reconstructed images was 6.7-mm FWHM. The final reconstructed volume had a matrix size of 128 × 128 and consisted of 63 planes, resulting in a voxel size of $2.06 \times 2.06 \times 2.425$ mm^3.

3.4.6 Factor Analysis

Factor analysis (*19, 20*) generated factor images from which blood and tumor uptake curves were derived. Briefly, the factor model assumes that in a dynamic image there are groups of voxels that have the same time behavior (*21*). In our implementation, 3 factor images (representing the brain vessels, tumor, and the rest) were generated. A 50% threshold of the maximum voxel in the vascular factor image (transverse and cavernous sinuses) was used to create a volume-of-interest (VOI) that would extract the blood time-activity curve (TAC) when overlaid on the dynamic PET image. The tumor TAC was extracted using a 75% threshold of the tumor factor image to get the most proliferative part of the tumor. Necrotic zones have low ^{18}F-FLT uptake and, therefore, do not reach the threshold of 75% uptake of the tumor maximum. Areas with necrosis (e.g., centrally "cold" tumors) were thus explicitly excluded during the VOI creation. The effects of using varying isocontours have been investigated earlier (*10*). The measured blood and tumor TACs were then used for kinetic modeling analysis.

3.4.7 ^{18}F-FLT Compartmental Model

The standard 3-compartment, 2-tissue model for ^{18}F-FLT is analogous to that of ^{18}F-FDG and is illustrated in Supplementary Fig. S3.1. After intravenous injection, ^{18}F-FLT is transported across the cell membrane by sodium-dependent (concentrative) and sodium-independent (equilibrative) nucleoside transporters (*22*). The transport of ^{18}F-FLT from the plasma compartment (C_P) into the exchangeable tissue compartment (C_E), as it crosses the disrupted blood-brain barrier (BBB), is represented by the rate constant K_1 $(\mathrm{mL \cdot cm^{-3} \cdot min^{-1}})$. The exchangeable tissue compartment represents ^{18}F-FLT in its intact, non-phosphorylated state. ^{18}F-FLT glucuronide, a metabolite that accumulates in the blood over time when ^{18}F-FLT is metabolized by the liver, does not cross into the exchangeable tissue compartment (i.e., it is restricted to the vascular space). Furthermore, it has been shown that there is no partitioning in the vascular space and that plasma and whole blood activity concentrations are the same (*23, 24*). The return of ^{18}F-FLT from the exchangeable tissue compartment back into the plasma compartment is represented by the rate constant k_2 $(\mathrm{min^{-1}})$.

At the intracellular level, ^{18}F-FLT in the exchangeable compartment is phosphorylated by TK-1 to produce the nucleotide ^{18}F-FLT monophosphate and, to a limited degree, the di- and triphosphate forms as well (*2*). The metabolic trapping of ^{18}F-FLT via the phosphorylation step is represented by the rate constant k_3 $(\mathrm{min^{-1}})$. ^{18}F-FLT nucleotides in the trapped compartment (C_M) are not incorporated into DNA (*2*). However, ^{18}F-FLT nucleotides in the trapped compartment can be dephosphorylated back into the exchangeable compartment, as represented by the rate constant k_4 $(\mathrm{min^{-1}})$.

The differential equations that describe the rate of change of ^{18}F-FLT concentration in each of the tissue compartments can be solved with the use of Laplace transforms with their solutions shown in ref. 25. Kinetic modeling yields 4 rate constants $(K_1 - k_4)$ and an estimated fifth parameter, the blood volume fraction (V_b), which is the fraction of vascular space in the tumor

VOI. For brain tumor regions where the BBB is disrupted, V_b contains some interstitial space as well. From these 5 estimated microparameters, certain physiologically important macroparameters can be calculated, such as the influx rate constant [$K_i = K_1 \cdot k_3 / (k_2 + k_3)$], the volume of distribution [$V_d = K_1 / (k_2 + k_3)$], and the phosphorylated fraction [$PF = k_3 / (k_2 + k_3)$]. PF is the fraction of ^{18}F-FLT transported via K_1 that ends up in the phosphorylated ^{18}F-FLT pool. In addition, ^{18}F-FLT uptake measurements (expressed as SUVs) were calculated at early (from 10 to 25 minutes) and late time points (from 50 to 60 minutes).

3.4.8 Metabolite and Partial Volume Corrections

Blood metabolites were not measured in this study. Metabolites in the blood were corrected by subtracting a metabolite fraction from the blood TAC as explained in our previous publication (*7*). The equation for the metabolite fraction over time was calculated as $0.42 \times (1 - e^{-0.029 \times t})$. A recovery coefficient of 0.7 was chosen to convert the image-based measured blood TAC to the input function (*7*). Because the tumors were relatively large (>15 mm) compared to the image resolution, the recovery coefficient of the output function was set to unity (*7*).

3.4.9 Statistical Analysis

The Mann-Whitney *U* test was used for between-group comparisons for all absolute parameters (at each study time point) and their relative changes (between each study time point). For paired samples, the Wilcoxon signed-rank test was applied. Spearman correlations were computed to assess the association between 2 variables. All statistical analyses were performed using SPSS (version 19.0; IBM Corporation). The results are reported as the mean ± standard deviation (unless otherwise noted) and are regarded as statistically significant if $P < 0.05$.

3.4.10 Discriminant Analysis

Given a common set of variables for 2 or more groups of individuals, discriminant analysis attempts to find linear combinations of those variables that best separate each group (*25*). These combinations are called discriminant (or classification) functions and have the form displayed as in Equation 3.1.

$$D = b_1 x_1 + b_2 x_2 + \ldots + b_n x_n + C \qquad \text{Eq. 3.1}$$

where D is the discriminant score formed by the discriminant function, b_n are the unstandardized discriminant coefficients, x_n are the predictor variables, and C is a constant. The values of the coefficients are chosen so that the discriminant scores of individuals in any group have the smallest possible variance and, at the same time, the difference between the average discriminant scores of the 2 groups is as big as possible (*25*). A graphical representation of the predictive technique is shown in Supplementary Fig. S3.2.

In this study, a discriminant function was generated on the original sample of 18 subjects for which group membership was known. All possible predictor combinations were exhaustively searched to maximize a test statistic called the Wilks λ (*26*). To produce a nearly unbiased estimate of the proportion misclassified, a leave-one-out cross-validation procedure was carried out whereby each subject was excluded and then classified with the use of the discriminant function based on the remaining subjects (*25*). For each predictor combination, the classification accuracies of the original grouped cases and the cross-validated grouped cases were computed. The Press's Q statistic was used to determine whether the discriminatory power of the classification model was statistically better than chance (*26*).

3.5 RESULTS

3.5.1 Outcome Analysis

Table 3.1 summarizes the clinical characteristics of all patients. At the time of writing this article, all patients had died and therefore all variables (clinical and imaging based) were known. Patients in the original sample ($n = 18$) were designated into 2 groups with regard to their OS and PFS and the cutoff points of 1 year and 100 days, respectively (as detailed under Patient Outcome). From here on, the groups for OS will be referred to as Short-OS and Long-OS and the groups for PFS will be referred to as Short-PFS and Long-PFS. The median OS and PFS for the entire sample were 330.5 days (11.0 months) and 88.5 days (2.95 months), respectively. The median OS for Short-OS ($n = 12$) and Long-OS ($n = 6$) was 276 and 398 days (9.2 and 13.3 months), respectively. The median PFS for Short-PFS ($n = 9$) and Long-PFS ($n = 8$) was 70 and 201 days (2.3 and 6.7 months), respectively. Patient 1 from Table 3.1 was not included in the PFS analysis because this patient's tumor progressed before the 6-week PET measurement. OS and PFS were shown to be correlated (Spearman's $\rho = 0.62$, $P < 0.007$).

3.5.2 Factor Analysis

Supplementary Figure S3.3 shows the vascular and tumor factor images along with the measured blood and tumor TACs. Three-dimensional movies of the factor images can be found in the Supplementary Materials section available online.

3.5.3 Tumor Kinetics and SUV

Mean ^{18}F-FLT SUVs for Short-OS and Long-OS at each of the 3 study time points are shown as bar graphs in Supplementary Fig. S3.4. Similar graphs for the 2 patient groups are shown in Supplementary Fig. S3.5 for various kinetic parameters and V_b (unitless). Supplementary Figure S3.6 visualizes the kinetic parameter values for all patients at each study time point (S1, S2, and S3) in the form of a kinetic microarray, similar to how gene expression levels are visualized in a DNA microarray.

At each study time point, detailed inspection of the absolute values of kinetic and SUV parameters revealed no significant group differences between Short-OS and Long-OS and between Short-PFS and Long-PFS; therefore, relative changes were calculated and analyzed. The percentage of change in SUV from S1→S2 $\left(\frac{(S2-S1)}{S1}\times 100\%\right)$, S1→S3 $\left(\frac{(S3-S1)}{S1}\times 100\%\right)$, and S2→S3 $\left(\frac{(S3-S2)}{S2}\times 100\%\right)$ is shown for both Short-OS and Long-OS in Supplementary Table S3.1. The percentage of change in kinetic and derived parameters from S1→S2 is shown in Supplementary Table S3.2, whereas those from S1→S3 and S2→S3 are shown in Supplementary Tables S3.3 and S3.4, respectively. From S1→S2, SUV (early and late) and K_i decreased for both Short-OS and Long-OS. However, from S2→S3, Short-OS increased in their SUV and K_i values whereas Long-OS continued to decrease in their SUV and K_i values. A slightly different scenario played out for k_3 and PF. From S1→S2, k_3 and PF increased for both Short-OS and Long-OS. However, from S2→S3, Short-OS continued to increase in their k_3 and PF values whereas Long-OS decreased in their k_3 and PF values.

The Wilcoxon signed-rank test was used for evaluating the within-group differences before and after the start of treatment. For Short-OS, significant paired sample differences were found for K_1, K_i, V_d, and SUV (early and late) from S1→S2, and for V_d and SUV_{early} from S1→S3. No significant paired sample differences were found from S2→S3 for Short-OS. For Long-OS, significant paired sample differences were found for V_b and SUV (early and late) from S1→S2, and for K_i and SUV (early and late) from S1→S3. No significant paired sample differences were found from S2→S3 for Long-OS.

For Short-PFS, significant paired sample differences were found for K_1, K_i, and SUV (early and late) from S1→S2, and for K_i and SUV_{late} from S2→S3. No significant paired sample differences were found from S1→S3 for Short-PFS. For Long-PFS, significant paired sample differences were found for K_1, V_b, K_i, V_d and SUV (early and late) from S1→S2, and for K_i and SUV (early and late) from S1→S3. No significant paired sample differences were found from S2→S3 for Long-PFS.

When analyzing the relative changes between studies, several significant between-group differences were revealed by the Mann-Whitney *U* test. The change in blood volume fraction (ΔV_b) from S1→S2, the change in influx rate constant (ΔK_i) from S1→S3, and the changes in k_3, K_i, and PF from S2→S3 were shown to be statistically significant between Short-OS and Long-OS. With regard to PFS, no significant group differences were found for all the various kinetic and SUV changes from S1→S2. However, the change in K_i from S1→S3 and the changes in k_3, K_i, and PF from S2→S3 were shown to be statistically significant between Short-PFS and Long-PFS.

3.5.4 Classification using SUV

Reductions in SUV (early and late) of more than 25% from S1→S2 and S1→S3 were used as one method (*11*) to classify patients into their known OS group membership (<1 or ≥1 year). A reduction in SUV_{early} of more than 25% from S1→S2 yielded the best results with a classification accuracy (or hit ratio) of 56% (10 of 18; Fig. 3.2A).

In another approach, when a change in SUV (early and late) from S1→S2, S1→S3, or S2→S3 was used as a single predictor variable in a discriminant function, ΔSUV_{early} from S2→S3 and ΔSUV_{late} from S2→S3 yielded the best results with hit ratios of 78% (14 of 18) each. ΔSUV_{late} from S1→S3 yielded the next best classification result with a hit ratio of 56% (10 of 18).

3.5.5 Classification using Kinetic Information

Table 3.2 summarizes the discriminant functions (DF1 and DF2) that best classify the 18 patients into their respective OS (<1 or ≥1 year) and PFS (<100 or ≥100 days) groups using an optimal group of ^{18}F-FLT kinetic parameter changes. The predictor variables are shown in descending rank order in terms of their standardized coefficients. None of the discriminating variables in DF1 and DF2 were found to be significantly correlated with each other.

The classification results showed that DF1 correctly predicted 100% (18 of 18) of the original sample into their appropriate OS groups (Wilks $\lambda = 0.264$, $\chi^2_{(4)} = 18.65$, $P = 0.001$). With cross-validation, the classification accuracy was 94% (17 of 18). The discriminant scores of each individual using DF1 are shown in Fig. 3.2B. Furthermore, if a change in K_i was used as the only predictor variable in the discriminant function, ΔK_i from S2→S3 yielded the best results with a hit ratio of 78% (14 of 18). ΔK_i from S1→S3 yielded the next best classification result with a hit ratio of 72% (13 of 18).

For PFS, the results showed comparable performance. The classification results indicated that DF2 correctly predicted 88% (15 of 17) of the original sample into their appropriate PFS groups (Wilks $\lambda = 0.402$, $\chi^2_{(3)} = 12.30$, $P = 0.006$). With cross-validation, the classification accuracy remained at 88%. The discriminant scores of each individual using DF2 are shown in Fig. 3.3. In addition, the Press's Q statistic showed that the discriminant models of DF1 and DF2 performed significantly better than pure chance expectations ($P < 0.005$).

3.6 DISCUSSION

To correctly predict the treatment response of a patient with cancer, it is prudent to collect as much biological/functional information about the patient's tumor before and after the start of treatment. Kinetic modeling in PET can provide such information. Instead of being limited to looking at just one part of the tumor biology, kinetic modeling with dynamic PET data can give us a better view of what is going on with the tumor dynamics as a whole. That is why PET is such a powerful tool for studying the biology of human disease (*27, 28*).

In this study, changes in ^{18}F-FLT kinetic parameters, taken at an early stage after the start of therapy, were used in a linear discriminant function to stratify clinical outcome in 18 patients with recurrent brain tumor. We showed that with this method, we could accurately classify the patient population into their respective OS and PFS groups with classification accuracies of 100% and 88%, respectively. It was the relative changes in ^{18}F-FLT kinetic parameters and not their absolute values that were of importance to the group classification. The leave-one-out cross-validation technique, which was a measure of robustness of the discriminant function, provided classification results that were also comparable. Taken together, these findings indicate that the proportion of variance in the discriminant functions explained by the predictor variables that define group membership was significantly high. Moreover, the kinetic analysis is completely image based and virtually operator independent.

The discriminant functions for OS and PFS included a parsimonious group of predictor variables that produced excellent classification results. The changes in K_1, PF, and V_b from S1→S2 as well as the change in K_i (includes K_1 and k_3) from S1→S3 were shown to be a powerful set of predictor variables for classifying patients into their respective known OS groups. For predicting PFS group membership, the changes in PF, K_1, and V_b from S2→S3 were shown to be a good set of classification variables. The predictor variables in the discriminant functions for OS and PFS were not the same, which seems reasonable because the cause of disease progression at 100 days is presumably different from the cause of death at 1 year. In addition, the tumor cell biology could change during the course of therapy. The predictor variables were not highly correlated within each function, indicating that they shared little redundant information in the group classification.

The predictor variables in the discriminant functions have biological relevance as well. ΔK_i (S1→S3) reflects the overall proliferation difference between the short-term and long-term survivors [ΔK_i (S1→S3) decreases more in the long-term survivors; ref. 10]. About a biological explanation for ΔK_1 (S1→S2), ΔPF (S1→S2), and ΔV_b (S1→S2), one could speculate on the following two levels.

First, normalization of the neovascularization by bevacizumab. Patients responding more favorably are expected to show a larger decrease in V_b, which is what we found. Transient normalization of the tumor vasculature could also enhance the delivery of administered cytotoxic agents (*29*). It has been previously shown that TK-1 is upregulated in response to DNA damage caused by genotoxic insults in tumor cells (*30, 31*). Irinotecan and its more potent metabolite, SN-38, are known to induce single- and double-stranded DNA breaks (*32*). This may be the early scenario with the tumors of the long-term survivors before they eventually succumb to the cytotoxic effects of additional chemotherapy. This would explain the larger initial increase in ΔPF and Δk_3 from S1→S2 for the long-term survivors.

Second, changes in the permeability of the vasculature and the tumor. Aggressive tumors most likely have a "leaky BBB" when compared with lower grade tumors. This explains why the baseline transport rate K_1 was high. If the therapy is able to restore a more "normal" situation, the K_1 value is expected to decrease as our data showed.

However, if the tumor has a K_1 value for the therapeutic agent that decreases less from S1→S2, then the patient is expected to be a long-term survivor, as the intracellular concentration of the drug is, on average, higher in patients with a favorable outcome. For the short-term survivors, the tumors have probably figured out how to get rid of the toxins (and ^{18}F-FLT) by pumping them out or preventing them from entering the cell [thus, ΔK_1 (S1→S2) decreases more]. In the above, it is assumed that changes in the transport rate constant K_1, as measured by ^{18}F-FLT, is similar for the chemotherapeutic agent. This assumption is based on previous studies that have shown that certain multidrug transporters in the BBB (e.g., MRP4 and BCRP) are known to transport camptothecin derivatives (such as irinotecan) and some nucleoside analogues such as azidothymidine and FLT (*33, 34*). The net effect on refractory tumors is that the initially observed change in K_i (from S1→S2) returns to its baseline value for the third study S3, whereas the patients who benefit from the therapy show a further decrease in K_i.

It is important to note that discriminant analysis can be determined at 6 weeks after the start of treatment, which can be months to more than a year before final outcome. This offers the possibility that ^{18}F-FLT PET could replace PFS as a surrogate end point for OS, considered the gold standard primary efficacy end point. However, further prospective studies would be needed to confirm this assertion. The results of this study show that kinetic modeling in PET can extract important molecular and biochemical information inherent to the tumor, which can be used to reliably distinguish patients who will respond favorably to a certain therapy (long-term survivors) from those who will not (short-term survivors).

In this patient population, changes in a single parameter, whether incorporated into a discriminant function as the sole predictor variable or using a more than 25% reduction criterion in the case of SUV, did not accurately classify patients into their known OS groups (hit ratios $\leq 78\%$). The reason for this is that there is less information about the tumor biology using just one-parameter change. A recent study (*10*) showed that a special subgroup of long-term survivors ($n = 5$) was found within their patient sample ($n = 15$) in which the SUV (early and late) for every patient in that group dropped by more than 25% (JCO 2007 criterion; ref. 11) from S1→S2 and S1→S3. However, these single-parameter changes (used in and of themselves) also misclassified the short-term survivors in their study (*10*), which is a situation that one may not be willing to tolerate. In contrast to these results, this article shows that the misclassification error of the short-term survivors is greatly reduced when a select group of kinetic parameter changes are used in a linear discriminant function. By including more biological information about the tumor, the discriminant function provides greater confidence in the survival (and therefore treatment response) prediction for each patient.

Unlike the *Journal of Clinical Oncology* article (*11*), no PET criterion was defined beforehand to categorize the patient's response to treatment. Our current study dealt with outcome analysis. The OS of the patients was used to categorize the data. SUV and kinetic information could also be integrated in the discriminant function analysis. Our study was different from the NCI-sponsored trial (*5*) as well. In their study, no statistical tool or criterion was provided to predict OS or PFS. Their main focus was using baseline ^{18}F-FLT kinetic parameters to distinguish recurrence from radiation necrosis. The treatment administered after the single ^{18}F-FLT PET scan in the NCI trial was also different from our study.

Other investigators have similarly used advanced imaging and quantitative techniques to assess treatment response in patients with glioma. Studies from Galldiks and colleagues (*12, 14*) and Wyss and colleagues (*12, 14*) showed that after temozolomide chemotherapy, PET imaging with ^{11}C-MET and ^{18}F-labeled O-(2)-fluoro-ethyl-L-tyrosine could detect responses after 3 months in high-grade and low-grade gliomas. From these findings, the deactivation of amino acid transport seemed to be an early indicator of chemotherapy response. Pope and colleagues (*15*) reported that for 41 bevacizumab-treated patients with recurrent GBM, apparent diffusion coefficient histogram analysis on "pre-treatment" diffusion-weighted MRI could predict a 6-month PFS or greater with 73% accuracy.

This was a small exploratory study with limitations. For example, the discriminant function used to predict OS group membership required kinetic information extracted from three dynamic PET studies. This may be inconvenient for the patient. If two imaging studies are done rather than three, the hit ratio would drop from 100% to 89%, with the function using changes from S1→S3 performing better than those using changes from S1→S2 or S2→S3. A larger study is warranted to confirm the predictive efficacy of the discriminant functions presented in this article. Furthermore, it is cautioned that if the estimated discriminant functions are used to classify individuals in the future, it is important that the future sample comes from a population similar to the one the discriminant functions were computed on.

Blood metabolites were not measured in this study, but corrections were applied using a model approach. Patients treated with chemotherapy may have altered liver function that could affect the metabolism of ^{18}F-FLT. If liver function were impaired, we would overestimate the true metabolite fraction, which would lead to a higher value in K_i. Because K_i is a composite parameter, this would lead to higher values in K_1 and k_3 and to a lower value in k_2. Underestimation of the true metabolite fraction would have the opposite effect. Nevertheless, this is a limitation of our study that still needs to be addressed in future experiments.

The cutoff points for PFS and OS were chosen as 100 days and 1 year, respectively, based on the article of Ballman and colleagues (*17*), where it was shown that these seemed as reasonable initial cutoff points for discriminant analysis. Previous results from an analysis of 12 phase II clinical trials conducted by the North American Brain Tumor Consortium showed that progression status at 2, 4, and 6 months (measured from time of registration) predicted subsequent survival time for patients with recurrent high-grade glioma (*35*). In our patient population, 3 patients had died within 3.5 months and 4 had died within 6 months. The median PFS and OS for the entire sample were shown to be 3 and 11 months, respectively. Although not carried out here, discriminant functions could just as well have been computed at other PFS and OS cutoff times, providing an even clearer interval of patient survival.

Future work can extend the statistical analysis to multiple linear regression, where the inputs will still be the relative changes in ^{18}F-FLT kinetic parameters but the output, instead of being a dichotomous categorical variable, will now be a continuous variable (i.e., each patient will get a numerical estimate of their survival time). Multimodality imaging parameters could also be implemented as added information about the tumor biology. Although we focused on patients with recurrent brain tumor using ^{18}F-FLT PET, the same methods presented in this study can be potentially applied to other molecular imaging probes and to other types of cancers undergoing different treatments, making the future of kinetic modeling in nuclear medicine and oncology exciting and promising.

3.7 CONCLUSIONS

Discriminant analysis using changes in ^{18}F-FLT kinetics after the start of treatment seems to be a powerful method for evaluating the efficacy of therapeutic regimens and could potentially replace PFS as a surrogate end point for OS. This is advantageous because by being able to determine whether a specific treatment is working shortly after its administration, clinicians can personalize therapy for each patient and decrease possible harmful side effects. Kinetic modeling with dynamic PET data may play an integral role in a clinician's assessment of treatment response, as it can extract pharmacokinetic signatures during the initial course of therapy that can be predictive of survival.

3.8 FIGURES

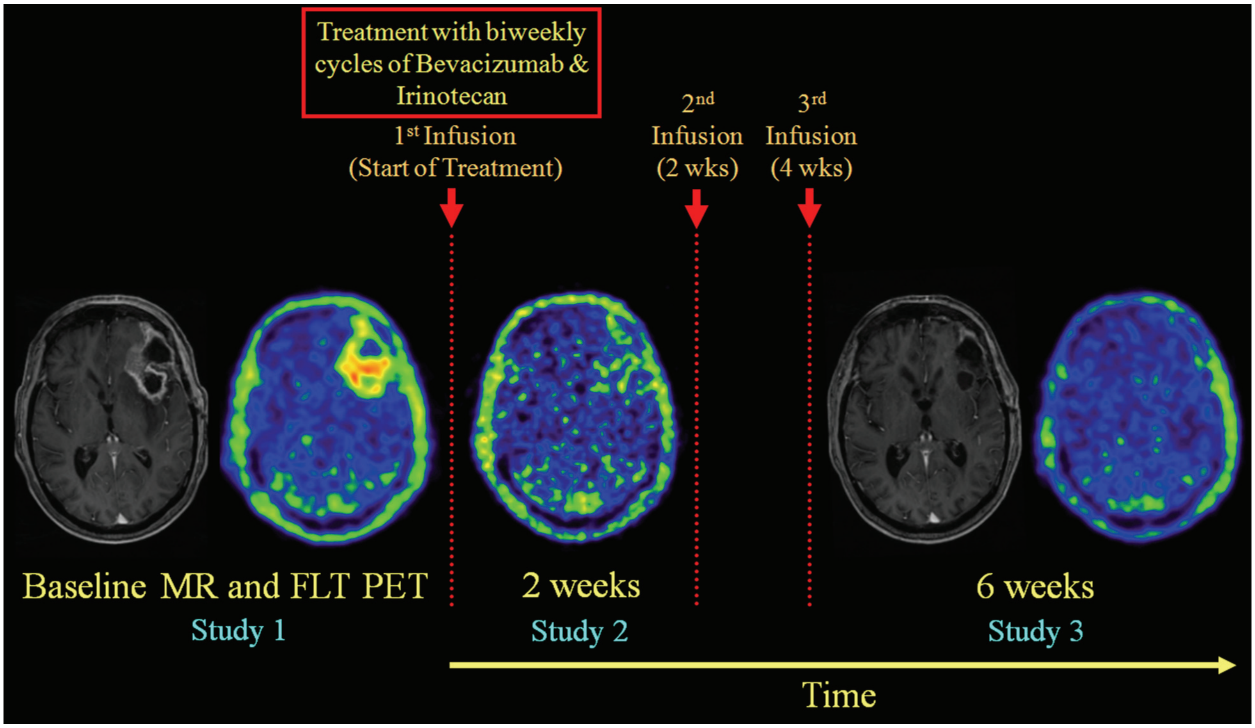

Figure 3.1 Experimental design used in this study. A baseline ^{18}F-FLT PET was carried out within 1 week before the start of treatment, and follow-up ^{18}F-FLT PET scans were carried out at 2 weeks and then again at 6 weeks after the start of treatment. Shown above are summed ^{18}F-FLT PET images (50-60 minutes) and their corresponding contrast-enhanced T1-weighted MRIs. No MRI was carried out at 2 weeks. ^{18}F-FLT PET images at 2 and 6 weeks were co-registered to the baseline PET, and the 6-week MRI was aligned to the co-registered baseline MRI. Images are displayed using the same color scale within each modality. The patient shown here was a long-term survivor.

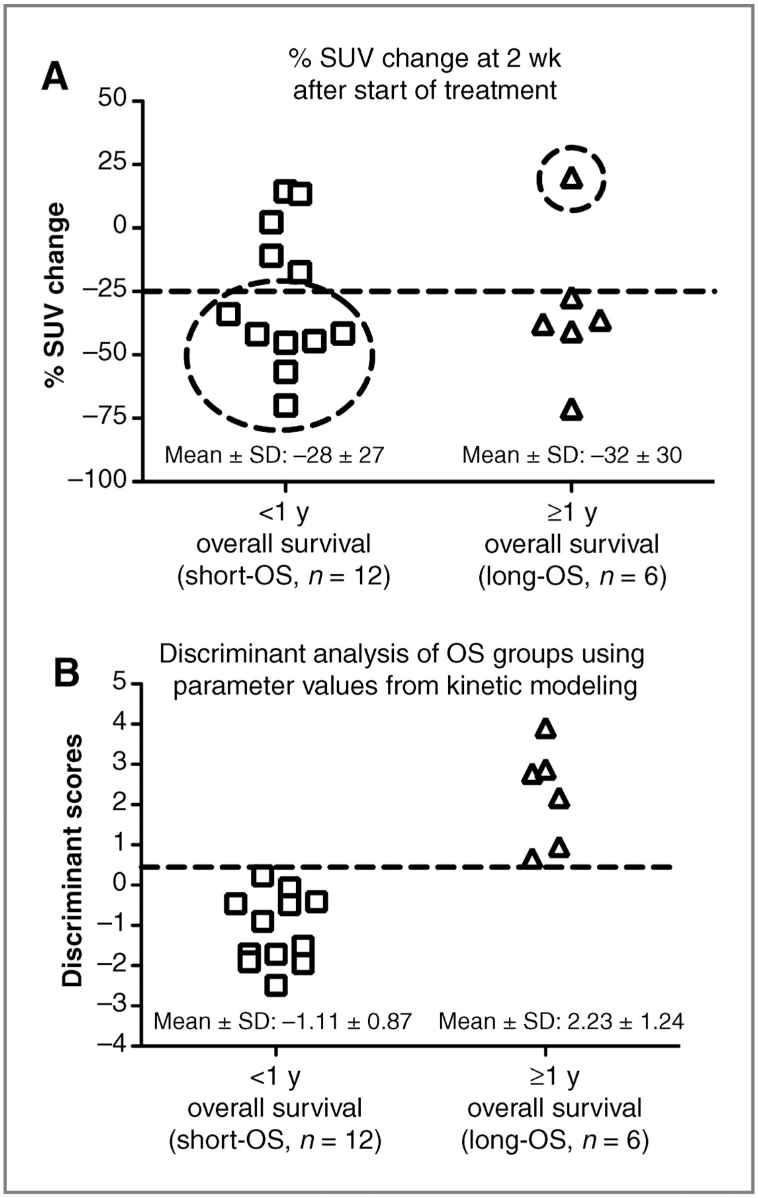

Figure 3.2 (A) Using a reduction in SUV_{early} of more than 25% after 2 weeks from the start of treatment correctly classified 10 of 18 patients. With this SUV reduction criterion, 7 patients in Short-OS would be misclassified as long-term survivors and 1 patient in Long-OS would be misclassified as a short-term survivor. (B) Discriminant analysis using changes in ^{18}F-FLT kinetics could correctly classify all 18 patients in their true OS group. Note the complete separation of the discriminant scores between the 2 groups.

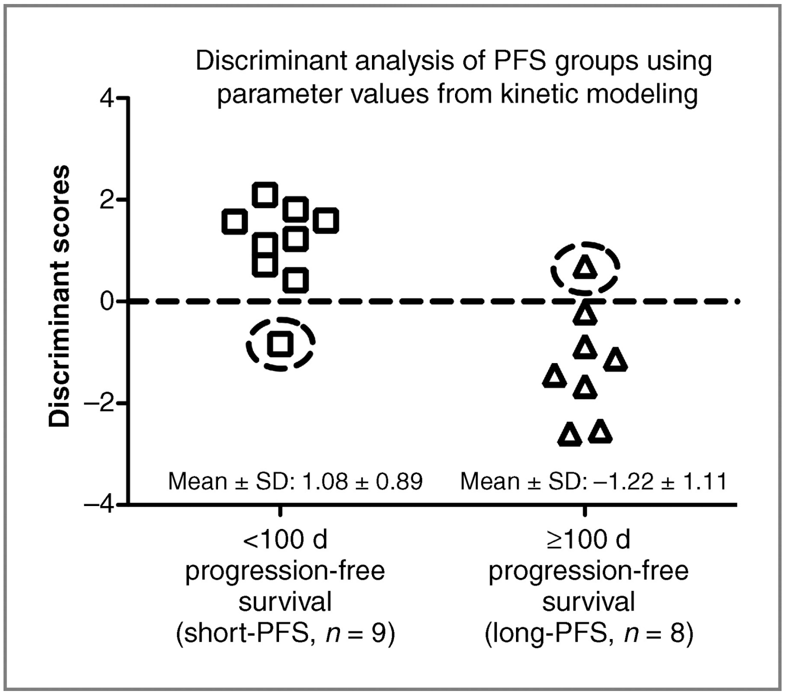

Figure 3.3 Discriminant analysis using changes in ^{18}F-FLT kinetics could correctly classify PFS group membership for 15 of 17 patients. Patient 1 from Table 3.1 was not included in the analysis because tumor progression occurred before the 6-week PET measurement.

3.9 TABLES

Table 3.1 Clinical characteristics of all patients.

Patient No.	Sex	Age (y)	Pathology at Recurrence	WHO Grade at Recurrence	Initial Therapy	Prior Treatments	Time from Initial Diagnosis[†] (d)	PFS (d)	OS (d)
1	M	50	AA	3	Chemotherapy/XRT	2	332	29	59
2	M	69	GBM	4	Chemotherapy/XRT	1	76	81	81
3	F	65	GBM	4	Chemotherapy/XRT	2	578	78	107
4	F	59	GBM	4	Chemotherapy/XRT	1	322	42	169
5	M	64	GBM	4	Chemotherapy/XRT	1	178	70	234
6	F	37	AMG	3	Chemotherapy/XRT	1	160	155	260
7	M	37	GBM	4	Chemotherapy	2	4225	62	292
8	M	68	GBM	4	Chemotherapy/XRT	2	332	218	315
9	F	35	GBM	4	XRT	3	2804	65	318
10	F	54	GBM	4	Chemotherapy/XRT	1	91	226	343
11	M	45	GBM	4	Chemotherapy/XRT	1	132	74	344
12	M	26	GBM	4	Chemotherapy	3	462	96	364
13	F	40	GBM	4	Chemotherapy/XRT	1	462	44	366
14	F	47	GBM	4	Chemotherapy/XRT	1	160	176	374
15	F	70	GBM	4	Chemotherapy/XRT	1	362	184	395
16	F	61	GBM	4	Chemotherapy/XRT	2	719	137	400
17	F	62	GBM	4	Chemotherapy/XRT	1	316	273	709
18	M	76	GBM	4	Chemotherapy/XRT	1	134	588	978

Abbreviations: GBM = glioblastoma multiforme; AA = anaplastic astrocytoma; AMG = anaplastic mixed glioma; XRT = radiation therapy.

[†] Time from initial diagnosis is the number of days from initial diagnosis to start of treatment in the current study.

Table 3.2 Discriminant functions for classifying patients into their respective OS and PFS groups using ^{18}F-FLT kinetic information.

Discriminant Function for Overall Survival (DF1)		
Predictor Variables	**Unstandardized Coefficients**	**Standardized Coefficients**
ΔK_1 (S1→S2)	3.994	1.101
ΔK_i (S1→S3)	-3.175	-0.951
ΔPF (S1→S2)	1.311	0.940
ΔV_b (S1→S2)	-3.019	-0.813
Constant	-0.364	—

Discriminant Function for Progression-Free Survival (DF2)		
Predictor Variables	**Unstandardized Coefficients**	**Standardized Coefficients**
ΔPF (S2→S3)	3.309	1.230
ΔK_1 (S2→S3)	1.250	0.988
ΔV_b (S2→S3)	0.640	0.637
Constant	-0.740	—

3.10 SUPPLEMENTARY FIGURES

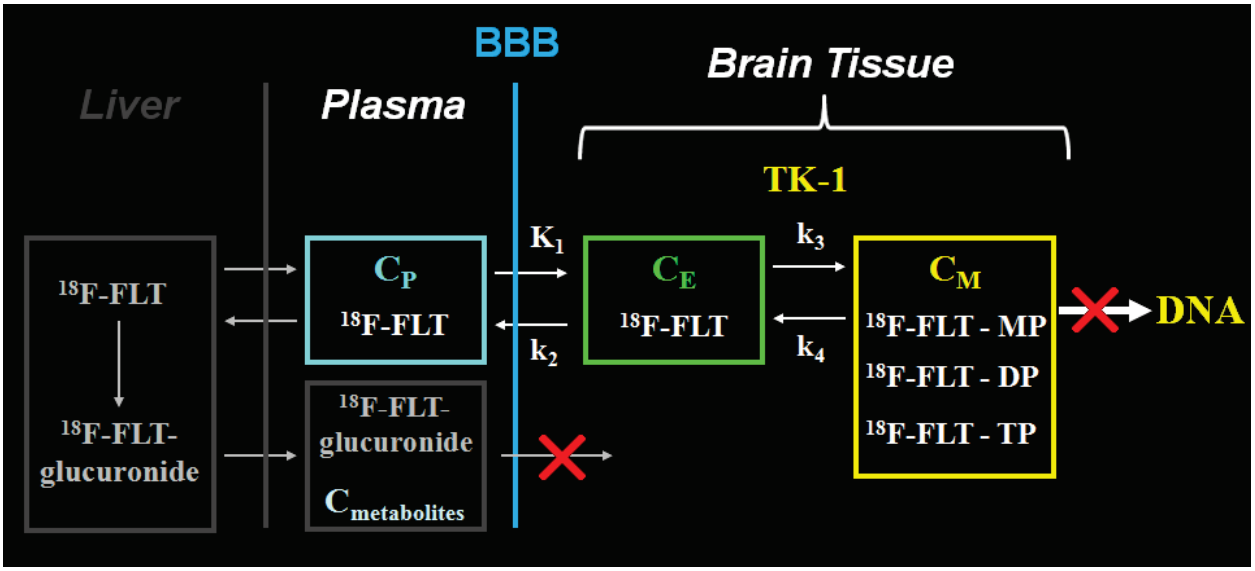

Supplementary Figure S3.1 An illustrated 3-compartment, 2-tissue kinetic model for ^{18}F-FLT.

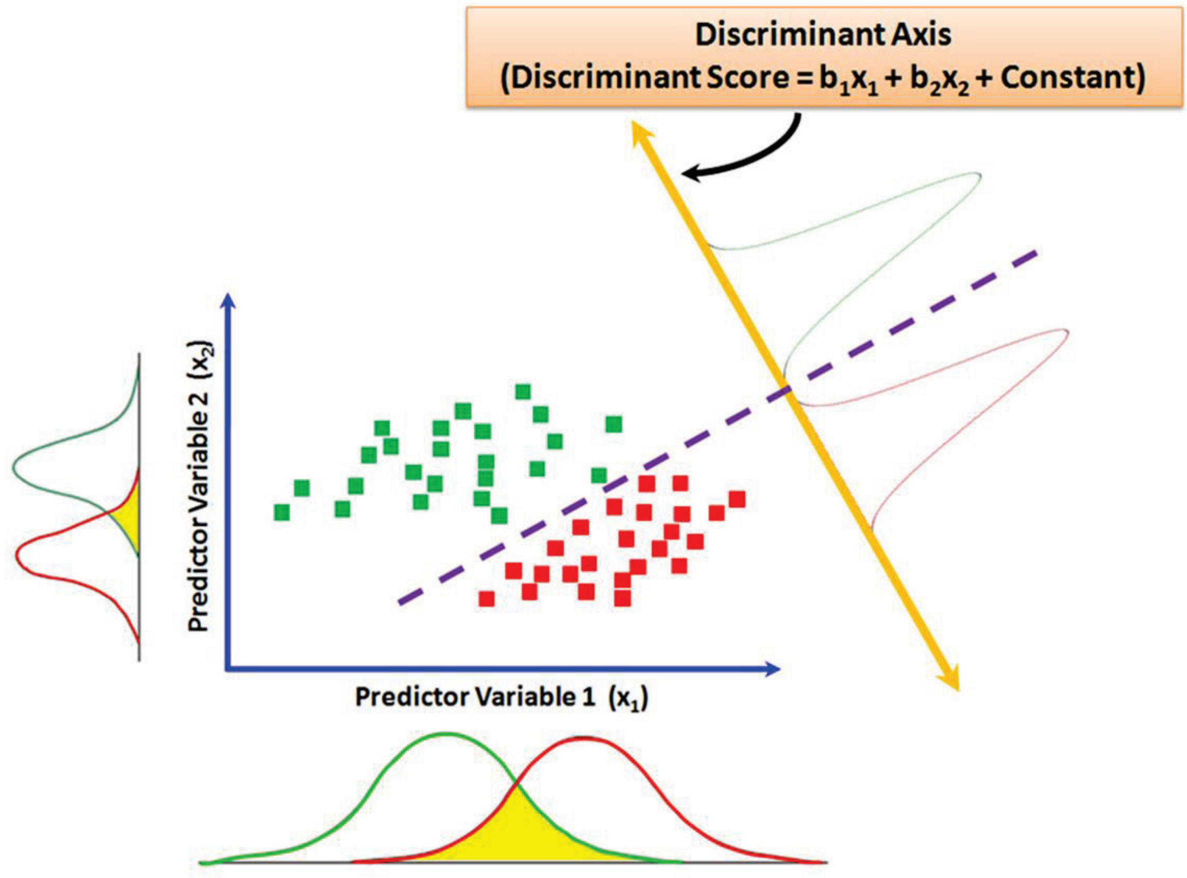

Supplementary Figure S3.2 Graphical representation of discriminant analysis. Scatter plots are shown above for a hypothetical data set made up of two groups and two predictor variables. Clearly, the two groups (shown in green and red dots) can be separated by these two variables, but there is a large amount of overlap on each single axis alone (although x_2 is a "better" discriminating variable than x_1). Obviously, with more than two groups or predictor variables, this graphical approach becomes impractical. It is possible, however, to construct a new axis that represents a new variable, which is a linear combination of x_1 and x_2 in this case (i.e., it is a discriminant function). Provided x_1 and x_2 are good classification variables, discriminant scores can be assigned to each person in each group such that the group distributions do not overlap on this new axis. The discriminant function can then be used as a predictive tool for determining group membership on new subjects who have measurements for the predictor variables but have unknown group membership. (Figure adapted from Burns RB, Burns RA. *Business research methods and statistics using SPSS*. Los Angeles; London: SAGE Publications; 2008).

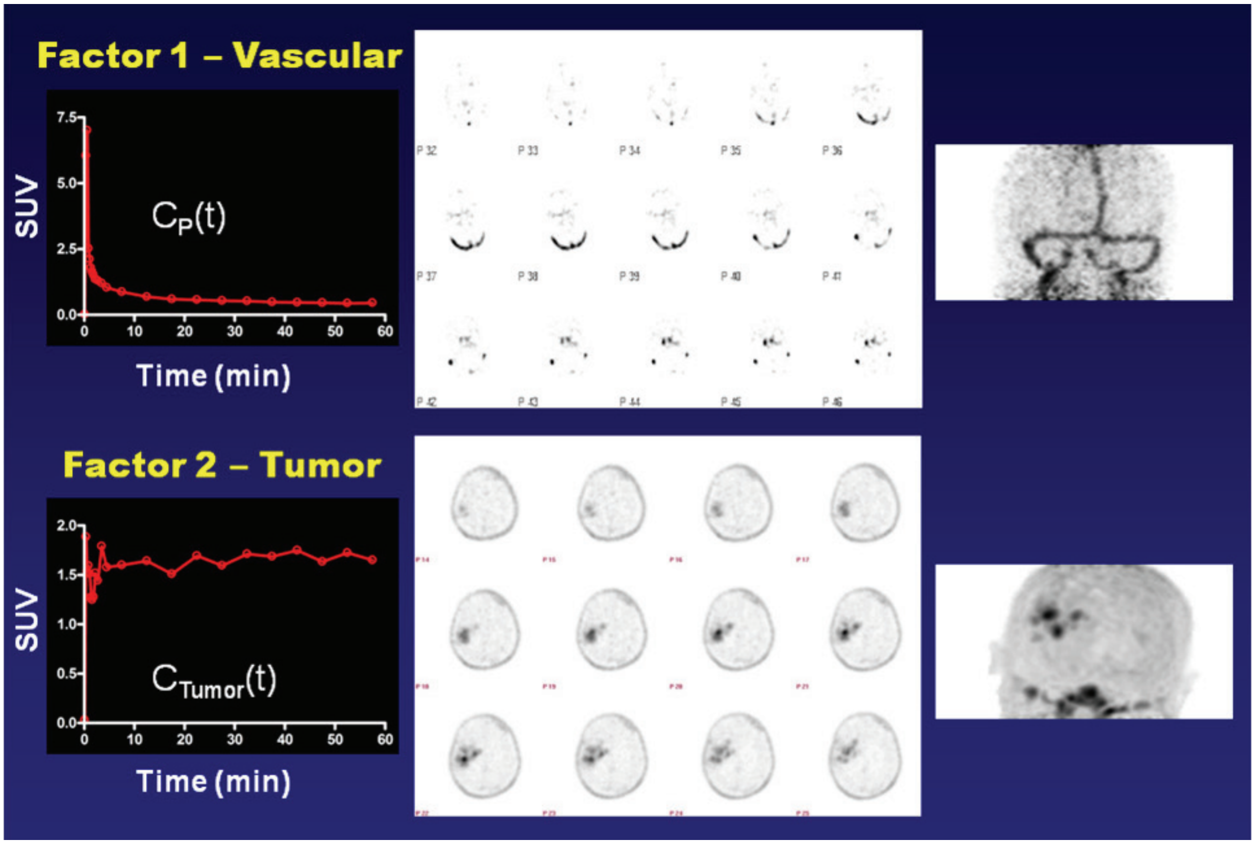

Supplementary Figure S3.3 Vascular and tumor factor images along with their corresponding blood and tumor time-activity curves. The superior sagittal sinus and the left and right transverse sinuses can be seen in the vascular factor image. Note the tumor and normal bone marrow in the tumor factor image. This figure nicely illustrates the different types of biological information provided by a dynamic PET scan at early and late times after tracer injection.

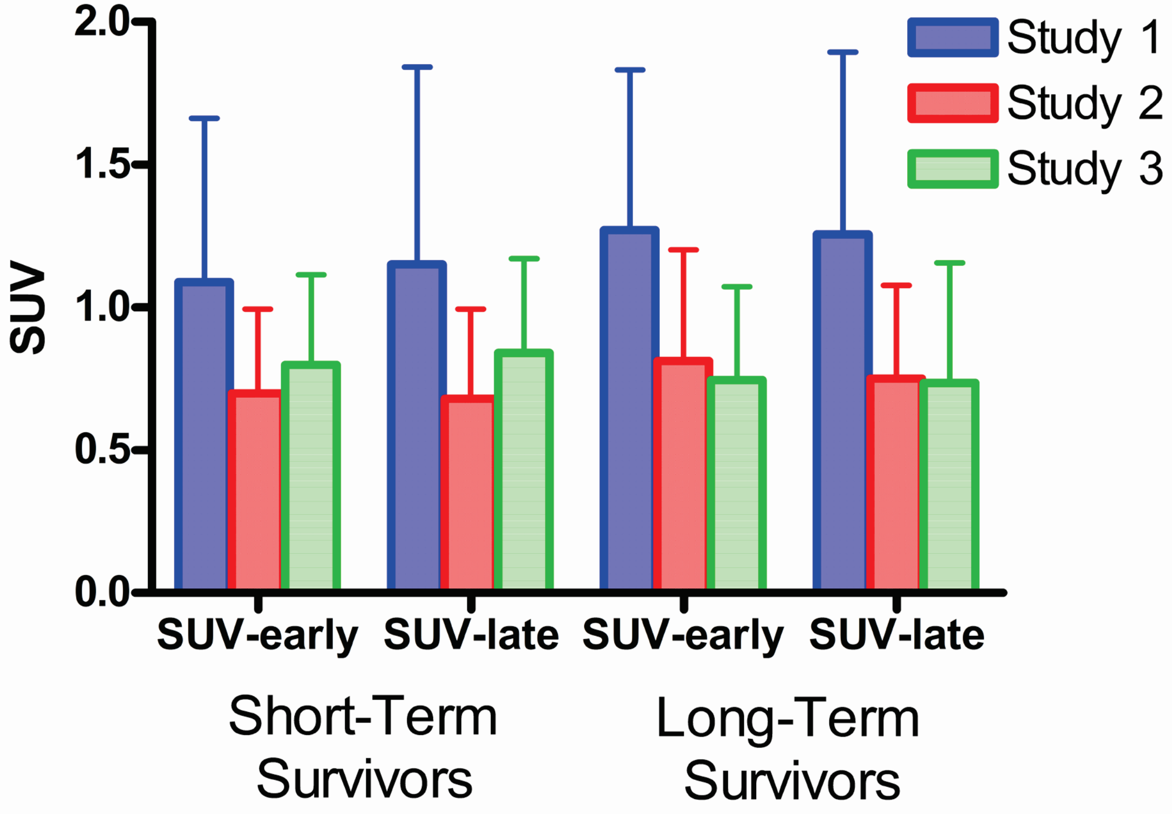

Supplementary Figure S3.4 Mean ^{18}F-FLT SUVs for short-term (Short-OS; *n* = 12) and long-term (Long-OS; *n* = 6) survivors at each of the three study time points. Error bars denote 1 SD. Patients who survived longer tended to have an SUV$_{early}$ (measured from 10-25 min) and SUV$_{late}$ (measured from 50-60 min) that decreased after the first study and continued to decrease after the second study. (Study 1 = Baseline FLT PET, Study 2 = FLT PET at 2 weeks after start of treatment, Study 3 = FLT PET at 6 weeks after start of treatment).

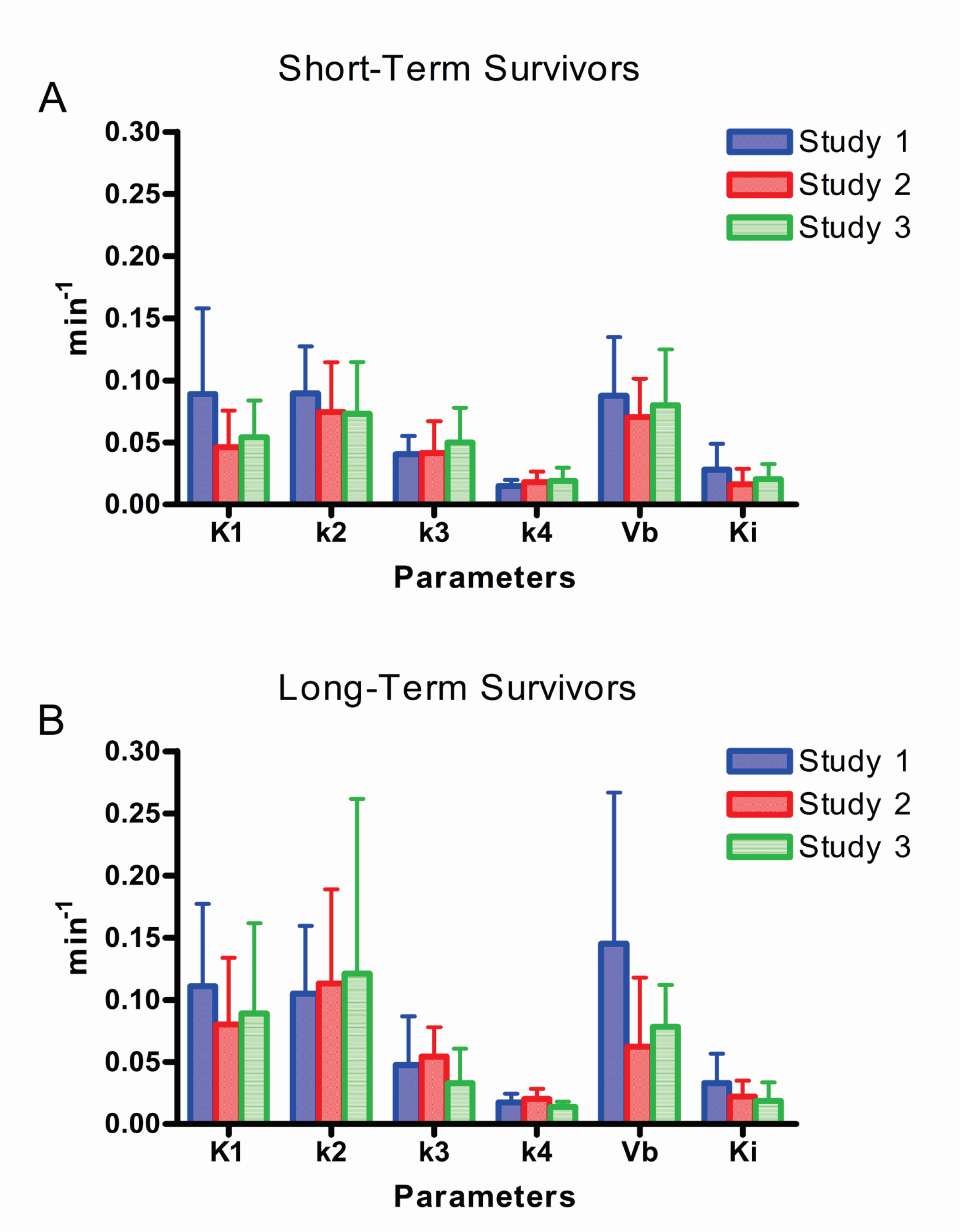

Supplementary Figure S3.5 Mean results per study for the ^{18}F-FLT rate constants ($K_1 - k_4$), tumor blood volume fraction (V_b), and influx rate constant K_i as shown for short-term (Short-OS; *n* = 12) and long-term (Long-OS; *n* = 6) survivors. The dimensions of k_2, k_3 and k_4 are min^{-1}, K_1 and K_i have units of $mL \cdot cm^{-3} \cdot min^{-1}$ and V_b is unitless. Error bars denote 1 SD. Patients who survived longer tended to have a K_i that decreased after the first study and continued to decrease after the second study. (Study 1 = Baseline FLT PET, Study 2 = FLT PET at 2 weeks after start of treatment, Study 3 = FLT PET at 6 weeks after start of treatment).

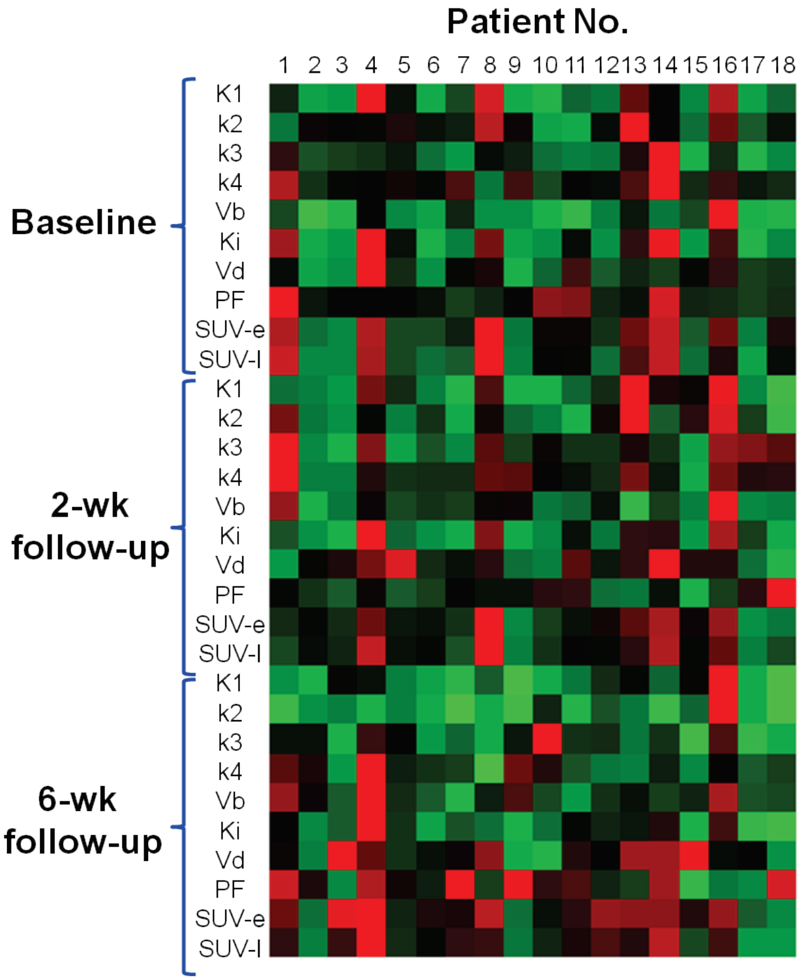

Supplementary Figure S3.6 ^{18}F-FLT kinetic parameter values for all patients at each study time point as visualized in the form of a kinetic microarray. By looking at the kinetic data in this way, one can apply the same statistical techniques as those applied to DNA microarrays. Kinetics from other tracers, if available, could also be integrated as added biological information into the microarray. Kinetic parameter changes between studies could also be presented in this manner.

3.11 SUPPLEMENTARY TABLES

Supplementary Table S3.1 Percentage of change in SUV between each study time point.

		ΔSUV-early (%)			**ΔSUV-late (%)**		
	Patient No.	**S1→S2**	**S1→S3**	**S2→S3**	**S1→S2**	**S1→S3**	**S2→S3**
Short-OS	**1**	-70	-49	70	-79	-55	115
	2	13	-42	-49	16	-35	-44
	3	12	143	116	-4	75	82
	4	-42	-31	19	-40	-26	24
	5	-18	-32	-18	-27	-31	-5
	6	-11	5	18	-1	6	8
	7	-42	-17	42	-40	31	118
	8	-34	-50	-24	-43	-58	-27
	9	-44	-40	6	-44	-36	15
	10	-57	-53	10	-59	-52	18
	11	-45	-32	25	-46	-30	29
	12	3	28	25	0	57	57
	Mean ± SD (*n* = 12)	-28 ± 27	-14 ± 55	20 ± 43	-31 ± 28	-13 ± 45	32 ± 51
Long-OS	**13**	-36	-38	-3	-49	-44	8
	14	-38	-48	-16	-45	-39	12
	15	21	18	-3	-1	-24	-23
	16	-27	-37	-13	-31	-29	3
	17	-42	-26	26	-29	-31	-3
	18	-72	-78	-22	-59	-72	-33
	Mean ± SD (*n* = 6)	-32 ± 30	-35 ± 31	-5 ± 17	-36 ± 20	-40 ± 17	-6 ± 18

S1 = Baseline FLT PET, S2 = FLT PET at 2 weeks after start of treatment, S3 = FLT PET at 6 weeks after start of treatment.

Supplementary Table S3.2 Percentage of change in ^{18}F-FLT kinetic parameters (Baseline → 2 weeks).

	Patient No.	**ΔK_1**	**Δk_2**	**Δk_3**	**Δk_4**	**ΔV_b**	**ΔK_i**	**ΔV_d**	**ΔPF**
Short-OS	**1**	-58	213	26	45	7	-74	-79	-37
	2	-24	-49	-38	-15	0	-13	41	15
	3	-40	-56	-65	-37	-14	-49	45	-15
	4	-54	-3	76	52	-49	-33	-62	46
	5	-49	-56	-65	-20	-33	-57	22	-15
	6	-16	-11	-5	2	-8	-11	-7	5
	7	-76	-59	-2	-32	-61	-55	-54	86
	8	-54	-30	26	255	16	-31	-45	50
	9	-47	-44	-29	31	23	-38	-13	18
	10	-32	43	64	86	-24	-27	-56	7
	11	-42	-2	23	13	22	-35	-47	12
	12	-8	31	20	5	-17	-14	-28	-7
	Mean ± SD (*n* = 12)	-42 ± 19	-2 ± 76	3 ± 46	32 ± 79	-12 ± 27	-36 ± 19	-24 ± 41	14 ± 34
Long-OS	**13**	-17	6	-20	36	-89	-33	-17	-19
	14	-32	-33	-69	-47	-40	-56	44	-35
	15	40	151	10	-49	-67	-29	-35	-49
	16	-33	32	74	39	-54	-17	-53	23
	17	-26	21	370	80	-35	80	-62	143
	18	-86	-81	162	105	-13	-51	-81	246
	Mean ± SD (*n* = 6)	-26 ± 40	16 ± 78	88 ± 160	27 ± 64	-50 ± 27	-18 ± 50	-34 ± 44	52 ± 118

Supplementary Table S3.3 Percentage of change in ^{18}F-FLT kinetic parameters (Baseline → 6 weeks).

	Patient No.	**ΔK_1**	**Δk_2**	**Δk_3**	**Δk_4**	**ΔV_b**	**ΔK_i**	**ΔV_d**	**ΔPF**
Short-OS	**1**	-52	-29	-30	14	9	-52	-32	0
	2	-28	-24	47	126	265	12	-23	56
	3	137	2	-55	-44	5	24	177	-48
	4	-60	-42	86	176	-7	-22	-58	94
	5	-51	-20	20	2	-20	-35	-46	31
	6	-8	-26	-26	8	-22	-7	24	0
	7	-68	-79	55	-30	-84	2	-34	216
	8	-71	-61	-64	-77	-10	-72	-23	-4
	9	-68	-74	7	50	54	-32	-36	111
	10	13	354	281	159	0	2	-73	-9
	11	-20	56	55	-9	-15	-20	-49	0
	12	39	40	60	-20	-29	53	-4	11
	Mean ± SD (*n* = 12)	-20 ± 60	8 ± 116	36 ± 91	30 ± 82	12 ± 86	-12 ± 34	-15 ± 65	38 ± 72
Long-OS	**13**	-40	-48	-56	-50	-53	-48	20	-12
	14	-50	-62	-63	-43	-39	-50	35	-1
	15	105	120	-48	-16	-44	-40	14	-71
	16	5	174	90	3	-62	-22	-59	-25
	17	-17	8	-26	-2	-2	-40	-18	-27
	18	-90	-84	-21	25	21	-74	-67	160
	Mean ± SD (*n* = 6)	-15 ± 67	18 ± 106	-21 ± 57	-14 ± 29	-30 ± 32	-46 ± 17	-13 ± 43	4 ± 80

Supplementary Table S3.4 Percentage of change in ^{18}F-FLT kinetic parameters (2 weeks → 6 weeks).

	Patient No.	**ΔK_1**	**Δk_2**	**Δk_3**	**Δk_4**	**ΔV_b**	**ΔK_i**	**ΔV_d**	**ΔPF**
Short-OS	**1**	14	-77	-44	-22	2	81	226	58
	2	-5	49	139	166	266	30	-46	36
	3	295	133	27	-10	23	143	91	-39
	4	-12	-40	6	82	83	17	11	33
	5	-2	82	240	27	19	49	-56	53
	6	9	-17	-22	6	-15	4	34	-4
	7	33	-49	58	3	-59	126	42	69
	8	-36	-45	-71	-94	-23	-59	41	-36
	9	-39	-53	51	15	25	9	-27	80
	10	67	218	132	39	32	40	-39	-15
	11	38	60	26	-19	-30	22	-3	-11
	12	51	7	34	-24	-14	79	34	19
	Mean ± SD (*n* = 12)	34 ± 88	22 ± 89	48 ± 87	14 ± 64	26 ± 84	45 ± 56	26 ± 77	20 ± 41
Long-OS	**13**	-28	-51	-46	-64	317	-22	45	9
	14	-25	-44	22	7	2	14	-6	53
	15	46	-12	-53	63	71	-16	77	-43
	16	55	107	9	-26	-16	-5	-13	-39
	17	12	-10	-84	-45	50	-66	114	-70
	18	-29	-18	-70	-39	40	-46	79	-25
	Mean ± SD (*n* = 6)	5 ± 38	-5 ± 57	-37 ± 43	-17 ± 46	77 ± 122	-24 ± 29	49 ± 51	-19 ± 44

3.12 REFERENCES

1. Shields AF, Grierson JR, Dohmen BM, et al. Imaging proliferation in vivo with [F-18]FLT and positron emission tomography. *Nat Med.* Nov 1998;4(11):1334-1336.

2. Bading JR, Shields AF. Imaging of cell proliferation: status and prospects. *J Nucl Med.* Jun 2008;49 Suppl 2:64S-80S.

3. Salskov A, Tammisetti VS, Grierson J, Vesselle H. FLT : measuring tumor cell proliferation in vivo with positron emission tomography and 3'-deoxy-3'-[^{18}F]fluorothymidine. *Semin Nucl Med.* Nov 2007;37(6):429-439.

4. Ullrich R, Backes H, Li H, et al. Glioma proliferation as assessed by 3'-fluoro-3'-deoxy-L-thymidine positron emission tomography in patients with newly diagnosed high-grade glioma. *Clin Cancer Res.* Apr 1 2008;14(7):2049-2055.

5. Spence AM, Muzi M, Link JM, et al. NCI-sponsored trial for the evaluation of safety and preliminary efficacy of 3'-deoxy-3'-[^{18}F]fluorothymidine (FLT) as a marker of proliferation in patients with recurrent gliomas: preliminary efficacy studies. *Mol Imaging Biol.* Sep-Oct 2009;11(5):343-355.

6. Jacobs AH, Thomas A, Kracht LW, et al. ^{18}F-fluoro-L-thymidine and ^{11}C-methylmethionine as markers of increased transport and proliferation in brain tumors. *J Nucl Med.* Dec 2005;46(12):1948-1958.

7. Schiepers C, Chen W, Dahlbom M, Cloughesy T, Hoh CK, Huang SC. ^{18}F-fluorothymidine kinetics of malignant brain tumors. *Eur J Nucl Med Mol Imaging.* Jul 2007;34(7):1003-1011.

8. Schiepers C, Chen W, Cloughesy T, Dahlbom M, Huang SC. ^{18}F-FDOPA kinetics in brain tumors. *J Nucl Med.* Oct 2007;48(10):1651-1661.

9. Muzi M, Spence AM, O'Sullivan F, et al. Kinetic analysis of 3'-deoxy-3'-^{18}F-fluorothymidine in patients with gliomas. *J Nucl Med.* Oct 2006;47(10):1612-1621.

10. Schiepers C, Dahlbom M, Chen W, et al. Kinetics of 3'-deoxy-3'-^{18}F-fluorothymidine during treatment monitoring of recurrent high-grade glioma. *J Nucl Med.* May 2010;51(5):720-727.

11. Chen W, Delaloye S, Silverman DH, et al. Predicting treatment response of malignant gliomas to bevacizumab and irinotecan by imaging proliferation with [^{18}F] fluorothymidine positron emission tomography: a pilot study. *J Clin Oncol.* Oct 20 2007;25(30):4714-4721.

12. Galldiks N, Kracht LW, Burghaus L, et al. Use of ^{11}C-methionine PET to monitor the effects of temozolomide chemotherapy in malignant gliomas. *Eur J Nucl Med Mol Imaging.* May 2006;33(5):516-524.

13. Chen W. Clinical applications of PET in brain tumors. *J Nucl Med.* Sep 2007;48(9):1468-1481.

14. Wyss M, Hofer S, Bruehlmeier M, et al. Early metabolic responses in temozolomide treated low-grade glioma patients. *J Neurooncol.* Oct 2009;95(1):87-93.

15. Pope WB, Kim HJ, Huo J, et al. Recurrent glioblastoma multiforme: ADC histogram analysis predicts response to bevacizumab treatment. *Radiology.* Jul 2009;252(1):182-189.

16. Dhermain FG, Hau P, Lanfermann H, Jacobs AH, van den Bent MJ. Advanced MRI and PET imaging for assessment of treatment response in patients with gliomas. *Lancet Neurol.* Sep 2010;9(9):906-920.

17. Ballman KV, Buckner JC, Brown PD, et al. The relationship between six-month progression-free survival and 12-month overall survival end points for phase II trials in patients with glioblastoma multiforme. *Neuro Oncol.* Jan 2007;9(1):29-38.

18. Walsh JC, Padgett HC, Ysaguirre T, inventors; Siemens Medical Solutions USA, Inc., assignee. Method for preparing radiolabeled thymidine having low chromophoric byproducts. U.S. patent 7419653, 2008.

19. Wu HM, Hoh CK, Choi Y, et al. Factor analysis for extraction of blood time-activity curves in dynamic FDG-PET studies. *J Nucl Med.* Sep 1995;36(9):1714-1722.

20. Schiepers C, Hoh CK, Dahlbom M, Wu HM, Phelps ME. Factor analysis for delineation of organ structures, creation of in- and output functions, and standardization of multicenter kinetic modeling. *Proceedings SPIE.* 1999;3661:1343-1350.

21. Sitek A, Di Bella EV, Gullberg GT. Factor analysis with a priori knowledge–application in dynamic cardiac SPECT. *Phys Med Biol.* Sep 2000;45(9):2619-2638.

22. Paproski RJ, Ng AM, Yao SY, Graham K, Young JD, Cass CE. The role of human nucleoside transporters in uptake of 3'-deoxy-3'-fluorothymidine. *Mol Pharmacol.* Nov 2008;74(5):1372-1380.

23. Muzi M, Vesselle H, Grierson JR, et al. Kinetic analysis of 3'-deoxy-3'-fluorothymidine PET studies: validation studies in patients with lung cancer. *J Nucl Med.* Feb 2005;46(2):274-282.

24. Muzi M, Mankoff DA, Grierson JR, Wells JM, Vesselle H, Krohn KA. Kinetic modeling of 3'-deoxy-3'-fluorothymidine in somatic tumors: mathematical studies. *J Nucl Med.* Feb 2005;46(2):371-380.

25. Phelps ME. *PET: molecular imaging and its biological applications*. New York: Springer; 2004.

26. Afifi AA, Clark V, May S. *Computer-aided multivariate analysis*. 4th ed. Boca Raton, Fla.: Chapman & Hall/CRC; 2004.

27. Chan YH. Biostatistics 303. Discriminant analysis. *Singapore Med J.* Feb 2005;46(2):54-61; quiz 62.

28. Phelps ME. Inaugural article: positron emission tomography provides molecular imaging of biological processes. *Proc Natl Acad Sci U S A.* Aug 1 2000;97(16):9226-9233.

29. Jain RK, di Tomaso E, Duda DG, Loeffler JS, Sorensen AG, Batchelor TT. Angiogenesis in brain tumours. *Nat Rev Neurosci.* Aug 2007;8(8):610-622.

30. Chen YL, Eriksson S, Chang ZF. Regulation and functional contribution of thymidine kinase 1 in repair of DNA damage. *J Biol Chem.* Aug 27 2010;285(35):27327-27335.

31. Nimmagadda S, Shields AF. The role of DNA synthesis imaging in cancer in the era of targeted therapeutics. *Cancer Metastasis Rev.* Dec 2008;27(4):575-587.

32. Goodman LS, Brunton LL, Blumenthal DK, Murri N, Hilal-Dandan R. *Goodman & Gilman's The pharmacological basis of therapeutics*. 12th ed. New York: McGraw-Hill Medical; 2011.

33. Szakacs G, Paterson JK, Ludwig JA, Booth-Genthe C, Gottesman MM. Targeting multidrug resistance in cancer. *Nat Rev Drug Discov.* Mar 2006;5(3):219-234.

34. Loscher W, Potschka H. Drug resistance in brain diseases and the role of drug efflux transporters. *Nat Rev Neurosci.* Aug 2005;6(8):591-602.

35. Lamborn KR, Yung WK, Chang SM, et al. Progression-free survival: an important end point in evaluating therapy for recurrent high-grade gliomas. *Neuro Oncol.* Apr 2008;10(2):162-170.

Chapter 4

^{18}F-FLT and ^{18}F-FDOPA PET Kinetics in Recurrent Brain Tumors: A Multi-Tracer Approach

4.1 ABSTRACT

Purpose:

Proliferation markers and amino acid analogs have been studied separately for brain tumor imaging with positron emission tomography (PET). In this longitudinal imaging study, kinetic parameters of the cellular proliferation tracer 3′-deoxy-3′-^{18}F-fluoro-L-thymidine (FLT) and the amino acid probe 3,4-dihydroxy-6-^{18}F-fluoro-L-phenylalanine (FDOPA) were measured before and early after the start of therapy, and were used to predict the overall survival (OS) of patients with recurrent malignant glioma using multiple linear regression (MLR) analysis. It was hypothesized that parameters from both molecular imaging probes together would provide better predictive results than using information from either tracer alone.

Materials and Methods:

High-grade recurrent brain tumors were investigated in 21 patients (11 male and 10 female; ages 26 to 76 years). For both probes, each patient had 3 dynamic PET studies: at baseline, after 2 weeks, and after 6 weeks from the start of treatment. Treatment consisted of biweekly cycles of bevacizumab (an angiogenesis inhibitor) and irinotecan (a chemotherapeutic agent). At each

study, ~3.5 mCi of FLT (or FDOPA) was administered intravenously and dynamic PET images were acquired for 1 hr (or 35 min for FDOPA). A total of 126 PET scans were analyzed. Factor analysis generated factor images, which were used to extract the blood and tumor uptake curves from the dynamic PET images. A three-compartment, two-tissue model was applied to estimate tumor FLT and FDOPA kinetic rate constants using a metabolite- and partial volume-corrected input function. Multiple linear regression analysis was used to model OS as a function of FLT and FDOPA kinetic parameters at each of the 3 studies as well as their relative changes between studies. An exhaustive search of MLR models using three or fewer predictor variables was performed to find the best models. No patient was lost to follow-up.

Results:

Kinetic parameters from FLT alone provided better results in predicting OS than using information from FDOPA alone. Parameters from FLT and FDOPA combined resulted in a better three-predictor MLR model (adjusted $R^2 = 0.83$) than using information from FDOPA alone (adjusted $R^2 = 0.41$), and only marginally different from using information from FLT alone (adjusted $R^2 = 0.82$). Information from standardized uptake values (either from FLT alone, FDOPA alone, or both together) gave suboptimal predictive results (best adjusted $R^2 = 0.25$).

Conclusions:

For recurrent malignant glioma treated with bevacizumab and irinotecan, FLT kinetic parameters taken early after the start of treatment (absolute values and their associated changes) can provide sufficient information to predict OS with reasonable confidence using MLR. The slight increase in accuracy for predicting OS with a combination of FLT and FDOPA PET information may not necessitate the additional acquisition of FDOPA PET for therapy monitoring in recurrent glioma patients. Whether the combined information from FLT and FDOPA PET images may help in the prediction of OS in patients with newly diagnosed glioma is motivation for a future study.

4.2 INTRODUCTION

In the United States, an estimated 69,720 new cases of primary brain and central nervous system tumors are expected to be diagnosed in 2013 (*1*). At least one-third of these tumors will be malignant and associated with a high mortality rate, especially among patients diagnosed with a glioblastoma (*1, 2*). Gliomas, which are tumors that arise in the glial cells of the brain, account for approximately 30% of all primary brain and other central nervous system tumors, and 80% of those that are malignant tumors (*1*). Glioblastoma accounts for the majority of gliomas and is the most frequent malignant primary brain tumor in adults (*1*). The life expectancy of a patient diagnosed with glioblastoma remains 12 to 14 months, only slightly better than it was a century ago (*3*). With such a poor prognosis, the ability to accurately predict treatment failure early during therapy would have immense value in clinical practice. Information from imaging technologies can play an important role in this effort.

Positron emission tomography (PET) is a powerful, non-invasive imaging technique used to visualize and quantify various biochemical and physiological processes in living subjects (*4-11*). PET employs positron-emitting elements such as carbon-11, nitrogen-13, oxygen-15 and fluorine-18, which are inserted into biologically active compounds and then injected into living subjects to interrogate molecular processes in health and disease (*4-7*). The resulting gamma ray emissions from the subject are collected by the PET camera and reconstructed into tomographic images. The temporal resolution of the PET imaging system permits external measurements of the tracer kinetics in tissue. When utilized with an appropriate tracer compartmental model, regional tissue function such as blood flow, membrane transport, substrate metabolism, enzyme activity and receptor-ligand interactions can be quantified (*5, 12, 13*). Thus, it is one of the unique and extraordinary beauties of PET that the detection of chemical abnormalities in tissue and the assessment of restoration of chemical function can be captured with this imaging technology.

Magnetic resonance imaging (MRI) is currently the modality of choice for diagnosing and monitoring brain tumors (*14*). MRI, however, is not without its pitfalls. The ability of MRI to differentiate between treatment-induced changes and residual or recurrent tumor is limited (*15, 16*). The determination of treatment response with MRI can also be difficult, especially after radiochemotherapy or anti-angiogenic therapy (*17*). It is in these and other areas that the power of functional information from PET can help.

Several PET tracers have been used to study various aspects of brain tumor metabolism (*11, 18*). Among them are 2-deoxy-2-^{18}F-fluoro-D-glucose (FDG) for imaging glucose uptake, 3′-deoxy-3′-^{18}F-fluorothymidine (FLT) for imaging cellular proliferation, and 3,4-dihydroxy-6-^{18}F-fluoro-L-phenylalanine (FDOPA) for imaging amino acid transport. In the study of FDG PET imaging for brain tumors, however, several studies have demonstrated diagnostic limitations (*19, 20*). For example, due to the high physiologic glucose metabolism of normal gray matter, the detectability of tumors with only modest increases in glucose metabolism, such as in low-grade tumors and in some cases recurrent high-grade tumors, has proved to be difficult (*21*). The uptake of FDG in low-grade tumors is usually similar to that of normal white matter, and the uptake in high-grade tumors can be less than or similar to that of normal gray matter, thus decreasing the sensitivity of lesion detection (*21, 22*). In addition, the specificity of FDG in tumor detection is sometimes limited by uptake in non-tumor regions of inflammation and at previous tumor sites exhibiting residual inflammation (*23*). FLT PET, on the other hand, has been shown to be more sensitive than FDG for detecting recurrent high-grade brain tumors (likely due to the low background uptake of FLT in normal brain tissue), correlated better with the *ex vivo* Ki-67 proliferation marker, and was a more powerful predictor of tumor progression and survival than FDG PET (*22*). FLT PET has also been shown to be more predictive than MRI for early treatment response in recurrent malignant glioma (*15*).

FDOPA PET offers the advantage of detecting primary and recurrent high- and low-grade brain tumors, and its uptake correlates with the grade of newly diagnosed glioma (*16, 24*). The transport of FDOPA also does not depend on a breakdown of the blood-brain barrier (BBB) (*16, 21*). In head to head comparisons, FDOPA was shown to be more accurate than FDG PET for imaging of low-grade tumors and in evaluating recurrent tumors (*25*). It was also found that FDOPA PET might prove especially useful for distinguishing tumor recurrence from radiation necrosis (*25*).

Our group at UCLA has previously shown that in patients with recurrent glioma on bevacizumab and irinotecan therapy, relative changes in FLT kinetic parameters (before and early after the start of treatment) were able to correctly classify patients into one of two groups: those that lived less than 1 y and those that lived greater than or equal to 1 y (*26*). In this study, 21 patients with recurrent high-grade glioma were given both FLT and FDOPA at baseline and at two time points early after the start of therapy. FLT and FDOPA kinetic parameters were then estimated and used to predict each patient's overall survival (OS) using multiple linear regression analysis. It was hypothesized that parameters from both probes together would provide better predictive results than either one alone.

4.3 MATERIALS AND METHODS

4.3.1 Patients

Twenty-one patients with recurrent high-grade glioma were investigated in this study. There were 11 men and 10 women, with a median age of 59 y at the start of the study (range: 26-76 y). All gliomas were confirmed by histopathology and graded according to the World Health Organization scheme. Twenty patients had glioblastoma multiforme (GBM; grade IV) and one patient had anaplastic astrocytoma (AA; grade III). Each patient had previously undergone surgical resection followed by adjuvant treatment with chemotherapy and/or radiation. Written informed consent was obtained from all patients in accordance with the procedures of the Office of the Human Research Protection Program at UCLA. An overview of the population data is shown in Table 4.1.

4.3.2 Treatment

Treatment consisted of biweekly cycles of bevacizumab (Avastin; Genentech) and irinotecan (Camptosar; Pfizer). All patients had their recurrent disease confirmed on MRI before treatment was started. Bevacizumab is a full-length recombinant humanized monoclonal antibody that was designed to bind and inhibit the vascular endothelial growth factor. It was given accelerated approval by the U.S. Food and Drug Administration in May 2009 for the treatment of recurrent GBM. Irinotecan is a prodrug that is converted by esterases (primarily in the liver) to its more potent phenolic form, SN-38. Both the parent drug and SN-38 can bind to topoisomerase I after it complexes with DNA, preventing repair of single-strand breaks caused by topoisomerase I. This complex of irinotecan or SN-38 with the topoisomerase and DNA is cytotoxic to the cell, which is both its therapeutic mechanism of action and the mechanism of action for its toxicity (*27*). Treatment with both agents continued until the patient experienced any signs of clinical or radiographic disease progression. All 21 enrolled patients finished the first course of 6 weeks. No patient was lost to follow-up.

4.3.3 Outcome Measurements

Patients had regular follow-up at the UCLA Neuro-Oncology Clinic, and the date of progression was diagnosed by the neuro-oncologist on the basis of physical examination, clinical evaluation, and imaging. Each patient's disease status was evaluated and monitored using gadolinium-enhanced and non-enhanced MRI within 1 week before and at approximately 6 week intervals after the start of treatment. Progression-free survival (PFS) was calculated from the date of baseline FLT PET to the date of disease progression. OS was calculated from the date of baseline FLT PET to the date of patient death. All patients were followed until death.

4.3.4 ^{18}F-FLT and ^{18}F-FDOPA Synthesis

The chemical structures of FLT and FDOPA are shown in Figure 4.1. FLT was synthesized according to the method developed by Walsh and colleagues (*28*). This method uses an FLT precursor that produces low amounts of chromophoric byproducts during the deprotection step. The chemical synthesis also uses a short number of steps and produces an adequate yield. FDOPA was synthesized according to the procedure pioneered by Barrio and colleagues (*29*). In this method, a protected aryl substituted trialkyl tin derivative was synthesized as an organic precursor for the preparation of FDOPA. The specific activity for FLT was more than 1,000 Ci/mmol, while the specific activity for FDOPA was 1-5 Ci/mmol. The maximum radiochemical yield for FLT and FDOPA was approximately 30% and 25%, respectively. The chemical and radiochemical purities for both imaging agents were more than 99%. The final products were sterile and pyrogen free.

4.3.5 Imaging Protocol

For each patient, baseline FLT and FDOPA PET scans [study 1 (S1)] were carried out within 1 week before the start of treatment, and follow-up FLT and FDOPA PET scans were carried out at 2 weeks [study 2 (S2)] and then again at 6 weeks [study 3 (S3)] after the start of treatment (Figure 4.2). A total of 126 PET scans were analyzed. PET imaging was carried out with an ECAT EXACT HR+ scanner (Siemens/CTI). The intrinsic spatial resolution of the scanner was 4.5 mm in full-width at half-maximum (FWHM) in the center of the field-of-view (FOV). Using a set of external rotating ^{68}Ge/^{68}Ga rod sources, a transmission scan was first acquired for 5 minutes in 2-dimensional mode to correct for photon attenuation. Shortly thereafter, approximately 3.5 mCi of FLT (or FDOPA) was administered intravenously as a bolus, and dynamic PET images were acquired in 3-dimensional mode for 1 hour (or 35 minutes for FDOPA).

The emission scan was reconstructed with iterative techniques using the maximum likelihood expectation maximization algorithm accelerated with ordered subsets (*30, 31*). After the reconstruction step, the image was smoothed with a 3-dimensional Gaussian filter (FWHM = 4 mm). The final reconstructed PET image had a spatial resolution of 6.0 mm in FWHM and was composed of an image matrix that consisted of $128 \times 128 \times 63$ voxels, with each voxel having near isotropic dimensions ($2.41 \times 2.41 \times 2.43$ mm^3). The study protocol was approved by the UCLA Institutional Review Board, the UCLA Medical Radiation Safety Committee and the UCLA Radioactive Drug Research Committee.

4.3.6 Factor Analysis

Factor analysis (FA) is a data-driven technique that identifies the predominant kinetic patterns present in a dynamic study (*32-35*). This essentially involves classifying the voxel time-activity curves into a preselected number of factors such that each factor represents a fundamental pattern of kinetic behavior. FA calculates the extent to which each voxel's time-activity curve corresponds to each factor curve. Voxels are assigned a coefficient (or weight) for each factor. Factor images can then be produced by storing the values of the coefficients in each volume element. When displayed, the color scale can depict the extent to which each voxel exhibits a factor's typical kinetic pattern.

In the case of a dynamic PET study, the value $x_{ij}(t)$, for each voxel, can be given by:

$$x_{ij}(t) = a_{ij}F_1(t) + b_{ij}F_2(t) + c_{ij}F_3(t) + \dots k_{ij}F_n(t) \qquad \text{Eq. 4.1}$$

where F_n represents the set of factor curves and a_{ij}, b_{ij}, c_{ij}, etc. are the factor coefficients (or weights) at each voxel location (ij). A coefficient close to 1 for a given factor means the voxel exhibits the typical kinetic pattern for that factor, whereas a coefficient close to 0 means that the voxel exhibits very little of that factor's typical kinetic behavior.

In our implementation, three factor images (representing the brain vessels, tumor, and the rest) were generated (see Chapter 3, Supplementary Figure S3.3). A 50% threshold of the maximum value on the vascular factor image was used to create a 3-dimenstional mask that would extract the blood time-activity curve when overlaid on the dynamic PET image. The time-activity curve of the tumor was extracted similarly, but with a 75% threshold, so as to capture the most active part of the tumor while excluding any necrotic zones (Figure 4.3). The blood and tumor time-activity curves were then used for kinetic modeling analysis. It is important to note that the factor curves themselves were not used in the kinetic modeling analysis but were only calculated to create the factor images. The tumor was usually seen on factor 2 images and, if not, was found on factor 3 images. FA was not able to separate the arterial vessels from the venous vessels, as the image acquisition duration of the first 8 frames for both tracers was 15 s. The extraction fraction for FLT and FDOPA in brain tissue was low, and the arterial-venous difference was small; therefore, our input function was a close approximation of the local arterial blood curve.

4.3.7 ^{18}F-FLT Compartmental Model

The compartmental model for FLT is shown in Figure 4.4. Briefly, the model assumes a transport step of FLT from the vascular space into the tissue space. There is no partitioning in the vascular space, and it has been previously shown that there are no differences in the FLT activity concentrations between plasma and whole blood (*36, 37*). In the tissue space, there is an exchangeable compartment (with intact FLT nucleosides) and a compartment with phosphorylated FLT (mono-, di-, and triphosphate FLT nucleotides). The phosphorylated products of FLT are retained in tissue at a rate proportional to thymidine kinase 1 (TK1) activity (*36*). TK1 is a cell cycle regulated enzyme with a several fold increased expression during the S phase of the cell cycle (*38*). After completion of mitosis, TK1 levels quickly return to basal levels (*23*). The up-regulation and down-regulation of TK1 are controlled by distinct regulatory and post-translational mechanisms (*23*, *39*). Furthermore, the ATP level is important for the phosphorylation of FLT. ATP initiates a transition from a dimer to a tetramer structure of TK1, which is about 20-fold more effective regarding the phosphorylation of FLT (*40*). Therefore, FLT can reflect cell proliferation, if there are no major differences in ATP levels (*40*). Very few to no FLT nucleotides are incorporated into DNA (*40*). FLT can be metabolized by the liver to FLT-glucuronide, which is present only in the vascular space (i.e., it is not transported into the brain-tissue compartment) (*40*). It is also possible for FLT and FLT-glucuronide to cross the red blood cell membrane via generalized nucleoside transporters (*37*). Thymidine is used as the structural blueprint for FLT because it contains the pyrimidine base thymine, which is uniquely incorporated into DNA and not RNA.

Kinetic modeling yields estimates of four rate constants (K_1, k_2, k_3, and k_4) and a fifth parameter, the blood volume (V_b) in the tumor. From these five estimated constants, the values of certain physiologically important macro-parameters can be derived. The overall flux of FLT into cells (K_i) is calculated as $K_1 \times k_3/(k_2+k_3)$, the volume of distribution (V_d) is calculated as $K_1/(k_2 + k_3)$, and the phosphorylated fraction (PF) is calculated as $k_3/(k_2 + k_3)$. The PF is the fraction of FLT transported via K_1 that ends up in the phosphorylated FLT pool. The dimensions of k_2 , k_3, and k_4 are min^{-1}, K_1 and K_i have units of $mL \cdot cm^{-3} \cdot min^{-1}$, V_b and V_d are in $mL \cdot cm^{-3}$, and PF is unitless.

4.3.8 ^{18}F-FDOPA Compartmental Model

The compartmental model for FDOPA kinetics in brain tumors is shown in Figure 4.5. The model was adapted from the classic paper written by Huang *et al.* (*41*), which focused on FDOPA kinetics in the striatum and cerebellum of normal human subjects. In brief, the model assumes transport of FDOPA from the vascular space into the tissue space. FDOPA is transported between plasma and tissue through membrane channels specific for large neutral amino acids (*42*). In the tissue space, there is an exchangeable compartment (with unbound FDOPA) and a compartment with bound FDOPA (*42*). In addition, FDOPA is converted by catechol-O-methyl transferase (COMT) in the peripheral tissues (e.g., liver, kidneys, and lungs) to L-3,4-dihydroxy-6-fluoro-3-O-methylphenylalanine (OMFD), which can cross the blood-brain barrier (BBB) bidirectionally (*43*). Metabolism of FDOPA to OMFD inside the brain has been demonstrated to be negligible (*41*). In the striatum, FDOPA is converted to 6-fluorodopamine (FDA) by the enzyme aromatic amino acid decarboxylase (AAAD), which is represented by the third compartment. Whereas the third compartment is well defined for the striatum (caudate and putamen), it is unclear for tumors (*42*).

Kinetic modeling yields estimates of four rate constants (K_1, k_2, k_3, and k_4) from which the influx rate constant K_i, V_d, and sequestration fraction (SF) can be calculated. The SF is the fraction of FDOPA transported via K_1 that is sequestered in the amino acid pool of the tumor, which is larger in tumors than in normal tissue. The blood volume in tissue can be estimated as a fifth parameter.

4.3.9 Standardized Uptake Value Measurements

Standardized uptake value (SUV) is a semi-quantitative index that is calculated by normalizing the measured tissue activity concentration to the patient's body weight and injected dose (*44*). SUV was calculated at both early and late time points in this study. For FLT, SUV-early and SUV-late were measured from 10-20 and 50-60 minutes, respectively. For FDOPA, SUV-early and SUV-late were measured from 10-20 and 25-35 minutes, respectively.

4.3.10 Metabolite and Partial Volume Corrections

In the present study, no metabolites of FLT and FDOPA were measured in blood. Instead, theoretical curves were fitted to FLT and FDOPA metabolite data that were pooled from previous publications (*36, 45, 46*). The fitted curves were then used as an approximation of the expected metabolite fraction over time for each individual's blood curve.

For FLT, the measured metabolite data in lung cancer and colorectal cancer were extracted from previous publications (*36, 45*). Because the metabolite data from these two studies appeared similar, they were pooled together and fitted with a theoretical curve, as an approximation of the metabolite fraction over time. The equation of the metabolite fraction for FLT was calculated as $0.42\times[1-\exp(-0.029\times T)]$, where T is the time (in minutes) after injection.

For FDOPA, correcting for metabolites in blood was a little more complicated. OMFD can cross in and out of red blood cells and thus occupies the total blood volume (*41, 46*). On the other hand, FDOPA and other ^{18}F labeled metabolites of FDOPA (collectively referred to as METS from here on) do not cross the red blood cell membrane and are confined to the plasma space (*41, 46*) (see Appendix Figure A4.1). We extracted the measured metabolite fractions of plasma radioactivity for OMFD and METS from the publication of Huang *et al.* (*46*) and fitted exponential curves to them (see Appendix Figure A4.2). Because no plasma samples for FDOPA and its metabolites were assayed, we had to convert the total ^{18}F activity concentration in whole blood (which we measured with dynamic PET) to the total FDOPA activity concentration in plasma. It was only after this conversion that we could input the time-activity curve of our authentic FDOPA tracer in plasma into our FDOPA kinetic model (see Appendix Figure A4.3). The conversion was done using derived mathematical equations as shown in the Appendix. We used the data by Huang *et al.* (*46*) because this was the only data found in the literature that measured OMFD and METS in a patient without carbidopa pretreatment, similar to what was done in our study. Carbidopa is a sentry drug that is sometimes given before an

FDOPA PET imaging study so that FDA formation is blocked in the peripheral tissues. Carbidopa pretreatment thus increases the bioavailability of FDOPA in plasma.

To address the effects of partial volume (*4*) (i.e., when a small object or structure being imaged appears to have a lower activity concentration in comparison to a larger one of equal activity concentration), we determined the recovery coefficient experimentally using commercially available intravenous tubings to simulate the size of the brain vessels. The measured recovery coefficient was plotted as a function of tubing diameter for our PET system (*40*). The size of the transverse sinuses was estimated to be 7−10 mm, and as a result, a recovery coefficient of 0.7 was chosen to convert the image-based measured blood time-activity curve to the input function. Because the tumors were relatively large (>15 mm) compared to three times the FWHM of the PET scanner, the recovery coefficient of the output function was set to unity (*40*).

4.3.11 Statistical Analysis

Multiple linear regression (MLR) was used to model OS as a function of FLT and FDOPA kinetic parameters as well as their associated changes after the start of therapy. In MLR, we attempt to model the relationship between a single outcome variable and two or more explanatory variables by fitting a linear equation to the observed data (*47*). It has been recommended that no more than one predictor variable for every five observations should be included in the MLR model (*48*). Therefore, we limited our MLR models to three or fewer predictor variables because our sample size ($n = 21$) was relatively small and we did not want to overfit the data. OS was chosen as the outcome variable in the regression analysis because it is the gold standard endpoint for demonstrating clinical efficacy; OS is unequivocal, easily measured and is not subject to investigator interpretation. Furthermore, because measurements were made on the same individual at three different time points, the Wilcoxon signed-rank test was used to assess whether the median of the differences in the paired data were significantly different from zero. Pearson and Spearman correlations were computed to assess significant associations between OS and the rest of the variables. All statistical analyses were performed using SPSS (version 19.0; IBM Corporation) and SAS (version 9.2; SAS Institute) software. The results are reported as the mean ± SD (unless otherwise noted) and are regarded as statistically significant if $P < 0.05$.

4.4 RESULTS

4.4.1 Outcome Analysis

Table 4.1 summarizes the clinical characteristics of the 21 patients. At the time of this writing, all patients had died and therefore all imaging and clinical variables were known. The mean ± SD of the true OS in this sample was 401 ± 252 d (13.4 ± 8.4 months) and the range was 81–1054 d (2.7 months – 2.9 y). The mean ± SD of PFS was 183 ± 156 d and the range was 42–588 d. The median OS and PFS for the entire sample were 364 days (12.1 months) and 135 days (4.5 months), respectively. Of the patients with a GBM diagnosis at recurrence, 17 patients had a primary (or de novo) GBM and 3 patients had a secondary GBM (i.e., when a low grade glioma transforms into a GBM over time). The mean age of the de novo GBM patients was 58 y, whereas the mean age of the secondary GBM patients was 33 y. In this cohort, OS and PFS were shown to be significantly correlated (Pearson $r = 0.85$, $P<0.0001$ and Spearman's $\rho = 0.69$, $P<0.001$).

4.4.2 ^{18}F-FLT and ^{18}F-FDOPA Data Analysis

The percent change in FLT and FDOPA kinetic parameters from S1→S2, S1→S3 and S2→S3 are shown in Supplementary Tables S4.1–S4.3. The percent change between any two studies could also be written as the ratio of the two studies minus one. For example, $(S2-S1)/S1=(S2/S1)-1$, $(S3-S1)/S1=(S3/S1)-1$ and $(S3-S2)/S2=(S3/S2)-1$. In the MLR analysis, we chose to input only the ratio portion of the percent change (i.e., neglecting the minus one), so that our inputs were greater than zero and not negative; this was done for convenience purposes. Additional information on FLT and FDOPA kinetic parameters at each of the three studies is listed in Supplementary Tables S4.4–S4.15. Measured and model fitted tumor time-activity curves for representative FLT and FDOPA PET studies are shown in Figure 4.6.

Figure 4.7 shows FLT PET images for a long-term survivor and two short-term survivors at baseline, and after 2 and 6 weeks from the start of treatment. Figure 4.8 shows similar images for the same set of patients but with FDOPA PET. Sample FDOPA time-activity curves of the tumor, striatum, and cerebellum at a baseline study are shown in Figure 4.9.

Bar graphs showing the sample mean ± standard error of the mean (SEM) at each of the three studies for various FLT kinetic and SUV parameters are plotted in Figures 4.10 and 4.11. For FDOPA, this is shown in Figures 4.12 and 4.13.

4.4.3 Multiple Linear Regression Analysis

Kinetic parameters from FLT alone provided better results in predicting OS than using information from FDOPA alone (Table 4.2). Parameters from FLT and FDOPA combined resulted in a better MLR model (adjusted $R^2 = 0.83$) than using information from FDOPA alone (adjusted $R^2 = 0.41$), and not significantly different from using information from FLT alone (adjusted $R^2 = 0.82$). Information from standardized uptake values (either from FLT alone, FDOPA alone, or both together) gave suboptimal predictive results (best adjusted $R^2 = 0.25$). For each probe, pooling parameter values (at each of the 3 study time points) along with their associated changes between studies resulted in a better regression model than using information provided by them alone (Table 4.2).

The partial regression coefficients for the MLR models when using information from FLT alone, FDOPA alone, and FLT and FDOPA combined are listed in Tables 4.3, 4.4, and 4.5, respectively. All of these models passed various regression diagnostics such as tests for multicollinearity, normality of the residuals, and constant error variance. The predictive results of the best three-parameter MLR model that uses only FLT kinetic information (MLR-1) are shown as scatter plots in Figure 4.14 and as bar graphs (with error bars) in Figure 4.15. The root mean square error for this model was 106 days (Table 4.3). To put the MLR results in perspective, if the sample mean was used for predicting the OS of every patient (and any new patient with a recurrent brain tumor who is undergoing treatment with bevacizumab and irinotecan), then each of these individuals would have a predicted OS of 401 ± 252 days (13 ± 8 months); with 1 SD, this prediction is anywhere from 149-653 d (5-21 months) (see Figure 4.16).

4.5 DISCUSSION

To our knowledge, this is the first longitudinal study to investigate and compare FLT *and* FDOPA kinetic parameters in patients with recurrent malignant glioma before and early after the start of therapy. In this study, we aimed to develop a multiple linear regression model to predict

OS as a continuous variable using information provided to us by two molecular imaging probes. Survival predictions are critical elements in the management of brain tumor patients, especially when the clinical course for glioblastoma is rapid and fatal.

We found that kinetic parameters from FLT alone provided better results in predicting OS than information from FDOPA alone when inputted into an MLR model that used a maximum of three predictor variables. This result seems to agree with findings from previous clinical investigations that were performed separately with FLT and FDOPA PET (*24, 49*). Yamamoto *et al.* reported that in patients with recurrent glioma, FLT uptake (calculated as tumor-to-normal ratio) was significantly correlated with tumor proliferative activity (*49*), as measured by the *ex vivo* Ki-67 tumor proliferation index. The Ki-67 antigen, which is targeted by the MIB-1 antibody, is expressed only in proliferative stages of the cell cycle (*21*). Fueger *et al.* found that FDOPA uptake (expressed as SUV) correlated significantly with the Ki-67 tumor proliferation index in newly diagnosed glioma but not in recurrent glioma (*24*). Although FDOPA PET information did not provide great results in predicting the OS of recurrent brain tumor patients using an MLR model, it might still offer other advantages such as capturing the extent of the tumor or for its use in tumor diagnosis. Whether the combined information from FLT and FDOPA PET images may help in the prediction of OS in patients with newly diagnosed glioma remains to be investigated.

In this study, the parameters from FLT and FDOPA combined resulted in a better MLR model (adjusted $R^2 = 0.83$) than using information from FDOPA alone (adjusted $R^2 = 0.41$), and not markedly different from using information from FLT alone (adjusted $R^2 = 0.82$). This led us to conclude that FLT kinetic parameters taken early after the start of treatment may provide sufficient information alone to predict OS with reasonable confidence using a multivariate regression analysis. The marginal increase in accuracy for predicting OS with a combination of FLT and FDOPA PET probes may not warrant the additional acquisition of FDOPA PET scans in a clinical setting where treatment response is being assessed in patients with recurrent glioma.

The MLR model that used the kinetic information from FLT alone (Table 4.3) revealed that patients that tended to live longer had a smaller absolute value in their tumor volume of distribution at 2 wks, a larger k_4 ratio from baseline→2 wks, and a larger k_2 ratio from 2 wks→6 wks when compared to short-term survivors. This seems to indicate that, in the tumors of the long-term survivors, the change in the dephosphorylation from baseline→2 wks (right after start of therapy) was more positively increased, the change in the efflux of FLT back into the plasma was more positively increased from 2 wks→6 wks (the rebound phase), and the volume of distribution of the tumor at 2 wks was smaller than that of the short-term survivors. Taken together, these results seem to suggest that the tumors of the long-term survivors may not be cycling through the cell cycle as much as the short-term survivors, or that the tracer goes in and out of the cell without doing anything inside. It must be kept in mind that although TK1 activity is a requirement for the accumulation of FLT, retention is dependent on nucleoside/nucleotide efflux and the retrograde metabolism of FLT nucleotides (*50, 51*).

The MLR model that used kinetic information from FDOPA alone (Table 4.4) revealed that patients that tended to live longer had a smaller absolute value in their sequestration rate constant k_3 at the baseline study when compared to short-term survivors, a smaller FDOPA tumor volume of distribution at the baseline study when compared to short-term survivors, and a more negative change in their K_1 membrane transport from 2 wks→6 wks (the rebound phase) than the short-term survivors. The relative demand for amino acids was thus generally lower in the tumors of the long-term survivors at baseline (before treatment) and the time period from 2 wks→6 wks, when multiple treatment infusions had already been administered.

In the MLR analysis, PFS was not entered as a possible predictor variable in any of the MLR models because we wanted to use only information available to us at the end of 6 weeks, which, for the most part, was the PET information from the dynamic FLT and FDOPA PET images. We did not want the MLR model to be dependent on the time it took to determine the PFS, which for most patients in our study was more than 6 weeks.

The predictor variables in this study were different from our *Clinical Cancer Research* article (*26*) because the aims of these two studies were different. In the *Clinical Cancer Research* article (*26*), we wanted to classify patients into one of two OS groups using discriminant analysis, while in this study we wanted to predict OS as a continuous outcome variable. The number of patients in this study was also larger than our *Clinical Cancer Research* investigation (*26*).

One of the limitations of this study was that we did not measure metabolite data from the patients but instead used theoretical curves as an approximation of the metabolite fractions over time. This can be a problem if there are fluctuations in the metabolite fractions due to impaired liver function as a result of chemotherapy (i.e., the greater the liver impairment, the more presence of the authentic tracer and the less presence of its metabolic products in plasma). Future work will try to address some of these issues by analyzing the data in a different way. One such approach is to use the reference tissue model (*52, 53*). If a brain region can be identified, which is devoid of specific binding, the time-activity curve for this "reference region" can be used as an indirect input function for the target region (*54*). An advantage of this method over “classical” compartmental methods is that no metabolite correction is needed (*54*). This is because the input function in these simplified reference tissue models can be built into the model itself, utilizing the fact that different tissue regions are exposed to the same input function. Another limitation of this study was the short acquisition time of the FDOPA PET scans (35 min). If we were able to measure out to 75 or 90 min, our MLR results for FDOPA may have yielded better predictive results because the shape of the descending portion of the tumor uptake curve can provide additional information (*42*).

Collectively, this study has demonstrated that the use of PET kinetic analysis and MLR can be a powerful tool for clinicians monitoring patient treatment as it may allow for a window of opportunity during which treatment regimens can be tailored accordingly, depending on the survival predictions from the MLR analysis. Specifically, it offers the neuro-oncologist an index on whether to wait and watch on the current therapy or to switch the patient to a different and potentially more efficacious treatment regimen earlier on. The clinical effect of this added information could potentially help increase patient lifespan and avoid multiple cycles of ineffective, morbid, and costly treatment. The PET methods used in this study could also augment the conventional assessment of tumor response with morphological imaging and could be added to standardized criteria for response evaluation in neuro-oncology. In the meantime, we need clinical chemists to come up with new, more effective, and less toxic therapeutics against this terrible disease. Working on brain tumor research can often be a Herculean task in that fighting against these cancer cells can be like trying to kill the Hydra, which grew back two heads when one was severed. However, we have to persevere like Hercules, and make leaping strides in trying to increase the lifespan of these patients.

4.6 CONCLUSIONS

For recurrent malignant glioma treated with bevacizumab and irinotecan, FLT kinetic parameters taken early after the start of treatment (absolute values and their associated changes) may provide sufficient information to predict OS with reasonable confidence using a multivariate regression analysis. This method could provide a powerful tool for clinicians monitoring patient treatment as it would enable the development of individualized therapeutic regimens and, in the process, avoid unnecessary drug toxicity to the patient, help increase patient lifespan, and reduce undue health care costs. This method could also augment the conventional assessment of tumor response to targeted therapies. The marginal increase in accuracy for predicting OS with a combination of FLT and FDOPA PET probes may not warrant the additional acquisition of FDOPA PET scans in a clinical setting for therapy monitoring of patients with recurrent malignant glioma; whether this is true for newly diagnosed tumors is uncertain. Kinetic analysis with dynamic PET imaging has an important advantage over static uptake measures in that it can quantify and capture multiple aspects of tumor biology and their changes in response to treatment.

4.7 FIGURES

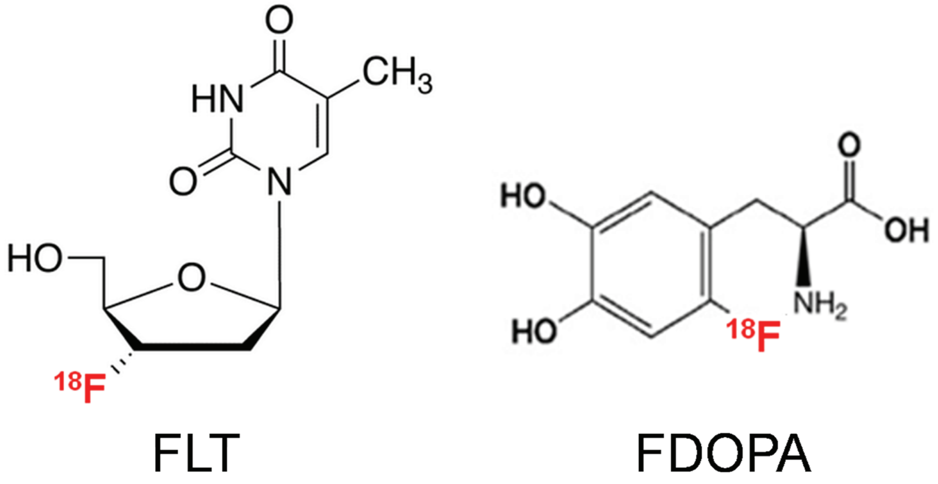

Figure 4.1 Chemical structures of FLT and FDOPA. Unlabeled FLT was originally synthesized as an anti-cancer and anti-retroviral agent, and is similar in concept to azidothymidine, the first approved anti-AIDS drug (*23, 55*). FLT acts as a DNA chain terminator because it lacks a 3′-hydroxyl group on the deoxyribose ring (*38*). FLT is not a substrate for thymidine phosphorylase (which is an enzyme that cleaves the sugar from the thymine base), but it is a good substrate for thymidine kinase 1 and therefore reflects metabolism by the DNA salvage pathway (*23*). PET imaging with FLT was first reported by Shields *et al. (56)*. FLT localizes in lung, breast, colorectal and brain tumors, providing a sensitive means for detecting these tumors (*57*). FLT does not significantly accumulate in inflamed tissues and is, therefore, less susceptible to inflammation-based tissue uptake as compared to FDG (*23*). FDOPA was initially used in PET to visualize and assess the presynaptic integrity of the nigrostriatal dopamine pathway in the evaluation of patients with movement disorders such as Parkinson’s disease (*58, 59*). FDOPA, however, is also an amino acid analog and was shown to be taken up at the BBB in the normal brain by neutral amino acid transporters (*60*). The initial report to demonstrate the value of FDOPA PET for the detection of brain tumors came as an incidental finding in a patient undergoing evaluation for a light movement disorder of the left arm and hand (*61*). The FDOPA PET scan showed that the patient not only had an asymmetric reduction in dopamine uptake in the putamen, but also a low-grade glioma in the right frontal lobe (*61*).

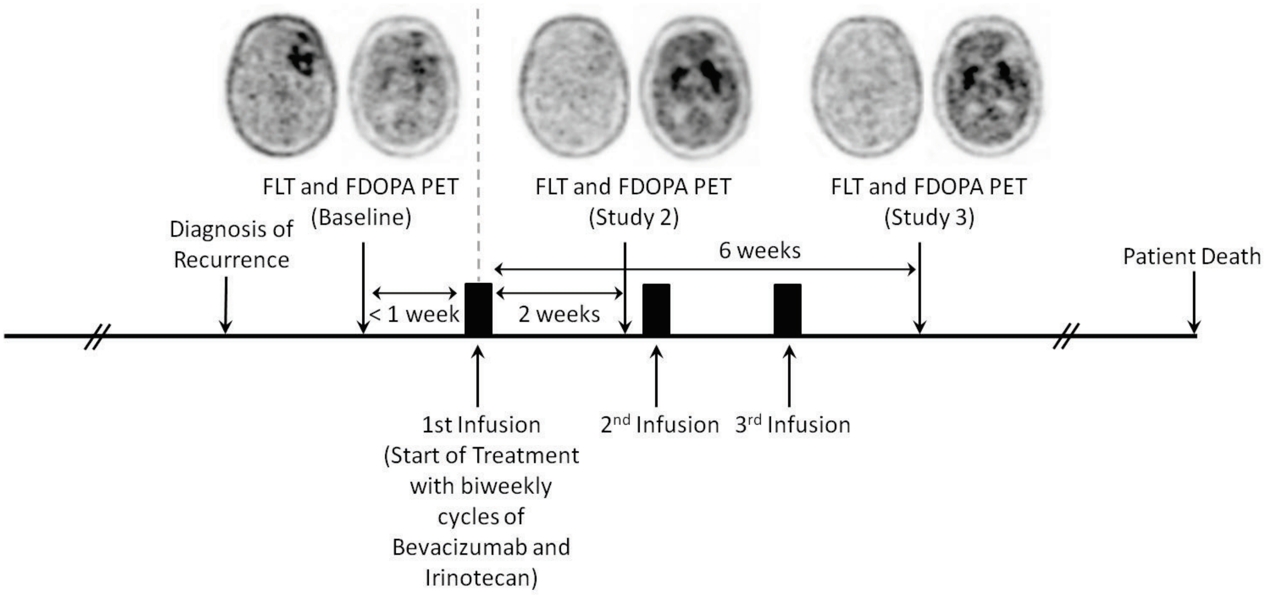

Figure 4.2 Experimental design showing the relative timing of treatment administration and PET image acquisition. Each patient was used as his or her own control.

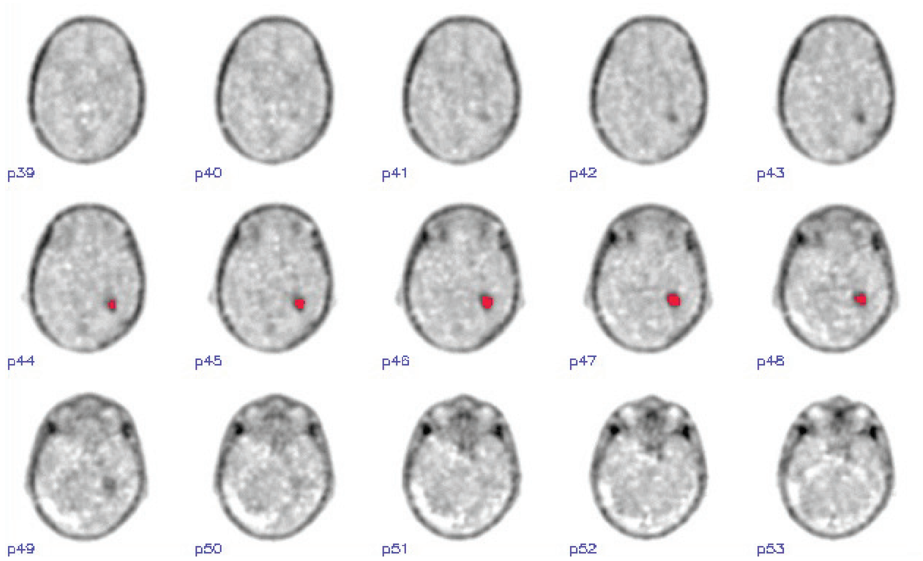

Figure 4.3 A 75% threshold on the tumor factor image was placed so as to capture the most active part of the tumor while excluding any zones of necrosis. The tumor mask (after thresholding) is shown in red above.

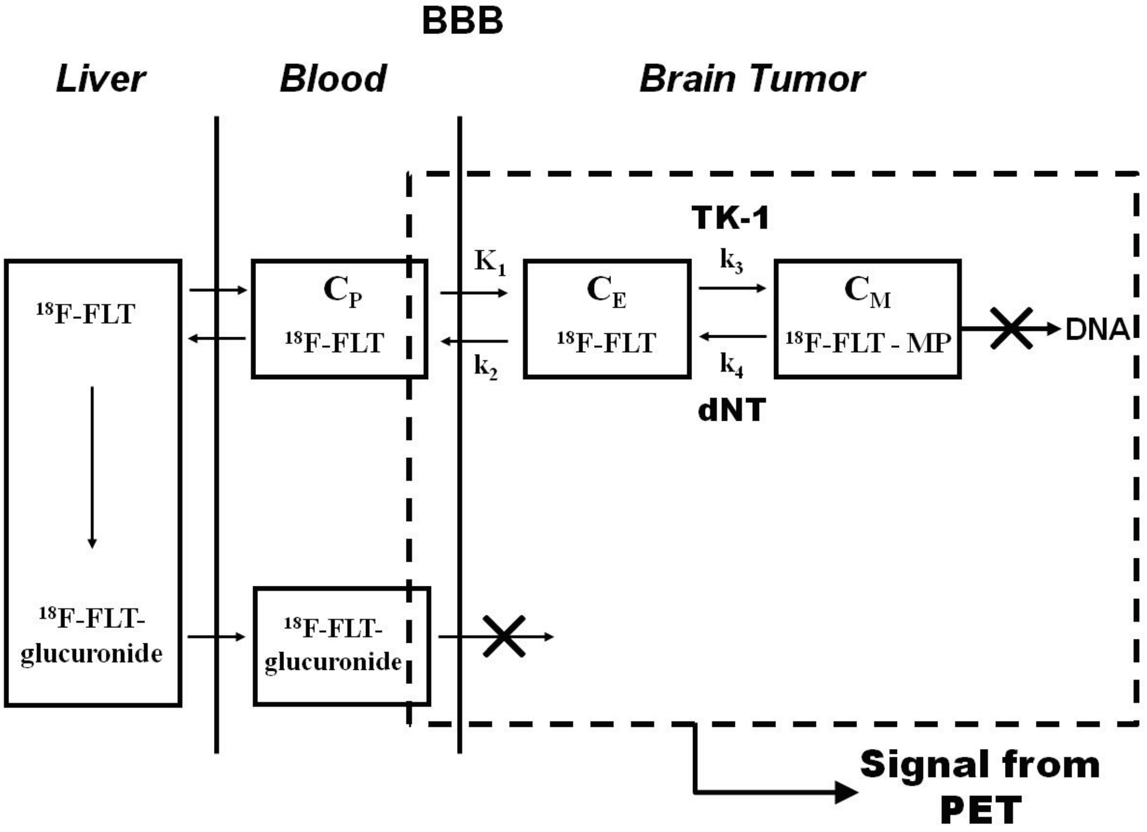

Figure 4.4 Tracer kinetic model for FLT in brain tumors. The catenary model consists of a vascular compartment and two tissue compartments, each of which represents FLT in one of two different chemical states. Intracellular radioactivity accumulation results from the formation of phosphorylated FLT nucleotides in competition with nucleotidase-mediated dephosphorylation and FLT efflux (*38*). K_1 is the transport rate constant of FLT from blood (or plasma) into the tumor cell via nucleoside-facilitated transporters, k_2 is the loss or leak from the system, k_3 is the rate constant for kinase-modulated phosphorylation of FLT, and k_4 is the rate constant that describes the dephosphorylation of FLT-monophosphate by phosphatases [such as 5′(3′)-deoxyribonucleotidase 1 (dNT1)] (*38*).

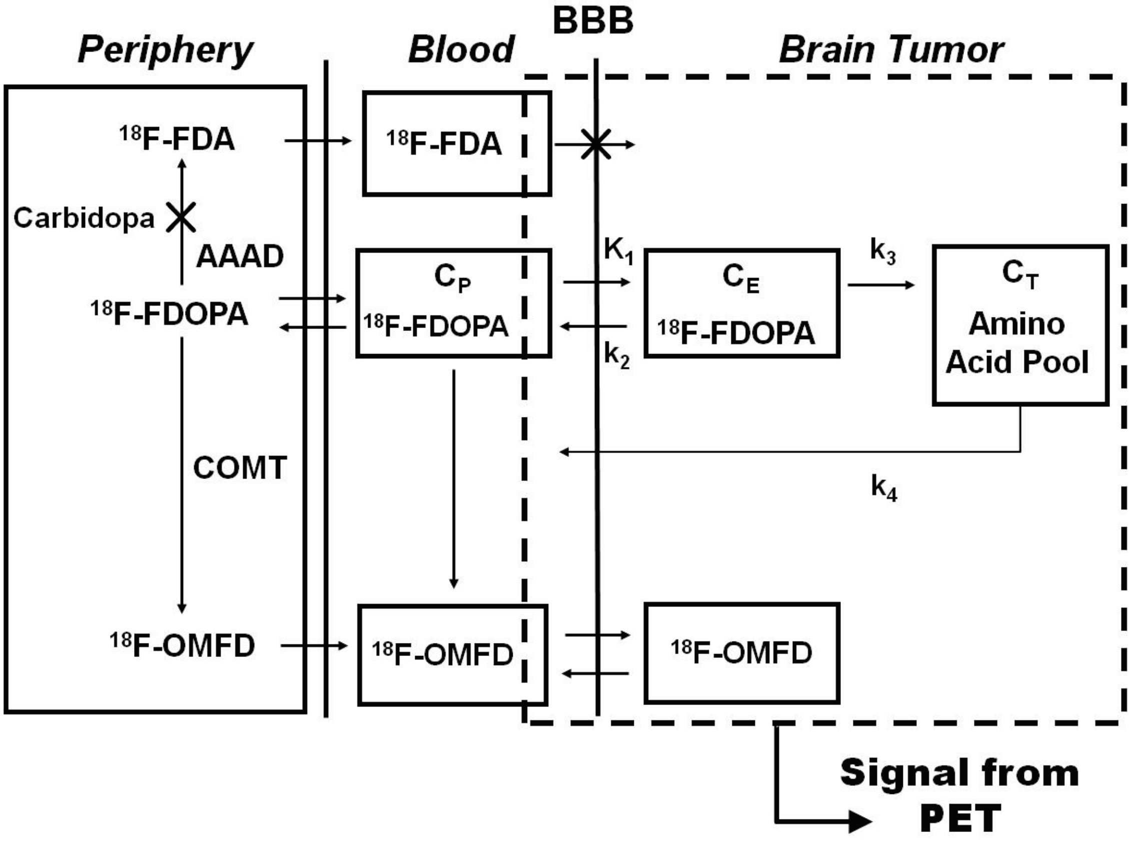

Figure 4.5 Tracer kinetic model for FDOPA in brain tumors. FDOPA is transported across tumor cell membranes by L-amino acid transporters, which are overexpressed in most gliomas (*32*). Increased transport of amino acids is most likely a result of increased demand for amino acids. The parameter k_3 is the sequestration rate constant which describes the transfer of FDOPA into the amino acid pool of the tumor, which is larger in tumors than in normal brain tissue (e.g., cerebral cortex and cerebellum), and is reflected in the increased radioactivity levels in tumors. Huang *et al.* was the first to estimate FDOPA kinetics in the brains of normal human subjects (*41*). Schiepers *et al.* was the first to report FDOPA kinetics in human brain tumors (*42*).

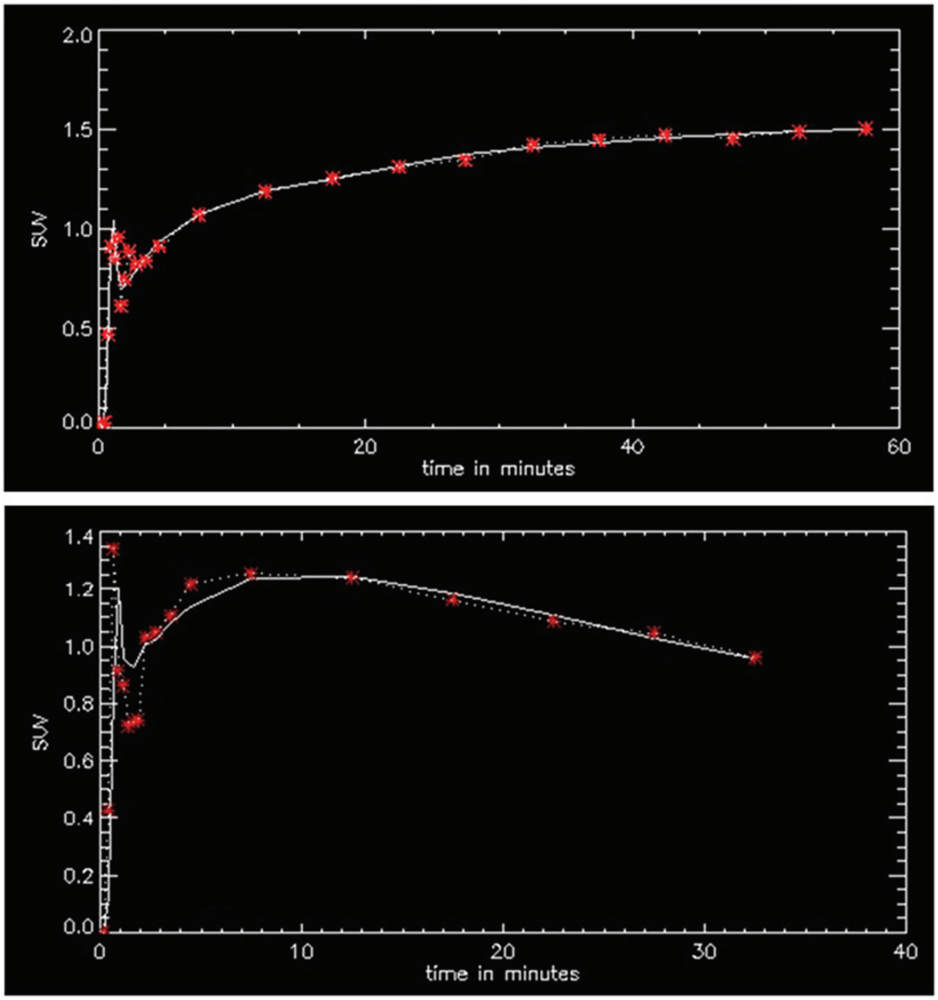

Figure 4.6 Measured (dashed line and red markers) and model fitted (solid white line) tumor time-activity curves for representative FLT (top) and FDOPA (below) PET studies. Notice the early vascular component in the measured and fitted data.

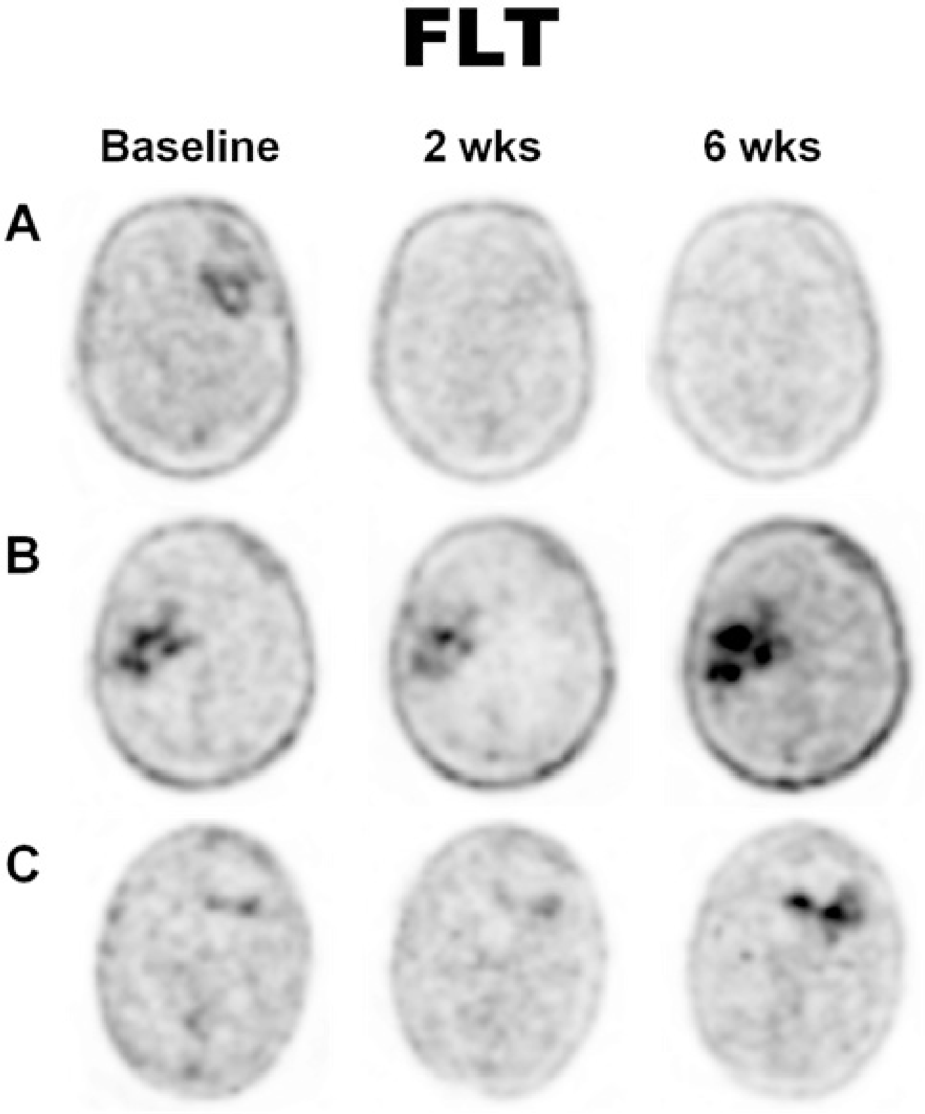

Figure 4.7 FLT PET images at baseline and after 2 and 6 weeks from the start of treatment as shown for a long-term survivor (A, top row) and two short-term survivors (B and C, middle and bottom rows). Images are displayed in radiological view, where the right side of the subject's brain is on the left side of the image and vice versa. Patients A, B, and C are Patients 20, 4, and 2 in Table 4.1, respectively.

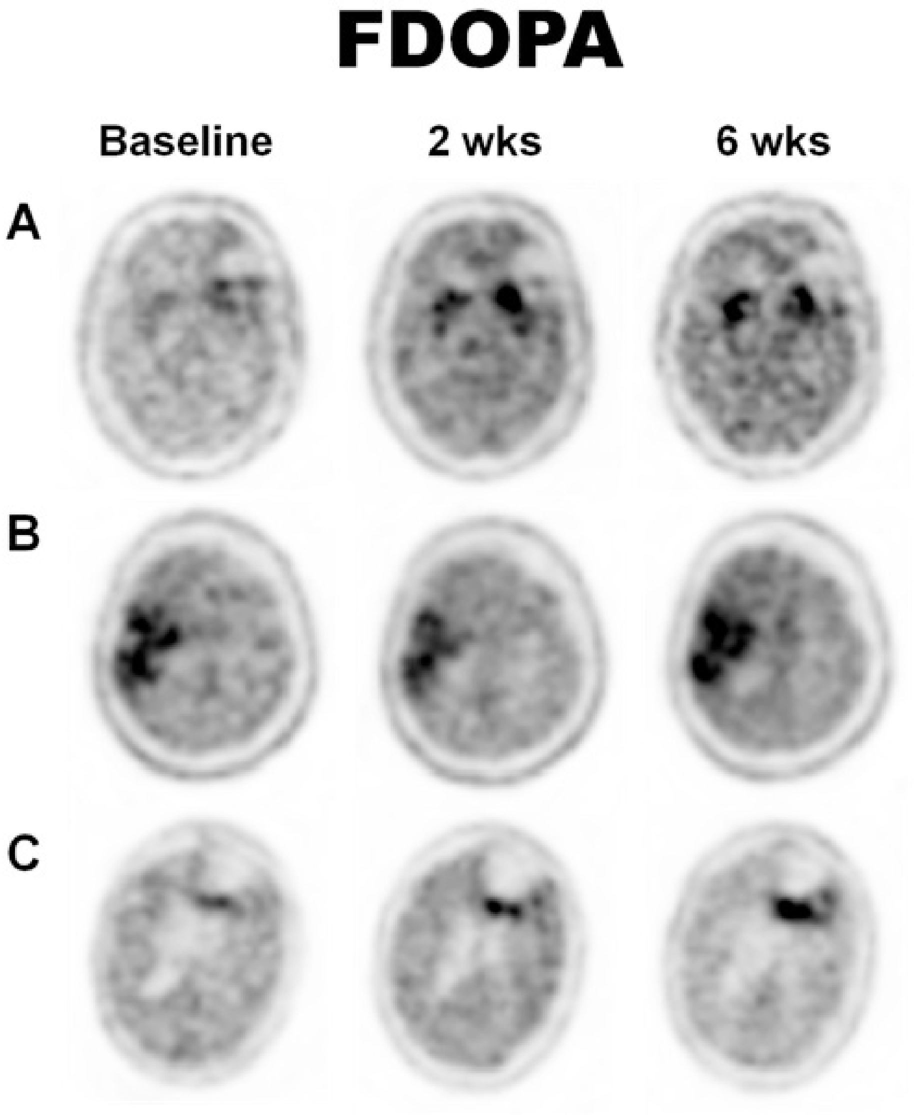

Figure 4.8 FDOPA PET images at baseline and after 2 and 6 weeks from the start of treatment as shown for a long-term survivor (A, top row) and two short-term survivors (B and C, middle and bottom rows). Images are displayed in radiological view, where the right side of the subject's brain is on the left side of the image and vice versa. Note that Patient A has a tumor near the left striatum. Patients A, B, and C are Patients 20, 4, and 2 in Table 4.1, respectively.

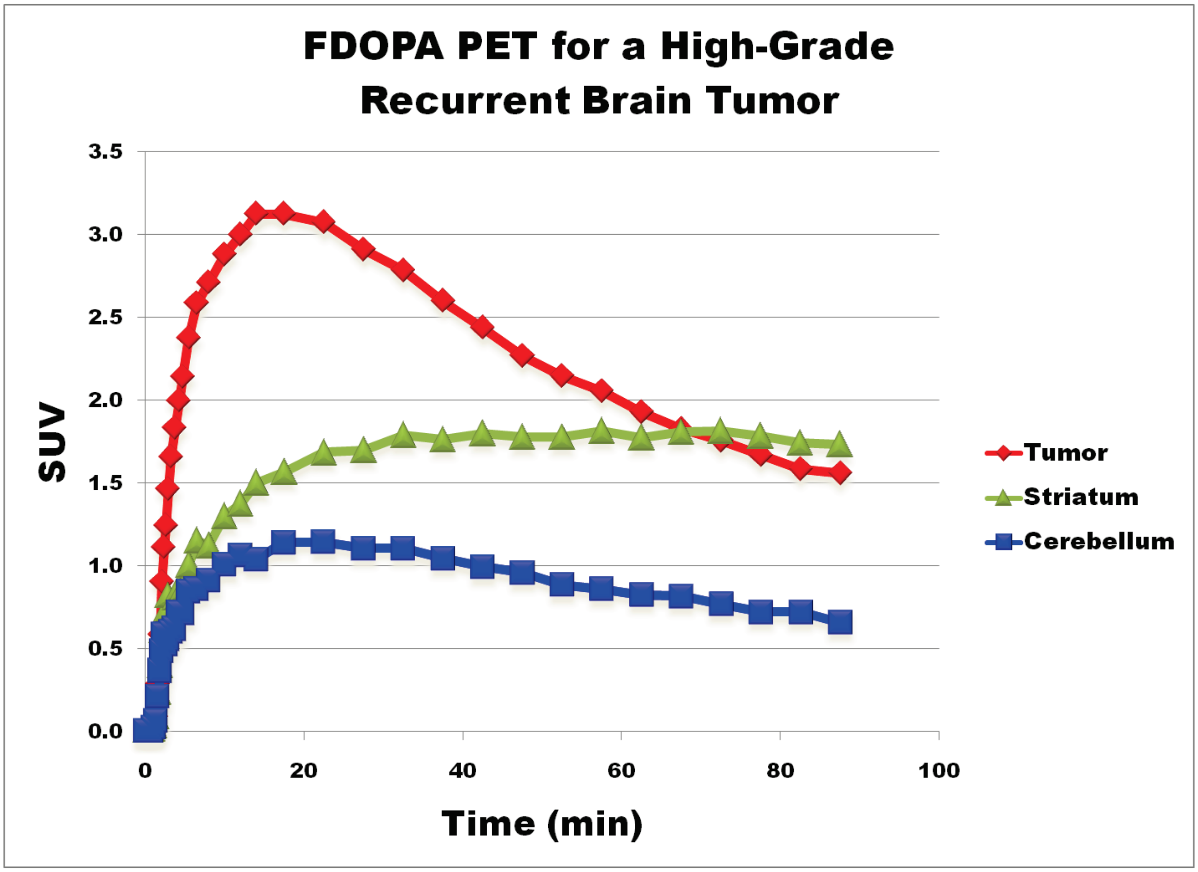

Figure 4.9 Sample FDOPA time-activity curves of the tumor, striatum, and cerebellum for a recurrent brain tumor patient at baseline. This particular patient had an FDOPA PET scan that was carried out to 90 minutes.

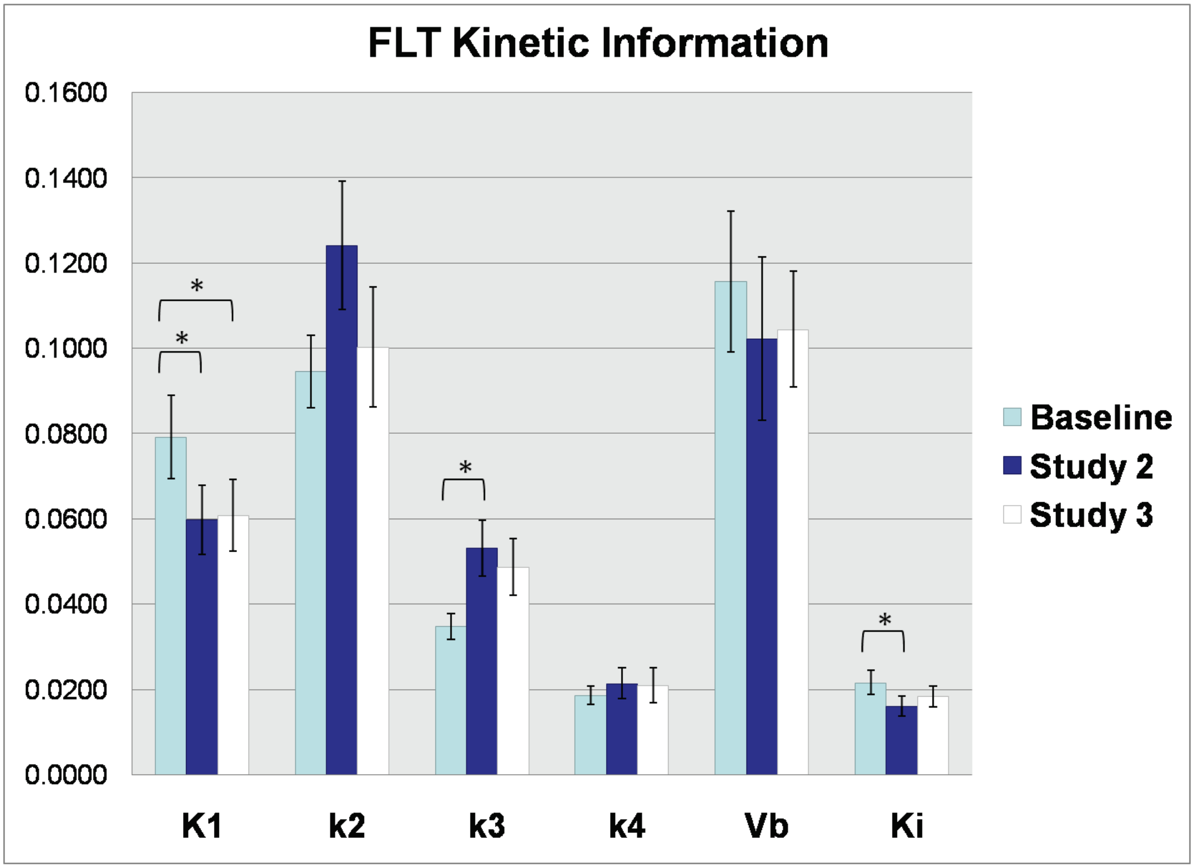

Figure 4.10 Bar graphs showing the sample mean ± SEM for the various FLT kinetic microparameters and the FLT influx rate constant K_i at each of the three study time points (i.e., at baseline and after 2 and 6 weeks from the start of treatment). Asterisks and hanging bars indicate where significant paired sample differences were found between time points using the Wilcoxon signed-rank test. If the Bonferroni method was applied to correct for multiple comparisons, then the paired sample differences for K_1 between baseline and study 3 would no longer be significant, while the other starred differences shown above would remain significant.

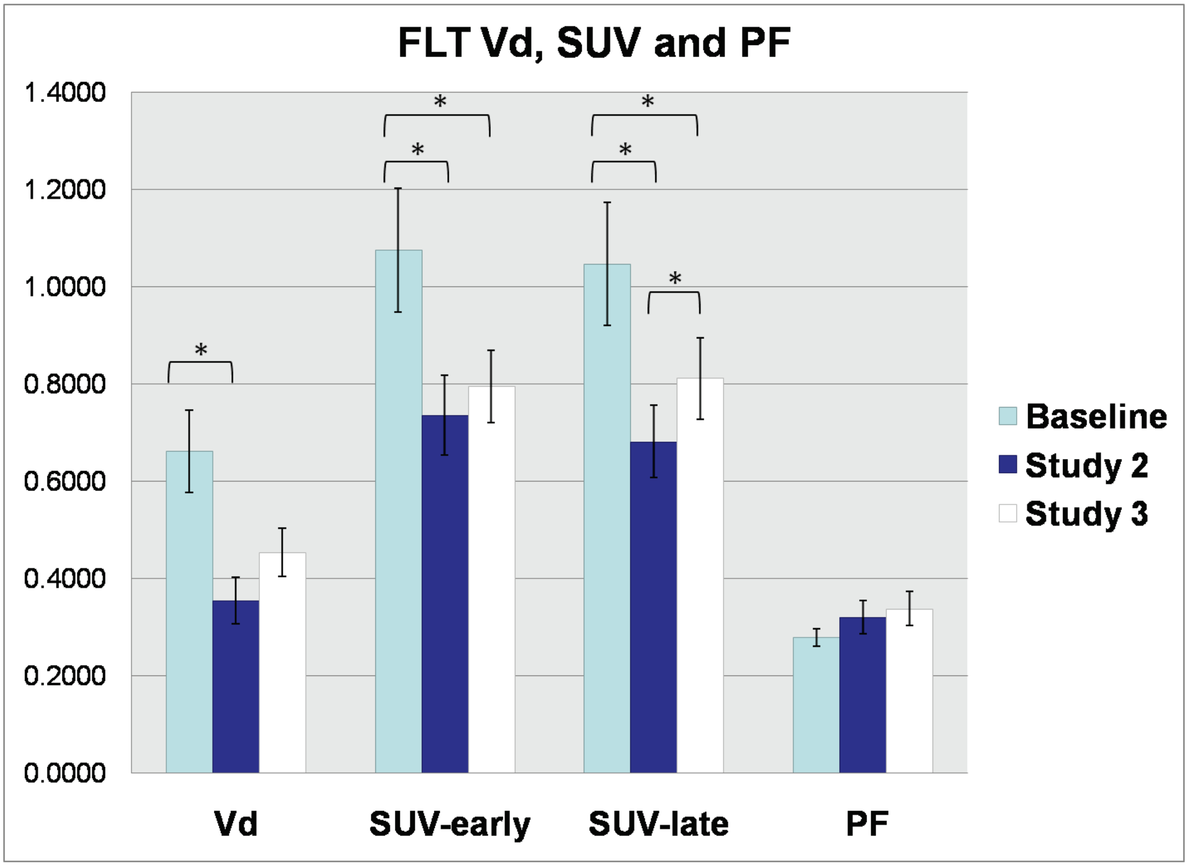

Figure 4.11 Bar graphs showing the sample mean ± SEM for FLT V_d, SUV (early and late), and PF at each of the three study time points (i.e., at baseline and after 2 and 6 weeks from the start of treatment). SUV is a unitless parameter. Asterisks and hanging bars indicate where significant paired sample differences were found between time points using the Wilcoxon signed-rank test. If the Bonferroni method was applied to correct for multiple comparisons, then the paired sample differences for SUV_{late} between baseline and study 3 would no longer be significant, while the other starred differences shown above would remain significant.

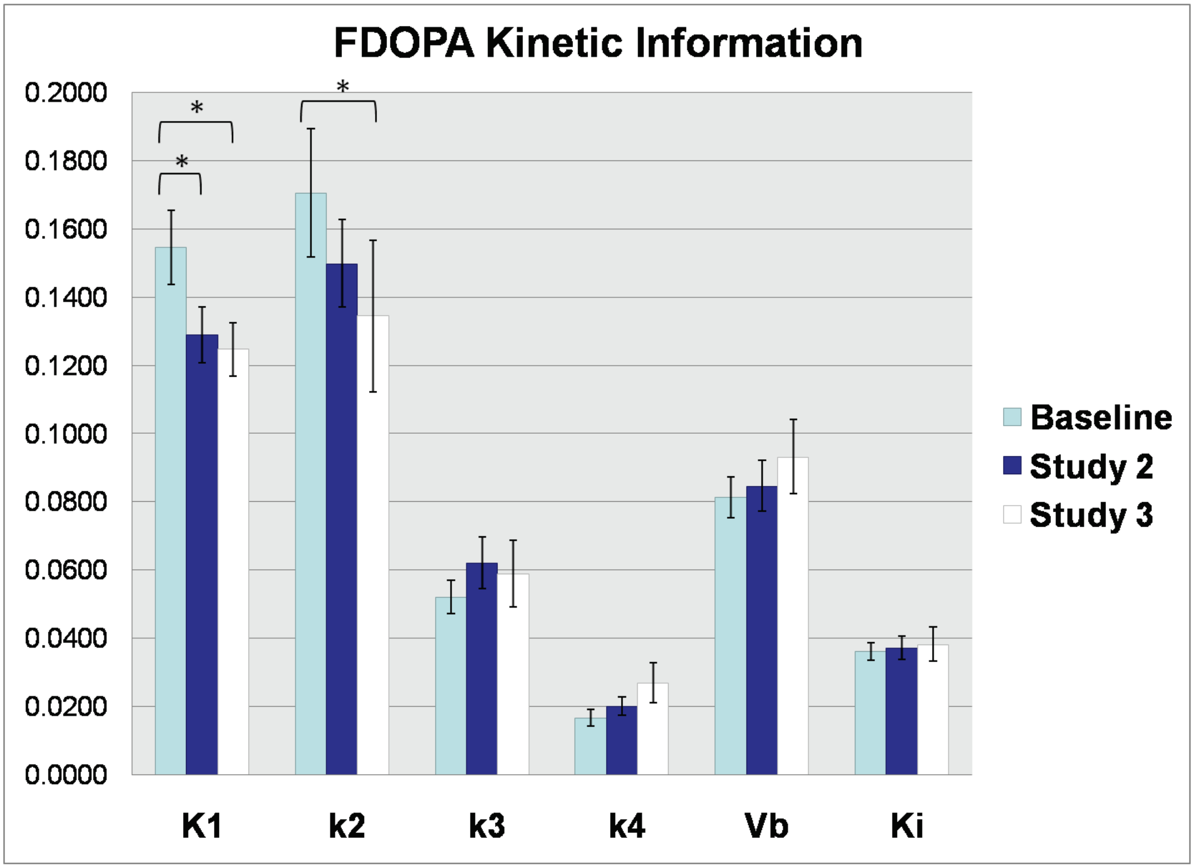

Figure 4.12 Bar graphs showing the sample mean ± SEM for the various FDOPA kinetic microparameters and the FDOPA influx rate constant K_i at each of the three study time points (i.e., at baseline and after 2 and 6 weeks from the start of treatment). Asterisks and hanging bars indicate where significant paired sample differences were found between time points using the Wilcoxon signed-rank test. If the Bonferroni method was applied to correct for multiple comparisons, then the starred differences shown above would remain significant even at the new adjusted *P*-value.

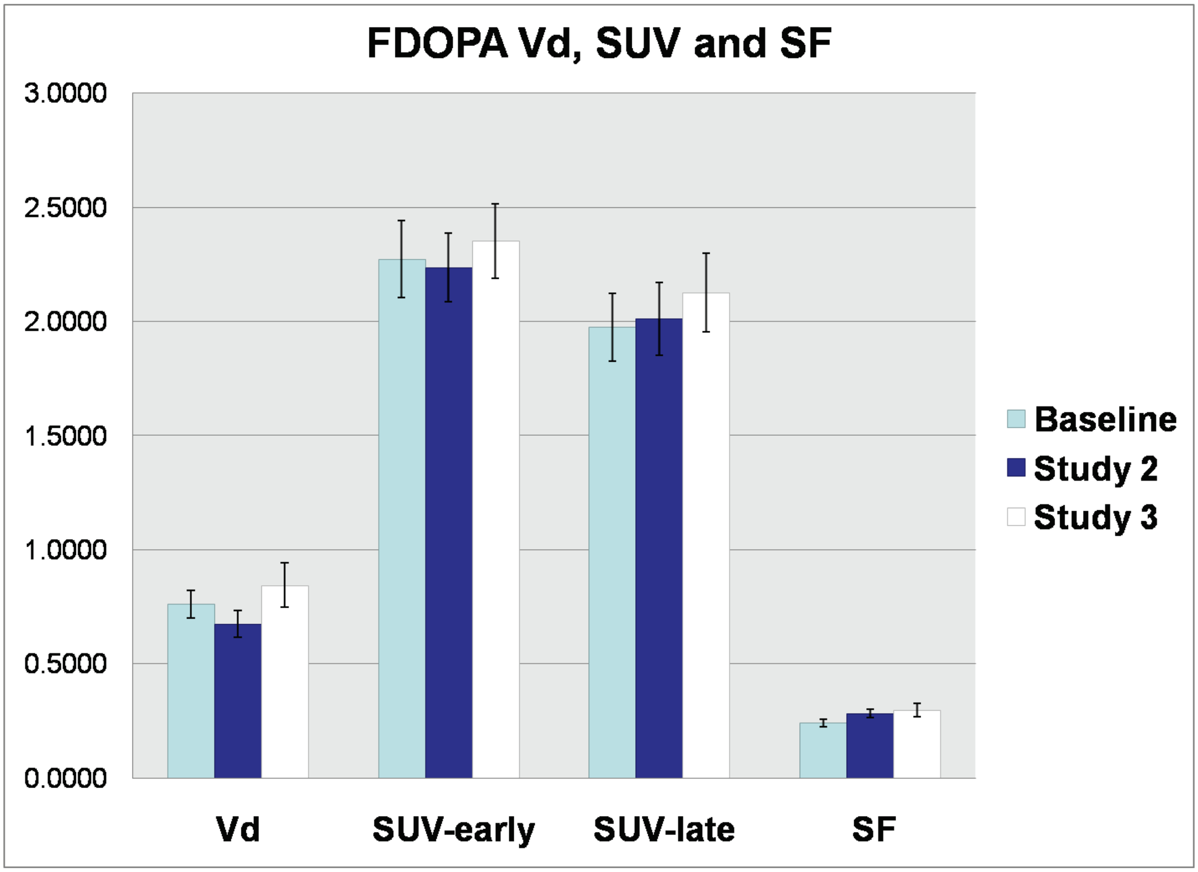

Figure 4.13 Bar graphs showing the sample mean ± SEM for FDOPA V_d, SUV (early and late), and SF at each of the three study time points (i.e., at baseline and after 2 and 6 weeks from the start of treatment). SF is a dimensionless parameter. No significant paired sample differences were found between time points using the Wilcoxon signed-rank test.

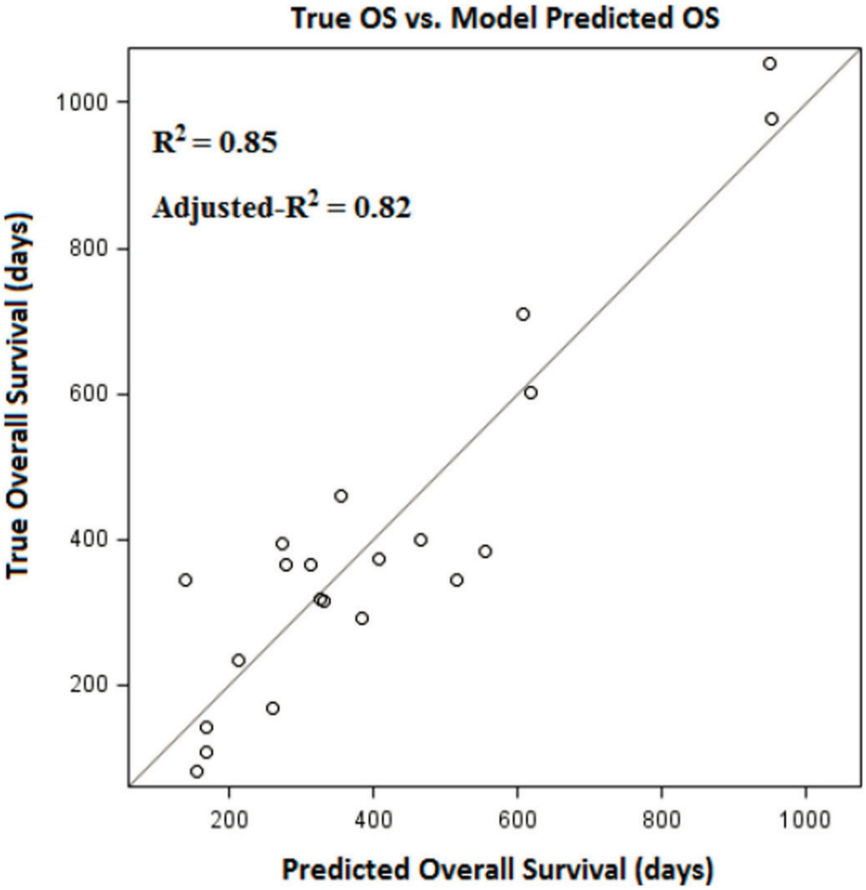

Figure 4.14 Actual OS versus model predicted OS using only FLT kinetic information in the MLR analysis. Results from the best three-predictor MLR model are shown above.

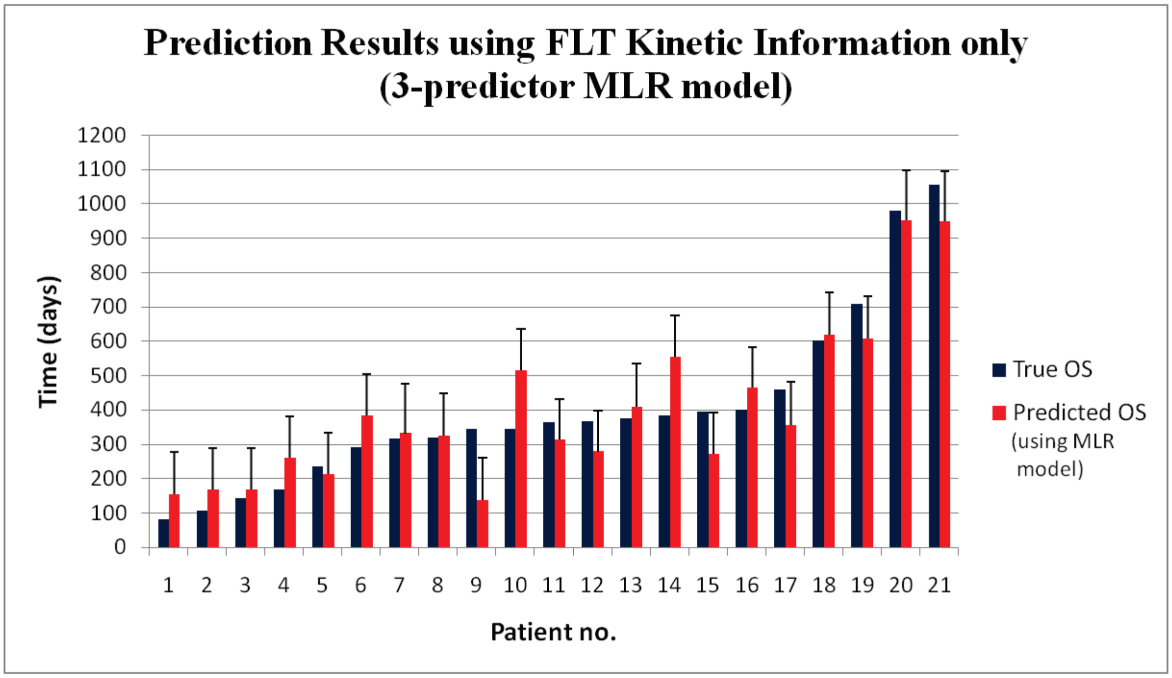

Figure 4.15 Bar graphs showing the true OS and model predicted OS when using only FLT kinetic information in selecting the best three-predictor MLR model. Error bars denote 1 SD.

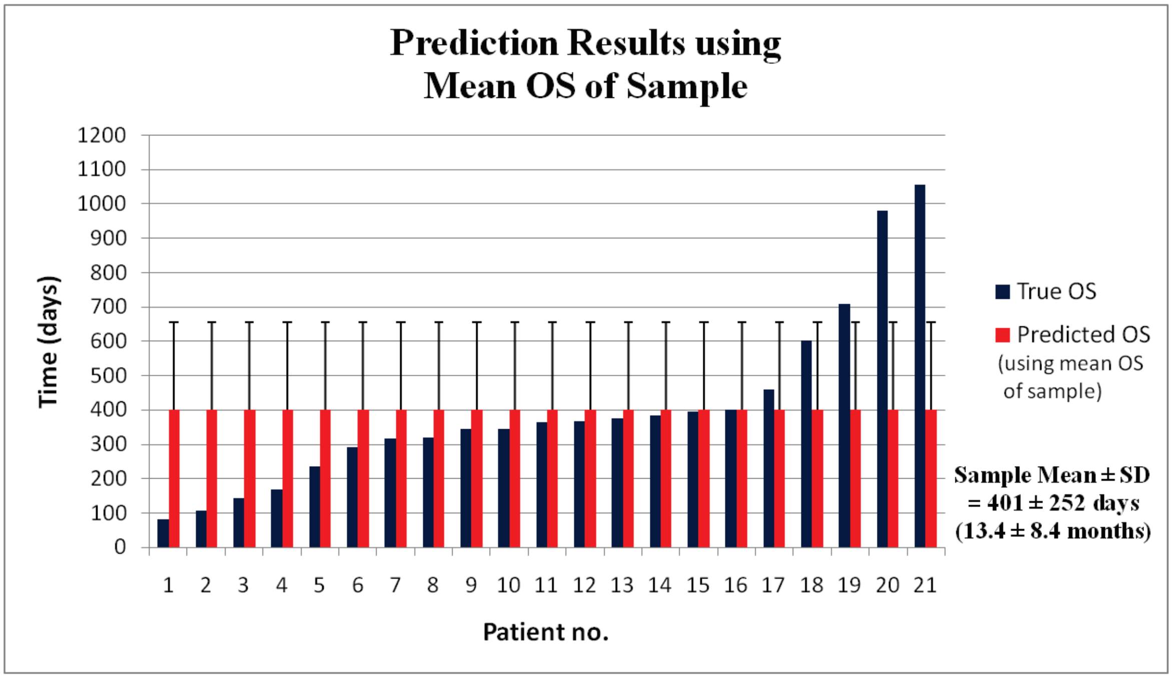

Figure 4.16 Bar graphs showing the true OS of each patient and the mean OS of the sample. If the mean OS of the sample was used for predicting each patient's OS, then every patient would have a predicted OS of 401 ± 252 days (13 ± 8 months); with 1 SD, this prediction is anywhere from 5-21 months. Error bars denote 1 SD.

4.8 TABLES

Table 4.1 Clinical characteristics of patients.

Patient No.	Sex	Age (y)	Pathology at Initial Diagnosis	Initial WHO grade	Pathology at recurrence	WHO grade at recurrence	Initial therapy	Prior treatments	Time from initial diagnosis (d)	PFS (d)	OS (d)
1	M	69	GBM	4	GBM	4	Chemotherapy/XRT	1	76	81	81
2	F	65	GBM	4	GBM	4	Chemotherapy/XRT	2	578	78	107
3	M	65	AA	3	AA	3	Chemotherapy/XRT	1	656	96	142
4	F	59	GBM	4	GBM	4	Chemotherapy/XRT	1	322	42	169
5	M	64	GBM	4	GBM	4	Chemotherapy/XRT	1	178	70	234
6	M	37	AA	3	GBM	4	Chemotherapy	2	4225	62	292
7	M	68	GBM	4	GBM	4	Chemotherapy/XRT	2	332	218	315
8	F	35	AA	3	GBM	4	XRT	3	2804	65	318
9	F	54	GBM	4	GBM	4	Chemotherapy/XRT	1	91	226	343
10	M	45	GBM	4	GBM	4	Chemotherapy/XRT	1	132	74	344
11	M	26	AA	3	GBM	4	Chemotherapy	3	462	96	364
12	F	40	GBM	4	GBM	4	Chemotherapy/XRT	1	462	44	366
13	F	47	GBM	4	GBM	4	Chemotherapy/XRT	1	160	176	374
14	M	68	GBM	4	GBM	4	Chemotherapy/XRT	1	488	343	383
15	F	70	GBM	4	GBM	4	Chemotherapy/XRT	1	362	184	395
16	F	61	GBM	4	GBM	4	Chemotherapy/XRT	2	719	137	400
17	F	37	GBM	4	GBM	4	Chemotherapy/XRT	1	126	304	460
18	M	57	GBM	4	GBM	4	Chemotherapy/XRT	1	1338	135	601
19	F	62	GBM	4	GBM	4	Chemotherapy/XRT	1	316	273	709
20	M	76	GBM	4	GBM	4	Chemotherapy/XRT	1	134	588	978
21	M	46	GBM	4	GBM	4	Chemotherapy/XRT	1	230	554	1054

* Time from initial diagnosis is the number of days from initial diagnosis to start of treatment in current study.
† GBM = glioblastoma multiforme; AA = anaplastic astrocytoma; XRT = radiation therapy.

Table 4.2 Multiple linear regression results using parameter information from FLT only, FDOPA only, and FLT and FDOPA combined.

Type of PET Information Inputted into a Three-Predictor Multiple Linear Regression Model	**FLT only**	**FDOPA only**	**FLT and FDOPA**
Kinetic Parameter Values at Each Study	Adjusted-R^2 = 0.56	Adjusted-R^2 = 0.32	Adjusted-R^2 = 0.58
Change in Kinetic Parameter Values Between Studies	Adjusted-R^2 = 0.80	Adjusted-R^2 < 0.20	Adjusted-R^2 = 0.83
Combination of Kinetic Parameter Values and their Changes	Adjusted-R^2 = 0.82	Adjusted-R^2 = 0.41	Adjusted-R^2 = 0.83

Table 4.3 Parameter estimates from MLR model using information from FLT only (absolute values and changes combined).

Multiple Linear Regression Model for Predicting Overall Survival (MLR-1)		
Predictor Variable	**Parameter Estimates**	***P*-value**
FLT V_d absolute value at S2	-443.29	<.0001
FLT k_4 ratio (S2/S1)	+158.44	<.0001
FLT k_2 ratio (S3/S2)	+289.66	<.0001
Intercept	+87.95	0.22

* $R^2 = 0.85$, adjusted-$R^2 = 0.82$, root MSE = 106 days, and the average variance inflation factors were $\cong 1.0$.

S1 = Baseline FLT PET, S2 = FLT PET at 2 weeks after start of treatment, S3 = FLT PET at 6 weeks after start of treatment.

Table 4.4 Parameter estimates from MLR model using information from FDOPA only (absolute values and changes combined).

Multiple Linear Regression Model for Predicting Overall Survival (MLR-2)		
Predictor Variable	**Parameter Estimates**	***P*-value**
FDOPA k_3 absolute value at S1	-7993.19	0.0042
FDOPA V_d absolute value at S1	-662.05	0.0049
FDOPA K_1 ratio (S3/S2)	-380.15	0.0135
Intercept	+1702.61	<.0001

* $R^2 = 0.50$, adjusted-$R^2 = 0.41$, root MSE = 194 days, and the average variance inflation factors were $\cong 1.5$.

S1 = Baseline FDOPA PET, S2 = FDOPA PET at 2 weeks after start of treatment, S3 = FDOPA PET at 6 weeks after start of treatment.

Table 4.5 Parameter estimates from MLR model using information from FLT and FDOPA combined (both absolute values and changes).

Multiple Linear Regression Model for Predicting Overall Survival (MLR-3)		
Predictor Variable	**Parameter Estimates**	***P*-value**
FLT k_4 ratio (S3/S1)	+158.66	<.0001
FLT k_2 ratio (S3/S2)	+314.86	<.0001
FDOPA tumor-to-striatum SUV_{late} ratio (S2/S1)	-450.85	<.0001
Intercept	+354.23	<.01

* $R^2 = 0.86$, adjusted-$R^2 = 0.83$, root MSE = 104 days, and the average variance inflation factors were $\cong 1$.

S1 = Baseline PET, S2 = PET at 2 weeks after start of treatment, S3 = PET at 6 weeks after start of treatment.

4.9 SUPPLEMENTARY TABLES

Supplementary Table S4.1 Percent change in FLT and FDOPA kinetic parameters (Baseline → 2 weeks).

	FLT								**FDOPA**							
Patient No.	**ΔK_1**	**Δk_2**	**Δk_3**	**Δk_4**	**ΔV_b**	**ΔK_i**	**ΔV_d**	**ΔPF**	**ΔK_1**	**Δk_2**	**Δk_3**	**Δk_4**	**ΔV_b**	**ΔK_i**	**ΔV_d**	**ΔSF**
1	128	143	59	-52	-63	69	7	-26	-30	29	-1	-95	-48	-43	-43	-20
2	69	202	58	-37	17	2	-36	-40	-43	-68	-17	1800	33	19	44	111
3	-20	67	-9	-13	7	-46	-41	-33	-11	5	-31	-59	-18	-36	-6	-27
4	3	324	236	32	-48	-12	-74	-14	26	76	67	31	36	21	-28	-4
5	-34	-11	-44	1	61	-53	-16	-29	-10	-26	-34	-30	-17	-16	27	-7
6	-78	-52	103	-12	-37	-52	-76	120	-42	-53	-71	-50	-2	-61	37	-32
7	-50	-47	-42	137	2	-46	-8	8	-33	27	246	143	-32	39	-60	108
8	-28	135	208	-42	-43	-10	-71	25	-33	-51	4	-13	21	13	9	67
9	-49	15	-25	-60	-81	-60	-47	-23	-2	-6	-24	-27	-10	-17	10	-15
10	-41	137	406	103	1	-8	-82	56	-17	61	30	4	11	-30	-46	-15
11	61	90	16	19	-52	10	-5	-32	-37	-20	-4	-59	-48	-27	-25	14
12	-23	24	24	33	-42	-22	-38	0	-14	-42	21	503	-36	52	26	76
13	-18	45	39	-12	-45	-21	-43	-3	48	1	1	29	6	48	47	0
14	-53	-40	-7	56	90	-37	-32	34	-17	-37	49	460	37	52	2	83
15	-18	89	-9	26	29	-56	-52	-47	-29	21	151	407	69	18	-53	68
16	-28	25	55	-3	-48	-18	-47	15	-8	-3	-6	-18	21	-10	-5	-2
17	-16	7	19	-65	-37	-8	-23	9	-29	-8	9	-6	30	-18	-25	14
18	-9	101	305	174	1247	55	-62	70	7	-12	-23	-74	6	-3	26	-9
19	-16	6	84	32	-13	19	-35	42	-8	27	153	256	94	64	-36	78
20	-76	-63	-13	35	45	-57	-51	80	18	32	124	129	96	69	-25	43
21	-72	-75	92	330	244	-22	-59	177	2	-3	-19	53	-40	-12	9	-14
Median	-23	25	39	19	-13	-21	-43	8	-14	-3	1	4	6	-3	-5	0
Mean ± SD	-18 ± 50	53 ± 98	74 ± 119	32 ± 92	59 ± 281	-18 ± 35	-42 ± 24	19 ± 57	-12 ± 23	-2 ± 37	30 ± 78	161 ± 416	10 ± 42	6 ± 38	-5 ± 33	25 ± 47

Supplementary Table S4.2 Percent change in FLT and FDOPA kinetic parameters (Baseline → 6 weeks).

	FLT								FDOPA							
Patient No.	ΔK_1	Δk_2	Δk_3	Δk_4	ΔV_b	ΔK_i	ΔV_d	ΔPF	ΔK_1	Δk_2	Δk_3	Δk_4	ΔV_b	ΔK_i	ΔV_d	ΔSF
1	21	-7	-28	-45	-52	1	41	-16	30	170	16	3	-43	-37	-46	-52
2	123	35	-6	-26	26	70	80	-24	-5	-32	112	2109	25	124	6	137
3	-52	3	119	8	45	-30	-68	46	-23	-25	-67	-44	-11	-60	21	-48
4	-26	72	127	26	15	-13	-62	18	-7	9	130	269	84	47	-36	58
5	-46	-27	-10	24	22	-38	-32	15	-18	-58	-63	174	11	-25	102	-9
6	-53	-66	-34	-63	-68	-28	8	54	-17	-37	16	35	63	27	10	53
7	-63	-43	-55	17	-60	-69	-31	-17	-57	-35	67	98	-11	-15	-49	101
8	-40	73	426	122	49	40	-73	135	-42	-80	-71	-76	-59	-26	157	28
9	-42	-60	-84	-53	-45	-68	98	-44	-20	7	69	83	4	8	-36	35
10	-33	99	269	108	-2	-3	-74	45	-38	-47	-43	51	71	-35	15	6
11	65	26	-15	-15	-26	22	44	-27	-11	22	75	20	-13	15	-34	30
12	-48	-21	53	9	-11	-15	-45	63	-24	-59	-44	124	-2	-3	73	28
13	-4	131	264	34	-37	25	-66	31	31	-61	-93	11	127	-64	417	-73
14	4	-35	-18	-1	23	22	49	19	-12	-59	205	1316	135	175	-10	213
15	-35	-23	-18	-20	-22	-31	-16	5	-37	-24	7	181	11	-18	-23	30
16	21	65	-14	-62	-46	-26	-14	-39	9	1	-23	-77	13	-11	16	-19
17	-29	72	179	-47	187	8	-62	50	-56	-50	-4	-40	2	-30	-26	60
18	49	20	187	226	949	186	-1	90	2	-5	38	33	-14	31	-5	29
19	16	39	-21	34	8	-24	-4	-35	-15	37	239	209	45	78	-48	109
20	-55	-4	13	28	-19	-48	-55	14	25	-9	2	-50	-58	34	32	8
21	-66	-82	120	400	8	2	-53	207	-25	-36	-60	72	-8	-50	26	-33
Median	-33	3	-6	9	-2	-13	-31	18	-17	-32	7	51	4	-11	6	29
Mean ± SD	-14 ± 49	13 ± 58	69 ± 133	34 ± 108	45 ± 214	-1 ± 55	-16 ± 52	28 ± 61	-15 ± 25	-18 ± 53	24 ± 90	214 ± 522	18 ± 53	8 ± 60	27 ± 103	33 ± 67

Supplementary Table S4.3 Percent change in FLT and FDOPA kinetic parameters (2 weeks → 6 weeks).

	FLT								FDOPA							
Patient No.	ΔK_1	Δk_2	Δk_3	Δk_4	ΔV_b	ΔK_i	ΔV_d	ΔPF	ΔK_1	Δk_2	Δk_3	Δk_4	ΔV_b	ΔK_i	ΔV_d	ΔSF
1	-47	-62	-55	16	28	-40	32	-47	85	110	18	1900	8	11	-6	-40
2	32	-55	-40	16	8	67	180	32	67	116	157	16	-6	88	-27	12
3	-40	-38	141	24	36	31	-46	-40	-14	-29	-52	38	9	-38	29	-28
4	-28	-59	-32	-4	120	-1	47	-28	-26	-38	38	182	36	21	-12	64
5	-18	-18	63	23	-25	33	-19	-18	-9	-43	-44	291	33	-11	59	-2
6	114	-30	-67	-58	-50	51	358	114	43	35	302	171	66	224	-20	126
7	-25	7	-24	-51	-61	-43	-25	-25	-37	-49	-52	-19	31	-38	27	-3
8	-17	-26	71	283	162	57	-9	-17	-15	-58	-72	-72	-66	-34	137	-23
9	13	-65	-78	16	185	-18	274	13	-18	15	124	151	16	30	-42	59
10	13	-16	-27	2	-3	5	45	13	-26	-67	-56	45	54	-7	111	25
11	3	-33	-27	-28	55	11	52	3	40	52	82	191	68	58	-13	13
12	-33	-37	23	-18	51	9	-11	-33	-12	-29	-54	-63	54	-36	38	-27
13	17	59	162	52	14	58	-40	17	-12	-61	-93	-14	114	-76	252	-73
14	120	7	-11	-37	-35	95	121	120	5	-36	104	153	72	81	-12	71
15	-21	-59	-10	-37	-39	58	76	-21	-10	-37	-57	-45	-35	-30	62	-23
16	69	32	-44	-61	5	-11	61	69	19	4	-19	-72	-6	-1	22	-17
17	-15	61	134	49	354	16	-50	-15	-38	-45	-12	-37	-21	-14	-1	40
18	65	-40	-29	19	-22	84	159	65	-5	8	80	420	-19	35	-25	42
19	39	31	-57	1	24	-36	48	39	-7	8	34	-13	-25	9	-18	18
20	91	158	30	-5	-44	20	-7	91	6	-31	-55	-78	-79	-20	75	-25
21	20	-27	15	16	-69	31	15	20	-27	-34	-51	12	53	-43	16	-23
Median	13	-27	-24	2	8	20	45	13	-10	-31	-19	16	16	-7	16	-2
Mean ± SD	17 ± 50	-10 ± 54	7 ± 70	10 ± 70	33 ± 101	23 ± 40	60 ± 107	17 ± 50	0 ± 33	-10 ± 52	15 ± 97	150 ± 422	17 ± 48	10 ± 65	31 ± 69	9 ± 46

Supplementary Table S4.4 FLT kinetic parameters at the baseline study.

Patient No.	**K_1**	**k_2**	**k_3**	**k_4**	**V_b**	**K_i**	**V_d**	**PF**	**SEE-K_1**	**SEE-k_2**	**SEE-k_3**	**SEE-k_4**	**SEE-V_b**
1	0.0224	0.0571	0.0307	0.0316	0.1720	0.0078	0.2549	0.3497	0.0078	0.0270	0.0267	0.0341	0.0391
2	0.0391	0.0541	0.0209	0.0193	0.0803	0.0109	0.5214	0.2787	0.0017	0.0033	0.0017	0.0054	0.0082
3	0.0656	0.0431	0.0297	0.0163	0.0748	0.0268	0.9014	0.4080	0.0036	0.0061	0.0057	0.0033	0.0198
4	0.1341	0.0650	0.0362	0.0120	0.1312	0.0479	1.3254	0.3577	0.0133	0.0135	0.0058	0.0044	0.0378
5	0.0792	0.0724	0.0353	0.0137	0.0599	0.0260	0.7355	0.3278	0.0042	0.0038	0.0048	0.0026	0.0132
6	0.0707	0.1120	0.0445	0.0399	0.1659	0.0201	0.4521	0.2843	0.0089	0.0277	0.0096	0.0106	0.0210
7	0.1731	0.1221	0.0377	0.0078	0.1174	0.0408	1.0830	0.2359	0.0122	0.0133	0.0057	0.0014	0.0221
8	0.0532	0.0864	0.0145	0.0129	0.0719	0.0077	0.5276	0.1437	0.0039	0.0148	0.0043	0.0147	0.0140
9	0.0569	0.0660	0.0519	0.0367	0.2577	0.0250	0.4825	0.4402	0.0094	0.0191	0.0142	0.0143	0.0480
10	0.0744	0.0293	0.0143	0.0122	0.0787	0.0244	1.7034	0.3280	0.0042	0.0037	0.0015	0.0039	0.0270
11	0.0510	0.0997	0.0364	0.0109	0.0745	0.0136	0.3746	0.2675	0.0042	0.0119	0.0047	0.0021	0.0116
12	0.1528	0.1650	0.0418	0.0180	0.1248	0.0308	0.7389	0.2021	0.0126	0.0201	0.0033	0.0036	0.0216
13	0.1103	0.0642	0.0357	0.0236	0.1551	0.0394	1.1041	0.3574	0.0027	0.0025	0.0015	0.0014	0.0114
14	0.0478	0.1146	0.0444	0.0117	0.0363	0.0134	0.3007	0.2792	0.0036	0.0137	0.0025	0.0019	0.0074
15	0.0864	0.1139	0.0223	0.0121	0.0967	0.0141	0.6346	0.1637	0.0085	0.0130	0.0022	0.0050	0.0228
16	0.1522	0.1542	0.0692	0.0394	0.3422	0.0472	0.6813	0.3098	0.0108	0.0177	0.0055	0.0075	0.0275
17	0.1222	0.1441	0.0215	0.0144	0.1110	0.0158	0.7379	0.1298	0.0092	0.0137	0.0015	0.0032	0.0147
18	0.0314	0.0556	0.0127	0.0050	0.0081	0.0058	0.4595	0.1859	0.0017	0.0059	0.0016	0.4303	0.0135
19	0.0356	0.1078	0.0452	0.0204	0.0902	0.0105	0.2325	0.2954	0.0057	0.0208	0.0082	0.0257	0.0159
20	0.0715	0.1250	0.0363	0.0127	0.0450	0.0161	0.4430	0.2250	0.0043	0.0099	0.0021	0.0036	0.0052
21	0.0327	0.1325	0.0477	0.0197	0.1336	0.0087	0.1817	0.2647	0.0072	0.0271	0.0113	0.0072	0.0206
Median	0.0707	0.0997	0.0362	0.0144	0.0967	0.0161	0.5276	0.2792	0.0057	0.0135	0.0047	0.0044	0.0198
Mean ± SD	0.0792 ± 0.0447	0.0945 ± 0.0387	0.0347 ± 0.0139	0.0186 ± 0.0102	0.1156 ± 0.0756	0.0216 ± 0.0132	0.6608 ± 0.3853	0.2778 ± 0.0835	0.0067 ± 0.0037	0.0137 ± 0.0079	0.0059 ± 0.0059	0.0279 ± 0.0926	0.0201 ± 0.0110

* SEE = standard error of the estimate.

Supplementary Table S4.5 FLT kinetic parameters at 2 weeks after the start of therapy.

Patient No.	**K_1**	**k_2**	**k_3**	**k_4**	**V_b**	**K_i**	**V_d**	**PF**	**SEE-K_1**	**SEE-k_2**	**SEE-k_3**	**SEE-k_4**	**SEE-V_b**
1	0.0510	0.1388	0.0487	0.0151	0.0645	0.0132	0.2722	0.2597	0.0067	0.0268	0.0096	0.0041	0.0137
2	0.0660	0.1634	0.0331	0.0122	0.0938	0.0111	0.3358	0.1684	0.0066	0.0202	0.0042	0.0033	0.0175
3	0.0528	0.0718	0.0270	0.0142	0.0797	0.0144	0.5344	0.2733	0.0045	0.0078	0.0051	0.0040	0.0190
4	0.1378	0.2753	0.1216	0.0158	0.0686	0.0422	0.3473	0.3064	0.0144	0.0353	0.0366	0.0037	0.0279
5	0.0519	0.0644	0.0196	0.0138	0.0967	0.0121	0.6188	0.2333	0.0041	0.0083	0.0041	0.0044	0.0167
6	0.0154	0.0541	0.0902	0.0353	0.1051	0.0096	0.1068	0.6251	0.0048	0.0366	0.0583	0.0236	0.0235
7	0.0867	0.0647	0.0220	0.0185	0.1198	0.0220	1.0003	0.2537	0.0035	0.0037	0.0015	0.0017	0.0098
8	0.0384	0.2028	0.0446	0.0075	0.0410	0.0069	0.1554	0.1803	0.0059	0.0334	0.0104	0.0059	0.0118
9	0.0293	0.0758	0.0390	0.0147	0.0494	0.0099	0.2551	0.3397	0.0031	0.0166	0.0056	0.0095	0.0112
10	0.0439	0.0693	0.0724	0.0248	0.0793	0.0224	0.3098	0.5109	0.0074	0.0200	0.0191	0.0077	0.0252
11	0.0821	0.1892	0.0421	0.0130	0.0359	0.0149	0.3549	0.1820	0.0061	0.0178	0.0035	0.0015	0.0060
12	0.1182	0.2050	0.0520	0.0240	0.0730	0.0239	0.4599	0.2023	0.0156	0.0374	0.0074	0.0028	0.0226
13	0.0903	0.0934	0.0495	0.0208	0.0852	0.0313	0.6319	0.3464	0.0031	0.0045	0.0029	0.0017	0.0091
14	0.0225	0.0693	0.0412	0.0183	0.0690	0.0084	0.2035	0.3729	0.0040	0.0268	0.0129	0.0106	0.0159
15	0.0712	0.2153	0.0204	0.0153	0.1252	0.0062	0.3023	0.0866	0.0100	0.0307	0.0025	0.0052	0.0189
16	0.1089	0.1930	0.1071	0.0384	0.1767	0.0389	0.3630	0.3569	0.0071	0.0176	0.0105	0.0038	0.0196
17	0.1028	0.1545	0.0256	0.0051	0.0702	0.0146	0.5707	0.1421	0.0089	0.0171	0.0027	0.0255	0.0168
18	0.0285	0.1116	0.0514	0.0137	0.1091	0.0090	0.1750	0.3153	0.0085	0.0439	0.0172	0.0078	0.0200
19	0.0298	0.1148	0.0832	0.0269	0.0787	0.0125	0.1506	0.4202	0.0051	0.0319	0.0124	0.0137	0.0130
20	0.0169	0.0464	0.0317	0.0171	0.0653	0.0069	0.2166	0.4059	0.0021	0.0113	0.0089	0.0044	0.0100
21	0.0092	0.0331	0.0915	0.0847	0.4592	0.0068	0.0741	0.7343	0.0047	0.0230	0.1250	0.1348	0.0583
Median	0.0519	0.1116	0.0446	0.0158	0.0793	0.0125	0.3098	0.3064	0.0059	0.0202	0.0089	0.0044	0.0168
Mean ± SD	0.0597 ± 0.0371	0.1241 ± 0.0686	0.0530 ± 0.0298	0.0214 ± 0.0166	0.1022 ± 0.0877	0.0161 ± 0.0104	0.3542 ± 0.2204	0.3198 ± 0.1586	0.0065 ± 0.0035	0.0224 ± 0.0116	0.0172 ± 0.0280	0.0133 ± 0.0286	0.0184 ± 0.0108

* SEE = standard error of the estimate.

Supplementary Table S4.6 FLT kinetic parameters at 6 weeks after the start of therapy.

Patient No.	**K_1**	**k_2**	**k_3**	**k_4**	**V_b**	**K_i**	**V_d**	**PF**	**SEE-K_1**	**SEE-k_2**	**SEE-k_3**	**SEE-k_4**	**SEE-V_b**
1	0.0270	0.0532	0.0221	0.0175	0.0827	0.0079	0.3591	0.2935	0.0021	0.0062	0.0047	0.0035	0.0146
2	0.0872	0.0730	0.0197	0.0142	0.1014	0.0185	0.9406	0.2125	0.0044	0.0047	0.0021	1.0482	0.0184
3	0.0317	0.0442	0.0650	0.0176	0.1081	0.0188	0.2900	0.5952	0.0027	0.0059	0.0115	0.0057	0.0183
4	0.0988	0.1119	0.0823	0.0151	0.1512	0.0419	0.5089	0.4238	0.0066	0.0078	0.0057	0.0020	0.0241
5	0.0428	0.0531	0.0319	0.0170	0.0729	0.0161	0.5031	0.3753	0.0043	0.0063	0.0101	0.0056	0.0237
6	0.0329	0.0377	0.0295	0.0147	0.0526	0.0145	0.4895	0.4390	0.0027	0.0048	0.0068	0.0062	0.0129
7	0.0648	0.0695	0.0168	0.0091	0.0473	0.0126	0.7515	0.1947	0.0048	0.0105	0.0042	0.0017	0.0100
8	0.0320	0.1496	0.0762	0.0287	0.1073	0.0108	0.1415	0.3375	0.0079	0.0492	0.0210	0.0120	0.0252
9	0.0331	0.0262	0.0085	0.0171	0.1407	0.0081	0.9530	0.2450	0.0021	0.0027	0.0019	0.0534	0.0230
10	0.0497	0.0582	0.0528	0.0254	0.0769	0.0236	0.4481	0.4757	0.0053	0.0109	0.0083	0.0113	0.0213
11	0.0844	0.1261	0.0308	0.0093	0.0555	0.0166	0.5378	0.1963	0.0056	0.0130	0.0040	0.0012	0.0109
12	0.0789	0.1296	0.0639	0.0196	0.1105	0.0261	0.4077	0.3302	0.0027	0.0053	0.0024	0.0008	0.0059
13	0.1057	0.1486	0.1299	0.0316	0.0971	0.0493	0.3794	0.4664	0.0089	0.0274	0.0119	0.0056	0.0139
14	0.0496	0.0740	0.0366	0.0116	0.0447	0.0164	0.4489	0.3309	0.0042	0.0081	0.0052	0.0038	0.0105
15	0.0565	0.0879	0.0183	0.0097	0.0758	0.0098	0.5324	0.1723	0.0065	0.0133	0.0034	0.0182	0.0200
16	0.1839	0.2548	0.0596	0.0148	0.1858	0.0348	0.5848	0.1896	0.0120	0.0276	0.0085	0.0020	0.0216
17	0.0873	0.2480	0.0599	0.0076	0.3185	0.0170	0.2836	0.1945	0.0101	0.0222	0.0065	0.9195	0.0273
18	0.0469	0.0668	0.0365	0.0163	0.0850	0.0166	0.4532	0.3533	0.0066	0.0164	0.0057	0.0075	0.0169
19	0.0413	0.1499	0.0359	0.0273	0.0977	0.0080	0.2226	0.1932	0.0050	0.0231	0.0069	0.0073	0.0134
20	0.0323	0.1196	0.0411	0.0163	0.0364	0.0083	0.2011	0.2558	0.0041	0.0183	0.0128	0.0036	0.0109
21	0.0110	0.0242	0.1051	0.0985	0.1446	0.0089	0.0850	0.8128	0.0025	0.0150	0.0732	0.0677	0.0383
Median	0.0496	0.0740	0.0366	0.0163	0.0971	0.0164	0.4489	0.3302	0.0048	0.0109	0.0065	0.0057	0.0183
Mean ± SD	0.0608 ± 0.0386	0.1003 ± 0.0645	0.0487 ± 0.0308	0.0209 ± 0.0189	0.1044 ± 0.0623	0.0183 ± 0.0114	0.4534 ± 0.2275	0.3375 ± 0.1599	0.0053 ± 0.0027	0.0142 ± 0.0110	0.0103 ± 0.0151	0.1041 ± 0.2937	0.0181 ± 0.0075

* SEE = standard error of the estimate.

Supplementary Table S4.7 FDOPA kinetic parameters at the baseline study.

Patient No.	K_1	k_2	k_3	k_4	V_b	K_i	V_d	SF	SEE-K_1	SEE-k_2	SEE-k_3	SEE-k_4	SEE-V_b
1	0.1440	0.1801	0.0397	0.0097	0.0883	0.0260	0.6550	0.1806	0.0186	0.0301	0.0055	0.0040	0.0280
2	0.1884	0.4193	0.0740	0.0011	0.0562	0.0283	0.3820	0.1500	0.0189	0.0314	0.0080	0.0693	0.0188
3	0.1682	0.0794	0.0300	0.0264	0.1146	0.0462	1.5371	0.2742	0.0060	0.0059	0.0025	0.5300	0.0111
4	0.1913	0.1630	0.0692	0.0143	0.1312	0.0570	0.8238	0.2980	0.0152	0.0250	0.0064	0.0030	0.0217
5	0.1006	0.1211	0.0588	0.0216	0.0849	0.0329	0.5594	0.3268	0.0131	0.0348	0.0146	0.0050	0.0218
6	0.1623	0.1610	0.0501	0.0179	0.0505	0.0386	0.7690	0.2373	0.0177	0.0286	0.0062	0.0099	0.0242
7	0.2059	0.1558	0.0343	0.0129	0.0865	0.0372	1.0831	0.1804	0.0323	0.0400	0.0071	0.0058	0.0461
8	0.2160	0.3544	0.1118	0.0360	0.0805	0.0518	0.4633	0.2398	0.0213	0.0419	0.0113	0.0079	0.0206
9	0.1671	0.1943	0.0776	0.0230	0.1083	0.0477	0.6147	0.2854	0.0149	0.0225	0.0055	0.0051	0.0257
10	0.1114	0.0826	0.0278	0.0146	0.0602	0.0280	1.0101	0.2518	0.0070	0.0082	0.0048	0.0058	0.0179
11	0.1737	0.1592	0.0513	0.0192	0.1247	0.0423	0.8249	0.2437	0.0107	0.0155	0.0039	0.0034	0.0135
12	0.1683	0.2274	0.0458	0.0058	0.0962	0.0282	0.6158	0.1676	0.0134	0.0197	0.0043	0.0258	0.0208
13	0.0686	0.1020	0.0752	0.0178	0.0414	0.0291	0.3871	0.4244	0.0080	0.0281	0.0148	0.0044	0.0107
14	0.1703	0.1169	0.0321	0.0088	0.0837	0.0367	1.1430	0.2154	0.0086	0.0103	0.0028	0.6135	0.0142
15	0.1937	0.1629	0.0462	0.0054	0.0610	0.0428	0.9265	0.2209	0.0063	0.0059	0.0029	0.0010	0.0105
16	0.1454	0.1607	0.0635	0.0407	0.1026	0.0412	0.6487	0.2832	0.0104	0.0160	0.0088	0.0121	0.0227
17	0.2680	0.2663	0.0706	0.0324	0.1005	0.0562	0.7955	0.2096	0.0329	0.0360	0.0135	0.0096	0.0392
18	0.0971	0.0996	0.0402	0.0235	0.0918	0.0279	0.6946	0.2876	0.0075	0.0135	0.0069	0.0148	0.0147
19	0.0978	0.0968	0.0135	0.0045	0.0435	0.0119	0.8864	0.1224	0.0073	0.0131	0.0036	0.4709	0.0135
20	0.1150	0.1374	0.0509	0.0068	0.0455	0.0311	0.6105	0.2703	0.0146	0.0359	0.0101	0.0029	0.0177
21	0.0922	0.1395	0.0297	0.0053	0.0536	0.0162	0.5446	0.1755	0.0078	0.0192	0.0030	0.5951	0.0088
Median	0.1671	0.1592	0.0501	0.0146	0.0849	0.0367	0.6946	0.2398	0.0131	0.0225	0.0062	0.0079	0.0188
Mean ± SD	0.1545 ± 0.0494	0.1705 ± 0.0860	0.0520 ± 0.0226	0.0166 ± 0.0110	0.0812 ± 0.0274	0.0361 ± 0.0120	0.7607 ± 0.2756	0.2402 ± 0.0684	0.0139 ± 0.0077	0.0229 ± 0.0114	0.0070 ± 0.0039	0.1143 ± 0.2197	0.0201 ± 0.0093

* SEE = standard error of the estimate.

Supplementary Table S4.8 FDOPA kinetic parameters at 2 weeks after the start of therapy.

Patient No.	K_1	k_2	k_3	k_4	V_b	K_i	V_d	SF	SEE-K_1	SEE-k_2	SEE-k_3	SEE-k_4	SEE-V_b
1	0.1015	0.2318	0.0393	0.0005	0.0463	0.0147	0.3744	0.1450	0.0107	0.0267	0.0035	0.0286	0.0130
2	0.1065	0.1322	0.0612	0.0209	0.0746	0.0337	0.5507	0.3164	0.0103	0.0174	0.0100	0.0053	0.0216
3	0.1494	0.0830	0.0206	0.0107	0.0935	0.0297	1.4417	0.1988	0.0082	0.0119	0.0060	0.0040	0.0153
4	0.2401	0.2869	0.1156	0.0187	0.1778	0.0690	0.5965	0.2872	0.0317	0.0412	0.0145	0.0048	0.0337
5	0.0909	0.0893	0.0388	0.0151	0.0707	0.0275	0.7100	0.3029	0.0094	0.0281	0.0153	0.0090	0.0126
6	0.0944	0.0752	0.0144	0.0089	0.0495	0.0151	1.0545	0.1607	0.0036	0.0044	0.0024	0.4948	0.0101
7	0.1382	0.1981	0.1186	0.0313	0.0590	0.0517	0.4364	0.3745	0.0097	0.0291	0.0151	0.0053	0.0088
8	0.1458	0.1741	0.1160	0.0315	0.0971	0.0583	0.5027	0.3999	0.0165	0.0347	0.0126	0.0155	0.0183
9	0.1632	0.1822	0.0586	0.0168	0.0973	0.0397	0.6775	0.2434	0.0125	0.0209	0.0038	0.0045	0.0188
10	0.0924	0.1329	0.0360	0.0152	0.0669	0.0197	0.5471	0.2131	0.0026	0.0059	0.0019	0.0262	0.0065
11	0.1102	0.1279	0.0494	0.0079	0.0643	0.0307	0.6220	0.2786	0.0066	0.0143	0.0048	0.1239	0.0131
12	0.1451	0.1319	0.0554	0.0350	0.0612	0.0429	0.7745	0.2958	0.0085	0.0151	0.0029	0.0081	0.0068
13	0.1018	0.1031	0.0759	0.0229	0.0438	0.0432	0.5687	0.4240	0.0037	0.0087	0.0040	0.0060	0.0039
14	0.1420	0.0736	0.0479	0.0493	0.1144	0.0559	1.1687	0.3942	0.0111	0.0127	0.0156	0.0141	0.0356
15	0.1366	0.1970	0.1161	0.0274	0.1031	0.0506	0.4364	0.3708	0.0125	0.0358	0.0090	0.0104	0.0183
16	0.1336	0.1559	0.0600	0.0333	0.1237	0.0371	0.6186	0.2779	0.0161	0.0338	0.0157	0.0158	0.0261
17	0.1911	0.2443	0.0771	0.0306	0.1302	0.0459	0.5947	0.2399	0.0120	0.0182	0.0129	0.0091	0.0183
18	0.1036	0.0878	0.0309	0.0060	0.0971	0.0270	0.8731	0.2603	0.0086	0.0166	0.0089	0.0012	0.0203
19	0.0896	0.1231	0.0342	0.0160	0.0842	0.0195	0.5695	0.2174	0.0070	0.0137	0.0051	0.0042	0.0139
20	0.1358	0.1811	0.1142	0.0156	0.0891	0.0525	0.4600	0.3867	0.0089	0.0183	0.0069	0.0033	0.0128
21	0.0943	0.1347	0.0240	0.0081	0.0321	0.0143	0.5940	0.1512	0.0039	0.0092	0.0021	0.3059	0.0046
Median	0.1336	0.1329	0.0554	0.0168	0.0842	0.0371	0.5947	0.2786	0.0094	0.0174	0.0069	0.0090	0.0139
Mean ± SD	0.1289 ± 0.0377	0.1498 ± 0.0590	0.0621 ± 0.0349	0.0201 ± 0.0120	0.0846 ± 0.0342	0.0371 ± 0.0159	0.6748 ± 0.2632	0.2828 ± 0.0855	0.0102 ± 0.0062	0.0198 ± 0.0105	0.0082 ± 0.0051	0.0524 ± 0.1222	0.0158 ± 0.0085

* SEE = standard error of the estimate.

Supplementary Table S4.9 FDOPA kinetic parameters at 6 weeks after the start of therapy.

Patient No.	K_1	k_2	k_3	k_4	V_b	K_i	V_d	SF	SEE-K_1	SEE-k_2	SEE-k_3	SEE-k_4	SEE-V_b
1	0.1875	0.4863	0.0462	0.0100	0.0501	0.0163	0.3522	0.0868	0.0358	0.0937	0.0053	0.0047	0.0225
2	0.1782	0.2850	0.1570	0.0243	0.0702	0.0633	0.4031	0.3552	0.0151	0.0238	0.0148	0.0026	0.0188
3	0.1288	0.0593	0.0099	0.0148	0.1019	0.0185	1.8595	0.1431	0.0087	0.0067	0.0040	1.0581	0.0288
4	0.1773	0.1783	0.1594	0.0527	0.2415	0.0837	0.5250	0.4720	0.0214	0.0294	0.0294	0.0245	0.0376
5	0.0826	0.0512	0.0217	0.0591	0.0942	0.0246	1.1324	0.2977	0.0056	0.0068	0.0063	6.2455	0.0165
6	0.1348	0.1015	0.0579	0.0241	0.0824	0.0489	0.8457	0.3632	0.0103	0.0126	0.0072	0.0085	0.0300
7	0.0877	0.1008	0.0573	0.0255	0.0772	0.0318	0.5545	0.3624	0.0054	0.0124	0.0060	0.0058	0.0111
8	0.1244	0.0723	0.0320	0.0087	0.0328	0.0382	1.1922	0.3068	0.0101	0.0122	0.0040	0.0398	0.0217
9	0.1340	0.2087	0.1312	0.0421	0.1127	0.0517	0.3942	0.3860	0.0128	0.0324	0.0091	0.0099	0.0162
10	0.0687	0.0436	0.0158	0.0221	0.1032	0.0183	1.1568	0.2660	0.0063	0.0091	0.0063	0.0885	0.0210
11	0.1539	0.1943	0.0898	0.0230	0.1079	0.0486	0.5416	0.3161	0.0063	0.0142	0.0101	0.0031	0.0127
12	0.1271	0.0937	0.0256	0.0130	0.0944	0.0273	1.0659	0.2146	0.0082	0.0107	0.0039	0.0065	0.0218
13	0.0898	0.0397	0.0052	0.0198	0.0938	0.0104	2.0001	0.1158	0.0052	0.0039	0.0873	1.6339	0.0225
14	0.1498	0.0474	0.0979	0.1246	0.1966	0.1009	1.0311	0.6738	0.0109	0.0130	0.0322	0.0349	0.0322
15	0.1226	0.1233	0.0496	0.0152	0.0675	0.0352	0.7090	0.2869	0.0082	0.0221	0.0251	0.0088	0.0149
16	0.1592	0.1629	0.0486	0.0094	0.1163	0.0366	0.7528	0.2298	0.0155	0.0263	0.0054	0.0058	0.0234
17	0.1179	0.1336	0.0676	0.0193	0.1027	0.0396	0.5861	0.3360	0.0097	0.0173	0.0067	0.0071	0.0211
18	0.0986	0.0945	0.0555	0.0312	0.0789	0.0365	0.6574	0.3700	0.0051	0.0085	0.0074	0.0045	0.0108
19	0.0829	0.1327	0.0457	0.0139	0.0631	0.0212	0.4644	0.2562	0.0079	0.0216	0.0059	1.2961	0.0138
20	0.1433	0.1257	0.0518	0.0034	0.0190	0.0418	0.8071	0.2918	0.0141	0.0185	0.0068	0.3991	0.0288
21	0.0693	0.0889	0.0118	0.0091	0.0491	0.0081	0.6876	0.1172	0.0036	0.0044	0.0022	1.0289	0.0077
Median	0.1271	0.1015	0.0496	0.0198	0.0938	0.0365	0.7090	0.2977	0.0087	0.0130	0.0067	0.0099	0.0211
Mean ± SD	0.1247 ± 0.0359	0.1345 ± 0.1018	0.0589 ± 0.0451	0.0269 ± 0.0265	0.0931 ± 0.0499	0.0382 ± 0.0231	0.8437 ± 0.4454	0.2975 ± 0.1317	0.0108 ± 0.0072	0.0190 ± 0.0189	0.0136 ± 0.0189	0.5675 ± 1.3954	0.0207 ± 0.0077

* SEE = standard error of the estimate.

Supplementary Table S4.10 Standardized uptake values of FLT at each of the three study time points.

	FLT SUV-early			FLT SUV-late		
Patient No.	**Baseline**	**2 wks**	**6 wks**	**Baseline**	**2 wks**	**6 wks**
1	0.44	0.64	0.37	0.44	0.61	0.37
2	0.53	0.62	1.22	0.56	0.47	1.05
3	0.75	0.50	0.51	0.85	0.45	0.58
4	1.64	0.85	1.29	1.91	1.15	1.64
5	0.72	0.51	0.50	0.85	0.51	0.55
6	0.82	0.44	0.69	0.67	0.44	0.78
7	2.56	1.79	1.23	2.57	1.58	1.07
8	0.78	0.29	0.44	0.66	0.33	0.42
9	1.33	0.50	0.74	1.30	0.46	0.76
10	1.38	0.65	0.77	1.41	0.68	0.85
11	0.86	0.84	1.44	0.79	0.78	1.48
12	1.72	0.96	0.94	1.57	0.84	0.99
13	1.71	1.35	1.18	1.74	1.25	1.40
14	1.06	0.62	0.61	0.90	0.53	0.61
15	0.74	0.70	0.67	0.68	0.51	0.55
16	1.37	1.02	1.08	1.19	0.90	1.07
17	1.41	1.30	1.00	1.13	1.08	1.07
18	0.18	0.48	0.65	0.31	0.49	0.64
19	0.44	0.27	0.40	0.40	0.26	0.29
20	1.63	0.55	0.65	1.52	0.57	0.53
21	0.51	0.56	0.30	0.52	0.41	0.33
Median	0.86	0.62	0.69	0.85	0.53	0.76
Mean ± SD	1.07 ± 0.58	0.74 ± 0.37	0.79 ± 0.34	1.05 ± 0.58	0.68 ± 0.34	0.81 ± 0.38

Supplementary Table S4.11 Standardized uptake values of FLT and their percent change between each of the three study time points.

FLT	**ΔSUV-early (%)**			**ΔSUV-late (%)**		
Patient No.	**Baseline → 2 wks**	**Baseline → 6 wks**	**2 wks → 6 wks**	**Baseline → 2 wks**	**Baseline → 6 wks**	**2 wks → 6 wks**
1	46	-16	-43	39	-16	-39
2	16	131	98	-17	85	122
3	-34	-32	3	-47	-32	29
4	-48	-21	52	-40	-14	43
5	-28	-30	-3	-40	-35	8
6	-47	-17	57	-34	18	78
7	-30	-52	-31	-39	-59	-32
8	-62	-43	50	-51	-36	30
9	-62	-44	48	-64	-42	63
10	-53	-44	19	-51	-40	24
11	-3	67	72	-2	87	90
12	-44	-45	-3	-46	-37	17
13	-21	-31	-12	-28	-19	12
14	-42	-43	-2	-40	-32	15
15	-5	-9	-4	-25	-19	7
16	-25	-21	6	-24	-10	19
17	-8	-29	-23	-5	-5	0
18	159	254	37	57	107	32
19	-38	-9	46	-36	-27	14
20	-66	-60	19	-62	-65	-8
21	11	-42	-48	-20	-36	-19
Median	-30	-30	6	-36	-27	17
Mean ± SD	-18 ± 50	-6 ± 74	16 ± 39	-27 ± 30	-11 ± 47	24 ± 39

Supplementary Table S4.12 FDOPA standardized uptake values at each of the three study time points.

	FDOPA SUV-early			**FDOPA SUV-late**		
Patient No.	**Baseline**	**2 wks**	**6 wks**	**Baseline**	**2 wks**	**6 wks**
1	1.85	1.38	1.05	1.46	1.25	0.82
2	1.44	1.81	2.03	1.39	1.64	2.14
3	2.43	2.11	2.27	2.28	1.78	1.72
4	3.16	3.12	3.43	3.13	3.11	3.38
5	1.15	1.34	1.69	1.04	1.15	1.51
6	2.38	1.83	2.85	2.03	1.44	2.64
7	3.51	2.25	2.00	2.84	2.16	1.85
8	2.12	2.50	1.85	1.85	2.34	1.68
9	2.46	2.30	2.83	2.33	2.02	2.48
10	2.34	1.50	1.95	1.93	1.20	1.69
11	3.07	2.73	2.69	2.45	2.38	2.47
12	2.46	2.76	2.89	2.03	2.36	2.35
13	1.76	2.35	2.16	1.77	2.25	1.83
14	2.70	3.09	2.99	2.28	2.80	2.97
15	2.17	2.03	1.99	2.01	1.96	1.87
16	1.58	1.82	2.37	1.23	1.52	2.07
17	4.03	3.05	3.13	3.30	2.57	2.80
18	2.02	2.73	2.57	1.74	2.42	2.29
19	0.89	1.20	1.22	0.64	1.00	1.05
20	2.64	3.68	4.05	2.50	3.81	4.06
21	1.55	1.35	1.37	1.21	1.03	0.98
Median	2.34	2.25	2.27	2.01	2.02	2.07
Mean ± SD	2.27 ± 0.77	2.24 ± 0.69	2.35 ± 0.75	1.97 ± 0.68	2.01 ± 0.73	2.13 ± 0.79

Supplementary Table S4.13 Percent change in FDOPA standardized uptake values between each of the three study time points.

FDOPA	**ΔSUV-early (%)**			**ΔSUV-late (%)**		
Patient No.	**Baseline → 2 wks**	**Baseline → 6 wks**	**2 wks → 6 wks**	**Baseline → 2 wks**	**Baseline → 6 wks**	**2 wks → 6 wks**
1	-25	-43	-24	-14	-44	-35
2	26	41	12	18	54	31
3	-13	-7	7	-22	-25	-4
4	-1	8	10	-1	8	9
5	16	47	26	10	45	31
6	-23	20	56	-29	30	83
7	-36	-43	-11	-24	-35	-14
8	18	-13	-26	27	-9	-28
9	-6	15	23	-13	6	23
10	-36	-17	29	-38	-12	41
11	-11	-12	-2	-3	1	4
12	12	17	5	16	16	0
13	33	23	-8	27	3	-19
14	14	11	-3	23	30	6
15	-7	-9	-2	-2	-7	-5
16	16	50	30	24	68	36
17	-24	-22	3	-22	-15	9
18	35	27	-6	39	32	-5
19	35	36	1	56	64	5
20	40	54	10	52	62	7
21	-13	-12	1	-15	-18	-4
Median	-1	11	3	-1	6	5
Mean ± SD	2 ± 24	8 ± 29	6 ± 19	5 ± 27	12 ± 33	8 ± 26

Supplementary Table S4.14 FDOPA tumor-to-striatum standardized uptake value ratios (early and late) at each of the three study time points.

	FDOPA Tumor-to-Striatum SUV Ratios (early)			**FDOPA Tumor-to-Striatum SUV Ratios (late)**		
Patient No.	**Baseline**	**2 wks**	**6 wks**	**Baseline**	**2 wks**	**6 wks**
1	1.38	0.76	0.60	1.02	0.67	0.47
2	0.92	1.04	1.68	0.89	0.97	1.61
3	1.41	1.90	1.98	1.25	1.53	1.38
4	1.49	1.45	1.34	1.33	1.39	1.29
5	1.02	1.12	1.26	0.90	0.93	1.06
6	1.36	1.18	1.57	1.01	0.90	1.34
7	1.29	1.32	1.13	0.98	1.20	0.97
8	1.16	1.46	1.20	0.96	1.30	1.09
9	1.17	1.14	1.07	1.09	0.95	0.97
10	1.05	0.94	1.00	0.82	0.73	0.86
11	2.29	1.73	1.53	1.77	1.46	1.35
12	1.82	1.59	1.85	1.47	1.34	1.41
13	0.97	1.52	1.22	0.93	1.38	0.96
14	1.27	1.29	1.35	1.05	1.15	1.28
15	1.39	1.07	1.00	1.20	0.97	0.86
16	2.00	1.87	2.18	1.51	1.51	1.79
17	1.63	1.38	1.49	1.32	1.18	1.36
18	1.09	1.14	1.11	0.90	0.96	0.99
19	1.65	0.86	1.06	1.17	0.65	0.90
20	1.32	1.32	1.19	1.22	1.31	1.10
21	1.02	0.95	0.96	0.79	0.69	0.67
Median	1.32	1.29	1.22	1.05	1.15	1.09
Mean ± SD	1.37 ± 0.35	1.29 ± 0.32	1.32 ± 0.38	1.12 ± 0.25	1.10 ± 0.29	1.13 ± 0.31

Supplementary Table S4.15 Percent change in FDOPA tumor-to-striatum standardized uptake value ratios (early and late) between each of the three study time points.

	Percent Change in FDOPA Tumor-to-Striatum SUV Ratios (early)			Percent Change in FDOPA Tumor-to-Striatum SUV Ratios (late)		
Patient No.	**Baseline → 2 wks**	**Baseline → 6 wks**	**2 wks → 6 wks**	**Baseline → 2 wks**	**Baseline → 6 wks**	**2 wks → 6 wks**
1	-45	-56	-21	-34	-54	-29
2	13	82	62	9	81	67
3	35	40	4	23	11	-10
4	-3	-10	-7	5	-3	-8
5	10	24	13	3	17	14
6	-13	16	33	-12	32	49
7	2	-13	-14	22	-1	-19
8	25	3	-18	35	13	-16
9	-3	-9	-6	-13	-11	2
10	-11	-5	6	-11	4	17
11	-24	-33	-11	-18	-24	-8
12	-13	1	16	-9	-4	6
13	57	26	-20	48	3	-31
14	1	6	5	9	21	11
15	-23	-28	-6	-19	-28	-11
16	-6	9	17	0	18	19
17	-15	-8	8	-10	3	15
18	4	2	-2	7	10	3
19	-48	-36	23	-44	-23	37
20	0	-10	-10	7	-10	-16
21	-7	-6	1	-13	-14	-2
Median	-3	-5	1	0	3	2
Mean ± SD	-3 ± 24	0 ± 29	3 ± 20	-1 ± 22	2 ± 27	4 ± 25

4.10 APPENDIX

Since FDOPA does not cross the red blood cell membrane and is confined to the plasma component when it is in blood (Appendix Figure A4.1), we had to somehow convert the total ^{18}F activity concentration in whole blood (which we measured from the dynamic PET images) to the total FDOPA activity concentration in plasma. To do this, we used the following formula:

$$\begin{aligned}
&C_{wb}(t) = (1-Hct)\times C_{FDOPA}(t)_p + \\
&f_{OMFD}(t)\times[C_{FDOPA}(t)+C_{OMFD}(t)+C_{METS}(t)]_p + \\
&(1-Hct)\times f_{METS}(t)\times[C_{FDOPA}(t)+C_{OMFD}(t)+C_{METS}(t)]_p
\end{aligned}$$

where

$$(C_{F\text{-}18\ total})_{plasma} = [C_{FDOPA}(t)+C_{OMFD}(t)+C_{METS}(t)]_p\,.$$

In order to solve the above equation, we need to find a relationship between the total ^{18}F activity in plasma and the total ^{18}F activity in whole blood. This can be done using the following formula:

$$\frac{(C_{F\text{-}18\ total})_{plasma}}{(C_{F\text{-}18\ total})_{wb}} = \frac{\left[C_{FDOPA}(t)+C_{OMFD}(t)+C_{METS}(t)\right]_p}{(1-Hct)\times\left[C_{FDOPA}(t)+C_{METS}(t)\right]_p + C_{OMFD}(t)_p}$$

which can be reduced in terms of the fractional plasma radioactivity using the following mathematical trick:

$$\frac{(C_{F\text{-}18\ total})_{plasma}}{(C_{F\text{-}18\ total})_{wb}} = \frac{\left[C_{FDOPA}(t) + C_{OMFD}(t) + C_{METS}(t)\right]_p}{(1-Hct)\times\left[C_{FDOPA}(t) + C_{METS}(t)\right]_p + C_{OMFD}(t)_p} \cdot \frac{\dfrac{1}{(C_{F\text{-}18\ total})_{plasma}}}{\dfrac{1}{(C_{F\text{-}18\ total})_{plasma}}}$$

$$\frac{(C_{F\text{-}18\ total})_{plasma}}{(C_{F\text{-}18\ total})_{wb}} = \frac{\left[f_{FDOPA}(t) + f_{OMFD}(t) + f_{METS}(t)\right]_p}{(1-Hct)\times\left[f_{FDOPA}(t) + f_{METS}(t)\right]_p + f_{OMFD}(t)_p}$$

This can be further reduced to:

$$\frac{(C_{F\text{-}18\ total})_{plasma}}{(C_{F\text{-}18\ total})_{wb}} = \frac{1}{(1-Hct)\times\left[1 - f_{OMFD}(t)_p\right] + f_{OMFD}(t)_p}$$

using the fact that $\left[f_{FDOPA}(t) + f_{OMFD}(t) + f_{METS}(t)\right]_p = 1$.

Since we now found a relationship between the total ^{18}F activity in plasma and the total ^{18}F activity in whole blood, we can solve our initial equation which sought to find a relationship between the total ^{18}F activity concentration in whole blood and the total FDOPA activity concentration in plasma.

Thus,

$$C_{FDOPA}(t)_p = C_{wb}(t) \times \frac{\left(1 - \mu(t)\cdot[f_{OMFD}(t) + (1-Hct)\cdot f_{METS}(t)]_p\right)}{(1-Hct)}$$

where

$$\frac{(C_{F\text{-}18\ total})_{plasma}}{(C_{F\text{-}18\ total})_{whole\ blood}} = \mu(t).$$

At very short t, $\frac{(C_{F\text{-}18\ total})_{plasma}}{(C_{F\text{-}18\ total})_{wb}} \cong \frac{1}{1 - Hct}$ since $f_{FDOPA}(t)_p$ is 1 and $f_{OMFD}(t)_p$ and $f_{METS}(t)_p$ are 0 (i.e., OMFD and METS have not formed yet). At very long t,

$$\frac{(C_{F\text{-}18\ total})_{plasma}}{(C_{F\text{-}18\ total})_{wb}} \cong 1.$$

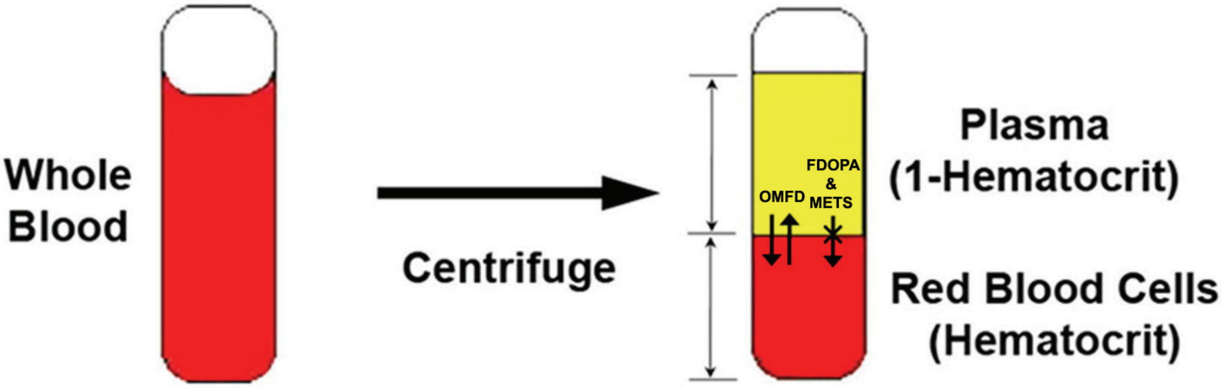

Appendix Figure A4.1 FDOPA does not cross the red blood cell membrane and is confined to the plasma space when it is in blood. OMFD, on the other hand, can cross the red blood cell membrane bidirectionally.

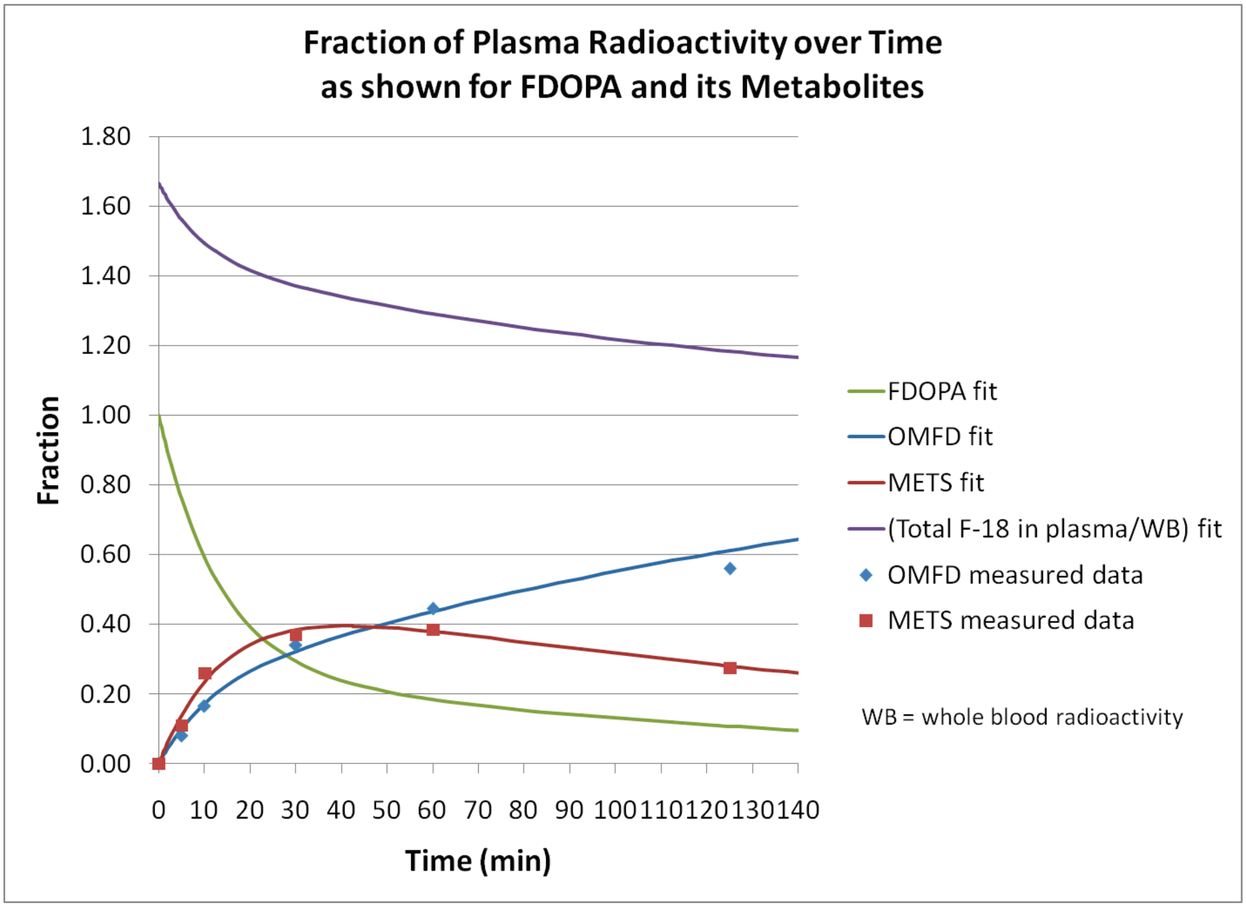

Appendix Figure A4.2 Fitted exponential curves to the measured fractions of plasma radioactivity for OMFD and METS. The measured data was taken from the publication of Huang *et al.* (*46*). The equations for the fitted exponential curves are shown below:

$$f_{METS}(t)_p = 0.52 \times (e^{-0.004997t} - e^{-0.06892t})$$

$$f_{OMFD}(t)_p = 0.80 \times (1 - e^{-0.005337t}) + 0.20 \times (1 - e^{-0.09695t})$$

The decaying exponential curve (shown in green) represents the fraction of plasma radioactivity over time for FDOPA and was derived using the following relationship:

$$f_{FDOPA}(t)_p = 1 - \left[f_{OMFD}(t) + f_{METS}(t) \right]_p$$

The top descending purple curve is the total ^{18}F activity in plasma divided by the total ^{18}F activity in whole blood [i.e., μ(t)].

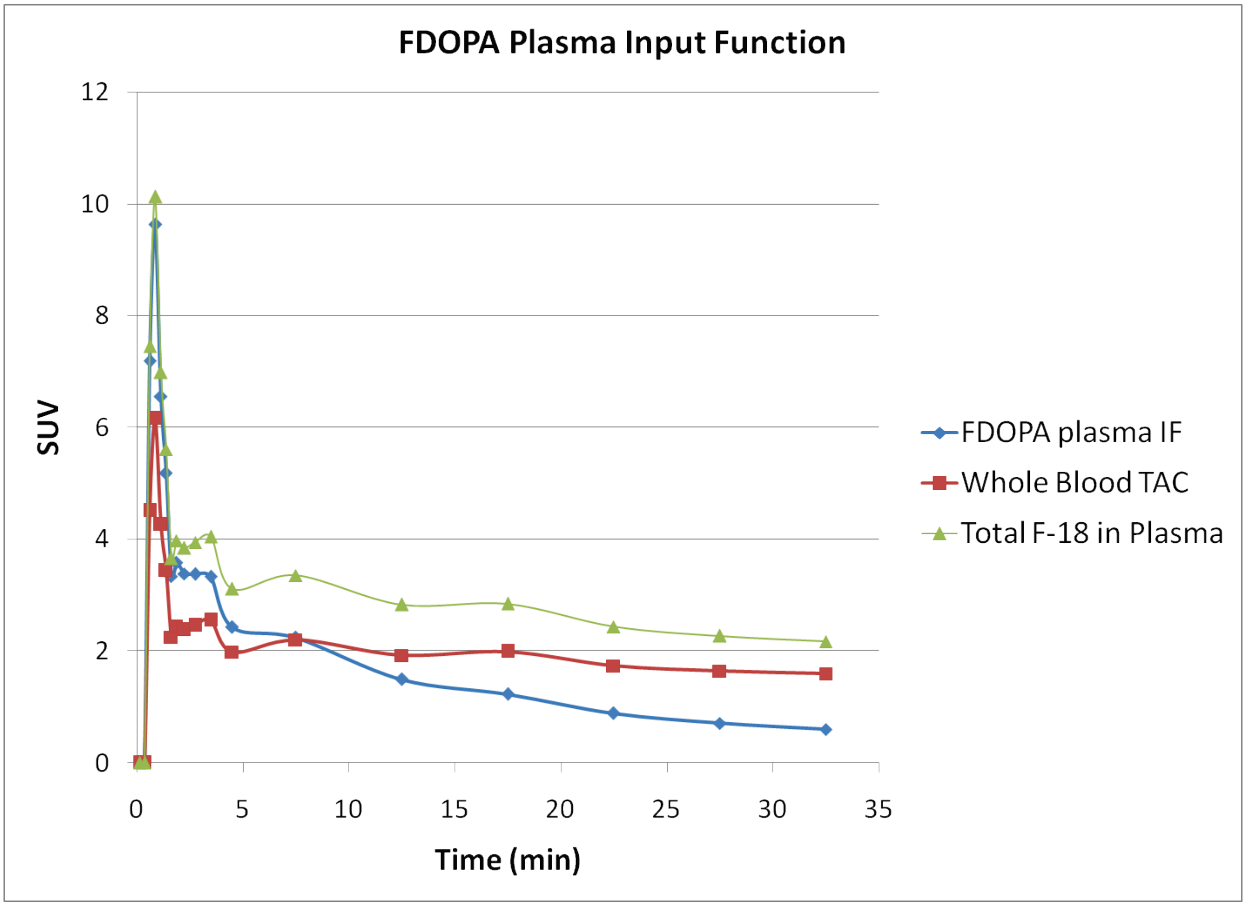

Appendix Figure A4.3 FDOPA plasma input function (shown in blue) after corrections for metabolites, hematocrit, and partial volume effects. Shown in red is the whole blood time-activity curve after partial volume correction only. Shown in green is the total ^{18}F radioactivity in plasma. The input function is generally required for absolute quantification in PET imaging (*5*). An erroneous input function in shape would not allow for a good fit of the tissue data, while an erroneous function of its amplitude would generate biased rate constant values (*4, 54*).

4.11 REFERENCES

1. CBTRUS (2013). CBTRUS Statistical Report: Primary Brain and Central Nervous System Tumors Diagnosed in the United States in 2005-2009. Source: Central Brain Tumor Registry of the United States, Hinsdale, IL. website: www.cbtrus.org.

2. Siegel R, Naishadham D, Jemal A. Cancer statistics, 2012. *CA Cancer J Clin.* Jan-Feb 2012;62(1):10-29.

3. Foltz G. New Hope For Battling Brain Cancer. *Scientific American Mind.* 2010;21(1):50.

4. Phelps ME. *PET : molecular imaging and its biological applications*. New York: Springer; 2004.

5. Phelps ME, Mazziotta JC, Schelbert HR. *Positron emission tomography and autoradiography : principles and applications for the brain and heart*. New York: Raven Press; 1986.

6. Phelps ME. PET: the merging of biology and imaging into molecular imaging. *J Nucl Med.* Apr 2000;41(4):661-681.

7. Phelps ME. Positron emission tomography provides molecular imaging of biological processes. *Proc Natl Acad Sci U S A.* Aug 1 2000;97(16):9226-9233.

8. Phelps ME, Mazziotta JC. Positron emission tomography: human brain function and biochemistry. *Science.* May 17 1985;228(4701):799-809.

9. Phelps ME, Huang SC, Hoffman EJ, Selin C, Sokoloff L, Kuhl DE. Tomographic measurement of local cerebral glucose metabolic rate in humans with (F-18)2-fluoro-2-deoxy-D-glucose: validation of method. *Ann Neurol.* Nov 1979;6(5):371-388.

10. Dumit J. *Picturing personhood : brain scans and biomedical identity*. Princeton, N.J.: Princeton University Press; 2004.

11. Weissleder R. *Molecular imaging : principles and practice*. Shelton, Conn.: People's Medical Pub. House-USA; 2009.

12. Huang SC, Phelps ME, Hoffman EJ, Sideris K, Selin CJ, Kuhl DE. Noninvasive determination of local cerebral metabolic rate of glucose in man. *Am J Physiol.* Jan 1980;238(1):E69-82.

13. Huang SC. Role of Kinetic Modeling in Biomedical Imaging. *J Med Sci.* 2008;28(2):57-63.

14. Clarke JL, Chang SM. Neuroimaging: diagnosis and response assessment in glioblastoma. *Cancer J.* Jan-Feb 2012;18(1):26-31.

15. Schwarzenberg J, Czernin J, Cloughesy TF, et al. 3'-Deoxy-3'-^{18}F-Fluorothymidine PET and MRI for Early Survival Predictions in Patients with Recurrent Malignant Glioma Treated with Bevacizumab. *J Nucl Med.* Jan 2012;53(1):29-36.

16. Walter F, Cloughesy T, Walter MA, et al. Impact of 3,4-dihydroxy-6-^{18}F-fluoro-L-phenylalanine PET/CT on managing patients with brain tumors: the referring physician's perspective. *J Nucl Med.* Mar 2012;53(3):393-398.

17. Clarke JL, Chang S. Pseudoprogression and pseudoresponse: challenges in brain tumor imaging. *Curr Neurol Neurosci Rep.* May 2009;9(3):241-246.

18. Herholz K, Langen KJ, Schiepers C, Mountz JM. Brain tumors. *Semin Nucl Med.* Nov 2012;42(6):356-370.

19. Olivero WC, Dulebohn SC, Lister JR. The use of PET in evaluating patients with primary brain tumours: is it useful? *J Neurol Neurosurg Psychiatry.* Feb 1995;58(2):250-252.

20. Ricci PE, Karis JP, Heiserman JE, Fram EK, Bice AN, Drayer BP. Differentiating recurrent tumor from radiation necrosis: time for re-evaluation of positron emission tomography? *Am J Neuroradiol.* Mar 1998;19(3):407-413.

21. Chen W. Clinical applications of PET in brain tumors. *J Nucl Med.* Sep 2007;48(9):1468-1481.

22. Chen W, Cloughesy T, Kamdar N, et al. Imaging proliferation in brain tumors with ^{18}F-FLT PET: comparison with ^{18}F-FDG. *J Nucl Med.* Jun 2005;46(6):945-952.

23. Bading JR, Shields AF. Imaging of cell proliferation: status and prospects. *J Nucl Med.* Jun 2008;49 Suppl 2:64S-80S.

24. Fueger BJ, Czernin J, Cloughesy T, et al. Correlation of 6-^{18}F-fluoro-L-dopa PET uptake with proliferation and tumor grade in newly diagnosed and recurrent gliomas. *J Nucl Med.* Oct 2010;51(10):1532-1538.

25. Chen W, Silverman DH, Delaloye S, et al. ^{18}F-FDOPA PET imaging of brain tumors: comparison study with ^{18}F-FDG PET and evaluation of diagnostic accuracy. *J Nucl Med.* Jun 2006;47(6):904-911.

26. Wardak M, Schiepers C, Dahlbom M, et al. Discriminant analysis of ^{18}F-fluorothymidine kinetic parameters to predict survival in patients with recurrent high-grade glioma. *Clin Cancer Res.* Oct 15 2011;17(20):6553-6562.

27. Zdanowicz MM, American Society of Health-System Pharmacists. *Concepts in pharmacogenomics*. Bethesda, MD: American Society of Health-System Pharmacists; 2010.

28. Walsh JC, Padgett HC, Ysaguirre T, inventors; Siemens Medical Solutions USA, Inc., assignee. Method for preparing radiolabeled thymidine having low chromophoric byproducts. U.S. patent 7419653, 2008.

29. Namavari M, Bishop A, Satyamurthy N, Bida G, Barrio JR. Regioselective radiofluorodestannylation with $[^{18}F]F_2$ and $[^{18}F]CH_3COOF$: a high yield synthesis of 6-$[^{18}F]$Fluoro-L-dopa. *Int J Rad Appl Instrum A.* Aug 1992;43(8):989-996.

30. Hudson HM, Larkin RS. Accelerated image reconstruction using ordered subsets of projection data. *IEEE Trans Med Imaging.* 1994;13(4):601-609.

31. Nuyts J, Michel C, Dupont P. Maximum-likelihood expectation-maximization reconstruction of sinograms with arbitrary noise distribution using NEC-transformations. *IEEE Trans Med Imaging.* May 2001;20(5):365-375.

32. Ell PJ, Gambhir SS. *Nuclear medicine in clinical diagnosis and treatment*. 3rd ed. Edinburgh ; New York: Churchill Livingstone; 2004.

33. Schiepers C, Hoh CK, Nuyts J, Wu HM, Phelps ME, Dahlbom M. Factor analysis in prostate cancer: delineation of organ structures and automatic generation of in- and output functions. *IEEE Trans Nucl Sci.* 2002;49(5):2338-2343.

34. Schiepers C, Hoh CK, Dahlbom M, Wu HM, Phelps ME. Factor analysis for delineation of organ structures, creation of in- and output functions, and standardization of multicenter kinetic modeling. *Proceedings SPIE.* 1999;3661:1343-1350.

35. Sitek A, Di Bella EV, Gullberg GT. Factor analysis with a priori knowledge--application in dynamic cardiac SPECT. *Phys Med Biol.* Sep 2000;45(9):2619-2638.

36. Muzi M, Vesselle H, Grierson JR, et al. Kinetic analysis of 3'-deoxy-3'-fluorothymidine PET studies: validation studies in patients with lung cancer. *J Nucl Med.* Feb 2005;46(2):274-282.

37. Personal Communication with Dr. John R. Grierson.

38. Reske SN, Deisenhofer S. Is 3'-deoxy-3'-^{18}F-fluorothymidine a better marker for tumour response than ^{18}F-fluorodeoxyglucose? *Eur J Nucl Med Mol Imaging.* Jul 2006;33 Suppl 1:38-43.

39. Shields AF. PET imaging of tumor growth: not as easy as it looks. *Clin Cancer Res.* Mar 1 2012;18(5):1189-1191.

40. Schiepers C, Chen W, Dahlbom M, Cloughesy T, Hoh CK, Huang SC. ^{18}F-fluorothymidine kinetics of malignant brain tumors. *Eur J Nucl Med Mol Imaging.* Jul 2007;34(7):1003-1011.

41. Huang SC, Yu DC, Barrio JR, et al. Kinetics and modeling of L-6-[^{18}F]fluoro-dopa in human positron emission tomographic studies. *J Cereb Blood Flow Metab.* Nov 1991;11(6):898-913.

42. Schiepers C, Chen W, Cloughesy T, Dahlbom M, Huang SC. ^{18}F-FDOPA kinetics in brain tumors. *J Nucl Med.* Oct 2007;48(10):1651-1661.

43. Beuthien-Baumann B, Bredow J, Burchert W, et al. 3-O-methyl-6-[^{18}F]fluoro-L-DOPA and its evaluation in brain tumour imaging. *Eur J Nucl Med Mol Imaging.* Jul 2003;30(7):1004-1008.

44. Huang SC. Anatomy of SUV. Standardized uptake value. *Nucl Med Biol.* Oct 2000;27(7):643-646.

45. Visvikis D, Francis D, Mulligan R, et al. Comparison of methodologies for the in vivo assessment of ^{18}FLT utilisation in colorectal cancer. *Eur J Nucl Med Mol Imaging.* Feb 2004;31(2):169-178.

46. Huang SC, Barrio JR, Yu DC, et al. Modelling approach for separating blood time-activity curves in positron emission tomographic studies. *Phys Med Biol.* Jun 1991;36(6):749-761.

47. Petrie A, Sabin C. *Medical statistics at a glance*. 3rd ed. Chichester, UK ; Hoboken, NJ: Wiley-Blackwell; 2009.

48. Dietz T, Kalof L. *Introduction to social statistics : the logic of statistical reasoning*. Chichester, West Sussex ; Malden, MA : Wiley-Blackwell; 2009.

49. Yamamoto Y, Ono Y, Aga F, Kawai N, Kudomi N, Nishiyama Y. Correlation of ^{18}F-FLT Uptake with Tumor Grade and Ki-67 Immunohistochemistry in Patients with Newly Diagnosed and Recurrent Gliomas. *J Nucl Med.* Dec 2012;53(12):1911-1915.

50. Plotnik DA, McLaughlin LJ, Chan J, Redmayne-Titley JN, Schwartz JL. The role of nucleoside/nucleotide transport and metabolism in the uptake and retention of 3'-fluoro-3'-deoxythymidine in human B-lymphoblast cells. *Nucl Med Biol.* Oct 2011;38(7):979-986.

51. Grierson JR, Schwartz JL, Muzi M, Jordan R, Krohn KA. Metabolism of 3'-deoxy-3'-[F-18]fluorothymidine in proliferating A549 cells: validations for positron emission tomography. *Nucl Med Biol.* Oct 2004;31(7):829-837.

52. Lammertsma AA, Hume SP. Simplified reference tissue model for PET receptor studies. *Neuroimage.* Dec 1996;4(3 Pt 1):153-158.

53. Lammertsma AA, Bench CJ, Hume SP, et al. Comparison of methods for analysis of clinical [^{11}C]raclopride studies. *J Cereb Blood Flow Metab.* Jan 1996;16(1):42-52.

54. Khalil MM. *Basic sciences of nuclear medicine*. Heidelberg: Springer; 2011.

55. Rasey JS, Grierson JR, Wiens LW, Kolb PD, Schwartz JL. Validation of FLT uptake as a measure of thymidine kinase-1 activity in A549 carcinoma cells. *J Nucl Med.* Sep 2002;43(9):1210-1217.

56. Shields AF, Grierson JR, Dohmen BM, et al. Imaging proliferation in vivo with [F-18]FLT and positron emission tomography. *Nat Med.* Nov 1998;4(11):1334-1336.

57. Barwick T, Bencherif B, Mountz JM, Avril N. Molecular PET and PET/CT imaging of tumour cell proliferation using F-18 fluoro-L-thymidine: a comprehensive evaluation. *Nucl Med Commun.* Dec 2009;30(12):908-917.

58. Garnett ES, Firnau G, Nahmias C. Dopamine visualized in the basal ganglia of living man. *Nature.* Sep 8-14 1983;305(5930):137-138.

59. Barrio JR, Huang SC, Phelps ME. Biological imaging and the molecular basis of dopaminergic diseases. *Biochem Pharmacol.* Aug 1 1997;54(3):341-348.

60. Stout DB, Huang SC, Melega WP, Raleigh MJ, Phelps ME, Barrio JR. Effects of large neutral amino acid concentrations on 6-[F-18]Fluoro-L-DOPA kinetics. *J Cereb Blood Flow Metab.* Jan 1998;18(1):43-51.

61. Heiss WD, Wienhard K, Wagner R, et al. F-Dopa as an amino acid tracer to detect brain tumors. *J Nucl Med.* Jul 1996;37(7):1180-1182.

Chapter 5

Summary and Conclusions

5.1 DISSERTATION SUMMARY AND FUTURE WORK

Positron emission tomography (PET) is a molecular imaging technique that provides unique information about the biochemical and physiological changes associated with disease (*1-6*). The functional information provided by PET is the major characteristic that differentiates this modality from other imaging technologies that primarily provide structural or anatomical information (*7, 8*). Biochemical processes form the basis of the human body's capacity to function and alterations in these processes can produce or result from abnormal function (*3, 4*). These changes occur at early stages of disease before anatomic alterations are seen by structural imaging modalities (*9, 10*). Information provided by PET can thus improve our knowledge and understanding of the underlying biochemical mechanisms associated with disease, as well as help monitor the effectiveness of patient treatment.

The unique capability of PET is derived from the use of compounds labeled with positron-emitting radionuclides to trace various biological pathways *in vivo* and from the use of coincidence detection to localize the distribution of these probes within the body (*1, 11, 12*). Compartmental modeling and tracer kinetic analysis can extend simple quantitative measures of the radiotracer's concentration and distribution in the body to more pertinent and informative measures of biologic function (*5, 13*). Analysis of a *temporal sequence* of PET images allows estimation of parameters that represent specific biologic processes such as regional blood flow, rates of substrate metabolism (e.g., glucose and oxygen), enzyme activity, receptor or binding site densities, and levels of gene expression (*1, 13-19*). The tracer kinetic method is thus one of the primary and fundamental principles underlying PET.

In this dissertation, we covered three projects that utilized the quantitative capability of PET for studying two neurological disorders: Alzheimer's disease (AD) and recurrent brain tumors. While studying these brain diseases in human patients, we also looked at the pharmacokinetics of three radiotracers: ^{18}F-FDDNP, ^{18}F-FLT, and ^{18}F-FDOPA. ^{18}F-FDDNP is a PET probe that binds to beta-amyloid plaques and neurofibrillary tangles, the cardinal pathological hallmarks of AD. ^{18}F-FLT is a thymidine analog used in PET to evaluate tumor cell proliferation and ^{18}F-FDOPA is an aromatic amino acid analog used in PET to image large neutral amino acid transport in tumors. The main purpose of this collective work was to extend the field of PET and to advocate the use of tracer kinetic modeling for routine clinical use.

One of the goals in PET imaging is to produce an image volume that accurately describes the true distribution of the injected radioactivity. The correction factor that has the most significant impact on the quantitative aspects of a PET image is attenuation correction. Without it, the reconstructed images will give a distorted view of the true activity distribution. Furthermore, the PET images will not be quantitative. Attenuation in PET depends on both the attenuation coefficient of the object and the total path length that the annihilation photons must pass through in the attenuating medium, but it is independent of the location of the annihilation event along a given line of response. This is unique to annihilation coincidence detection and greatly simplifies the attenuation correction procedure. In stand-alone PET imaging systems, the transmission scan (usually measured by placing a rotating positron-emitting source outside the object and just inside of the PET detector rings) is used to correct for photon attenuation. Head movement during a PET scan (especially a dynamic scan) can complicate matters by inducing misalignment between the transmission scan that is acquired at the start of the study and the serial emission scans that are acquired afterwards. This is particularly true when performing PET scans in the elderly, with increased significance in patients with dementia or movement disorders. Head movement can thus affect both the qualitative and quantitative aspects of a PET image, making it difficult to accurately interpret the results.

In Chapter 2, we described a retrospective image-based movement correction method and evaluated its implementation on dynamic ^{18}F-FDDNP PET images of cognitively intact controls and patients with AD, each with varying degrees of head movement. The movement correction method corrected for transmission-emission misalignments as well as for emission-emission misalignments that might have been present in the dynamic PET scan. We saw that after applying the movement correction method, the image quality, tracer kinetics, and diagnostic accuracy of the ^{18}F-FDDNP PET images were significantly improved. Our lab has recently extended the application of the movement correction method to integrated PET/CT imaging systems (*20, 21*), where the CT image (instead of the PET transmission image) is used for PET attenuation correction. Motion artifacts could also be introduced during acquisition of MRI data (Figure 5.1). With the advent of the first integrated whole-body PET/MR imaging system in 2010, this can be a problem since the MR data is used for attenuation correction of the PET data (*22-24*). Future work needs to address this issue and could possibly incorporate methods that have been presented in this dissertation.

In Chapter 3, we investigated whether changes in tumor ^{18}F-FLT kinetic parameters, taken early after the start of therapy, could predict overall survival and progression-free survival in patients with recurrent malignant glioma undergoing treatment with bevacizumab (an angiogenesis inhibitor) and irinotecan (a chemotherapeutic agent). We found that when a group of optimal kinetic parameter changes are incorporated into a linear discriminant function, one could accurately classify patients into their known survival groups. This method could help physicians provide personalized treatment regimens by discontinuing ineffective therapies and switching to more advanced treatment regimens that could help improve patient outcome. Future work will explore the incorporation of *a priori* biological information on temporal parameter changes before going through discriminant analysis to improve the robustness of the discriminant function. The use of such approaches for developing signatures associated with different temporal progression patterns of tracer kinetics is thus expected to become a powerful tool, for clinical as well as preclinical studies. A proposed study schema for utilizing ^{18}F-FLT PET imaging as an informative platform for evaluating the combination of bevacizumab and irinotecan with other therapies in patients with recurrent glioblastoma is shown in Figure 5.2.

In Chapter 4, we expanded on what we did in Chapter 3 by acquiring longitudinal ^{18}F-FDOPA PET scans in addition to ^{18}F-FLT PET scans. We also tried to predict overall survival as a continuous outcome variable using multiple linear regression (MLR) as opposed to a dichotomous categorical variable with discriminant analysis from before. We found that in patients with *recurrent* malignant glioma, kinetic information from ^{18}F-FLT alone was more predictive than using information from ^{18}F-FDOPA alone. Moreover, we found that parameters from ^{18}F-FLT alone may provide sufficient information to predict overall survival with reasonable accuracy than using both probes combined (which provided comparable results). The slight increase in accuracy for predicting overall survival with a combination of ^{18}F-FLT and ^{18}F-FDOPA PET information may not necessitate the acquisition of an ^{18}F-FDOPA PET scan for therapy monitoring in patients with *recurrent* glioma. Whether the combined information from

^{18}F-FLT and ^{18}F-FDOPA PET images may help in the prediction of overall survival in patients with *newly diagnosed* glioma requires future study.

The study presented in Chapter 4 demonstrated that the use of PET kinetic analysis and MLR can be a powerful tool for clinicians monitoring patient treatment. This method could provide a window of opportunity during which treatment regimens can be tailored according to the survival predictions from the MLR analysis. Specifically, it offers the neuro-oncologist an indicator on whether to wait and watch on the current therapy or to switch the patient altogether to a different and potentially more efficacious treatment regimen earlier on. The clinical effect of this added information could potentially avoid unnecessary drug toxicity to the patient, help increase patient lifespan, and reduce undue health care costs. This method could also augment the conventional assessment of tumor response to anti-cancer therapies and be included in standardized criteria for response evaluation in neuro-oncology. In the future, one may incorporate anatomical and functional information from integrated imaging systems (such as PET/CT and PET/MR) in the MLR analysis.

A potential shortcoming of the experimental design presented in the projects described in Chapters 3 and 4 is that both therapeutic agents were administered at approximately the same time. In the future, one could circumvent this hurdle by optimizing the scheduling of the therapeutic agents. For example, rather than administering both types of drugs to a patient during the same period, treatment with blood-distributed cytotoxic agents could be followed by anti-angiogenic therapy at a later time. Thus, the sequential scheduling of irinotecan and bevacizumab (or a smarter combination of these drugs with pharmaceutical agents targeting other cancer signaling pathways) could help improve future treatment plans.

In conclusion, the culmination of the work presented in this dissertation has demonstrated in three examples that the utility of kinetic quantification can significantly improve the value of PET for imaging biological functions in brain tissues *in vivo*. The developed methodologies in these examples are also expected to be useful in other quantitative brain PET imaging studies – for other applications or using other radiotracers. Although this dissertation focused on the human brain, the principles, approaches, and use of PET as they are discussed in this text can be applied to other organ systems as well; the technology of PET is directed at the biochemical processes that underlie *all* body functions and their alterations in disease.

5.2 FIGURES

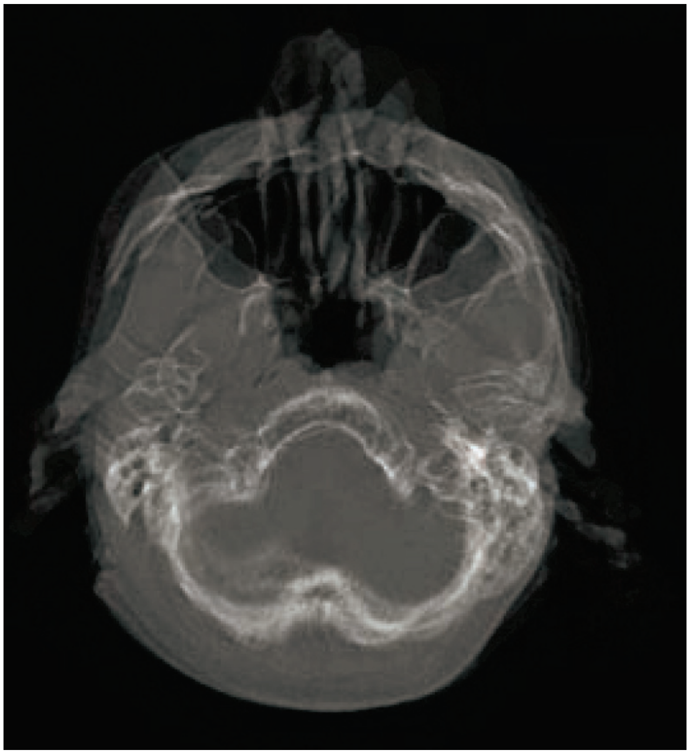

Figure 5.1 Like with PET, motion artifacts can be introduced during acquisition of MRI data. In PET/MR hybrid imaging systems, head movement could thus serve as a barrier to ensuring the integrity of the the resulting PET images since the MR data is used to correct the PET data for photon attenuation. Methods similar to those presented in this dissertation (which worked with a stand-alone PET imaging system) need to be developed to address this issue in the future.

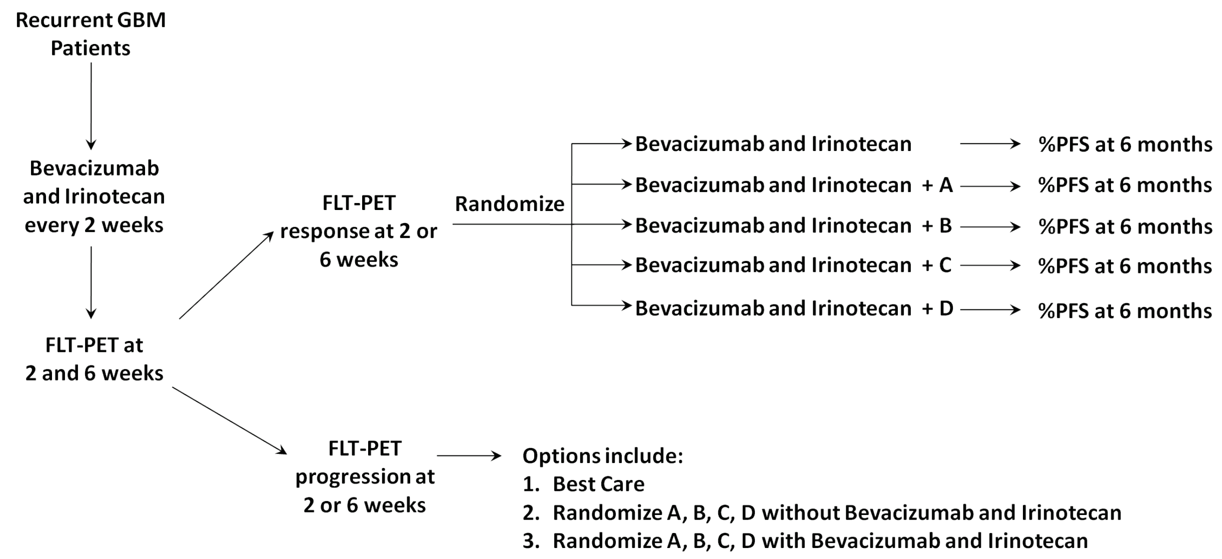

Figure 5.2 Proposed study schema using ^{18}F-FLT PET as an informative imaging platform for assessing treatment response early during the course of cancer therapy in patients with recurrent glioblastoma. The idea is that those patients without any metabolic evidence of tumor response on ^{18}F-FLT PET early in the course of treatment should stop the present therapy and consider alternative treatment. The predictive effect of ^{18}F-FLT PET would afford the opportunity to stratify patients into responders and non-responders early in their therapy and to focus the investigational combinations in the treatment group that responds. Information from ^{18}F-FLT PET could thus be used as a platform for identifying active combinations to eventually be added to bevacizumab and irinotecan in upfront glioblastoma with chemoradiation. In the clinical trial design, patients will be followed until progression and death.

5.3 REFERENCES

1. Phelps ME. *PET : molecular imaging and its biological applications*. New York: Springer; 2004.

2. Phelps ME, Mazziotta JC, Schelbert HR. *Positron emission tomography and autoradiography : principles and applications for the brain and heart*. New York: Raven Press; 1986.

3. Phelps ME, Schelbert HR, Mazziotta JC. Positron computed tomography for studies of myocardial and cerebral function. *Ann Intern Med.* Mar 1983;98(3):339-359.

4. Phelps ME, Mazziotta JC. Positron emission tomography: human brain function and biochemistry. *Science.* May 17 1985;228(4701):799-809.

5. Henkin RE. *Nuclear medicine*. 2nd ed. Philadelphia: Mosby Elsevier; 2006.

6. Heiss WD, Phelps ME. *Positron emission tomography of the brain*. Berlin ; New York: Springer-Verlag; 1983.

7. Cherry SR, Sorenson JA, Phelps ME. *Physics in nuclear medicine*. 3rd ed. Philadelphia, Pa.: Saunders; 2003.

8. Bushberg JT. *The essential physics of medical imaging*. 2nd ed. Philadelphia: Lippincott Williams & Wilkins; 2002.

9. Phelps ME. PET: the merging of biology and imaging into molecular imaging. *J Nucl Med.* Apr 2000;41(4):661-681.

10. Phelps ME. Positron emission tomography provides molecular imaging of biological processes. *Proceedings of the National Academy of Sciences of the United States of America.* Aug 1 2000;97(16):9226-9233.

11. Huang SC. Role of Kinetic Modeling in Biomedical Imaging. *J Med Sci.* 2008;28(2):57-63.

12. Cherry SR, Phelps ME. Imaging Brain Function with Positron Emission Tomography. In: Toga AW, Mazziotta JC, eds. *Brain mapping : the methods*. San Diego: Academic Press; 1996.

13. Wahl RL. *Principles and practice of positron emission tomography*. Philadelphia: Lippincott Williams & Wilkins; 2002.

14. Weissleder R. *Molecular imaging : principles and practice*. Shelton, Conn.: People's Medical Pub. House-USA; 2009.

15. Wu HM, Huang SC, Hattori N, et al. Subcortical white matter metabolic changes remote from focal hemorrhagic lesions suggest diffuse injury after human traumatic brain injury. *Neurosurgery.* Dec 2004;55(6):1306-1315; discussion 1316-1307.

16. Wright EM, Barrio JR, inventors; The Regents of the University of California, assignee. Tracers for monitoring the activity of sodium/glucose cotransporters in health and disease. US patent 0008856A1, 2010.

17. Wright EM, Loo DD, Hirayama BA. Biology of human sodium glucose transporters. *Physiol Rev.* Apr 2011;91(2):733-794.

18. Maddahi J, Czernin J, Lazewatsky J, et al. Phase I, first-in-human study of BMS747158, a novel ^{18}F-labeled tracer for myocardial perfusion PET: dosimetry, biodistribution, safety, and imaging characteristics after a single injection at rest. *J Nucl Med.* Sep 2011;52(9):1490-1498.

19. Huang S-C, Dahlbom M, Maddahi J, et al. Streamlined quantification of absolute MBF at rest and stress with flurpiridaz F-18 injection PET in normal subjects and patients with coronary artery disease (CAD). *Society of Nuclear Medicine Annual Meeting Abstracts.* 2011;52(Supplement 1):1114.

20. Ye H, Wardak M, Wong K-P, Dahlbom M, Huang S-C. Movement correction improves the quality of dynamic PET-CT images. *Society of Nuclear Medicine Annual Meeting Abstracts.* 2010;51:518.

21. Ye H, Wong K-P, Wardak M, et al. Movement correction method for dynamic PET/CT images: Application to Down syndrome ^{18}F-FDDNP dynamic scans. *Society of Nuclear Medicine Annual Meeting Abstracts.* 2011;52:213.

22. Catana C, Drzezga A, Heiss WD, Rosen BR. PET/MRI for neurologic applications. *J Nucl Med.* Dec 2012;53(12):1916-1925.

23. Drzezga A, Souvatzoglou M, Eiber M, et al. First clinical experience with integrated whole-body PET/MR: comparison to PET/CT in patients with oncologic diagnoses. *J Nucl Med.* Jun 2012;53(6):845-855.

24. Pichler BJ, Kolb A, Nagele T, Schlemmer HP. PET/MRI: paving the way for the next generation of clinical multimodality imaging applications. *J Nucl Med.* Mar 2010;51(3):333-336.